Subwavelength engineering of silicon waveguides and cavities for nonlinear photonics

Jianhao Zhang

Subwavelength engineering of silicon waveguides and cavities for nonlinear photonics

Thèse de doctorat de Zhejiang University
et de l'Université Paris-Saclay
préparée à l'Université Paris-Sud

École doctorale n°575
Electrical,Optical,Bio: physics and Engineering (EOBE)

Spécialité de doctorat:
Electronique et Optoélectronique, Nano- et Microtechnologies

Thèse présentée et soutenue à Hangzhou,19/10/2019, par

Jianhao Zhang

Composition du Jury :

M. Xinliang Zhang
Professeur,   Huazhong University of Science and Technology   Président
M. Régis Barille
Professeur,   Université Angers   Rapporteur
M. Liu Liu
Professeur,   South China Normal University   Rapporteur
Mme Béatrice Dagens
Professeur,   CNRS/ Université Paris-Sud   Examinateur
M. Jianjun He
Professeur,   Zhejiang University   Examinateur
M. Eric Cassan
Professeur,   Université Paris-Sud   Directeur de thèse
M. Sailing He
Professeur,   Zhejiang University/ Royal Institute of Technology   Co-Directeur de thèse

Acknowledgement

This thesis would have been impossible without the contribution of many colleagues and friends. First of all, I would like to acknowledge my supervisor, Prof. Eric Cassan and Prof. Sailing He. I could not have imagined conducting the doctoral study without Prof. Eric Cassan, without his tireless efforts helping me my thesis, publications, research in general and everything else. His great enthusiasm, perceptiveness and patience that I have gained as a student and friend will be leading me in my future career in sciences and educations. Thank Prof. Sailing He, who never spare the encouragement on me to pursue of high-quality, innovative research which drives me to reflect on my work from time to time and cultivate my cautiousness and conscientiousness. None of my achievement would have been possible without their supports.

I would like to thank the research group Minaphot in Center for Nanoscience and Nanotechnology, which was and will always be really fun to work at. I enjoyed the freedom it provided to me to explore new ideas and the scientifically challenging environment to improve my decency in scientific research. I would like to thank all the other people involved in this Group: thank Prof. Laurent Vivien and Prof. Delphine Marris-Morini for their endless supports on my research, from instrument assistance to professional advices; thank Researcher Carlos Alonso-Ramos for his valuable suggestions in characterization experiments and devices design; thank Researcher Xavier Le-Roux and Dr. Durán-Valdeiglesias for their kind and professional supports in micro-nano device fabrication; Thank Dr. Joan-Manel Ramirez, Dr. Daniel Benedikovic, Dr. Guillaume Marcaud, Dr. Samuel Serna, Dr. Vladyslav Vakarin, Dr. Mathias Berciano, Dr. Weiwei Zhang for all the helpful discussions in advancing my work and inspiring me in photonic devices and physics; Thank Qiankun, Zhengrui, Alicia, Daisy, Dorian, Christian, Miguel, Dinh, Lucas, Sylvain for all the pleasant time I have spent with and learning from them, on both sciences and life. Particularly, I am very grateful to Alicia who gave me a lot of encouragement and kind concerns when life setbacks wreaked havoc in my confidence in the future.

I would like to express my deep gratitude to Prof. Beatrice Dagens, Prof. Regis Barille, Prof. Liu Liu, Prof. Xinliang Zhang, Prof. Jianjun He for their valuable efforts in improving the quality of my thesis and thank many others whose names I forgot to list.

I am deeply grateful to my brother, my mother and my father for their love, care and all the sacrifice they made for my education. In particular, I am thankful to my brother for his never-ending support, love and encouragements throughout my Ph.D.

They are always proud of my every little success. Thank Yvonne, who met me in my period of tough and depressing, brought me beautiful, enjoyable days and desire again in future life

.

Finally,

"Do not pray for an easy life, but pray for the strength to endure a difficult one."

- Bruce Lee.

Jianhao Zhang
Novermber 2019

Contents

Introduction

The telecommunication field based on electrical millions-calculation-per-second microprocessors has completely reshaped the way we think and human comes to an age that signal can be transferred and processed almost instantaneously. However, electrical transmissions do not scale up to the data rates needed for long-distance communication backbones. The vast acceleration of information request in the past decades triggered scientists to develop optical fibers. Optical fibers consist of deionized glass material, and can guide light over large distances with ultra-small propagation loss (around 0.2dB/km at 1.55µm wavelength, or even below). The success of optics [I1-I3] in modern telecommunication systems and optical interconnects has already been evidenced in the last century, but the versatility of light is continuously promoted with the development of semiconductor technologies.

In 1969, Mr. S. E. Miller proposed the idea "Integrated Optics" [I4] for the purpose of surpassing the anticipated bottleneck of electrical interconnects. By integrating various kinds of electronic and photonic elements on a single chip and linking them by optical paths, hybrid integrated processors were expected to have order-of-magnitude's improvement compared to the previous microelectronic processors. The development in integrated photonics has led to significant success in optoelectronics, especially in the field of optical interconnects [I5, I6] and data centers [I7, I8]. Taking a panoramic view of the development of optical networks and the current stage of optical interconnects, the direction that has driven photonic integrated chips [I9] is now going toward to a more-compact, lower-cost and low power consumption technologies. Numerous difficulties [I9], including production cost, optoelectronic packaging and function expanding, are viewed to find solutions in the convergence of electronic and photonic systems. The increasing request on data processing is just creating a strong demand in integrated photonics for new-generation technologies including 5G communications [I10], Internet of Things [I11], remote sensing [I12] and Photonic Lab-on-chips [I13], etc. These trends lead to a needed technology transition in the near term. Active optical cables are one successful example of a retro-benefit of photonics to the electronic technology. The development of complex photonic systems [I9] is expected to lead to new functionalities combining active components (including light sources, light modulators, and light detectors, etc) and stronger capability of on-chip light manipulation to support applications and researches (including nonlinear light processes, opto-mechanical devices, quantum optics, etc). One of the hints among these topics is to enhance the light-matter interactions.

Silicon is well-known to be the mainstream photonic platform and this matter of fact obviously comes from the CMOS electronic technology which offers a wide range of mature etching, lithography, and packaging technologies for guided optics

and photonic circuits, and considerable development potential in terms of applications and large-scale diffusion. Silicon photonics is now a mature domain, and the main disadvantage of silicon is well known: it is its indirect band structure that eliminates the possibility of making integrated silicon laser sources. At the same time, hybrid material integration paths are possible on silicon, starting with III/V laser diodes which can be integrated on silicon, either locally or by transferring substrates. The silicon option, or rather onon-silicon, is therefore a preferred method of photonic integration for various applications, including datacom, metrology, on-chip quantum optics, microwave photonics, and sensing in the near and mi-infrared.

Silicon is also not a very good material from the point of view of electro-optical modulation, with no Pockels effect in bulk material. The contribution of a local mechanical constraint provides a partial solution to this problem, but it is absolutely essential in this configuration to develop high-performance optical resonators, i.e. with a giant ON/OFF ratio under the action of a modification of the refractive index Pockels which remains very low. At the same time, it appears that silicon has a very strong third order non-linearity, and that other materials such as Si_3N_4 or rich silicon can be reported on silicon for the same purpose. These non-linear properties open up a whole range of possible applications for the realization of supercontinuum sources or frequency combs by the Kerr effect. Though in-situ laser composing is difficult due to the lack of direct bandgap for light emission (which is emerging issues and most difficult problems in the field of photonics.), the abundant nonlinear effect in silicon has drawn a lot attention in composing active functions. The exploitation of these very interesting properties nevertheless requires a drastic control of the phase agreement conditions (frequency and wave vector), which is not always easy to guarantee in these high contrast structures of core/sheath refractive index.

In this context, which has great potential but at the same time presents important challenges, my thesis work has focused on two main aspects:

- The **realization of original Fano integrated resonators perfectly adapted to the exploitation of a low electro-optical Pockels effect for the realization of ultra-fast compact modulators** with low power consumption.

- The **exploration of a new family of waveguides leading to an automatic and generalized condition of frequency/wave vector phase matching conditions** in high index contrast waveguides. The proposed theoretical contribution is based on an approach that can be generalized to any integrated photonic platform (e.g. III/V, polymers, etc), but has been applied in the manuscript to two specific types of situations: graded waveguides for Four-Wave-Mixing applications, and frequency comb generation, respectively.

A tool that runs through all the proposals we make and taking advantages of the versatility of silicon nonlinearities in this work is to use the **engineering of**

subwavelength photonic structures, whose toolbox is decisive in practice for the concrete achievement of the objectives pursued.

The manuscript is organized as follows:

Chapter 1 reviews the state-of-art of silicon photonics and recalls the required concepts for understanding nonlinear devices and the most representative works carried out on silicon nonlinear devices. Based on several examples, we will point out some difficulties and demands on silicon light modulation and light generation, respectively. Next, we recall the advantages and elements of optical propagation in periodically structured waveguides, and give a brief review on the most recent progress in silicon subwavelength optics. We then draw the main lines of using subwavelength structural approaches to improve silicon nonlinear applications and present the interest of relying subwavelength nonlinear photonics in view of nonlinear photonic applications.

Chapter 2 introduces how subwavelength engineering can be considered to shape micro resonators for the purpose of cutting down the driven swing and increasing the modulation efficiency of integrated electro-optical modulators by generating Fano resonances. Using derived concepts, we propose a method for tuning the introduced nanobeam resonator resonance to reach one step towards tunable Fano modulators. The methodology of cleanroom fabrication of structures and device characterization used throughout this thesis is then reviewed.

Chapter 3 introduces a novel kind of waveguide with a proposed operating condition for all the exploited modes, entitled "self-adaptive boundary" and introduces how silicon nonlinear devices based on Kerr nonlinearities can benefit from this configuration. Explanation is given about the practical realization of photonic waveguide structures satisfying this condition by the mean of subwavelength structures. From this point, a variation of this type of waveguide is made in two configurations, the first corresponding to multimode guides for the realization of a universal phase matching adapted to FWM, and a second based on single mode guides with particular properties useful for the generation of very wide frequency combs.

Chapter 4 will summarize these works and open perspectives.

1 Introduction and motivations

In this chapter we are going to introduce the background of silicon photonic integration. For the purpose of composing active functions in/with silicon, we will introduce the concepts of nonlinear optical effects. Especially we will review some representative silicon nonlinear devices which take advantages of the silicon Pockels and Kerr effects, respectively, and extrude the merits and limits/issues of them by closely explaining them with demonstrations taken from the state of the art. Next, as a tool used in our work to address these issues in silicon photonics, subwavelength structures will be reviewed. Besides, we believe that most of the contributions of this thesis work derive from a contribution from the engineering of subwavelength photonic structures to the problems of non-linear silicon optics.

1.1 Silicon photonics: a versatile platform for light processing

As the fundamental material of the semiconductor industry, silicon is widely adopted for versatile electronic devices and widely accepted as a key technology in next-generation communications systems and data interconnects [1-3]. The design and fabrication process flow for electronic devices based on silicon wafers has already been well developed completely since 50 years ago and is called CMOS ("Complementary Metal Oxide Semiconductor").
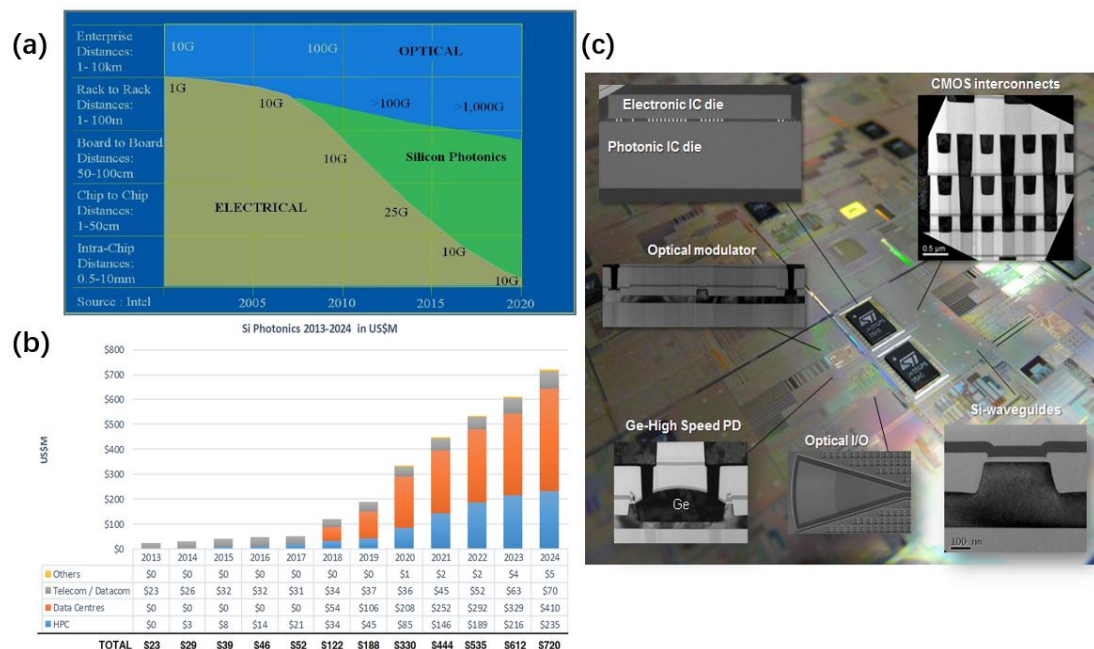

Figure 1 (a) The comparison in capacity between electrical, classical optical methods and silicon photonics, reproduced from [1]. (b) Industry scale in different field of silicon photonics, including telecom/datacom, data centers and high-performance computation. (c) Schematic of integrated silicon photonics. (b) and (c) are reproduced from [5].

Silicon photonics is based on the idea of reusing CMOS fabrication methods and processes and transferring them to guided-wave optics for the realization of photonic integrated circuits [2, 3]. As shown in Figures 1 (a) and (b), silicon photonics is progressively leading an advanced position, especially in optical telecommunications [4], data centers and high-performance computing [5]. This is because it brings the advantages of integration of photonics - high data densities and transmission over longer distances - in a platform where high levels of integration (including electronic IO, waveguides, photonic detectors, etc) can be achieved with low manufacturing costs using conventional silicon integrated circuit infrastructures.

Driven by originally this purpose of optical interconnects and later demand in parallel applications, various kinds of fields in optics are strongly promoted. As shown in Figure 2, various applications including light sources, spectroscopy, light distance optical communications, optical data processing and sensors are covered by this technology.
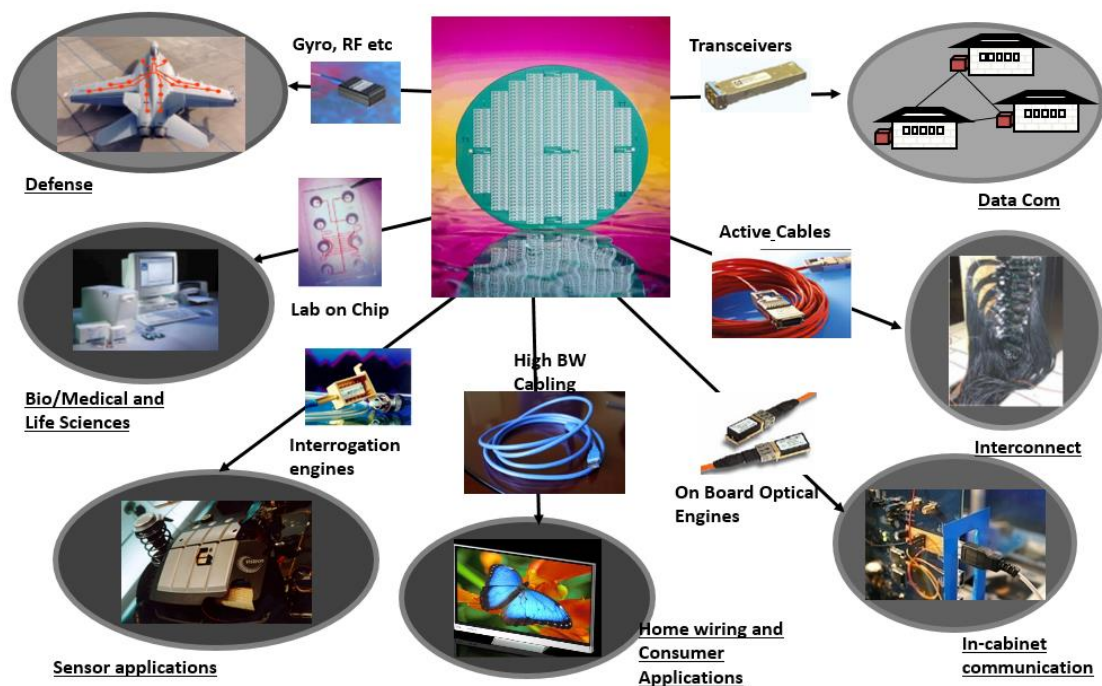
Figure 2. Future evolution and applications in silicon photonics, reproduced from [6].

1.1.1   Progress and merits in silicon photonics

In silicon photonics, a silicon waveguide layer is used as a waveguide core on top of a buried oxide which acts as its lower cladding. The refractive index values of this silicon core and oxide layer are 3.476 and 1.444 for 1500 nm wavelength, respectively. This high index contrast allows confining light in the very small area of waveguide core and explains why bending radii silicon-on-insulator waveguides can be as small as a few microns with almost no losses. A direct consequence is that the devices' footprints reduce significantly. This makes the integration density very high. Figure 3 (a)-(d) shows the schematic and transverse electric-field profiles of silicon photonic

waveguides [7, 8] with strip and rib shapes, respectively.

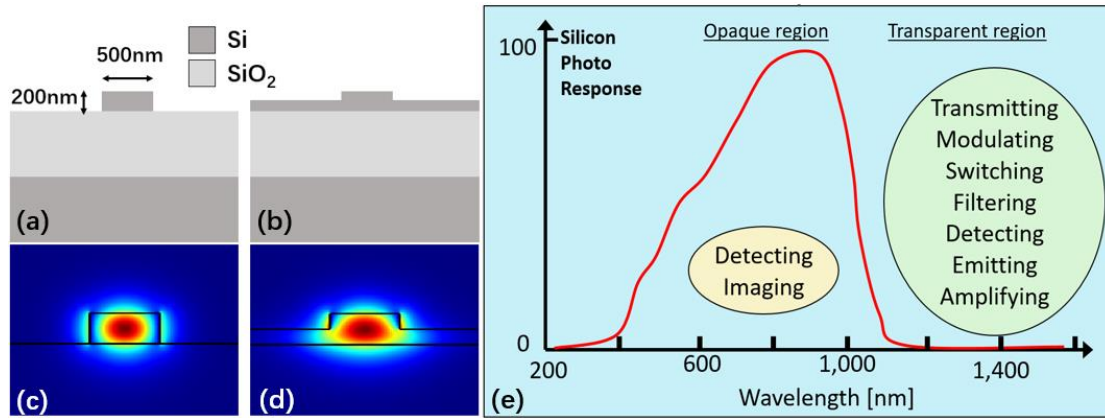**Figure 3.** Schematic of silicon strip (a) and rib (b) waveguide. (c) (d) Corresponding transverse electric-field profile. (e)Future evolution and applications in silicon photonics, reproduced from [6].

Thanks to the great flexibility supported by the high index contrast between silicon and surrounding materials, a lot of basic elements in photonic circuits, including couplers, multiplexers, splitters, bends, etc., have been demonstrated [9] and widely used in on-chip photonic systems. In addition, as shown in Figure 3 (e), due to the wide transparent spectrum of silicon in the telecom window, components like transmitters, switches, and detectors can be integrated [9]. Based on these building blocks, the stage of silicon photonics has been more recently extended to new fields including silicon quantum photonics [10], integrated microwave photonics [11], and on-chip sensing and metrology [12]. Overall, the merits of silicon platform/devices can be summarized as follows:

1. High Crystalline qualities with tiny material defect that can be processed in a massive growing scale.

2. High index contrast with the oxide upper cladding and substrate, in favor of ultra-small photonic devices.

3. Compatibility with the mature CMOS fabrication processes and possibility of a somewhat easy integration of various on-chip optoelectronic components.

4. Large 3rd nonlinearities for creating active building blocks (introduced later).

5. Ultra-wide transparent windows covering from near-infrared to far-infrared range.

1.1.2   Limits in the performance of active functions

Despite all the qualities of the silicon platform mentioned above, Si photonics has also significant disadvantages. Its main difficulties are presented in Figure 4. As mentioned above, the rapidly increasing demand for optical interconnects leads to the strong requirement of ultralow power consumption and tens-to-hundreds-gigabits devices, among which silicon-based light sources and silicon optical modulators

(Figure 5 (a), [13]) play an essential role. However due to the Si indirect bandgap, the full integration of the prime element – the light source - is more than challenging (though tiny emission can be produced light emission [14, 15]). As shown in the rest of Figure 5, beyond silicon and silicon nitride [16-19], the path that has been chosen and which has led to the best results is based on the integration of III/V semiconductor diodes [20-25] on silicon. In addition to these classical semiconductor materials, new materials like for instance $LiNbO_3$ [26-31], organic polymers [32-37], two-dimension materials (graphene, MoA2 etc. [37-39]) have been also considered for modulation.
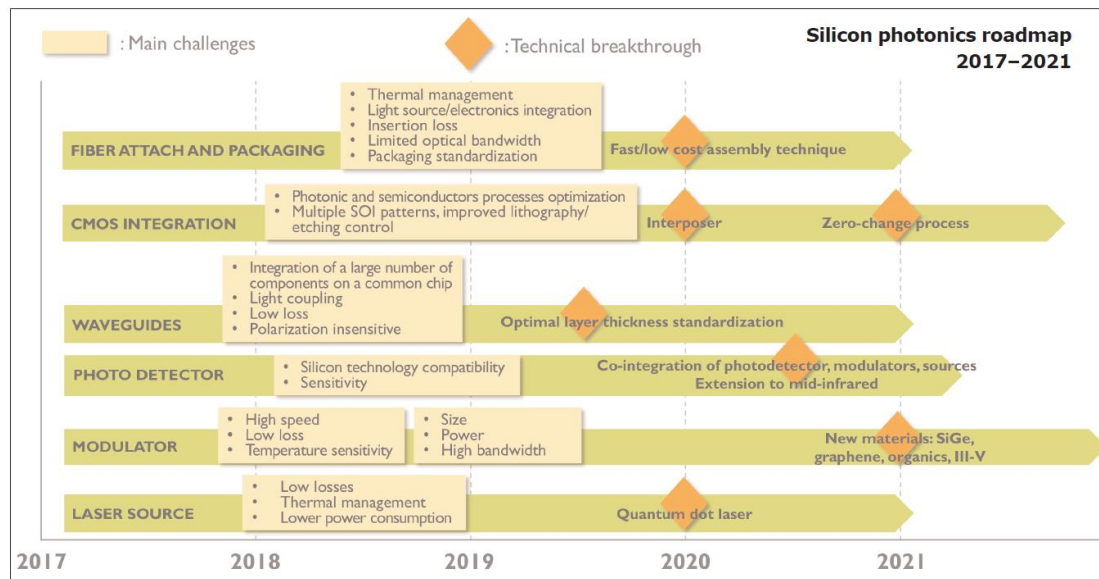

Figure 4. Main challenges and technical breakthroughs in silicon photonics, reproduced from [3].
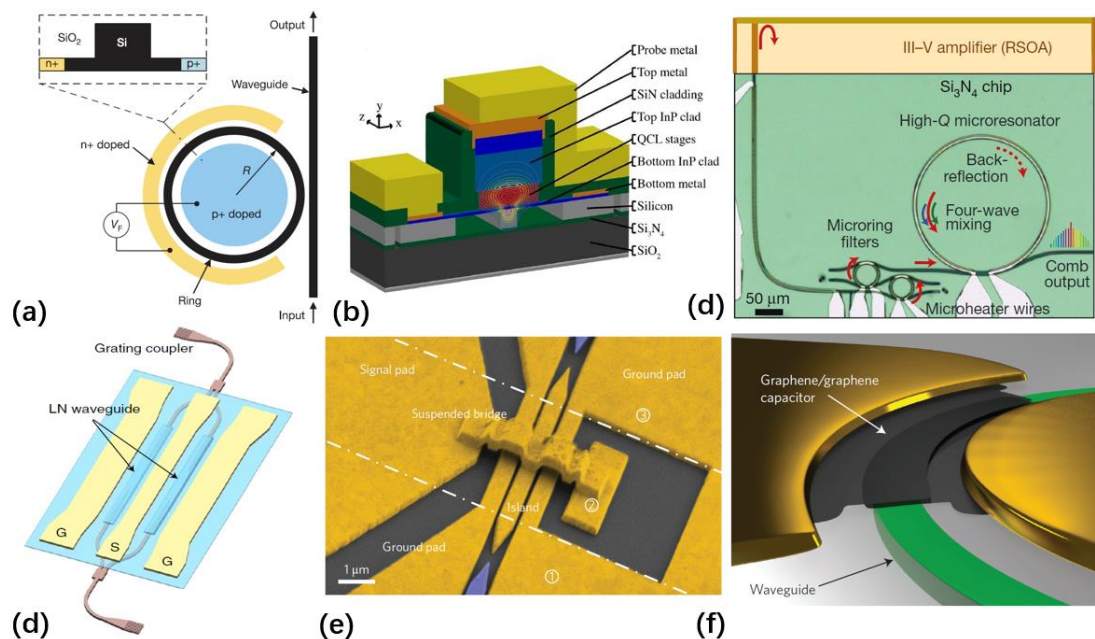

Figure 5. Schematic of silicon modulators (a), silicon/III-V hybrid integrated mid-infrared laser (b), silicon nitride frequency comb (c), Lithium niobate/silicon hybrid modulator (d), Silicon-organic

modulator and silicon-graphene modulators (f). Schematic of Silicon/III-V hybrid integrated tunable laser. Figures are reproduced from [13], [21], [19], [29], [33] and [35], respectively.

As you could know in all these references, though, 2D, $LiNbO_3$ and organic materials can produce higher modulation performance or novel functions to optical modulation but the complexity in fabrication also make a cost on the further photonic integration. III-V as the most capable materials for developing light sources are preferably expected in silicon photonics, but their superior performance are made at the expense of cost and accessibility, in both industry and academic research. In contrast, though light emission through direct bandgap is not possible in silicon, the silicon nonlinearities however are also considered as one of the alternatives for the silicon-based light sources. Based on the strong silicon Kerr effect, silicon Raman laser [40, 41] has first been proposed by Intel in the early years of the 21th century. In these designs, a high-power pump signal circulates in a high-quality factor silicon race-track resonator. By taking advantage of the flexible fabrication of silicon devices [42] and the possibilities of composing broadband light source based on strong nonlinearities in silicon, on-chip spectroscopic sensing was expected [43]. The source problem finally can find solution via the integration of active materials on silicon and leads to very good results. At the same time, the development of laser sources is not the only possible option to address this issue. It is indeed possible to take advantage of the third order non-linear optical effects, which are very strong in silicon, for the production of supercontinuum sources or frequency combs. This does not entirely exempt the use of an optical source, as a pump harness is necessary to achieve these effects. That being said, only one source being necessary, it is quite easily possible to inject this pump from an external source and to take advantage of it for the realization of multi wavelength or wide spectrum sources in an integrated configuration. The on-demand implementation of third order non-linear optical effects is therefore a key point in the development of silicon photonics, both for the telecom waveband and for mid infrared wavelengths [44-50].

1.2 Nonlinear silicon active functions: progress and difficulties

As introduced above, the use of third order non-linear optical effects is now a key point in the development of Si photonics. It turns out that silicon has a very high Kerr index but, at the same time, its gap is too small to effectively block the phenomenon of two-photon absorption (TPA) in the near infrared. Active materials can naturally be grown on silicon to overcome this disadvantage, among which materials such as Si_3N_4 or silicon-rich compounds can be considered.

In any case, we need to make some reminders of non-linear photonics in order to be able to understand the studies that will be carried out in chapters 2 and 3 of this manuscript. We will have a short review on the principles of silicon nonlinearities,

followed by the representative applications and researches in which 3rd order nonlinear effect is considered.

1.2.1　Generalities on optical nonlinear effects

As shown in Figure 6 (a), when light propagates in a linear material, the collection of vibrating dipoles constituting the material results in a linear polarization, while in nonlinear materials (6 (b)), the dependence of the restoring forces with the displacement of the electric charge center of mass leads to nonlinear collection of vibrating dipoles and harmonic waves.
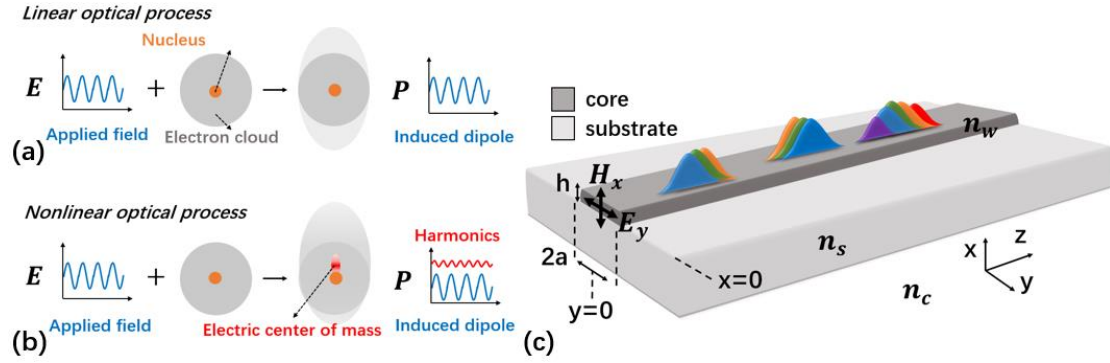
Figure 6. Schematic of light polarization in linear (a) and nonlinear (b) media. (c) Schematic of light propagating in waveguide with nonlinearities.

Light propagation is governed by the Maxwell's Equation which consists of four basic equations [7, 8] as below:

$$\nabla \times \boldsymbol{E} = -\frac{\partial \boldsymbol{B}}{\partial t} \tag{1.1}$$

$$\nabla \times \boldsymbol{H} = \boldsymbol{J} + \frac{\partial \boldsymbol{D}}{\partial t} \tag{1.2}$$

$$\nabla \cdot \boldsymbol{D} = \rho_f \tag{1.3}$$

$$\nabla \cdot \boldsymbol{B} = 0 \tag{1.4}$$

in which $\boldsymbol{E}$ and $\boldsymbol{H}$ are vectorial variables of the electric and magnetic fields, respectively, and $\boldsymbol{D}$ and $\boldsymbol{B}$ are the corresponding electric and magnetic flux densities, respectively. The current density vector $\boldsymbol{J}$ and the charge density ρ_f represent the sources for electromagnetic field generation. The electric and magnetic fields are bonded with curl revolution, in response to the Gaussian flux of charge density and the local current density while the electromagnetic field is propagating inside the medium. The flux densities D and B are described by:

$$\boldsymbol{D} = \varepsilon_0 \boldsymbol{E} + \boldsymbol{P} \tag{1.5}$$

$$\boldsymbol{B} = \mu_0 \boldsymbol{H} + \boldsymbol{M} \tag{1.6}$$

where ε_0 and μ_0 are the vacuum permittivity and vacuum permeability, respectively. $\boldsymbol{P}$ and $\boldsymbol{M}$ are the electric and magnetic polarizations induced by the electromagnetic energy. By taking the curl of equation (1.1) and substituting the curl of (1.2) into it, we can simplify it into

$$\nabla \times (\nabla \times \boldsymbol{E}) = -\frac{\partial}{\partial t}[\nabla \times (\mu_0 \boldsymbol{H} + \boldsymbol{M})] = -\frac{\partial}{\partial t}\left[\nabla \times \boldsymbol{M} + \mu_0 J + \mu_0 \frac{\partial}{\partial t}(\varepsilon_0 \boldsymbol{E} + \boldsymbol{P})\right]$$

(1.7)

For most of the media we consider in integrated photonics, especially the silicon-based materials, the current densities, charge densities and the magnetic polarizations can be ignored as: $M = 0$, $J = 0$ and $\rho_f = 0$. Therefore:

$$\nabla \times (\nabla \times \boldsymbol{E}) = -\mu_0 \frac{\partial^2}{\partial t^2}(\varepsilon_0 \boldsymbol{E} + \boldsymbol{P})$$
(1.8)

This equation is primarily restricted by the boundary conditions $\nabla \cdot \boldsymbol{D} = \nabla \cdot (\varepsilon_0 \boldsymbol{E} + \boldsymbol{P}) = 0$, which means that crossing the interface between materials the tangential component of $\boldsymbol{E}$ and the normal component $\boldsymbol{D}$ should be continuous. For an electromagnetic field propagating through a homogeneous material, the polarization can be written as $\boldsymbol{P} = \varepsilon_0 \chi \boldsymbol{E}$, by which we have:

$$\boldsymbol{D} = \varepsilon_0 \boldsymbol{E} + \varepsilon_0 \chi \boldsymbol{E} = \varepsilon_0 \varepsilon_r \boldsymbol{E} = \varepsilon_0 n^2 \boldsymbol{E}$$
(1.9)

where by definition $n = \sqrt{\varepsilon_r} = \sqrt{1 + \chi}$ is the refractive index of the material, with linear susceptibility χ. By simply expanding the curl operator in equation (1.8) with $\nabla \times (\nabla \times \boldsymbol{E}) = \nabla(\nabla \cdot \boldsymbol{E}) - \nabla \cdot (\nabla \boldsymbol{E}) = \nabla(\nabla \cdot \boldsymbol{E}) - \nabla^2 \boldsymbol{E}$ then equation (1.8) can be simplified as:

$$\nabla^2 \boldsymbol{E} - \nabla(\nabla \cdot \boldsymbol{E}) - \mu_0 \varepsilon_0 \frac{\partial^2}{\partial t^2}(1 + \chi)\boldsymbol{E} = 0$$
(1.10)

Since $\nabla \cdot \boldsymbol{D} = 0$, and the vacuum light speed is corresponding to $\mu_0 \varepsilon_0 = \frac{1}{c^2}$, we can further simply it in to into:

$$\nabla^2 \boldsymbol{E} - \frac{1}{c^2}\frac{\partial^2}{\partial t^2}(1 + \chi)\boldsymbol{E} = 0$$
(1.11)

With boundary conditions:

$$\nabla \cdot \boldsymbol{D} = \nabla \cdot \boldsymbol{E} = 0$$
(1.12)

This is the wave equation for an electromagnetic field propagating in a homogeneous linear material. Typically, electromagnetic wave propagating along the z axis with

14

single-frequency ω_0 can be described by:

$$E(z,t) = \frac{1}{2}F(x,y)A(z,t)e^{i(k_0 nz - \omega_0 t)} + cc. \tag{1.13}$$

Where $F(x,y)$ is the electromagnetic distribution normal to the propagation direction while $k_0 = \frac{\omega_0}{c}$ is the corresponding wavevector while $c.c.$ is the complex conjugate. With $\varepsilon = \varepsilon_0 \varepsilon_r = \varepsilon_0(1+\chi)$, the wave equation generally can be represented, and is also called as the Helmholtz equation as:

$$\nabla^2 E + k_0^2 \varepsilon E = 0 \tag{1.14}$$

Once nonlinear effects are nonzero, with instantaneous response to electromagnetic field is [51]:

$$P = P_L + P_{NL} = \varepsilon_0 \chi^{(1)} E + \varepsilon_0 \big(\chi^{(2)} E + \chi^{(3)} EE + \cdots \big) E \tag{1.15}$$

where $\varepsilon(\omega) = \varepsilon_L + \varepsilon_{NL} = \varepsilon_0 \big(1 + \chi^{(1)} \big) + \varepsilon_0 \big(\chi^{(2)} E + \chi^{(3)} EE + \cdots \big)$, The wave equation can then be rewritten as:

$$\nabla^2 E - \frac{1}{c^2}\frac{\partial^2}{\partial t^2} E - \mu_0 \frac{\partial^2}{\partial t^2} P_L = -\mu_0 \frac{\partial^2}{\partial t^2} P_{NL} \tag{1.16}$$

or

$$\nabla^2 E + k_0^2 \varepsilon_L E = -\mu_0 \frac{\partial^2}{\partial t^2} P_{NL} \tag{1.17}$$

In equation (1.17) the part on the right can be considered as the electromagnetic source governed by nonlinearities, which is responsible for the generation of new frequencies. For materials with non-instantaneous response, the polarization P should be replaced by

$$P = \varepsilon_0 \int_{-\infty}^{+\infty} \chi(t-t') E \, dt' \tag{1.18}$$

where $\chi(t-t')$ represent the non-instantaneous response with time delay $t-t'$.

In electric polarization $P = P_L + P_{NL} = \varepsilon_0 \chi^1 E + \varepsilon_0(\chi^2 E + \chi^3 EE + \cdots)E$, the complex first-order susceptibility $\chi^{(1)}$ corresponds to the dipole excitations with bound and free electrons induced by a single photon. The real part of χ^1 directly contributes, as mentioned above, to the real part of the linear refractive index while the imaginary part contributes to the gain and loss from of the material. A remarkable matter of fact for silicon is that due to its crystal structure inversion symmetry, the the

second-order susceptibility $\chi^{(2)}$ vanishes to zero, strongly restricting the application of this effect for electro-optical modulation and switching.

Third order nonlinearities, on their side involve three electromagnetic waves simultaneously and can be described as follows in optical waveguides:

$$\boldsymbol{E}(z,t) = \sum_{j=1}^{3} \left[\frac{1}{2} F(x,y) A(z,t) e^{i(k_j nz - \omega_j t)} + c.c. \right]$$

$$= \sum_{j=1}^{3} \left[\frac{1}{2} E_{\omega_j}(z,t) e^{-i\omega_j t} + cc. \right] \tag{1.19}$$

With equation (1.15), the polarization governing the third nonlinearity [52] can be represented by multiple terms as:

$$P_{NL} = \frac{3}{4} \varepsilon_0 \chi^{(3)} \left[|E_{\omega_1}|^2 \right] E_{\omega_1}$$

$$+ \frac{6}{4} \varepsilon_0 \chi^{(3)} \left[|E_{\omega_2}|^2 + |E_{\omega_3}|^2 \right] E_{\omega_1}$$

$$+ \frac{1}{4} \varepsilon_0 \chi^{(3)} \left[E_{\omega_1}^3 e^{-i3\omega_1 t} + c.c. \right]$$

$$+ \frac{3}{4} \varepsilon_0 \chi^{(3)} \left[\frac{1}{2} E_{\omega_1}^2 E_{\omega_2} e^{-i(2\omega_1 + \omega_2)t} + c.c. \right]$$

$$+ \frac{3}{4} \varepsilon_0 \chi^{(3)} \left[\frac{1}{2} E_{\omega_1}^2 E_{\omega_2}^* e^{-i(2\omega_1 - \omega_2)t} + c.c. \right]$$

$$+ \frac{6}{4} \varepsilon_0 \chi^{(3)} \left[\frac{1}{2} E_{\omega_1} E_{\omega_2} E_{\omega_3} e^{-i(\omega_1 + \omega_2 + \omega_3)t} + c.c. \right]$$

$$+ \frac{6}{4} \varepsilon_0 \chi^{(3)} \left[\frac{1}{2} E_{\omega_1} E_{\omega_2} E_{\omega_3}^* e^{-i(\omega_1 + \omega_2 - \omega_3)t} + c.c. \right] \tag{1.20}$$

where, on the right side, the first and second terms correspond to the self-phase modulation (SPM) and cross-phase modulation (XPM) effects, respectively. An illustrative picture of the main classical third-order mechanisms is presented in Figure 7.
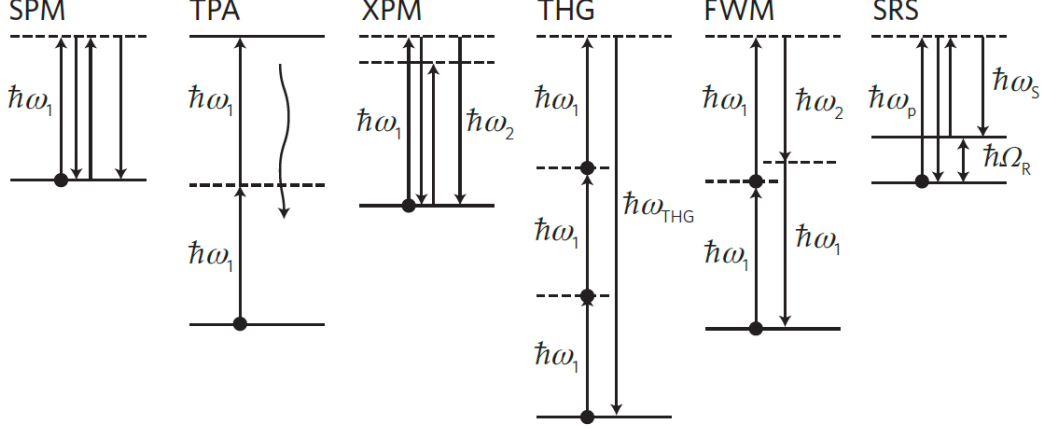
Figure 7. Schematic of nonlinear process, reproduced from [14].

1.2.2   Silicon plasma dispersion and Pockels effects for light modulation

Second-order nonlinearity $\chi^{(2)}$ is preferably expected for optical modulation in most of photonic platforms. The Pockels effect indeed traditionally makes it possible to obtain a variation in the optical refractive index by applying an RF electric field, i.e. by simply applying a modulation RF voltage after manufacturing a set of metal electrodes judiciously placed on either sides of the waveguides. Though $\chi^{(3)}$ can be considered for light modulation, difficulties stem from the request of strong power for driving the modulator since the on-chip modulators are basically driven by a radio-frequency (RF) electrical source. As this $\chi^{(2)}$ effect is absent in bulk silicon due to the centro-symmetry of crystal lattice in silicon, it has proved necessary to exploit another phenomenon, which has finally turned out to be simply based on an essential property of silicon: it is a semiconductor and is therefore characterized by a possible transport of free charges (electrons and holes) induced by doping and modulable by the application of a voltage (PN junction).

1.2.2.1   Plasma dispersion effect and modulator

As mentioned above, free carrier concentrations can be modulated in silicon waveguide by the use of a PN junction, i.e. relying on the so-called plasma dispersion effect. In turn, the modulation of the free carrier plasma is responsible for the modification of the material conductivity, which leads to a simultaneous change of the real (Δn) and imaginary parts ($\Delta\alpha$) of the refractive index. Preferentially playing on one or the other of these contributions leads to the classification of electro-optical modulators into electro-refraction or electro-absorption modulators.

Quantitatively [53]:

$$\Delta n = \Delta n_{\mathrm{e}} + \Delta n_{\mathrm{h}} = -[8.8 \times 10^{-22} \Delta N_{\mathrm{e}} + 8.5 \times 10^{-18} (\Delta N_{\mathrm{h}})^{0.8}] \tag{1.21}$$

$$\Delta\alpha = \Delta\alpha_{\mathrm{e}} + \Delta\alpha_{\mathrm{h}} = [8.5 \times 10^{-18} \Delta N_{\mathrm{e}} + 6.0 \times 10^{-18} (\Delta N_{\mathrm{h}})^{0.8}] \tag{1.22}$$

where $\Delta N_{e,h}$ are the variations of the electron and hole concentrations, while $\Delta n_{e,h}$ is the index variation induced by the electrons/holes. $\Delta \alpha_{e,h}$ shares the similar definitions. Electrical manipulation of the carrier density interacting with the propagating light is achievable through mechanisms categorized as carrier injection, carrier accumulation or carrier depletion. The difference of these free methods is shown in Figure 8. As the most preferred mechanism, carrier depletion provides most promising electro-optic bandwidth due to most effective carrier motion from filling to vanishing, controlled by reverse electric field. In practice, an electrical polarization structure must be designed and realized (PN junction, MOS capacitance: Figure 9 (a), [54]) and an interferometric structure must be implemented for electro-refraction modulators (Figure 9 (b), [55]).
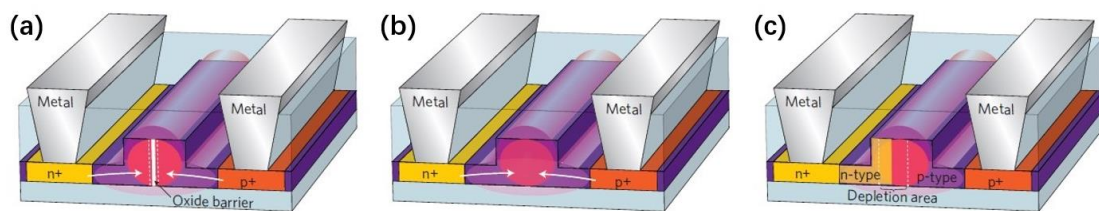

Figure 8. Schematic of silicon modulators using carrier-accumulation (a), carrier injection (b) and carrier depletion (c) effects. Figures are reproduced from [67].
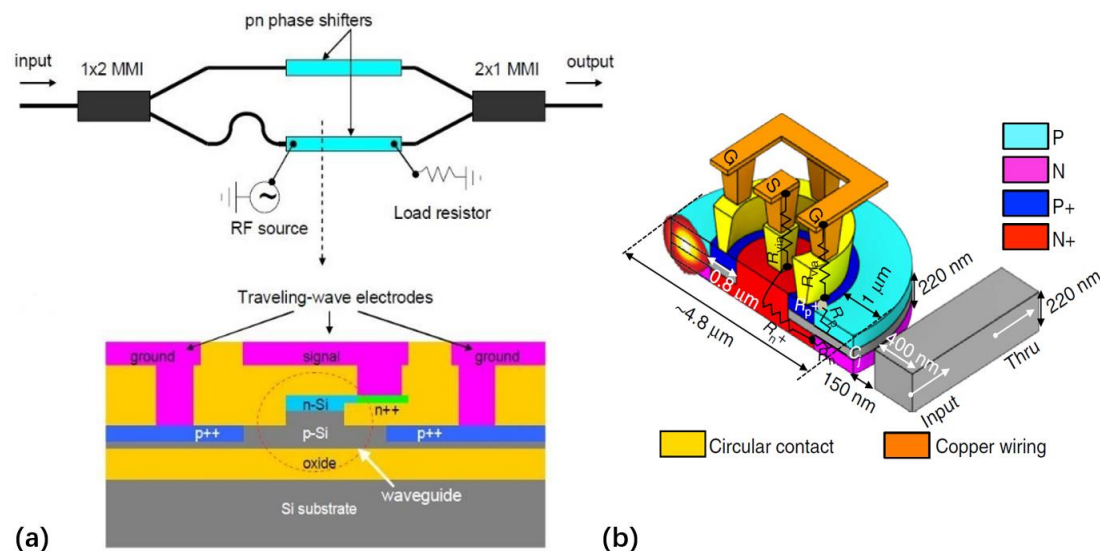

Figure 9. Schematic of silicon modulators using Mach-Zehnder Interferometer (a) and ring resonators (b). Figures are reproduced from [68] and [69].

1.2.2.2   Strain-induced Pockels effect and optical modulation

In addition to the plasma dispersion effect, a new emerging and interesting approach reported in the last decade is the strain induced Pockels effect in silicon [56]. This topic has drawn lots of attention from the silicon photonics community since it presents two important merits: an ultra-fast modulation capability based on the Pockels effect (removing the contribution of free carriers removes the carrier transport

transit time blockade) and a simple fabrication and integration (as no PN junction if then needed). The basic idea of this approach is to break the centro-symmetry of bulk silicon by straining its lattice unit cell through the use of straining external layers [57], as shown in Figure 10, for producing non-zero $\chi^{(2)}$.
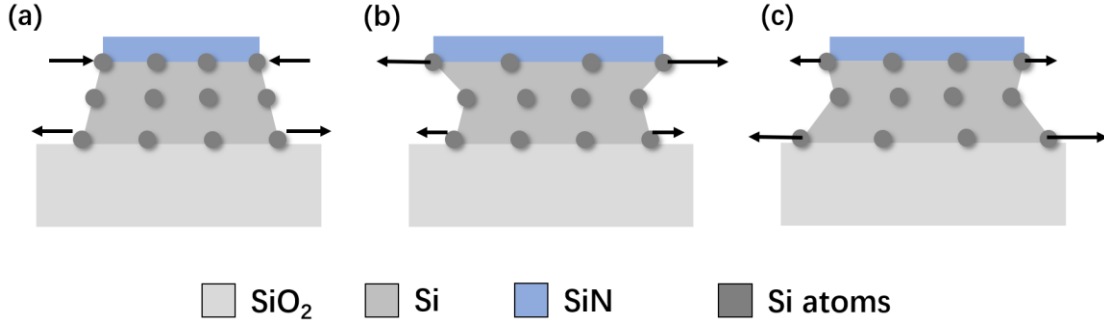

Figure 10. Schematic of straining host lattice with external material. Cases with different tensile/compressive strain are distinguished by the arrows.
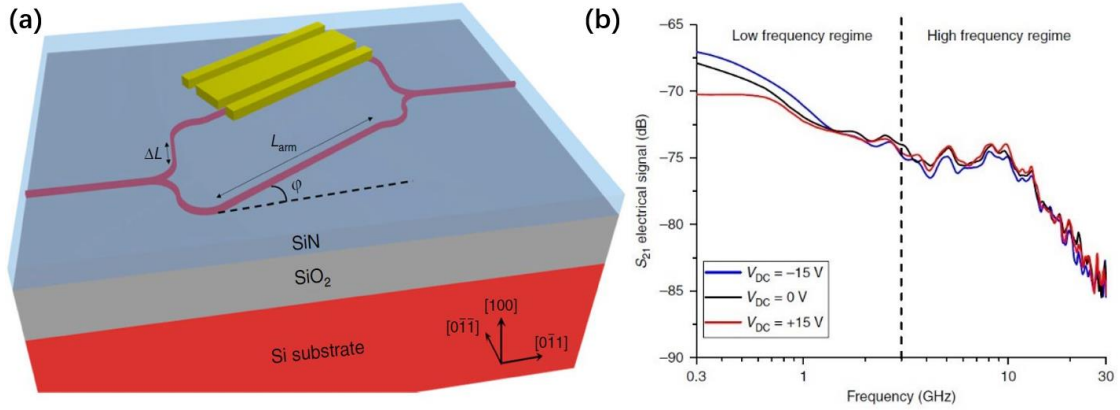

Figure 11. Schematic (a) and performance (b) of strained silicon modulator. Figures are reproduced from [63].

This technique to generate $\chi^{(2)}$ in silicon has been theoretically as well as experimentally investigated in the past years. Interestingly, the strain induced $\chi^{(2)}$ was first strongly overestimated in early works where the contributions of the Pockels and carrier effects were not properly separately estimated [58-60]. New works performed later in 2014 and 2015 corrected this trend [61,62], and a first high-speed (up to 20GHz) characterization was then demonstrated in 2018 [63] using the silicon-nitride-on-silicon platform. In this demonstration (Figure 11), a long (2mm) Mach-Zehnder interferometer was adopted in a first approach to estimate for the electro-optical response that turned to be around -1.8 pm/V in still non-optimized structures.

Further work is needed in this direction to improve and strengthen the observed effects. We will come back to this point later in this manuscript.

1.2.2.3   Demand in addressing the power-bandwidth trade-off

The universal motivation for reducing the power consumption and increasing the modulation efficiency has never been stopped and triggered for novel modulation approaches. The reason is that the index change resulting from the application of a control voltage is relatively small, usually by a few 10^{-5}, or by a few 10^{-4} at most. As a result, this places relatively high constraints on the interferometric structure in charge of converting index modulation into intensity modulation with high modulation contrast. A first option is to use a very long interferometer (typically an MZM of a few mm [64, 65]), so that the interaction length compensates for the low index modulation. To circumvent this drawback, another option is to enhance light matter interaction by the use of high Q resonators. One of the common methods is to use ring resonators in this purpose. Numerous works have contributed to silicon ring modulators [66, 68, 55]. In addition to ring resonators, PhC slow-light waveguides (Figure 12(a)) have also been adopted to enhance light-matter interactions, with slow light group velocity engineering. Almost ten-times higher efficiency was demonstrated with one tenth footprint in such structures [68, 69]. In addition to waveguides, 2D PhC cavities (Figures 12(c) and (d)) have also been considered for light modulation [70] with ultra-low powers (few µW) required for reasonable extinction ratio (ER, 10dB).

Comparisons between these modulators are presented in Table 1. As it can be seen, both ring resonators and PhC cavities can enhance modulation efficiency by providing much larger wavelength shifts when identical driven swings are applied to them. However, at the same time, the high photon lifetime resulting from the outstanding resonance ($Q>>10^3$) in return restricts the achievable electro-optic bandwidth. This power-bandwidth trade-off has been witnessed [66, 67] experimentally and especially when quality factor is raised up to hundreds of thousands, the modulation speed is then limited to no more than few GHz [70, 71]. Another point is that a higher-Q resonator normally indicates a bigger active volume and in return a reduction of the efficiency which can be improved by compressing the device volume [55]. Though high-bandwidth silicon PhC cavity modulator has not been experimentally demonstrated, some recent theoretical works on silicon photonic crystal cavity modulators [72-74] indicated promising results (Figure 12(e)) [75] to beat this limit, which yet remains essentially unsolved.

Therefore, to universally improve silicon resonant modulator and especially promote the strain silicon platform, the power-bandwidth need to be addressed. This leaves us the first issue that we will address in chapter 2, with subwavelength engineering of 1D photonic crystal cavities.

Type	Electrical bandwidth	Eye diag. Extinction ratio (dB)	Efficiency V*cm	Quality factor	Drive swing V_{pp} (V)	Length /diameter µm
Silicon,	60 Gbps	7.4	2.3	-	5.75	800

depletion M.-Z. [64], [65]	25 Gbps	5	1.15		3.3	1000
Silicon, depletion PhC M.-Z. [68], [69]	10 Gbps 25 Gbps	7.9 > 6	0.056 -	-	4.2 3.5	200 200
Silicon, depletion Ring [66], [67], [67]	10 Gbps 25 Gbps 25/40 Gbps	8 7 8	50 fJ/b 0.76 0.9 fJ/b	14500 7500 ~ 3000	2 2.3 0.5/2.2	30 >100 4.8
Silicon, PhC cavity [71], [72]	~ GHz 20 GHz	10 6	~ µW 14 AJ/b	5.4e5 8500	1.5 0.6	~10 2
Strained Silicon, M.-Z. [63]	$A2_1$, 10GHz	> 3	-	2 mm	20	2000

Table 1. Comparison between different kinds of silicon electro-optic modulators.
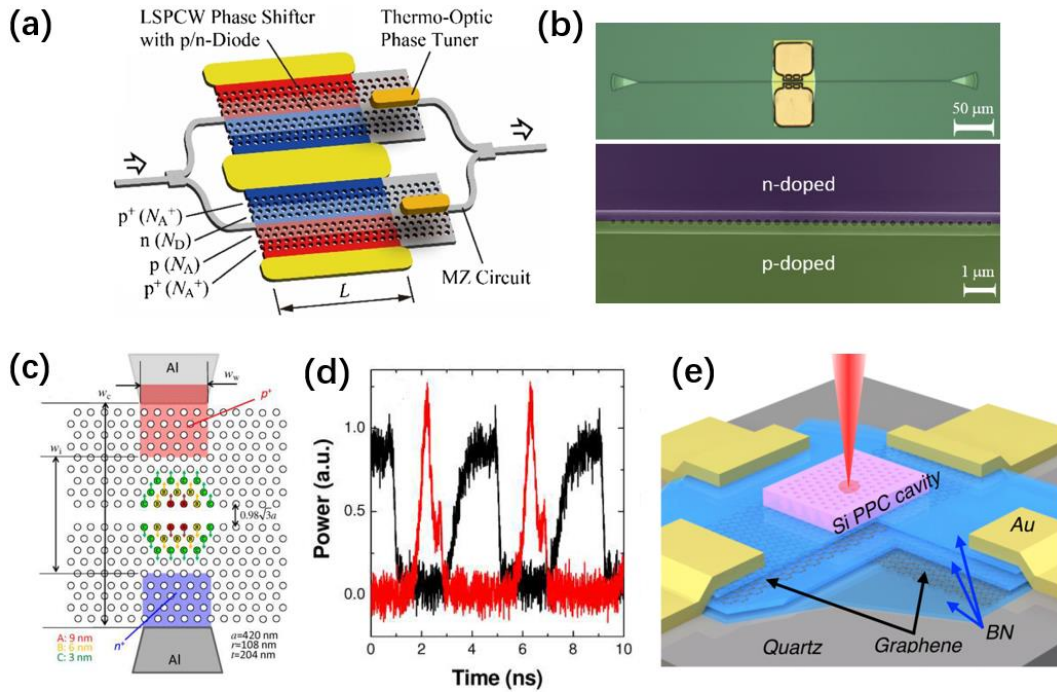

Figure 12. Schematic of silicon PhC slow-light Mach-Zehnder modulator (a) and nanobeam cavity (b) with optical bistability. (c) and (d) schematic of a 2D PhC cavity silicon modulator. (e) schematic of a 2D PhC cavity silicon hybrid modulator. Figures are reproduced from [69], [74], [71], [71] and [75].

1.2.3 Silicon optical Kerr effect and nonlinear frequency generation

1.2.3.1 Optical Kerr effect and Two-photon absorption in silicon

As mentioned above, silicon is not a material naturally suited for electro-optical modulation. On the other hand, it has a strong third order non-linearity which potentially opens up a wide field of exploitable phenomena, starting with the four-wave mixing processes (FWM), and therefore the possibility of parametric amplification, wavelength conversion, etc. Our enthusiasm must be somewhat tempered by a significant penalty related to the phenomenon of two-photon absorption, as we will see, affecting wavelengths below 2.2µm but yet not beyond.

Generally speaking, the Kerr effect can be described as follows:

$$P = P_L + P_{NL} = \varepsilon_0 \left(\chi^{(1)} + 3\chi^{(3)} |E|^2 \right) E \tag{1.23}$$

With the definition $n = \sqrt{\varepsilon_r}$, the refractive index, including the nonlinearity-induced absorption, can be represented (with the assumption that the nonlinear susceptibility is much smaller than the linear counterpart) as:

$$n = \sqrt{\varepsilon_r} = \sqrt{(1 + \chi^{(1)} + 3\chi^{(3)}|E|^2)} \approx \sqrt{(1 + \chi^{(1)})} + \frac{3\chi^{(3)}|E|^2}{2(1+\chi^{(1)})} \tag{1.24}$$

Since $n_1 = \sqrt{(1 + \chi^{(1)})}$ is the linear material refractive index, then equation 1.22 can be simplified as:

$$n = n_1 + \frac{3\chi^{(3)}|E|^2}{2n_1} = n_1 + \frac{3\chi^{(3)}}{4n_1^2\varepsilon_0 c} (2n_1\varepsilon_0 c|E|^2) \tag{1.25}$$

By expanding $\chi^{(3)}$ into its real and imaginary part, the refractive index n can be rewritten as:

$$n = n_1 + n_2 I + i\alpha_2 I \tag{1.26}$$

where $n_2 = \frac{3}{4n_1^2\varepsilon_0 c} Re(\chi^{(3)})$ and $\alpha_2 = \frac{3}{4n_1^2\varepsilon_0 c} Imag(\chi^{(3)})$ is the nonlinearities induced index change and absorption, respectively.

Kerr effect is very strong in silicon, with $n_2 = 3 \times 10^{-18} m^2/W$, i.e. is a factor of 100 higher than in silica fibers, which promises silicon as a solid candidate for on-chip light conversion and generation. Yet, as shown in Figure 7, the couple of pump photons do not only contribute to the Kerr-induced SPM effect, but also to the two-photon absorption (TPA) process. This phenomenon occurs non-negligibly in the near-infrared wavelength region due to the fact that the double of the photon energy can easily surpass the energy gap between the valence and conduction bands. This effect typically influences the degenerate FWM ($\omega_{P2} = \omega_{P1}$) by sacrificing part of the pumping photon for higher energy conversion without direct optical repay. Due to the non-negligible TPA (Figure of merit FOM $= \frac{n_2}{\lambda\alpha_2}$) in silicon, with a coefficient

$\beta_2 = 5 \times 10^{-12} m/W$ in the O band (around λ=1550nm), light all-optical modulation and wavelength conversion are hindered with threshold powers of few mW only. This absorption contribution has also to be integrated into α_2 in equation (1.26).

In addition to the direct absorption behavior, the absorbed photons can in return, produce new free carriers with long lifetime leading to free-carrier absorption (FCA) and free-carrier index (FCI) changes. This combination of TPA and the long lasting FCA jointly work against the FWM by reducing the parametric gain and slow down the bandwidth of silicon Kerr switches. However, some methods can be applied that can effectively reduce the influence of FCA and TPA. For example, an external electric field produced by PN junction can be used to deplete the free carrier while ultrafast pump will temporal scale faster than the TPA process suppress TPA. The simplest approach to eliminate TPA and FCA is also to perform the nonlinear processes with a pump wavelength larger than 2.2 μm since the double of the photon energy then no longer reaches the Si bandgap. Impressive results have been obtained by this approach, that yet does not solve the need for telecom wavelength all-optical signal processing techniques.

1.2.3.2   Four-wave mixing enhanced by resonators and photonic crystal

Four-wave mixing has a wide range of applications including parametric amplification, wavelength conversion, nonlinear microscopy and spectroscopy, etc. Particularly, light amplification in silicon has been demonstrated using FWM [76] for more than a decade. Unlike the Raman effect which is restricted by the availability of the phonons in materials, the FWM effect is able to provide a larger parametric amplification in a broader wavelength range. The needed elements for these parametric amplifications are the fine control of the involved waves phase matching condition and the realization of low waveguide propagation losses. Starting from the energy conservation ($\omega_I = \omega_{P2} + \omega_{P1} - \omega_S$) being satisfied, the phase matching condition is described by the condition of involved wavevectors as: $\Delta\beta = \beta_{P1} + \beta_{P2} - \beta_S - \beta_I = 0$. In this condition, S, I, $P1$ and $P2$ are labels with respect to the signal, the idler, and the pump waves, respectively. This condition typically requires careful dispersion engineering of the waveguide cross-section. In the control of phase matching, not only the waveguide dimensions controlling its chromatic dispersion, but also the nonlinearities-induced phase variation needs to be taken into account. This is where SPM or XPM in that Kerr nonlinearities are widely used for ultrafast phase modulation, which can be translated into intensity modulation with the assistance of Mach-Zehnder interferometers or micro resonators. Using optimized designs, different kinds of applications have been demonstrated, such as near-infrared broadband optical parametric gain [76, 77] (see Figure 13).

In order to enhance the nonlinear light-matter interaction, ring resonators were adopted for simultaneously making three waves circulate with a self-aligned frequency spectrum [77, 78]. Similar works were also performed in multi-resonant PhC cavities (see Figure 14) for further improvement of the light-matter interaction

within ultra-small active volumes [79, 80]. By introducing the coupled mode scheme to produce parity-varied eigen modes in photonic molecules [81-83], new freedom was given to control FWM. This photonic molecule was also found to be able to improve the light-matter interaction with a mis-alignment cavity lattice [84].
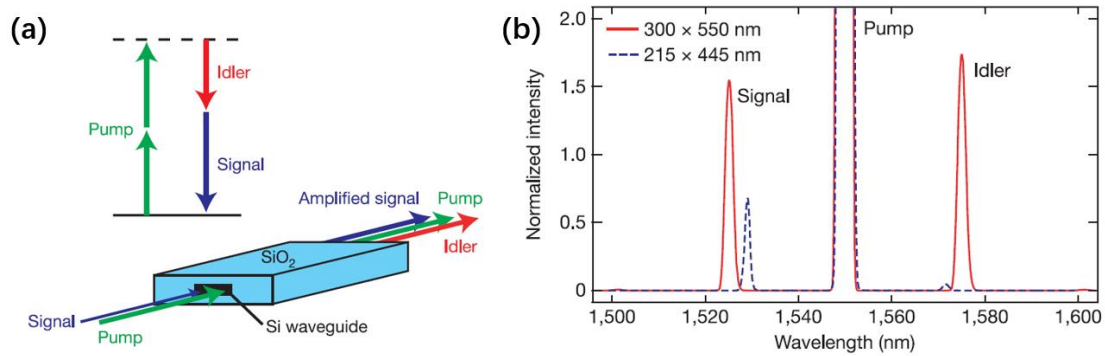

Figure 13. (a) Schematic of silicon degenerate four-wave mixing (b) Frequency spectrum of (a). Figures are reproduced from [76] and [77].

Though resonators are powerful in promoting strong light-matter interaction, the resonant nature of these cases however puts difficulties on the broadband or tunable functions which are highly expected in practical applications. In this context, PhC slow-light waveguides [85] were applied to improve the light-matter interaction [86] while leaving access to broadband purpose (see Figure 15). Based on this method, third-order harmonic generation (green light) based on silicon Kerr effect was demonstrated [87]. Numerous works on group velocity control for enhancing silicon Kerr nonlinearities using photonic crystal waveguides have been later reported [88, 89].
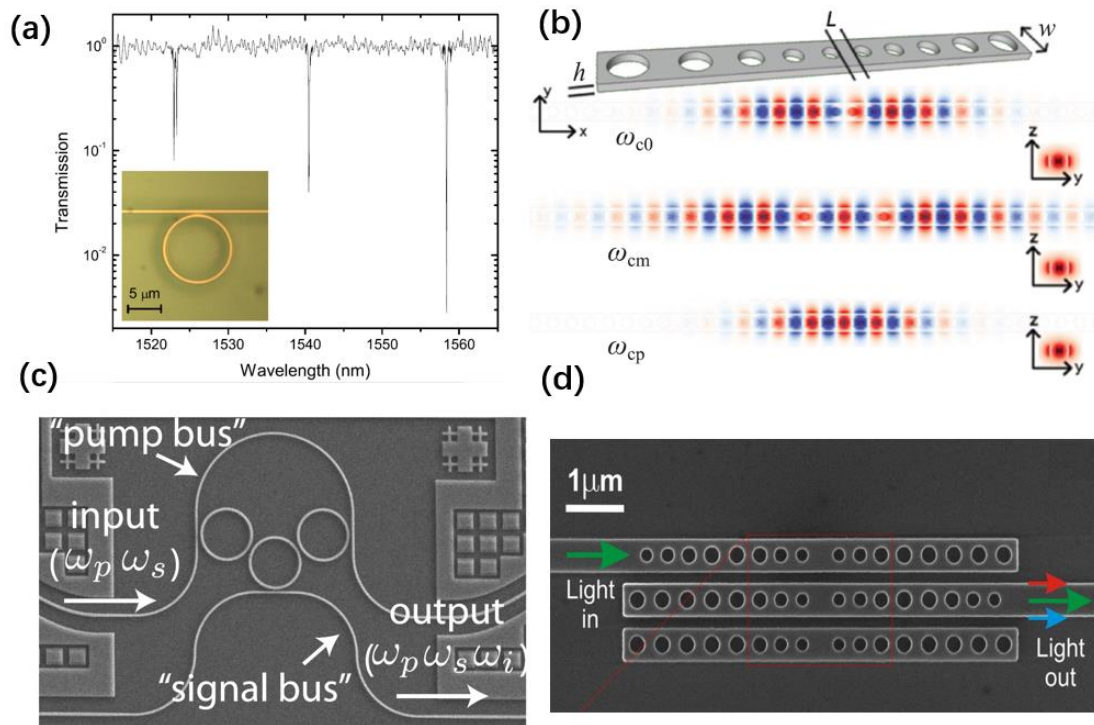
Figure 14. Methods of enhancing the silicon four-wave mixing with (a) ring resonator, (b) multi-resonance PhC cavity, (c) coupled rings molecule and (d) coupled PhC molecule. Figures are reproduced from [77], [79], [81], [83].
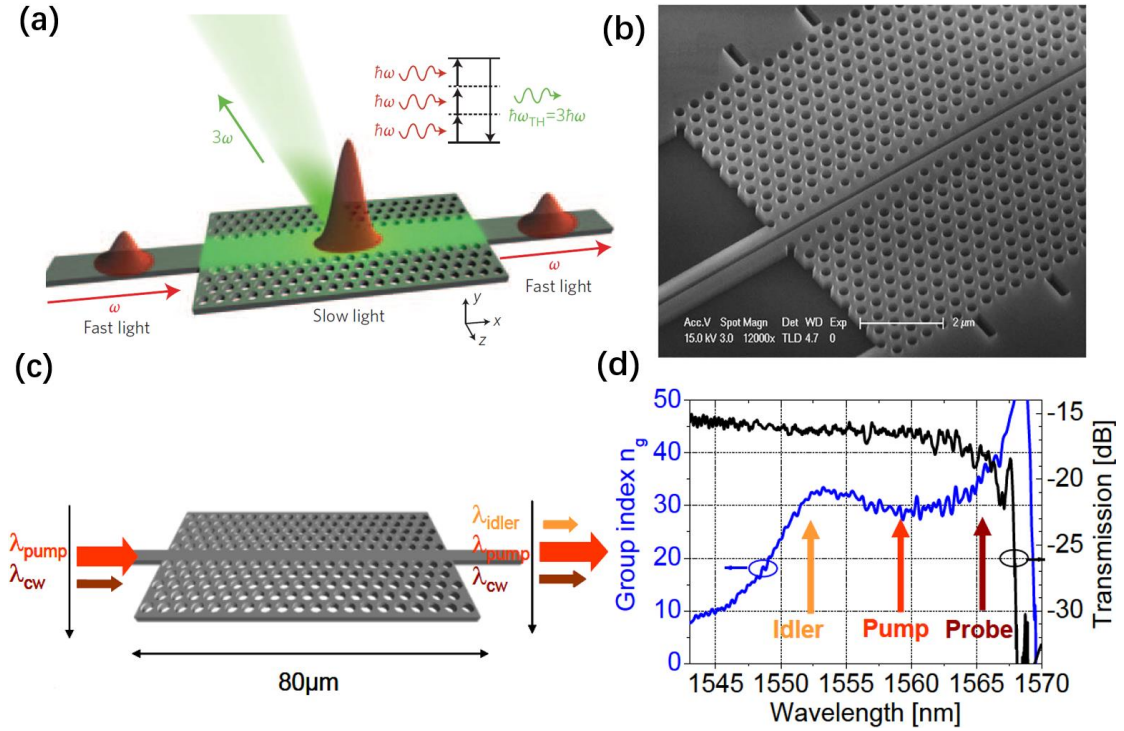

Figure 15. (a) Schematic of 3rd harmonics in silicon enhance by photonic crystal slow-light waveguide. (b) Microscope of silicon slotted photonic crystal slow-light waveguide. (c) Schematic and (d) performance of using photonic crystal slow-light waveguide to enhance four-wave mixing. Figures are reproduced from [87], [89], [85], [85].

1.2.3.3 Demand in flexible dispersion control

As was introduced above, the Kerr nonlinearities highly depend on the energy conservation and phase matching conditions, no matter classical strip waveguides or PhC waveguides are considered. In this context, careful waveguide dimension design for controlling the waveguide dispersion to compensate the nonlinear phase induced-mismatch [90] is necessary and important. However due to the fact that semiconductor platforms, especially silicon, present a high core/cladding index-contrast, standard waveguides normally exhibit sharp dispersion changes (see Figure 16 (a)). These unflatten dispersion behaviors intrinsically lead to narrow bandwidths of the conversion wavelength range, as shown in Figure 16 (b). Similar results are also found at longer wavelengths around λ=2 microns [91]. Photonic crystal patterns are able to offer flexible engineering capability of the waveguide dispersion but also bring another drawback with their huge sensitivity to changes of the light group velocity dispersion and to the fabrication techniques, as shown in Figure 15 (c) and (d).

This issue on dispersion control gives us another question: **Do we have more robust and flexible methods to engineer the dispersion for simultaneously fulfilling energy conservation and phase matching conditions？**
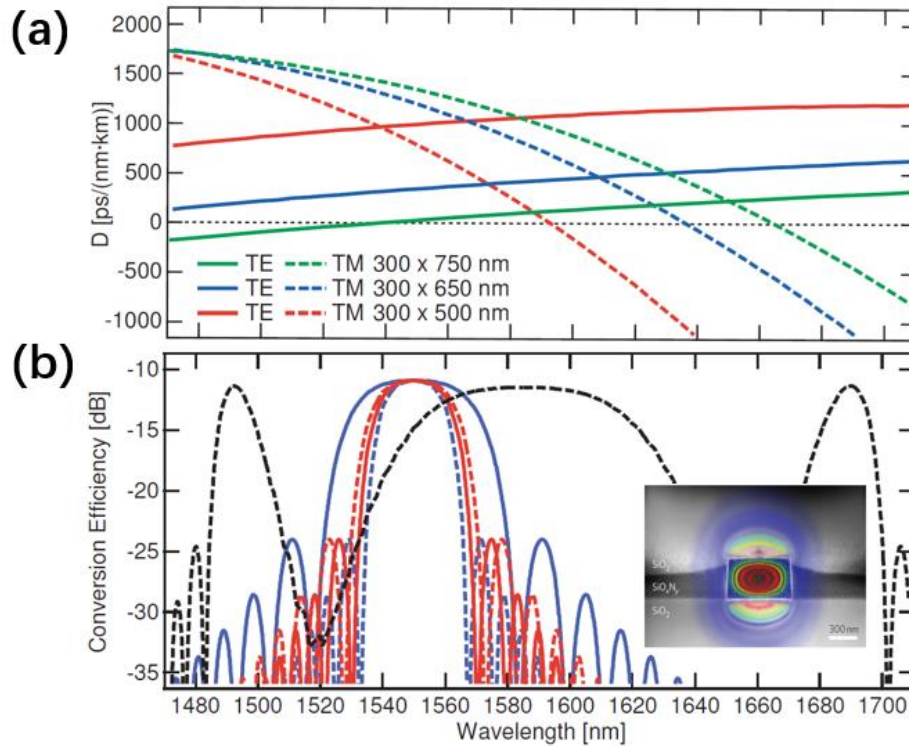

Figure 16. (a) Dispersion of silicon waveguide with different cross-section and (b) Corresponding conversion efficiency of four-wave mixing. Figures are reproduced from [90].

1.3 Subwavelength structures at the services of passive and active functions

To address those two issues laid on section 1.2.2.3 and 1.2.3.3, i.e. the *power-bandwidth trade-off in a silicon resonant modulator* and the *management of waveguide dispersion in silicon waveguides to enable phase-matched nonlinear optical processes*, we think that *subwavelength waveguide structures can bring a decisive help*. Based on subwavelength optics, we expect, from a novel point of view, to address those issues, improve device performances and open new opportunities for the relevant applications.

1.3.1 Subwavelength structures: a powerful tool for passive devices

Subwavelength optics has been proposed for more than two decades [92] and benefits from the rapid development of fabrication technologies which makes it accessible experimentally. Subwavelength optics [92] has found many applications in the realization of vertical cavity surface emitting lasers [93-96] where light penetration length and photon life are dramatically reduced with this approach and

tunable functions can be realized when combined with MEMS technologies. In addition to membrane mirrors, subwavelength structures can be also applied to develop meta-surfaces [97], non-conventional optical lenses [98], holographic and nonlinear devices [99], as well as on-chip photonic mode convertors [100], to quote a few examples.

In a photonic crystal perspective (see Figure 17), sub-wavelength photonics occurs in fact when light frequency is much smaller than the period of a periodic structure (at least locally periodic), meaning a much larger wavelength than the geometrical corrugation scale (A) that $\lambda \gg 2nA$ (where n is material index). Spatially averaging the optical material properties then becomes relevant. Band structure and the dispersion curves of periodic structures waveguide are shown in Figure 17 for comparison. In this context, the diffraction (Mie scattering, radiation, Bragg reflection) is strongly suppressed and especially when they are much larger than the pitch, the particles work like Rayleigh scatters. In this situation the stratified structure behaves like a homogeneous anisotropic material with an equivalent anisotropic permittivity tensor with respect to the macroscopic electromagnetic field [92], which has been discussed 50 years ago. It was difficult to conduct experiments in the visible or near-infrared ranges but of the progress of micro fabrication has rapidly reduced this limitation (e.g. with electron-beam lithography and other techniques) in the last 15 years
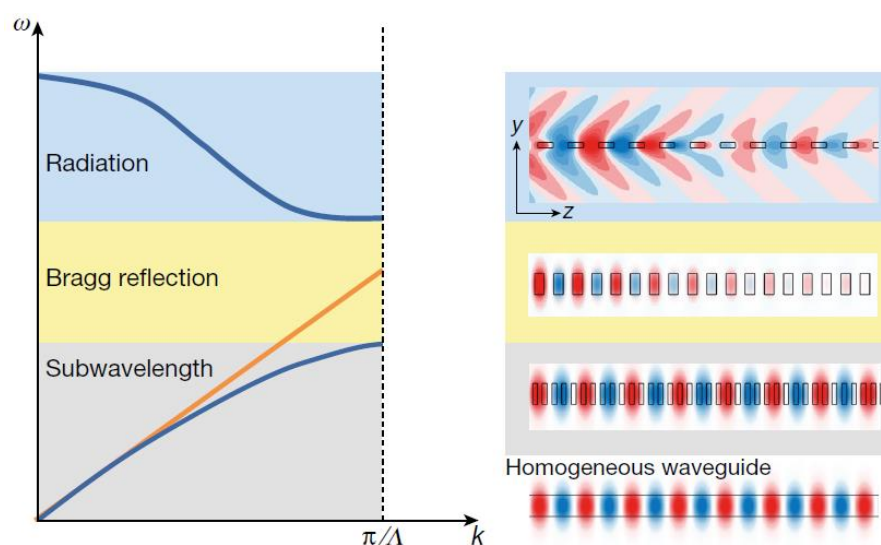

Figure 17. Schematic of the optical response in different regions of periodically structured waveguide. Figures are reproduced from [102].

In [92], Dr. Rytov found that if the period of subwavelength structures consisting of alternating slabs of dielectric materials with refractive indices n_H and n_L is much smaller than the incident wavelength, the overall medium is optically equivalent to a uniaxial crystal with an optical axis perpendicular to the layers (see Figure 18). With a quasi TE light polarization injection, if the segment is arranged along the propagation

direction (i.e. polarization is parallel to periodical interface) or the normal direction (i.e. polarization is perpendicular to the periodic interface), the global photonic structure can be considered as a homogeneous material with an index being [101-103]:

$$\text{Either } n_{||}^2 = \frac{w}{A}n_H^2 + (1 - \frac{w}{A})n_L^2, \tag{1.27}$$

$$\text{Or } n_{\perp}^{-2} = \frac{w}{A}n_H^{-2} + (1 - \frac{w}{A})n_L^{-2}, \tag{1.28}$$

where $n_{||}$ and $n_{\perp}$ are the equivalent material index values in the two considered cases, with n_H and n_L standing for the high-index and low-index materials, respectively. The pitch and the filling factor of the high-index segment are called here A and w/A, respectively. With this approximation, index-engineering is available for creating artificial media being designed to have a greater range of material properties than those available in nature.
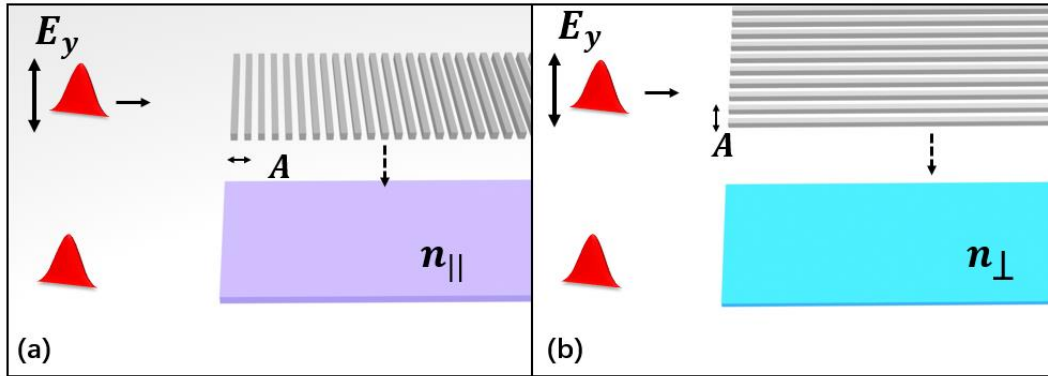

Figure 18. Schematic of the equivalence of periodically structures, for electric field polarizing parallel and perpendicular to periodic surface.

These "all-dielectric metamaterials" bring new degrees of freedom in the design space parameter of optical waveguide structures, for the purposes including splitter, coupler [104-106], biosensing [107], inverse photonic designs [108, 109], automatic calculation [110, 111], etc. Unlike the typical bulk metamaterials, these "all-dielectric metamaterials" are integrated easily with the on chip photonic component using planar fabrication technologies (see Figure 19), with numerous advances, which are the reason why they are so interesting.
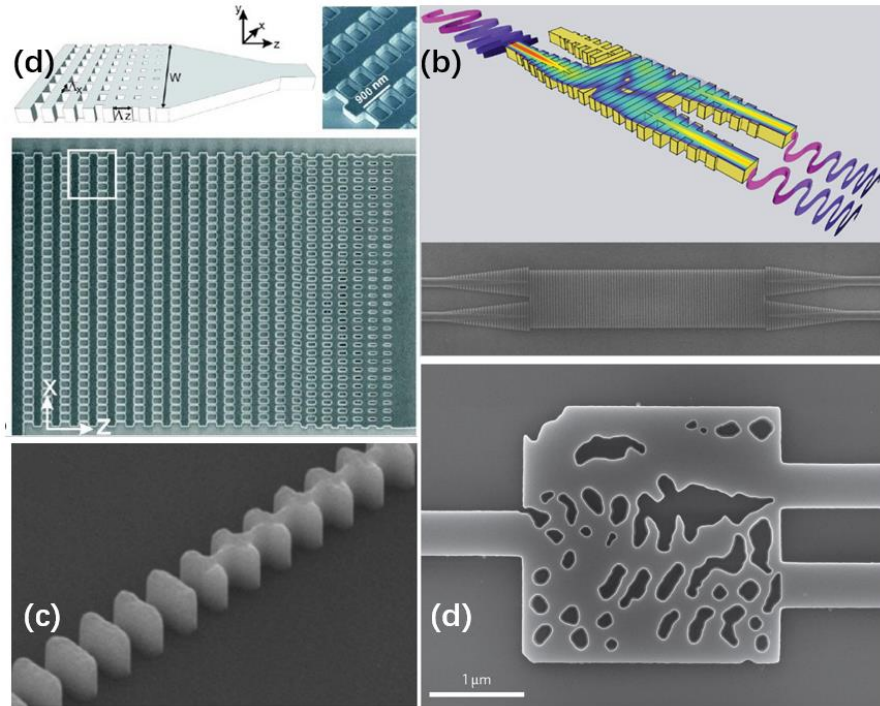
Figure 19. (a) Schematic of subwavelength structured silicon grating coupler. (b) Schematic and scanning electron microscopy image of subwavelength broadband beam splitter. (c) Scanning electron microscopy image of subwavelength spot convertor. (d) Scanning electron microscopy image of a polarization beam splitter using inverse design. Figures (a), (b), (c) and (d) are reproduced from [104], [105], [106] and [109].

1.3.2   Subwavelength engineering: a toolbox to help light-matter interaction

The powerfulness of subwavelength engineering has been witnessed [93-111] and introduced in section 1.3.1. This is a take-home message that we expect to use subwavelength engineering to address those two issues laid on section 1.2.2.3 and 1.2.3.3: i.e. **power-bandwidth trade-off in a (strained) silicon resonant modulators and the dispersion manipulation for exploring Kerr-induced optical effects in silicon waveguides (with a special focus, as shown later on FWM and frequency comb generation).**

- ✓ In chapter 2, we will first address the power-bandwidth trade-off using subwavelength engineering to enhance efficient light modulation in silicon photonic crystal (Fano) cavity silicon resonant modulators.

- ✓ In chapter 3, we will introduce a method (called "Self-Adaptive Boundary" (SAB)) for flexibly controlling waveguide dispersion and enabling an automatic FWM phase matching condition. Taking its root from ideas derived from quantum mechanics and being practically achieved by the use of subwavelength waveguide structures, this method will be applied to waveguide FWM processes and frequency comb generation. Soliton comb

generation and dynamics will be studied in the engineered waveguides based on the nonlinear Schrödinger equation in the form of the Lugiato-Lefever equation.

We believe that the proposed method opens even wider perspectives for the exploitation of 3rd-order non-linear optical properties from the silicon photonic platform or any other platform (IIV/V semiconductors, polymers, etc). The story began on this background but will definitely not limited in just nonlinear optics and subwavelength optics and cases we mentioned. The hint among all these contents is, the **flexible control of light-matter interaction**. Harnessing these preliminary researches presented following, we hope new visions can be reached for our further researches in nonlinearities-based photonics and other researches including quantum light source, on-chip spectroscopy, on-chip temporal signal control etc.

2 Subwavelength structures for enhanced electro-optical modulation

In this chapter, *we first explain the bandwidth-consumption trade-off in silicon resonant modulators and indicate that by sharping the resonant spectrum of the in-modulator constitutive resonator, modulation efficiency can be improved without sacrifice on the bandwidth.* More specifically, we will describe the mechanism based on a subwavelength engineering approach to produce an *asymmetric-spectrum Fano resonance in a single nanobeam cavity*, i.e. made on a single optimized strip silicon waveguide channel. Analytical analysis will be presented to sustain the proposed idea and, with the parameters derived from the design, fabrication and characterization results will be presented, before concluding.

Next, the design of a strained silicon modulator based on this single-waveguide subwavelength structured Fano resonator will be developed. In addition, we will indicate how a wavelength tunable operation can be achieved with such a single-waveguide resonator through both analytical and experimental demonstrations.

Overall, the feasibility of high-bandwidth low-consumption silicon resonant modulators will be reported, with outlook of tunable function and new application using this subwavelength structured resonator.

2.1 Sharpening the resonant spectrum of PhC Fano cavities with subwavelength structures

2.1.1 Introducing a Fano resonance to a single-waveguide resonant cavity

As we introduced it above, micro-resonators (including micro rings/disks and photonic crystal cavities) are capable for small footprints and relatively small off/off operation (typically > 15dB) in on-chip integrated configurations [112]. However, the considerable photon lifetime in an ultra-high-quality factor ($Q >> 10^3$) cavity is detrimental to the target modulated bandwidth (at least >10GHz). Generally speaking, the photon dynamics in a Lorentzian shape cavity modulator fed directly by a bus can be understood as it is shown in Figure 20. Since the cavity we consider here is a nanobeam cavity (one of 1D photonic crystal cavities) fed directly by a bus waveguide, as Figure 20 (b), Lorentzian shape with highest transmission on resonance is shown in Figure 20 (a).
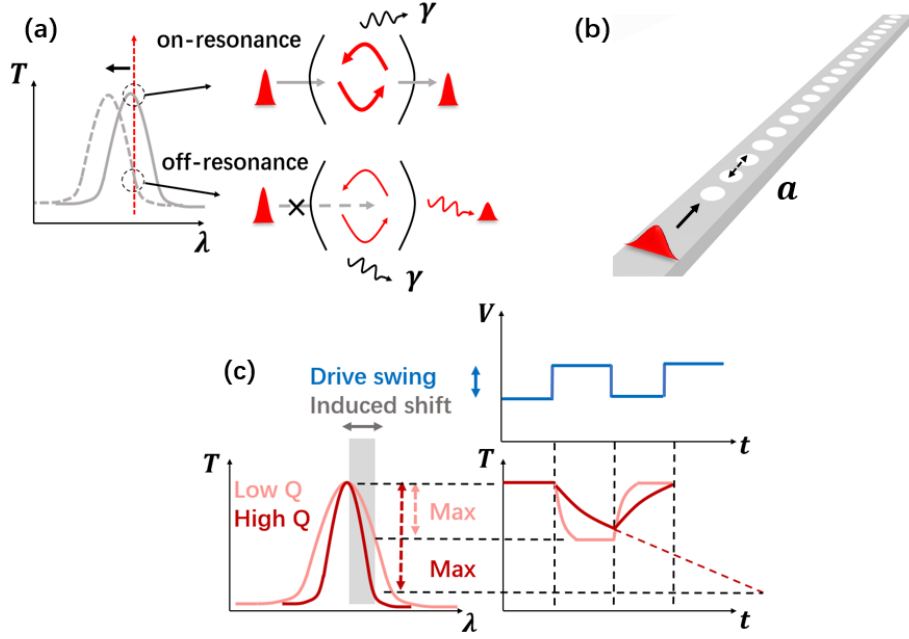
Figure 20. (a) Schematic of on/off-resonance photon dynamics. (b) Schematic of a nanobeam cavity based on a strip optical waveguide drilled by holes. (c) Schematic of in-complete light extinction in high-Q and low-Q case.

In such a cavity, strong light reflection is formed for a wideband spectrum and only light wave with on-resonant frequency can be transferred to the cavity core, with an in-cavity optical power built up, and then remitted to the output port. The on/off modulation operation is obtained at a specific wavelength by shifting the cavity resonance from an "on-resonance" to "off-resonance" thanks to any relevant possible mechanism (e.g. thermal effect, electro-optical and other nonlinear effects, free carrier plasma dispersion effect). As the cavity energy decay time is proportional to Q (where photon lifetime which determined by time duration for a power decay factor of e^{-2}.) A long-lasting output energy decay of a high-Q cavity can be actually observed and lead to non-instantaneous transition on modulator (see Figure 20 (c)). Given a certain spectrum shift that determined by materials and applied signal, the "high-Q" spectrum can give a larger "accessible (maximum) extinction ration" (or to say, transmission contrast) than that of "low-Q" spectrum. This high accessible contrast can give the possibility for reducing the required driven power. However, as the Figure 20 (c), this large contrast cannot be fully used since photons decay is cut at next raising/falling edge of the driven signal. In contrast, though smaller maximum extinction ratio is obtained with a low-Q spectrum, but full light falling back then occurs before the signal flip.

For example, for a quality factor of only 10^4, the bandwidth f_{3dB} limited by photon lifetime (with negligible RC constant) can be calculated as: $\frac{1}{f_{3dB}^2} = (2\pi\tau)^2 + (2\pi RC)^2 \approx (2\pi\tau)^2$ and $\tau = \frac{Q}{\omega} = \frac{\lambda Q}{2\pi c}$, which gives no more than 20GHz for a

working wavelength at around $1.5\mu m$ [66]. Though the experimental bandwidth is later found can be a bit larger than this estimation [112], resonators designed for high bit rate modulators have usually limited Q factors of a few thousands [113, 114]. Such a limit on Q factors leads to the request of higher driving swing for enlarging the wavelength shift and the accessible extinction ratio compared to a higher-Q cavity. This has no doubt caused a larger power consumption, e.g. of tens to hundreds of femtojoules per bit for acceptable extinction ratio (>~8 dB). Various approaches like different-signal driving [115] and vertical P-N structures [116] for silicon disk resonators have been implemented to reduce power consumption. However, these kinds of doping schemes are complex and challenging with respect to fabrication accuracy control. Therefore, new and simple solutions are expected for low power consumption and high-bit rate optical modulation.

In fact, modulation inefficiency comes largely from the shape of the spectral resonance used, very symmetrical, and which therefore implies to be significantly shifted in frequency in order to induce an on/off extinction ratio >>1. If we can, as illustrated in Figure 21, rotate the Lorentzian-lineshape spectrum without any increase on the Q factor, we can take advantage of the fast light response and simultaneously improve the obtained modulation extinction ration (ER). This is the reason why Fano resonances, which arise from the interference of a discrete resonant mode and a continuum background, have been proposed to solve this issue [117]. As it is shown hereafter and already illustrated in Figure 21, their asymmetric spectrum signature can be used to address the bandwidth-power trade-off of silicon resonant optical modulators and potentially minimize the power consumption of silicon switching and modulation devices. Different types of Fano-resonance-based cavities have already been proposed including spatial membrane structures [118], plasmonic resonators [119] and integrated side-coupled one/two-dimensional (1/2D) photonic crystal cavities [120-123]. Thanks to the advances of fabrication technology, novel integrated devices based on these Fano cavities like nonreciprocal transmission structures [124], Fano lasers [125] and switches [126] have been demonstrated. Especially, an all-optical high-bit rate modulation behavior combining the free carrier response of indium phosphide and a Fano cavity was demonstrated [127].
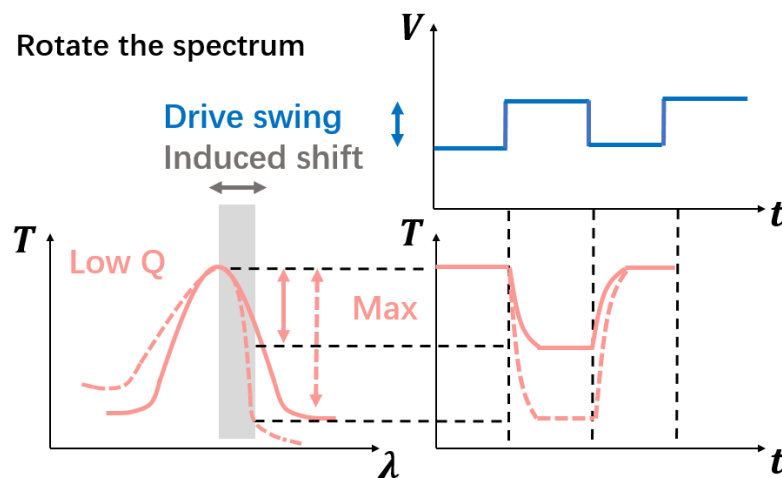
Figure 21. Schematic picture of the effect of an asymmetrical resonance lineshape on modulation properties

2.1.2 Design of the single-waveguide Fano nanobeam cavity

Photonic crystals (see Figure 22 (a), (b)) were first experimentally introduced by Eli Yablonovitch in 1987 as a method of controlling spontaneous emission in a material [128] and have been intensively studied since then [129]. There also came from the motivation of manipulating light using small photonic components bringing the density of functional elements to the same level as that in current electronics and triggering investigation of the light-matter interaction and discovering multi-physical effects. These motivations led to the development ultra-high-Q photonic crystal cavities [130-132], which (see Figure 22 (c)), compared to the ring/disk resonators [133, 134], present significant improvement on the Purcell factor [135] and strong potentials in applications including quantum optics [136], matter detection [137], optical memory [138] and biosensing [139] etc. The nanobeam cavities, in form of strip-shape 1D PhC cavity (see Figure 22 (d), (e) and (f)), are also found as presenting ultra-high quality factors [140], in the meanwhile give novel freedoms to researches including optomechanical control [141, 142], particle manipulation [143], extreme light concentration [144], low-power switch [145-147], etc. The theory of photonic bandgap and PhC cavities has already been well developed and detailed in [129-132, 140] and we will not recall their properties here.
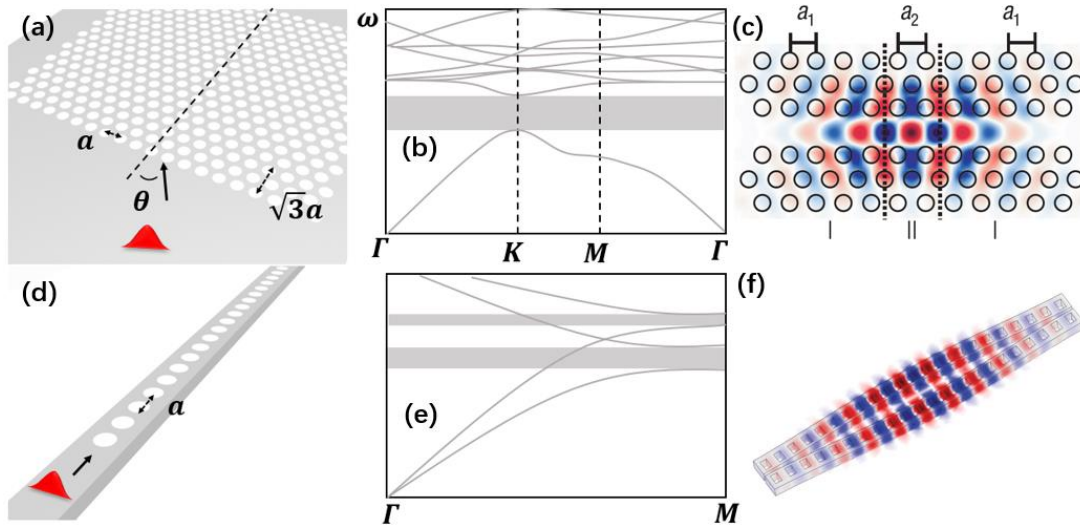

Figure 22. Schematic views, dispersion diagrams and mode profiles of PhC cavities reproduced from [131] and [137].

PhC cavities have been used in previous works as an element for creating Fano spectra, most of which operating with a side-coupled bus waveguide [121, 124], as shown in Figure 23 (a). A practical implementation can be to consider a line-defect PhC waveguide close to a 2D PhC cavity or a strip bus waveguide to the vicinity of nanobeam, as shown in Figures 22 (b) and (c). In this configuration, the first behaves

as a localized resonance, while the second behaves as a continuum of possible frequencies, the interference of a wave exciting these two paths leading to a Fano spectral resonance. A partially transmitting element is then placed between to control the balance between both light paths.

However, though structures are basically as simple as two strip waveguides, this type of side-coupled photonic-wire configurations leads to some issues for optical modulation. A first drawback of such configurations arises from the high sensitivity of the bus waveguide/cavity region optical coupling ratio on the technological fabrication imperfections of the structure (in particular on the width of the bus waveguide) [145]. The imperfection of hole sizes can also introduce light unbalance from the in the strip and resonator, which influences their spectra and distort their resonances. Unless a post-trimming method of controlling the light balance is provided, this control is somewhat challenging. A second issue stems from the fact that the cross-sectional structure of the modulator is intrinsically both asymmetric and more spatially extensive than a simple waveguide one. For instance, considering this configuration in a free carrier plasma dispersion effect with an embedded PN junction as shown in Figure 23 (d), the bus waveguide somewhat brings complexity to the realization of the needed doping profiles and is more importantly responsible for an increase of the electrode-to-electrode distance that is likely to kill the modulator bandwidth. Since the electrodes need to be set a distance away from the waveguide for to avoid ohmic losses, this extension indeed increases both the capacitance and the access resistance of the whole structure equivalent circuit [146]. Therefore, for the full exploitation of the Fano signature of active cavities, it is particularly important to look for fully integrable configurations in a single waveguide (strip or strongly engraved rib [147]) with a good strategy of controlling the light balance between the two light channels interfering with each other.
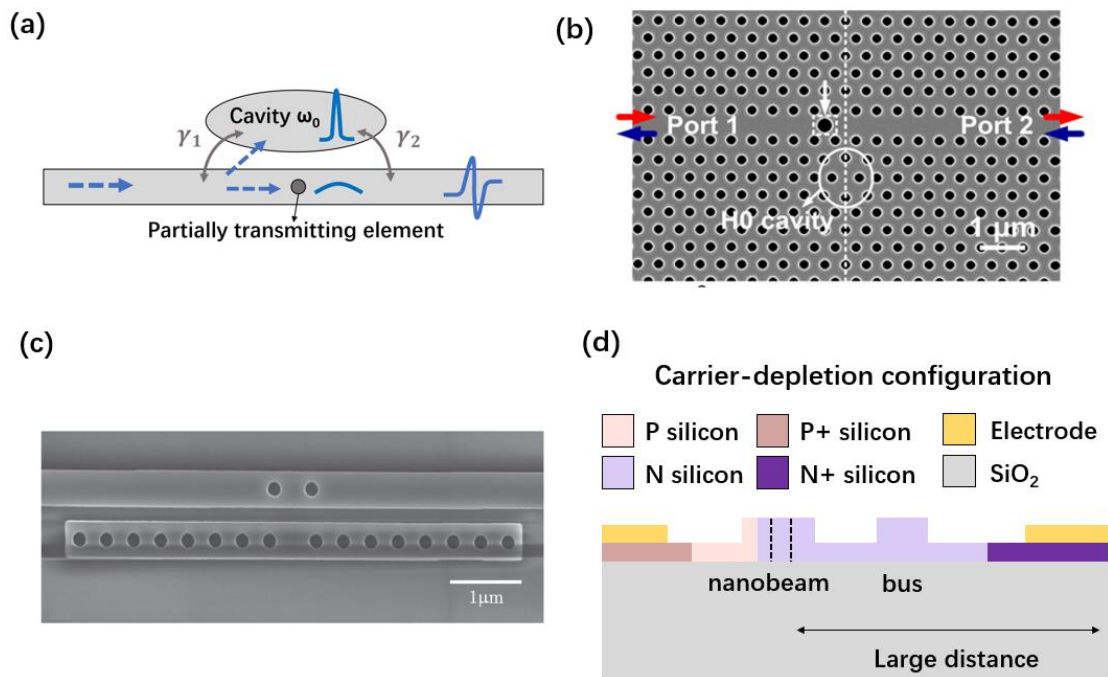

(a)

(b)

(c)

(d)

Figure 23. (a) Schematic of side-coupled Fano resonator. (b) Fano resonator using side-coupled 2D PhC cavity. (c) Fano resonator using side-coupled nanobeam cavity. (d) Cross-section of a side-coupled modulator using plasma dispersion effect and a two-strip waveguide Fano cavity

Since a Fano resonance arises from the interference between a discrete resonance and a continuum [117], the idea is to create the non-resonant background with a higher order propagating mode, i.e. to shape Fano resonances using slightly multimode waveguides. We propose here is to take advantage of a two-mode spatial multiplexing scheme to generate the resonant and the transmitting modes in the same physical optical waveguide, as shown in Figure 24 (a). As introduced in chapter 1, the Bragg condition for creating a mirror is $\lambda = 2n_{eff}a$, where n_{eff} and a are the effective index of the propagating mode and lattice period, respectively. **The basic principle of the approach we propose to implement is thus to design a single guide but dual mode structure, of which one of the two resonant modes could play the role of narrow resonance and the other of wide resonance acting as a pseudo-continuum of frequencies, respectively, and then to force their interference to obtain a Fano resonance signature**.
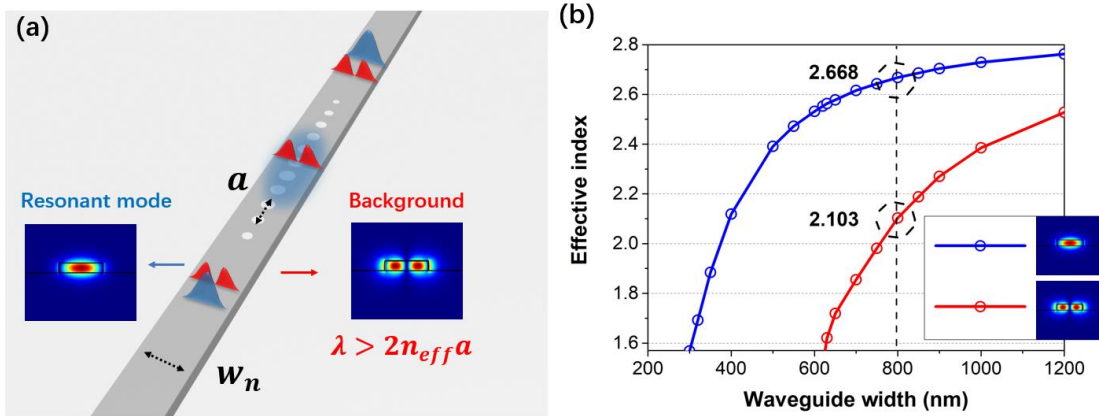
Figure 24. (a) Schematic of using a high-order optical mode working in sub-wavelength region as a non-resonant background. (b) Dispersion curves of the TE modes at 1550nm wavelength in a 220nm-thick silicon on insulator strip waveguide as a function of the waveguide width.

In order to study the feasibility of the proposed single-waveguide principle of operation, eigen mode solving and FDTD methods were used to calculate the mode dispersion and field and power transmission levels of the TE modes in the nanobeam structure, as Figure 24 (a). The corresponding platform we considered started from a typical silicon-on-insulator (SOI) photonic platform with a 220nm thick silicon core and a 2μm thick buried silicon dioxide layer. The dispersion curves of both TE propagating modes obtained for different nanobeam widths (w_n) are presented in Figure 24 (b). In principle, in order to provide a high transmission level for the TE_1 mode with a weak perturbation from the nanobeam cavity, the difference of effective index values between the TE_1 and TE_1 propagating modes should be as large as possible to prevent Bragg reflection for the TE_1 mode. A waveguide width w_n=630

nm ($n_{eff,TE0}$~2.55 and $n_{eff,TE1}$~1.6) corresponds to the ideal value but due to the rapid change of the TE$_1$ propagating mode dispersion close to this condition, this option can lead to fabrication-sensitivity issues. Thus, a moderate value w_n=800nm was selected, providing an acceptable index contrast between the TE$_0$ and TE$_1$ propagating modes of ~ 0.565. We also notice that due to the diverged mode distribution as shown in Figure 24 (b), the overlap of the mode and the central etched can be controlled in no more than 10%, which gives good promise to the week perturbation.

Next, a nanobeam cavity with a 50-holes array under a period of 300nm was considered. To obtain a resonant high quality (Q) factor and a high transmission for the TE$_0$ mode, the hole radii were tapered from 100nm in the center to 70nm in a 15-periods length [148]. Extra 10-holes mirror sections with identical 70nm radius holes were added at the end of each taper. The total length of the nanobeam cavity was close to 15 μm. The calculated transmission spectra for both TE propagating modes are shown in Figure 25 (a). As visible, and as desired, the TE$_0$ and TE$_1$ modes present strongly different spectra. Considering for example the spectral region centered on the first TE0 resonance, for example from 1.51μm to 1.53μm, it is obvious that each of the two modes TE0 and TE1 makes its expected contribution (a sharp resonance and an almost flat resonance, i.e. no resonance at all), respectively.

The simulated quality factor/transmission values with TE$_0$ input (merely TE$_0$ propagating mode in the nanobeam waveguide) for the 1st and 2nd cavity modes are 230000/55%, and 19000/95%, respectively. Quality factor is calculated using formula $Q = \omega\tau/2$ in which ω and τ are the resonant angular frequency and corresponding photon lifetime, respectively. For the TE$_1$ propagating mode, an average transmission larger than 90% is obtained in the 1500nm to 1600nm wavelength range. Overall this high distinctly diverse transmission response thus gives promise to the feasibility of generating asymmetric spectrum by mixing the two waveguide mode channels together. Though the peak transmission of these two TE propagating modes are not exactly balanced, the related excitation ratio can easily be engineered by adjusting the input waveguide width of the MMI-like structure to find the right balance between the two optical modes.
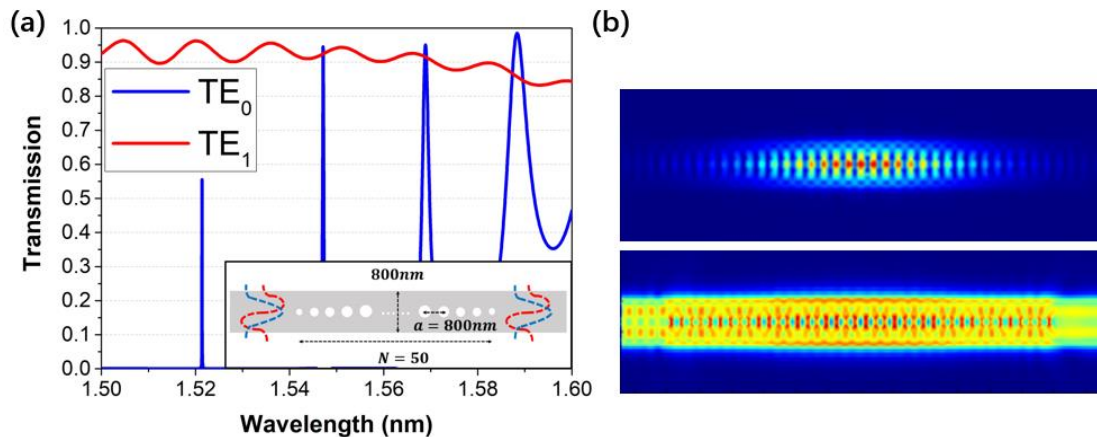

Figure 25. (a) Transmission spectra through a nanobeam, with excitation of onlu TE$_1$ or TE$_2$

propagating modes through a classical nanobeam cavity with w_n=800nm, 50 holes and 300nm period.

Knowing the possibility of guiding one resonant and one propagating mode simultaneously in a nanobeam, now we can build a preliminary model like that the one shown in Fig. 26. In that purpose analytical calculation using the temporal coupled-mode theory can be considered [120, 149] (TCMT). This whole study will be carried out by considering a single TE$_0$ resonance, i.e. by restricting the analysis frequency range around a single resonance.

As shown in Fig. 26, the total structure can be considered as a two-port scattering system. S_I^+, S_I^- are the forward and backward field amplitudes from port I (left side port), respectively. S_{II}^+ and S_{II}^- share the same definitions for port II (right side port). t_{F0} is the complex transmission coefficient of electric field (then $T_{F0} = |t_{F0}|^2$ is the power transmission) of the TE$_0$ propagating mode after the whole structure. For a nanobeam cavity with a resonant angular frequency ω_0 and corresponding electric field a_0 for the TE$_0$ mode, the decay rate for this resonant mode due to coupling to the two feeding waveguides, the decay rate due to out-of-plane scattering and intrinsic absorption are γ_1, γ_2, γ_v, γ_i, respectively. Therefore, the total decay rate (TE$_0$ propagating mode) can be written as $\gamma_t = \gamma_1 + \gamma_2 + \gamma_v + \gamma_i$. The energy excitation from input source to the TE$_0$ and TE$_1$ modes in the distribution region (left deep gray region in Figure 26) are labeled by η_0 and η_1, respectively. Meanwhile the conservation from the TE$_0$ and TE$_1$ modes to the TE$_0$ mode (TE$_0$ is chosen because fundamental is normally preferred for out-coupling with grating coupler) is considered in the "interference" region which will be addressed later, with conversion efficiencies C_{00} and C_{01}, respectvely. The transmission of the nanobeam cavity for the TE$_1$ propagating mode called T_1 ($T_1 = |t_1|^2$) can be assumed as nearly uniform due to the weak interaction of this mode with the array of patterned holes.
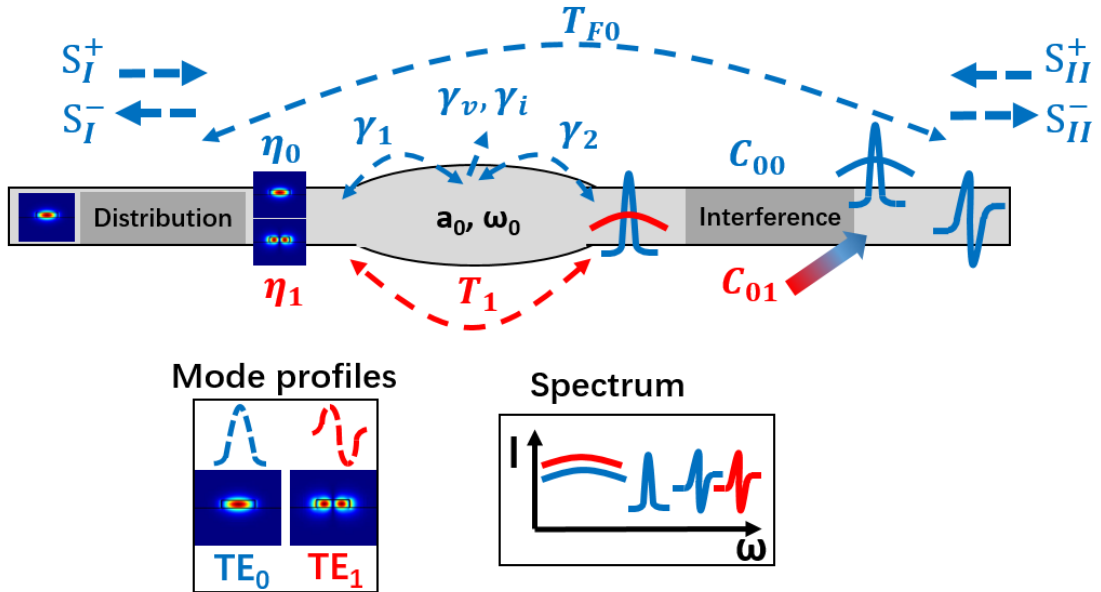

Figure 26. Schematic of the dynamics of optical waves in a standalone two-port waveguide nanobeam

Fano cavity. TE_0 and TE_1 propagating modes are marked by blue and red dashed curves, respectively. The spectrum of TE_0 and TE_1 propagating modes are depicted by the blue and red curves, respectively.

According to the TCMT and considering a detuning of angular frequency $\delta_r = \omega - \omega_0$, the coupled equations of the resonant and backward waves can be written as follows:

$$\frac{da(t)}{dt} = (-i\delta_r - \gamma_t)a + \sqrt{2\gamma_0}e^{i\theta_1}\sqrt{\eta_0}S_I^+ \tag{2.1}$$

$$S_I^- = r_m\sqrt{\eta_0}S_I^+ + \sqrt{2\gamma_1}e^{i\theta_1}a \tag{2.2}$$

$$S_{II}^- = \sqrt{2\gamma_2}e^{i\theta_2}a\sqrt{C_{00}} + \sqrt{\eta_1}S_I^+ t_1\sqrt{C_{01}}ie^{i\Delta\theta} \tag{2.3}$$

in which θ_1 and θ_2 are the phase factors of the cavity waveguide modes at the left and right ports, respectively. $\Delta\theta$ is the phase difference between the TE_0 and TE_1 propagating modes, which is counted from the input source to the interference region after the core part of nanobeam cavity. The reflection coefficient of the nanobeam cavity mirrors for the TE_0 mode is r_m, which can be considered as 1 for simplification (Confirmed by an estimated reflection power level at slightly off-resonant wavelength which indicated a reflection coefficient ~0.98, a nearly unitary value being indeed consistent with the large Q factor of the TE_0 cavity mode).

For steady state condition, $da(t)/dt=0$ and the field transmission coefficient for the TE_1 mode through the whole structure ($T_{F0} = |t_{F0}|^2$) can be written as:

$$t_{F0} = \frac{S_{II}^-}{S_I^+} = \frac{2\sqrt{\gamma_1\gamma_2\eta_0 C_{00}}e^{i(\theta_1+\theta_2)}}{i\delta_r+\gamma_t} + i\sqrt{\eta_1 C_{01}}t_1 e^{i\Delta\theta} \tag{2.4}$$

For symmetric cavity design, $\theta_1 = \theta_2$, $\gamma_1 = \gamma_2$, and for a highly confined cavity mode, $e^{i(\theta_1+\theta_2)} = \cos(\theta_1 + \theta_2) + i\sin(\theta_1 + \theta_2) = -r_m \approx -1$[125], therefore

$$t_{F0} = \frac{S_{II}^-}{S_I^+} \approx \frac{-2\gamma_1\sqrt{\eta_0 c_{00}}}{i\delta_r+\gamma_t} + i\sqrt{\eta_1 c_{01}}t_1 e^{i\Delta\theta} \tag{2.5}$$

If there is no excitation of the TE_1 mode and no interference region after the nanobeam ($\eta_0 = c_{00} = 1$, $\eta_2 = C_{01} = 0$), then

$$T_F = |t_{F0}|^2 \approx \frac{4\gamma_1^2}{\delta_r^2+\gamma_t^2} \tag{2.6}$$

The total transmission of the TE_0 mode then goes back to a typical Lorentzian shape.

For a case where $\eta_1 \neq 0, C_{10} \neq 0$:

$$t_{F0} \approx \frac{\frac{-2\gamma_1}{\gamma_t}\sqrt{\eta_0 C_{00}}}{i\frac{\delta_r}{\gamma_t}+1} + i\sqrt{\eta_1 C_{01}}\, t_1 e^{i\Delta\theta} \quad = \frac{\frac{2\gamma_1}{\gamma_t}\sqrt{\eta_0 C_{00}}\left(i\frac{\delta_r}{\gamma_t}-1\right)}{\frac{\delta_r^2}{\gamma_t^2}+1} + i\sqrt{\eta_1 C_{01}}\, t_1 e^{i\Delta\theta} \tag{2.7}$$

$$T_{F0} \approx \left(\frac{\frac{-2\gamma_1}{\gamma_t}\sqrt{\eta_0 C_{00}}}{\frac{\delta_r^2}{\gamma_t^2}+1} - \sqrt{\eta_1 C_{01}}\, t_1 \sin\Delta\theta\right)^2 + \left(\frac{\frac{2\gamma_1}{\gamma_t}\sqrt{\eta_0 C_{00}}}{\frac{\delta_r^2}{\gamma_t^2}+1}\frac{\delta_r}{\gamma_t} + \sqrt{\eta_1 C_{01}}\, t_1 \cos\Delta\theta\right)^2 \tag{2.8}$$

$$= \frac{\frac{4\gamma_1^2}{\gamma_t^2}\eta_0 C_{00}}{\frac{\delta_r^2}{\gamma_t^2}+1} + \eta_1 t_1^2 C_{01} + \frac{\frac{4\gamma_1}{\gamma_t}t_1\sqrt{\eta_0 C_{00}\eta_1 C_{01}}}{\frac{\delta_r^2}{\gamma_t^2}+1}\left(\frac{\delta_r}{\gamma_t}\cos\Delta\theta + \sin\Delta\theta\right)$$

Assume that the phase relative variable is written as $C_p = -\frac{\delta_r}{\gamma_t} + \frac{\delta_r}{\gamma_t}\cos\Delta\theta + \sin\Delta\theta$, we simplify T_{F0} as:

$$T_{F0} \approx \eta_2 t_2^2 C_{12}\left(\frac{\frac{4\gamma_1^2\eta_0 C_{00}}{\gamma_t^2\eta_1 t_1^2 C_{01}}}{\frac{\delta_r^2}{\gamma_t^2}+1} + \frac{\frac{\delta_r^2}{\gamma_t^2}+1}{\frac{\delta_r^2}{\gamma_t^2}+1} + \frac{\frac{4\gamma_1\sqrt{\eta_0 C_{00}}}{\gamma_t t_1\sqrt{\eta_1 C_{01}}}}{\frac{\delta_r^2}{\gamma_t^2}+1}\left(\frac{\delta_r}{\gamma_t}+C_p\right)\right)$$

$$= \eta_2 T_2 C_{12}\frac{\left(\frac{\delta_r}{\gamma_t}+\frac{2\gamma_1\sqrt{\eta_0 C_{00}}}{\gamma_t t_1\sqrt{\eta_1 C_{01}}}\right)^2}{\frac{\delta_r^2}{\gamma_t^2}+1} + \eta_1 T_1 C_{01}\frac{\left(1+\frac{4\gamma_1\sqrt{\eta_0 C_{00}}}{\gamma_t t_1\sqrt{\eta_1 C_{01}}}C_p\right)}{\frac{\delta_r^2}{\gamma_t^2}+1} \tag{2.9}$$

Assuming that $\frac{\delta_r}{\gamma_t} = \epsilon$, $\frac{2\gamma_1\sqrt{\eta_0 C_{00}}}{\gamma_t t_2\sqrt{\eta_1 C_{01}}} = q$, and taking into account that the total energy of the TE$_1$ propagating mode coupled back to TE$_0$ mode is $T_{01} = \eta_1 T_1 c_{01}$, we can simplify equation (2.9) as:

$$T_{F0} \approx T_{01}\frac{(\epsilon+q)^2}{\epsilon^2+1} + T_{01}\frac{(1+2qC_p)}{\epsilon^2+1} \tag{2.10}$$

The first term of equation (2.10) is the same as the traditional expression for Fano resonance in a two-port cavity [150]. The variable q is the asymmetric parameter, which quantifies the Fano spectrum asymmetry. The normalized energy amplitude of the continuum part of the TE$_0$ propagating mode, e.g. the T_{10}, becomes the amplitude coefficient of the Fano spectrum in Eq. (2). Similarly, the classical Fano spectrum in which the amplitude coefficient is the transmission of the partially transmitting element [117]. However, the above equations indicate that the phase quantity also contributes to the transmission and can cause a small deviation to the perfect Fano line shape. By controlling C_p, this phase related item can be minimized and high quality Fano lineshapes can then be obtained. As a whole, **the above analytical calculation shows that the obtained pseudo Fano expression opens room to design a sharp Fano-like behavior**. Analysis for TE$_1$ mode can be made similarly and is not

shown here. To study the effect of excitation efficiencies and mixing efficiencies to the spectrum, we assume that $\Delta\theta = 0$ (then $C_p = \epsilon(-1 + cos\Delta\theta) + sin\Delta\theta = 0$) for simplification, thus:

$$T_t = T_{12}\frac{(\epsilon+q)^2}{\epsilon^2+1} + T_{12}\frac{1}{\epsilon^2+1} \tag{2.11}$$

Based on this analytical calculation, we need to introduce mode excitation and interference as $\eta_1 \neq 0, C_{10} \neq 0$. The mode distribution/excitation can be performed by the Multimode Interference (MMI)-like structure shown in Figure 27 (a). This simple structure allows a tight control of the balance between the excited TE_0 and TE_1 propagating modes through the choice of the narrow (input) and wide (nanobeam) waveguides' widths, labelled w_i and w_n, respectively (see Figure 27 (a)). With the nanobeam width w_n being fixed at 800nm (again, throughout this work), the out excitation efficiency of the TE_0 propagating mode, increases with the waveguide width, while the excitation efficiency of the TE_1 mode first reaches a maximum at $w_i =$400nm, and then gradually decreases with increasing w_i values. These monotonous trends of the TE_0 mode curve can be understood with the related increased effective index value which minimizes the impedance mismatch between the input access waveguide and the nanobeam waveguide modes. On the other hand, the increased TE_1-mode efficiency arises from an improved effective index matching and the largest mode overlap (Figure 26 (b)) at the input/nanobeam waveguide interface. Figure 27 (a) indicates that the excitation efficiency of the TE_0/TE_1 mode can be adjusted in a large range (from nearly 55%/40% to infinity). For input waveguide widths larger than 400nm, the summation of the TE_0 and TE_1 excitation efficiencies is close to 1, which also indicates an available width range for low-loss light injection. As stated before, the he key of the design is also to widen the contrast between the effective indices of these two modes so that the TE_0 propagating mode strongly feels the influence of the cavity, thus generating a marked spectral resonance, while the second propagating mode TE_1 is only slightly insensitive to the periodic corrugation of the waveguide geometry and thus presents a very flat transmission spectrum (i.e. an ultra-wide resonance).
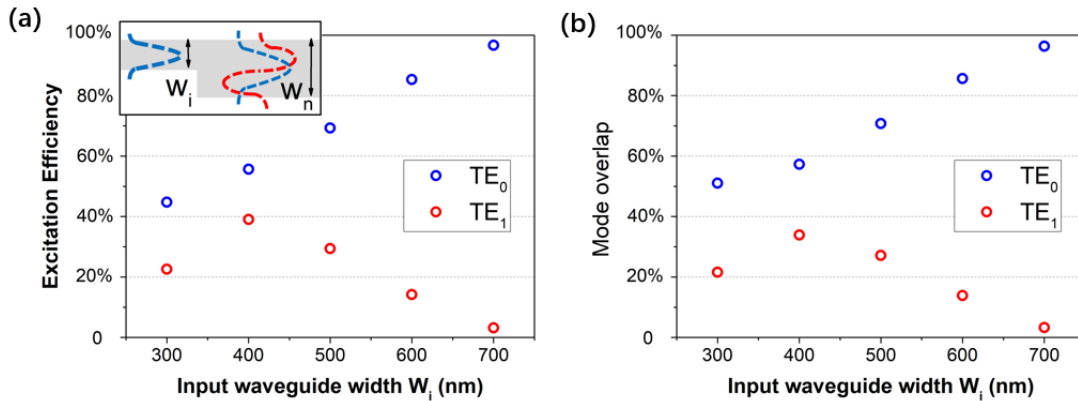
Figure 27. (a) Excitation efficiencies of the TE_1 and TE_2 propagating modes at plane 2 in a nanobeam waveguide with w_n=800 nm, connected with an input waveguide with different widths w_i ranging from

300-700nm. (b) The corresponding mode overlap between the input waveguide and nanobeam waveguide.

Corresponding to the mode mixing, the mode interference/mapping can be performed using several subwavelength approaches. **We designed a subwavelength mixer which consists of several rectangle-shape asymmetrically-located etched holes** for this purpose. The schematic of a mixer of this kind is shown in the inset of Figure 28 (a). The period P_e and filling f actor (*ff*) of these holes are 200nm period and 0.5, respectively, which are moderate values acceptable for fabrication and at the same time well located away from the condition of Bragg reflection ($P_e \sim 300nm$), i.e. in the subwavelength propagation regime, for the working wavelength ($\sim 1.5 \mu m$). The etched holes have a length (L_e) of half of W_n, i. e. 400nm and are 200nm displaced from the center of the waveguide. Such a structural asymmetry in an infinite periodically etched-hole array gives birth to the two modes whose mode dispersion curves are shown in Figure 28 (a). The effective index values of these two Bloch modes at λ=1550nm are about 2.3 and 1.6, respectively. The approximate spatial parities (Figure 28 (b)) of these two Bloch modes have been verified separately using a directional coupler. A fundamental TE mode in a 450nm-wide side waveguide was used to excite merely the 0th Bloch mode while a fundamental TM mode in 500nm-wide side waveguide served to excite merely the 1st one. This property enables an efficient projection of the two TE_0 and TE_1 waveguide modes on the base on the two Bloch modes basis in an ultra-short distance (<1 µm). After being excited in a controllable balance through the convertor, the two excited TE Bloch modes can excite back the TE_0 and TE_1 modes in the output strip waveguide, the overall process being responsible for the desired mode mixing (i.e. TE_0 and TE_1 mode excitations at the output are each made of TE_0 and TE_1 mode mixing from the input channel).
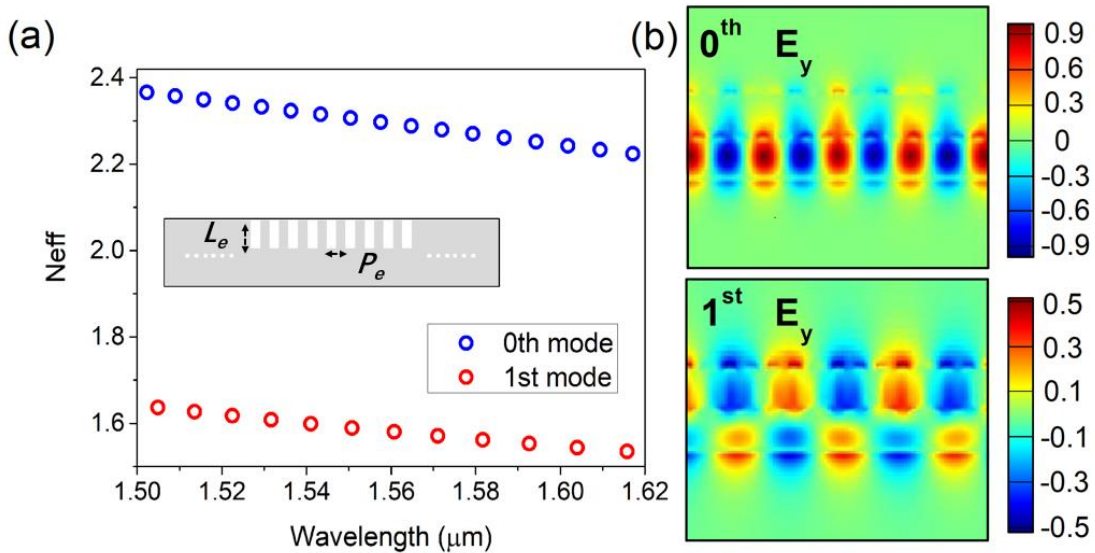
Figure 28. (a) Dispersion of the first two order Bloch modes in a waveguide with an infinite periodic subwavelength etch-hole array. (b) The spatial parities of 0th and 1st Bloch modes.

To find a proper mixer length with desirable mode mapping for efficient Fano generation, mixers of different numbers of etched holes (3, 5, 10 ,15) are shown Figure 29. The efficiencies of TE_0-TE_1 modes inter-mode mixing (C_{01} and C_{10}) and forward transmission factors (C_{00} and C_{11}) for each case are shown on the bottom Figures, while the energy distributions with TE_1/TE_2 mode injections are provided on top left/right Figures. The 3N, 5N and 15N cases give better inter-mode mixing efficiencies than the 10N case. In terms of mixing efficiency/conversion to the TE_0 mode (C_{00} and C_{01}), the 5N case shows better performances (C_{00} and C_{01} are balanced and both close to 0.4) than the 15N and 3N ones. However, compared to the 3N case, the TE_1 forward transmission C_{11} of the 5N case is much worse than for the 3N case one. Therefore, the 3N configuration was chosen as the best.
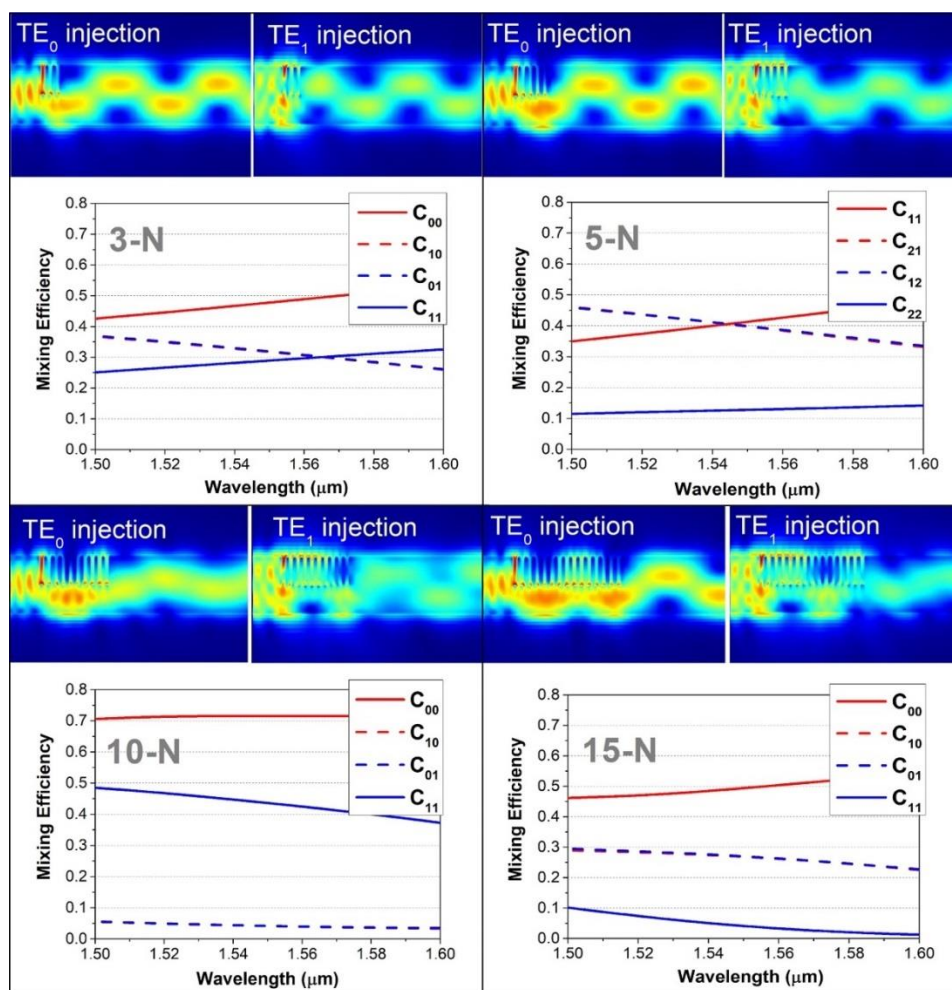
Figure 29. Mixing efficiencies and energy distributions of subwavelength mixers with different numbers of etched holes. The mixing efficiencies of TE_0 mode to TE_0 mode, TE_{10} mode to TE_1 mode, TE_1 mode to TE_0 mode and TE_1 mode to TE_1 mode, are labeled by red solid, red dashed, blue dashed and blue solid lines, respectively.

Now with all these elements, we can evaluate the spectrum based on equation (2.11). We accordingly adjust the energy ratio of the TE_0/TE_1 propagating modes and

the mixing efficiencies to search the optimization operation point. The related details are shown in Figure 30. Clear Fano curves presenting sharp spectral transitions and high extinction ratio are demonstrated from $\eta_1 = 0.1$ and $\eta_1 = 0.9$. In this study, mode interference was fixed at $C_{11} = 0.45$, $C_{12} = 0.35$, which comes directly from the 3N case in Figure 29. The best configuration for Fano behavior, indicated by $q \approx 1$ (the largest asymmetry), is generally linked to the most rapid change (maximum slope) of the structure spectral transmission. This condition is satisfied here when $\eta_1 = 0.55$, as shown in Figure 30 (a). Especially, the comparison between the $\eta_1 = 0.9$ and $\eta_1 = 0.999$ cases shows that values of η_1 close to 1 are necessary to recover a Lorentzian shape cavity spectral lineshape.

We also investigated the effect of the mixer with different coupling efficiencies (C_{00} and C_{01}) on the Fano spectra, as shown in Figure 30 (b). The selection on C_{xx} are based on the results on Figure 29, while in this study, mode excitation was fixed at $\eta_1 = 0.55$ and $\eta_2 = 0.45$, which directly came from the 400nm case in Figure 27. The q parameter variation is much more limited than in the previous case and the spectra keep a fairly marked Fano shape even in the severe C_{11}; C_{12} =70%;5% condition, which indicates the robustness of the proposed Fano cavity scheme against variations of the mixer geometry. Overall, the main trends reported in Figure 30 (a) and (b) provide a design strategy to target a trade-off between correct Fano lineshapes and large extinction ratio values.
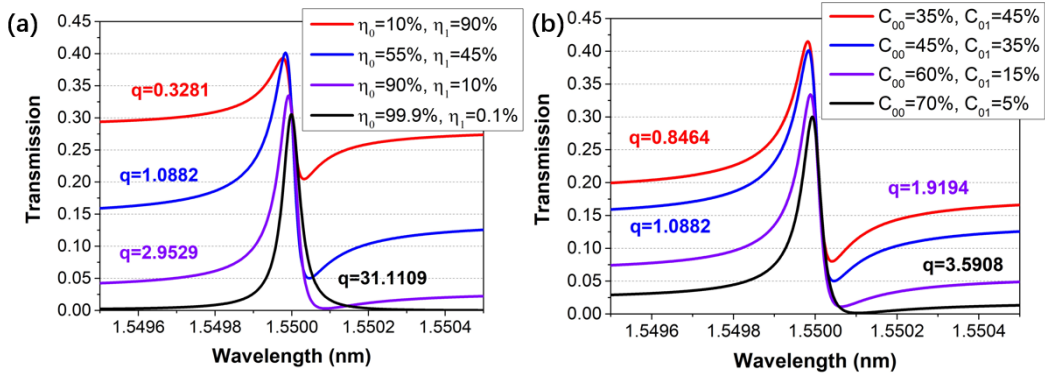
Figure 30. (a), (b) The transmission of the TE_1 mode versus the varying excitation efficiencies η_1, η_2 and mixing efficiencies C_{11}, C_{12}. The exchange efficiencies in (a) are fixed as: $C_{11} = 0.45$, $C_{12} = 0.35$, while the excitation efficiencies in (b) are: $\eta_1 = 0.55$ and $\eta_2 = 0.45$, respectively. Both (b) and

(c) share the following parameters: $\omega_1 = 2\pi * 193.414 THz$, T_2= 90%, $Q_1 = \frac{\omega_1}{2\gamma_1} = 7 \times 10^4$, $Q_v =$

$\frac{\omega_1}{2\gamma_v} = 1.6 \times 10^5$ and $Q = \frac{\omega_1}{2\gamma_t} \approx 30000$.

With these analytical evaluations, a full Fano nanobeam cavity is proposed as shown Figure 31 (a), which produces two Fano resonances, i.e. for each of the TE modes. Five planes marked by black dash lines (1,2, 3, 4, and 5) at different positions in Figure 31 (a) are used to illustrate the structure principle of operation: plane 1 at the input waveguide, plane 2 before the cavity, plane 3 before the mode mixer, plane 4

after the mode mixer, and plane 5 at the bifurcation of the TE mode. The period, filling factor, and length of the mixer region hole are as mentioned above: P_e=200 nm, ff=0.5 and L_e=400nm, respectively. This is for the purpose of a TE_1-TE_1 and the TE_1-TE_0 mixing efficiency of ~45% and ~35% from a 3-N subwavelength mixer. The simulated propagating distribution corresponding to a TE_0 light injection is shown in the left inset in Figure 31 (a). The transmission levels of the TE propagating modes through the complete device (inset in Figure 31 (b), i.e. from plane 1 to plane 4) including the input waveguide width w_i=400nm (which provides excitation efficiencies of 55% and 40%, for TE_0 and TE_1 mode, respectively) are also shown.

Unambiguous Fano line spectra for the TE_0/ TE_1 propagating mode (blue/red curve in Figure 31 (b)) are observed, which confirms the adequate interference of the resonant and the flat spectra. Interestingly and as it could be anticipated, the TE_1 mode also exhibits a Fano spectrum lineshape, since part of the TE_0 and TE_1 modes are indeed coupled back to the TE_1 mode as well after the subwavelength mixer. An additional narrow side waveguide forms a directional coupler to convert the TE_1 propagating mode to the TE_0 mode of the side waveguide (see the right inset of Figure 30 (1)). Uncomplete destructive interferences marked by the appreciable but not complete Fano dips (transmission does not drop to 0) result from the unbalanced TE_0/TE_1 energy levels. Each of both Fano resonance behaviors can be separately optimized by adjusting either the TE_0-TE_0, TE_1-TE_0 mixing efficiencies or the TE_1-TE_1, TE_0-TE_1 ones. **Overall our cavity effectively compresses the physical dimensions of a Fano cavity and gives great convenience to the design of modulator as easily as in a single wire waveguide.**
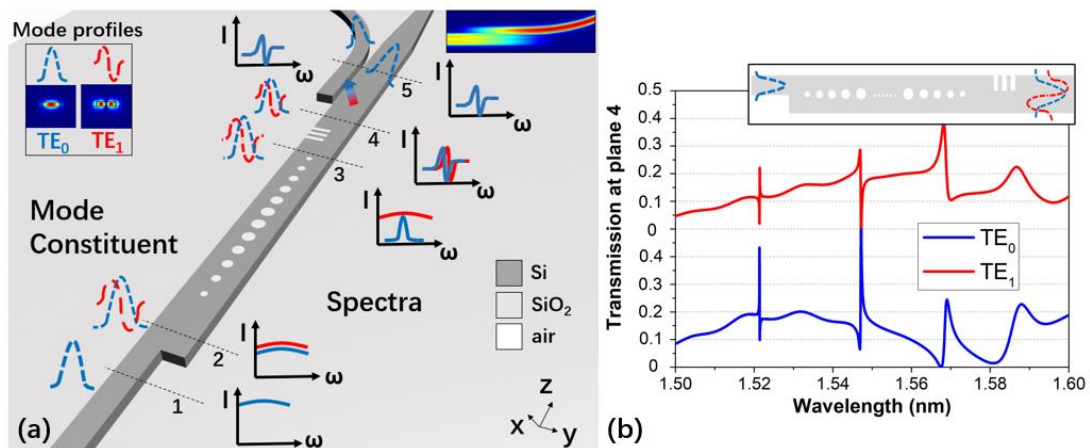
Figure 31. (a) Schematic of the proposed standalone Fano cavity, consisting of a MMI-like input structure, a nanobeam cavity, a subwavelength mixer and a directional coupler. The blue and red dashed curves represent the spatial mode profiles (bottom right inset) of the TE_0 and TE_1 propagating modes, respectively. The blue and red solid curves represent the spectral lineshapes of the TE_0 and TE_1 propagating modes, respectively. Top right inset: the propagating distribution of the TE_1 propagating mode coupled with and converted into the TE_0 mode of the side waveguide. (b) Transmission spectra of the TE_0 and TE_1 propagating modes through the proposed Fano cavity with a 400nm-wide input waveguide. The period, filling factor and length of the subwavelength holes array are P_e=200 nm,

ff=0.5 and L_e=400nm, respectively. Other parameters are identical to that reported previously. In each Figure, the TE_1 and TE_2 propagating modes are depicted by blue and red curves solid lines or circles, respectively.

2.1.3   Fabrication and characterization of Fano nanobeam cavities

Based on the parameters developed in section 2.1.2, we performed the device fabrication with mask generated using python package. The fabrication process introduced in this part is used throughout the manuscript which is shown Figure 32. The fabrication of SOI chip can be separated in several steps in which most of these fabrication steps have been carried out by Mr. Xavier Le Roux from the C2N laboratory.

Cleaning; The silicon on insulator (SOI) wafer can be first cleaned using NH4F solution for removing the surface oxide created in the growing process. This step can provide a good adhesion with the silicon and the photo resist. Following this, acetone, isopropanol is then used step-by-step, with the ultra-sonic machine to clean the surface of silicon. Sometimes there's some carbon contaminant stuck on the silicon surface which cannot be removed by an organic solution. In these cases, a combined solution of concentrated sulfuric acid and hydrogen peroxide can be considered.

Spin coating; after drying the wafer from step one (a) with a hot plate with temperature up to 120 Celsius degrees, the sample can be transferred to the spin coater for covering it with photo-resist. For different purposes and design, two kinds of photoresist can be used, i.e. a positive resist or a negative resist. A positive resist (e.g. ZEP series, PMMA) is exposed to dedicated light source and removed in a later developing process, while the exposed parts of negative resist (e.g. Ma-N 24xx series, HSQ) are the remaining areas after the developing process. After the spin coating, the sample with hundreds of nm of photoresist (the thickness of the photoresist can be easily controlled by the rotation rate of the spin coater) on top of the surface is put on the hot plate for pre-baking. In this step, the photo resist is dried out and strengthened.

Electron-beam Lithography; taking the sample from spin coating, an electronic lithography machine is used to transfer the pattern that were generated from Python GDS tool, as shown in Figure 32 (c) and (d).

Developing; the sample from exposure is soaked into the developing solution for the pattern recover (e). The solution used is chosen according to the polarity of the photoresist. Following this, the sample is again put on the hot plate for drying out.

Etching; sample is transferred to the chamber of Induced Couple Plasmas (ICP) etching machine for pattern transfer (f). In this process, a dry run with pure oxygen is preferred before etching the sample, which can clean the chamber and stabilize the etching rate. With conductive silicone grease, sample is stuck on the spacer for thermal dissipation. The gas used for silicon etching is C_4F_8 and SF_6 while the recipe for silica and silicon nitride CF_4 and CH_3.

Postprocess; after etching, the sample is rinsed in acetone with the assistance of shaking table for roughly removing the photoresist. Then, it is followed by the fine cleaning of combined solution of concentrated sulfuric acid and hydrogen peroxide

(g). Once cleaning is finished, sample can be put on the hot plate again for dehydration.

Surface polishing; waveguide roughness can be created during all these processes above, including patterning roughness, transfer roughness or etching roughness. To polish the surface of structures, samples are put into the high-temperature oven to generate sacrificed oxide which can be removed by rinsing fabricated samples in diluted hydrofluoric acid.

Overlay; In cases that multi-step patterning is needed. The pattern can be again transferred to the sample by performing alignment to the labeled structures which are formerly generated during the first etching step. Then, spin coating, exposure and etching can be repeated as described above.

Deposition; In cases that external materials are expected (e.g. top silica cladding), we can use a plasma enhanced chemical vapor deposition (PECVD) machine for depositing amorphous material. In terms of metal (e.g. for electrode purpose), magneto sputtering and evaporation deposition technologies can be used, followed by the lift-off method.
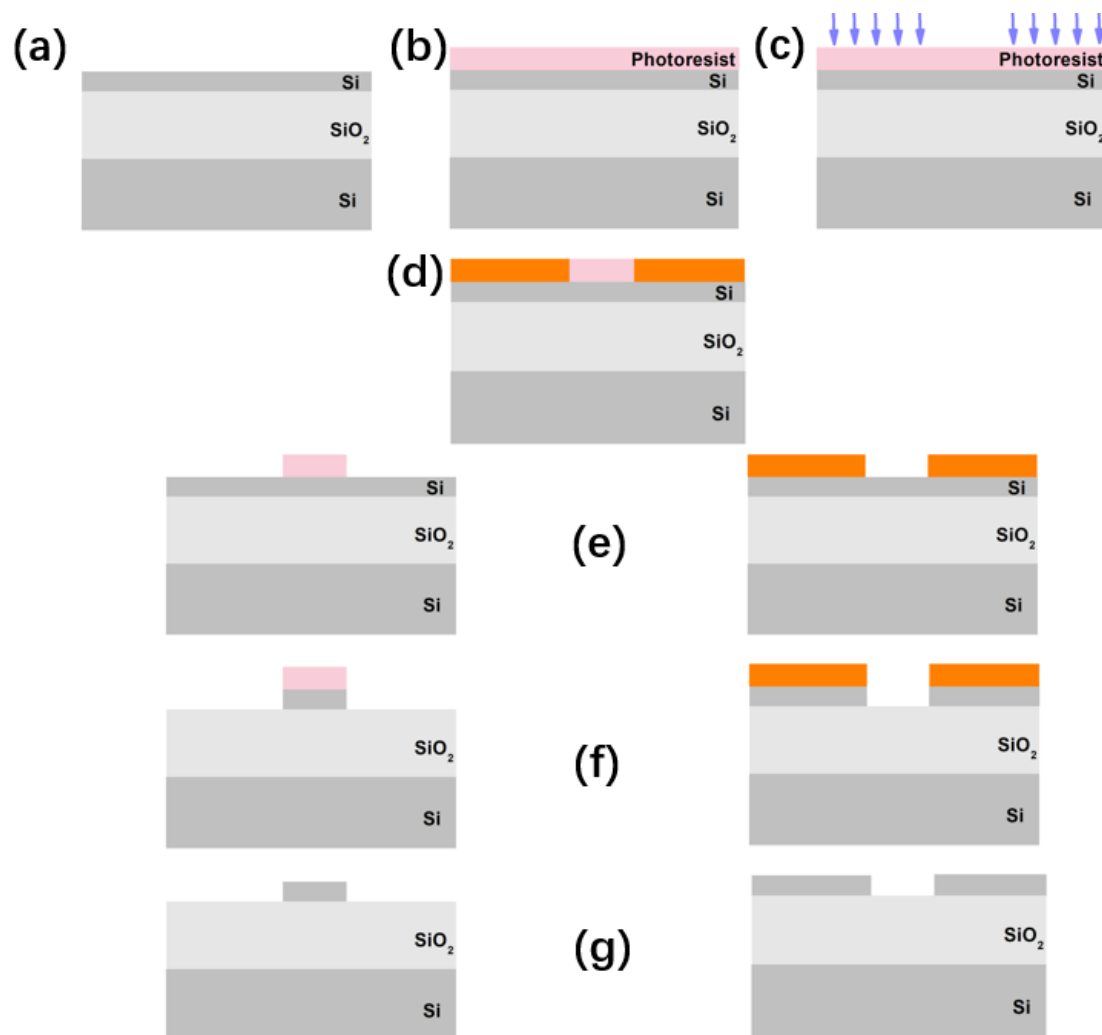
Figure 32. Schematic of our silicon fabrication process flow. (a) Cleaning. (b) Spin coating. (c) Lithography. (d) Post-baking. (e) Developing. (f) Etching. (g) Post-cleaning.

A silicon-on-insulator (SOI) wafer with 220nm silicon thickness was used for fabrication. Since photonic waveguides have a high index contrast with the surroundings, the most convenient method to interface the input fiber connected with light source and the fabricated sample appeared to be the use of grating couplers, taking advantages of the efficient radiation [151, 152] A scanning electron microscope (SEM) of our fabricated grating coupler is presented in Figure 32. Since the cross-section of a single-mode on-chip silicon photonic waveguide width is usually less than 200 or 300 nm, optical waveguides are needed first to be tapered from their narrow cross-section to the larger grating one in order to interact with the grating corrugation. A simpler design to shorten the taper length is to directly combine the taper and the grating as shown in Figure 33, which is widely stated the "focusing grating coupler".
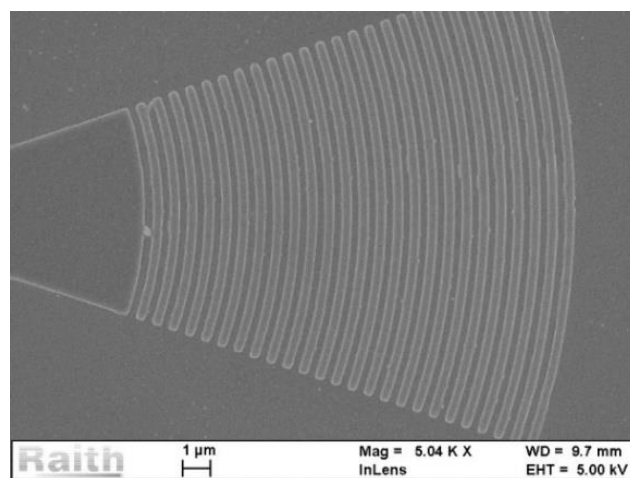
Figure 33. Scanning electron microscopic image of one of our fabricated focusing grating coupler using our design and fabrication process.

With such a focusing coupler, the sample can be further considered for optical characterizations. Typical experimental conditions and optical benches are shown in Figures 34, 35, and 36. In Figure 34, a tunable/broadband coherent light source (Yenista TUNICS, operating in the 1260-1640nm wavelength range), a polarization controller, a spectrometer (Yokogawa, AQ 637x series), a power detector (Yenista CT400), and a source meter (Keithley 24xx series) are used to characterize the sample transmission. One practical picture of handling the fiber is shown in Figure 35. In the zoom-in picture of Figure 35 (b), the fiber is almost vertically placed (10-30 degrees, according to the design of the grating coupler) and placed to inject/extract the light to/from the grating coupler. Such a slight tilted angle is normally requested since a perfect vertical coupling configuration can lead to the sacrifice of half on the input energy to the backward waveguide propagation direction. With this method, coupling efficiency can be achieved experimentally up to nearly 50%), which is definitely enough for the proper characterization of the structures.

In some cases, grating couplers are unsuitable for the fiber/photonic circuit interfacing. For example, high-power lasers delivering spatial output preferably request alignment using lenses as high power can be responsible for fiber mechanical instabilities. Broadband light sources and low index-contrast design also go beyond the grating coupler since grating coupler have limited coupling bandwidths and efficiencies strongly dependent on the waveguide index-contrast. In these cases, butt coupling (or edge coupling), as shown in Figure 36, can be used. Lensed single-mode fibers fiber are usually adopted by approaching it to the facet of the sample.
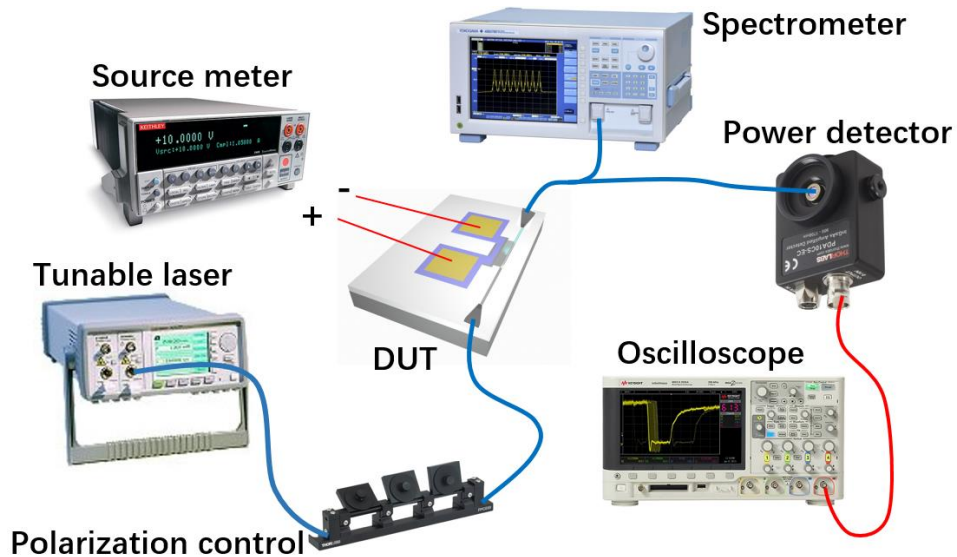
Figure 34. Schematic of an experimental bench for characterizing passive opto-electronic devices. DUT: devices under test. Optical and electrical path are represented by blue and red curves, respectively.
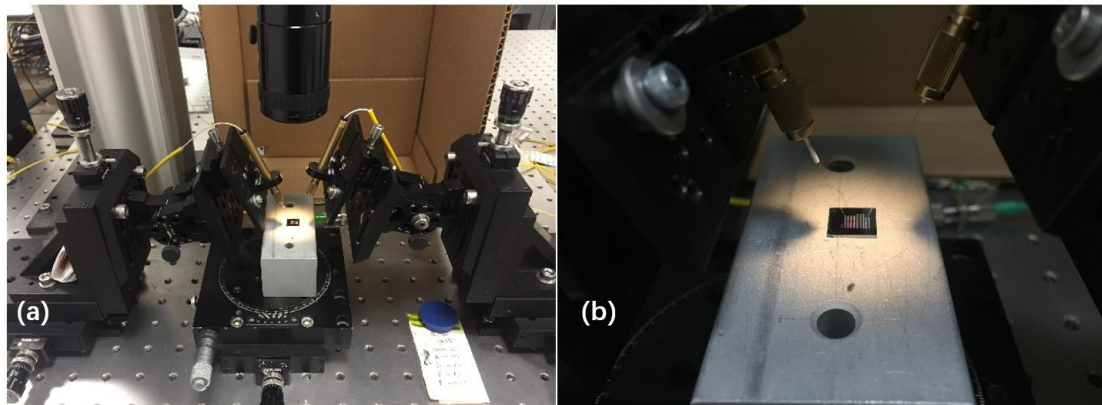
Figure 35. Zoom-out (a) and zoom-in (b) image of our grating coupler bench.
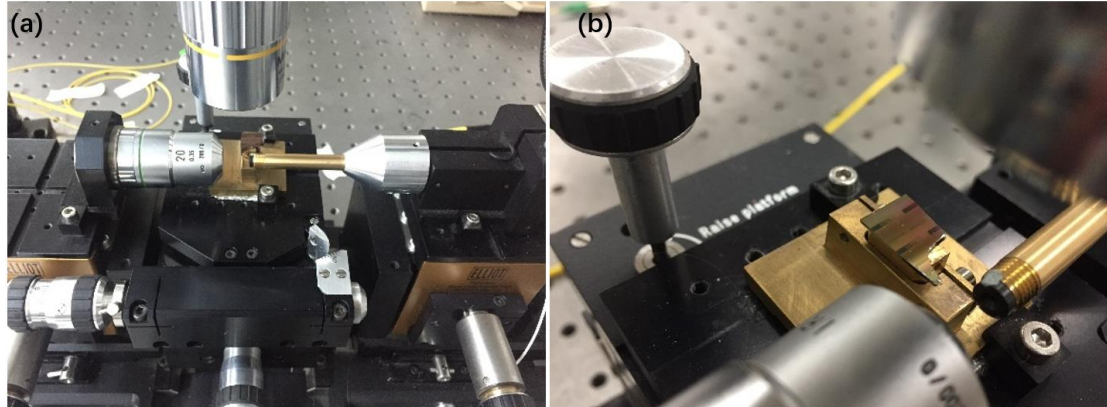
Figure 36. Zoom-out (a) and zoom-in (b) image of our butt coupler bench.

The scanning electron microscopy (SEM) picture of a typical fabricated device is shown in Figure 37. The gap between the nanobeam waveguide and the side waveguide (w_s=400nm) is here of 150nm. A straight coupling length of 16 µm was chosen to completely couple the TE_1 propagating mode in the nanobeam waveguide to the TE_0 mode in the side waveguide. Then the side waveguide was turned into a bend waveguide with a radius of 40 µm for an ultra-low loss separation of both modes. The performances of this directional coupler were confirmed by 3D-FDTD simulations and from fabricated devices characterizations. The width of the input waveguide was chosen as 500nm since the experimental transmission of resonant mode was usually lower than the theoretical one. Other parameters about the nanobeam cavity were directly inherited from the design stages. i.e. a nanobeam waveguide width w_n=800nm, 50 holes, and a hole radius profile quadratically tapered from 100nm in the center to 70nm at the edges.
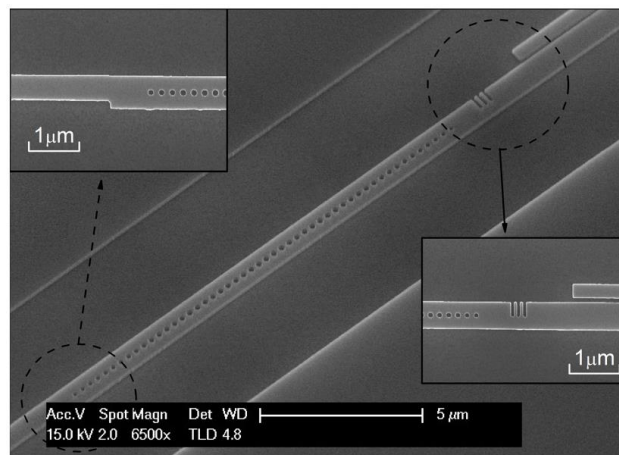
Figure 37. SEM views of fabricated devices. The MMI-like structure and subwavelength mixer are shown in the top-left and bottom-right insets, respectively.

The experimental transmission curves of the full structure are shown in Figure 38 (a). All the transmission curves were normalized to straight waveguides with identical

grating couplers. Clear Fano lineshapes for the 1st and 2nd order cavity modes are observed, with resonance wavelengths located at around 1515 nm and 1531 nm, respectively, which are close to the values (1510nm and 1533nm) obtained from 3D-FDTD simulation in Figure 31 (b). Simulated distributions for these two modes are presented in the insets of Figure 38 (a). Simultaneous Fano lineshapes of the 2nd cavity mode in the nanobeam and side waveguides are also shown in Figure 38 (b), as the blue and orange curves, respectively. Zoomed-in views of the transmission curves of the around the two spectral resonances are shown in Figure 38 (c) and (d), respectively. The blue circles and the orange solid curves are experimental results and fitting curves from equation (2.11), respectively.

In Figure 38 (c), we see that **in a wavelength detuning of 56pm, the cavity optical transmission experiences a transition drop of about 17 dB**. To experimentally obtain the quality factor, another device with same parameters but an input width of 700nm was further analyzed. This wide-input device can be considered as a classical nanobeam cavity without any TE_1 propagating-mode excitation (Figure 24 (a)).
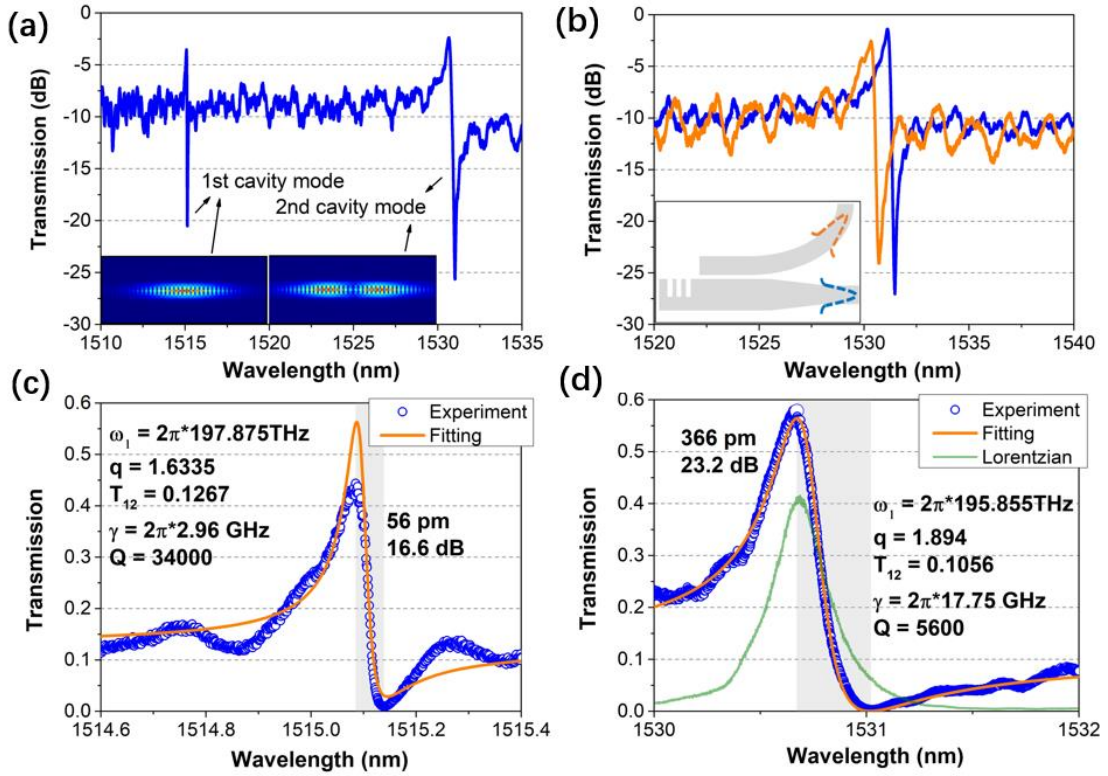
Figure 38. (a) Experimental transmission of the nanobeam waveguide. (b) Experimental transmission around 2nd cavity mode detected in nanobeam and side waveguides, depicted by blue and orange curves, respectively. (c) Experimental transmission and fitting curve of 1st cavity mode of nanobeam waveguide, depicted by blue circles and orange curve, respectively. (d) Experimental transmission and fitting curve of 2nd cavity mode of nanobeam waveguide, depicted by blue circles and orange curves, respectively. Lorentzian curve is labeled by a green curve while transition between maximum and

minimum are depicted by grey regions.

According to our previous analysis, the transmission spectrum is then pretty close to a Lorentzian resonance. Using $Q=\Delta\omega/\omega_0$, a Q factor of ~32000 was obtained (the transmission of this Lorentzian spectrum is low and not shown in Figure 38 (c)). The Q factor value was also extracted from equation (2.11), by fitting the experimental Fano spectrum. The asymmetric total decay rate γ_t was $2\pi * 2.96$GHz, which indicated a Q factor of 34000, well coincident with that given by the Lorentzian-kind device. The **asymmetric parameter q was estimated as $q=1.6335$**, i.e. close to the perfect Fano condition (i.e. $|q|\approx 1$) proving the consistency of the carried-out optimization. In addition, the total measured energy transmission from the TE$_1$ propagating mode to the TE$_0$ one ($T_{01} = \eta_1 T_1 c_{01}$) was found around 0.1267. Considering the excitation ratio of TE$_1$ mode (η_1) for a 500nm width input waveguide of about 0.3 and the nanobeam transmission (T_1) of 0.9 and a mixing efficiency (c_{01}) of 0.35, this value of T_{01} (0.1267) is thus in good agreement with analytical prediction (0.0945).

Similar analysis **for the 2nd cavity mode was performed as well from which a more than 23.2 dB extinction ratio was obtained for a wavelength detuning of 366pm**, as shown in Figure 38 (d). The calculated asymmetric parameter q, the Q factor and the total transmission T_{12} were 1.894, 5600 and 0.1056, respectively (the phase variables C_p for both cases were calculated to be close to zero and are not shown). Using a device made of an identical nanobeam cavity but with a 700nm-width input waveguide, an overall transmission T=0.88 was experimentally monitored. According to the estimation[31] $T = \left(\frac{Q_{total}}{Q_{wg}}\right)^2$ and the classical relationship $\frac{1}{Q_{total}} = \frac{1}{Q_{wg}} + \frac{1}{Q_{i+v}}$, quality factors Q_{wg} and Q_{i+V}, both accounting for waveguide coupling and intrinsic absorption and vertical losses were estimated as Q_{wg}=5930 and Q_{i+V}=100000, respectively. This estimate thus demonstrated the **negligible nature of optical losses by absorption and out of plane scattering**. An experimental Lorentzian spectrum with nearly the same Q-factor of 5600 is reported as well (green curve) in Figure 38 (d) for comparison, which is clearly less efficient. For a lossless Lorentzian resonance $\frac{\gamma_t^2}{(\omega_0-\omega)^2+\gamma_t^2}$ with the same Q factor of 5600 (γ_t=$2\pi * 17.75$GHz), the Extinction Ratio (*ER*) for a wavelength detuning of 366pm ($\Delta\omega \approx 2\pi * 46.83$GHz) is $-10\log(\frac{\gamma_t^2}{(\Delta\omega)^2+\gamma_t^2})$=9dB. This value is 14dB smaller than that of the experimentally reported Fano resonance (~23dB). From another perspective, with the same Q factor (5600) and *ER* (23 dB), the wavelength detuning required in a Lorentzian case is 1.96nm ($\Delta\omega \approx 2\pi * 251$GHz), which would lead to a much higher driven power.

In order to have a clear observation on how Fano resonance is influenced by the balance between modes, a series of configurations with different TE_0/TE_1 excitation ratios was performed by **making the input waveguide width w_i vary**. The related evolution of an array of fabricated Fano cavities with different w_i ranging from 300 nm to 700 nm is reported in Figure 39 (a)-(h). The different lineshapes first behave as all-pass filters and become asymmetric with increasing the input waveguide width, achieving almost a maximum asymmetry within the range of 500-600 nm of input waveguide width, then coming back to an add-drop-type Lorentzian shape resonator at $w_i \approx 700$ nm. Clear Fano lineshapes are widely observed from w_i=450nm to 650 nm. This easiness highlights the **robustness of our design even in the case of possible tens of nanometers of fabrication errors**.
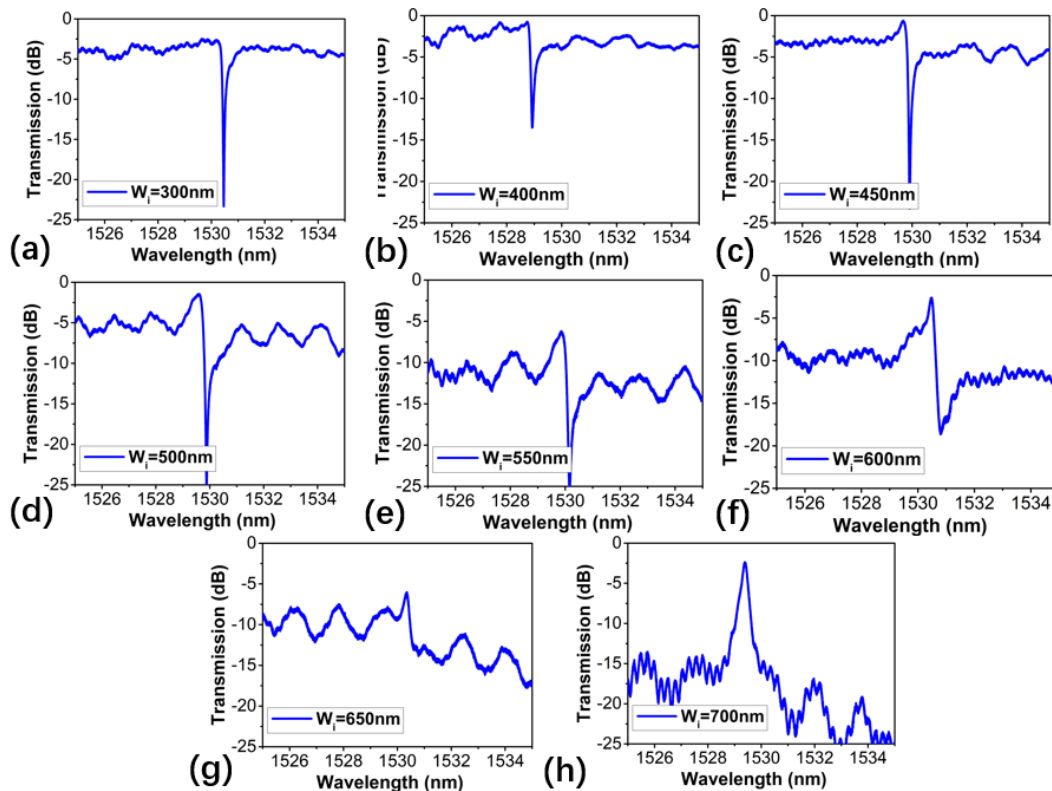
Figure 39. (a)-(h) Evolution of the Fano spectra by considering the variation of the overall nanobeam Fano cavity input waveguide width w_i from 300nm to 700nm.

Since the mode mixing efficiencies of the proposed subwavelength structure are important parameters driving the obtained Fano spectra, different practical parameters (different filling factors, i.e. the width of the etched rectangle normalized to the period, and etch lengths L_e) were chosen to check the Fano performances in a broad set of situations.
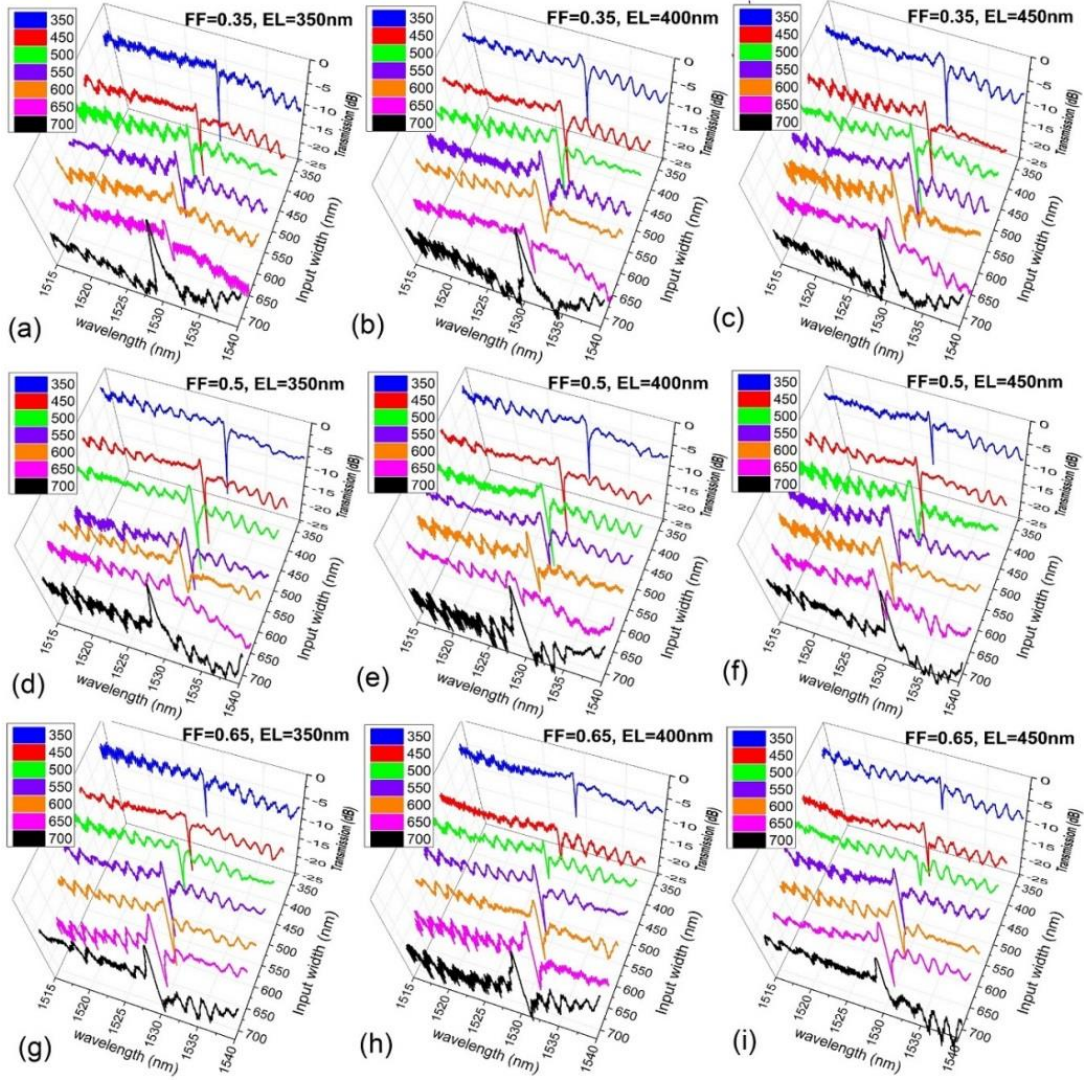
Figure 40. (a) – (i) Evolution of Fano cavities with different mixer parameters, i.e. varying and the length of rectangle etch hole L_e (350nm, 400nm and 450nm) in each row. The filling factor varies from *FF*=0.35 to *FF*=0.65, from first top row to bottom row.

Filling factor (*ff*, the size of etched hole compared to the silicon) was arranged from 0.35 to 0.65, while L_e was varied from 350 nm to 450nm. The related collected spectra are shown in Figure 40. Fano signatures are observed from all configurations. We note that small variations of L_e tend to lead to only minor spectral changes, even difficult to perceive. However, increasing *ff* allows increasing the energy exchange efficiencies C_{10} and C_{01}. The best configurations (q being close to 1) are driven to the cases with higher input waveguide widths (e.g. w_i =500nm for *ff*=0.35, w_i=600nm for *ff*=0.65). Fano resonance can even be seen with a 700nm input waveguide with *ff*=0.65 (bottom row of Figure 40). These results bring here a new confirmation of the robustness of the proposed mixer.

So far, a method for generating Fano resonances in a standalone silicon nanobeam cavity has been reported and investigated both analytically and experimentally. We now consider it for the realization of plasma-dispersion based electro-optical modulators.
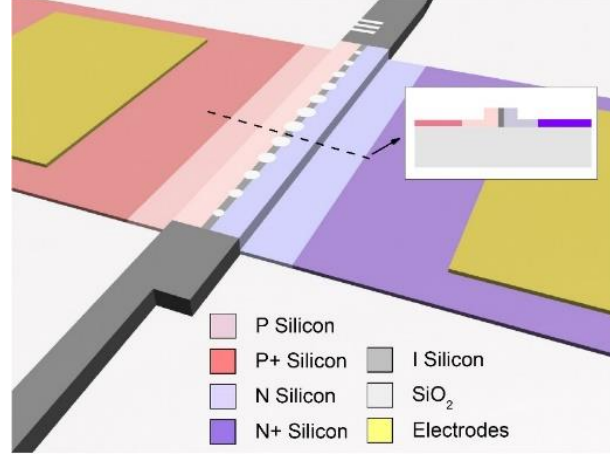
Figure 41. Proposed Fano modulator based on a rib silicon P-N depletion active structure. Inset is the cross-section of the rib structure at the position labeled by dot line.

The proposed P-N Fano modulator is shown in Figure 41 and the analysis is performed on the 220nm SOI platform with 170 rib thickness and 50 nm slab thickness. The Fano cavity is slightly doped in both side and a depletion region formed in the center. Meanwhile, the free carriers induced index change in silicon can be described at 1.55μm wavelength by [153]:

$$\Delta n = \Delta n_e + \Delta n_h = -[8.8 \times 10^{-22} \times \Delta N_e + 8.5 \times 10^{-18} \times (\Delta N_h)^{0.8}$$

$\Delta n_e, \Delta n_h$, ΔN_e and ΔN_h are here the electron induced index change, hole induced index change, the density changes of electrons, and density change of holes. For a common doping change level of $\Delta N_e = \Delta N_h = 5 \times 10^{17}$, the index change is $\Delta n = -1.7 \times 10^{-3}$. We consider a nanobeam cavity with symmetric P-N junctions, i. e. with identical widths for the P-type and N-type regions. The optical index in the P doped/depletion regions can be considered as 3.4783 and ~3.48, respectively. Since the depletion width of the P-N junction can be described as [154]:

$$W_d = \left[\frac{2\varepsilon_0 \varepsilon_r (N_D + N_A)}{q(N_D \cdot N_A)} \left(V_P + V_{ext} - \frac{2k_B T}{q} \right) \right]^{1/2} \tag{2.12}$$

$\varepsilon_0 = 8.8542 \times 10^{-12} F/m$ and $\varepsilon_r = 12$, V_P, V_{ext} and q are the vacuum silicon dielectric constant, the silicon dielectric constant, the build-in potential, external applied voltage and the unit charge. k_B is the Boltzmann constant and T is the temperature fixed at 300K.

For a 0.35nm shift of the Fano resonance (consistent with the 2nd cavity mode discussed above, with Q~5600 and an extinction ratio larger than 20dB), the required width change of the depletion region (ΔW_d) calculated by using 3D-FDTD simulation was estimated to about $15nm$. The peak-peak voltage for such a width change at a bias of $V_B \approx -0.5V$ is $\Delta V_{ext} \approx 0.5V$ (i. e. V_{ext} is within the range of $V_B - \Delta V_{ext}/2$ to to $V_B + \Delta V_{ext}/2$). Considering an average depletion width of 100nm and a cavity length L=$15\mu m$, the capacitance of the P-N junction is [154]:

$$C_d = \varepsilon_0 \varepsilon_r \frac{H_{rib}(\sim 220nm)}{W_d} L \approx 4\text{fF} \tag{2.13}$$

Therefore, the energy consumption per bit can be estimated to [66]:

$$E = \frac{C \cdot V_{pp}^2}{4} = \frac{C_d \cdot \Delta V^2}{4} \approx 0.25 fJ/bit \tag{2.14}$$

Even considering a practical capacitance (i.e. an experimental capacitance taking other capacitance and fabrication imperfection into account besides the depletion capacitance) of C=50fF like for earlier reported ring resonators [66], the energy consumption per bit is still as low as $3.125 fJ/bit$. Such a low energy consumption per bit, which is supported by the small wavelength detuning of 366pm required to obtain an ER of 23dB in the proposed Fano cavity with a low Q factor of 5600 is not possible to be achieved in Lorentzian-lineshape resonant modulators. For the 1st cavity mode of Q~34000, (0.056nm shift for ER>15dB), the energy consumption per bit is reduced down to $E \approx 0.5 fJ/bit$. Besides, asymmetric doping profiles could be further considered to optimize the active structure performances [155]. The absorption resulting from the free carriers we obtained for this structure is $\Delta\alpha = 7.25\text{cm}^{-1}$, from which we derived an imaginary part ($n = n + ik$, at 1550nm wavelength) of refractive index of $\Delta k = 0.89 \times 10^{-4}$. Taking this value into account, we recalculated the quality factor of the nanobeam cavity with and without free carriers. The quality factor for the 2nd cavity mode in the passive case being 1.89×10^4, while it was estimated to 1.29×10^4 when free carriers were accounted for, indicating an additional decay rate of only $\Delta\gamma_i$=$2\pi * 2.38\text{GHz}$. Comparing this value to the experimental total decay rate of the 2nd mode (γ_t=$2\pi * 17.75\text{GHz}$), we observe that the **impact of free-carrier absorption on the Fano resonance decay is small**. This result brings a confirmation that the cavity **quality factor is dominated by the strong coupling between the propagating mode in the feeding waveguide and the cavity mode**, rather than by free-carrier absorption losses (i.e., with the notations of the paper, the resonance is mainly governed by γ_1, γ_2, γ_v, rather than γ_i), let alone the further lossy contribution from fabrication. Thanks to this small additional decay rate, **q is only weakly influenced by free carriers so that the asymmetric spectral lineshape of the cavity is preserved in the active modulation configuration**.

2.1.4 Exploring the strained silicon Fano modulator

Plasma dispersion effect modulation based on such a Fano single waveguide cavity brings very nice performance, however, in terms of the emergency, it would be much more interesting to explore the strained silicon modulator since the Pockels effect in strained silicon is way much weaker than the plasma dispersion effect in doped silicon. While in strained silicon, extremely huge driven voltage is requested to run an eye diagram, as we introduced in chapter 1. Therefore, taking into account the feasibility of strained silicon fabrication and the interests of improving strained silicon modulator, we try here to explore the possibility of combining the Fano resonator and the strained silicon platform, as shown in Figure 42 (a). To strain the silicon waveguide, a layer of silicon nitride with thickness 700nm is deposited on top on the silicon. Details of the strain formation is reported in [63] and no longer repeated here. Above the silicon nitride, a layer of Au electrode with 500nm thickness is deposited. Due to the introduction of silicon nitride, longer mirrors are required to compensate the reduction of index perturbation in each cell, but a nanobeam of 60 holes is enough to reach Q factors of 70000 and 8000 for the 1st and 2nd cavity modes, respectively. Accordingly, the transmission spectra of the TE$_0$ and TE$_1$ are presented in Figure 42 (b). The distinct response is maintained well in this longer cavity. With an optimized 6-N subwavelength mixer, a clear Fano resonance can be observed in Figure 42 (d). In this Figure, the longer wavelength (thus the 2nd and 3rd cavity modes) was primarily optimized instead of the 1st cavity mode because the 2nd cavity mode presents a more appropriate Q factor for optical modulation.

As the Pockels effect is relatively weak, a travelling wave [156, 157] electrode is preferred to reduce the microwave reflection and losses. The equivalent electrical model of proposed strained silicon modulator is shown in Figure 43. A configuration of coplanar metallic type waveguide is used with electric field pointing at the vertical direction at the region of silicon core. The impedance of a two electrical probe is labeled as source impedance Z_S and the terminal impedance is called Z_T. The gap between electrodes, the width for S pad and the thickness of the gold electrode are chosen as $10\mu m$, $30\mu m$ and 500nm, respectively. This configuration gives us a characteristic impedance of $Z = 50\Omega$ at 30 GHz, i.e. matching the source impedance Z_S and terminal impedance Z_T. Based on this model, the effective average voltage drops on the device, including microwave losses and group velocity mismatch, can be considered as [158, 159]:
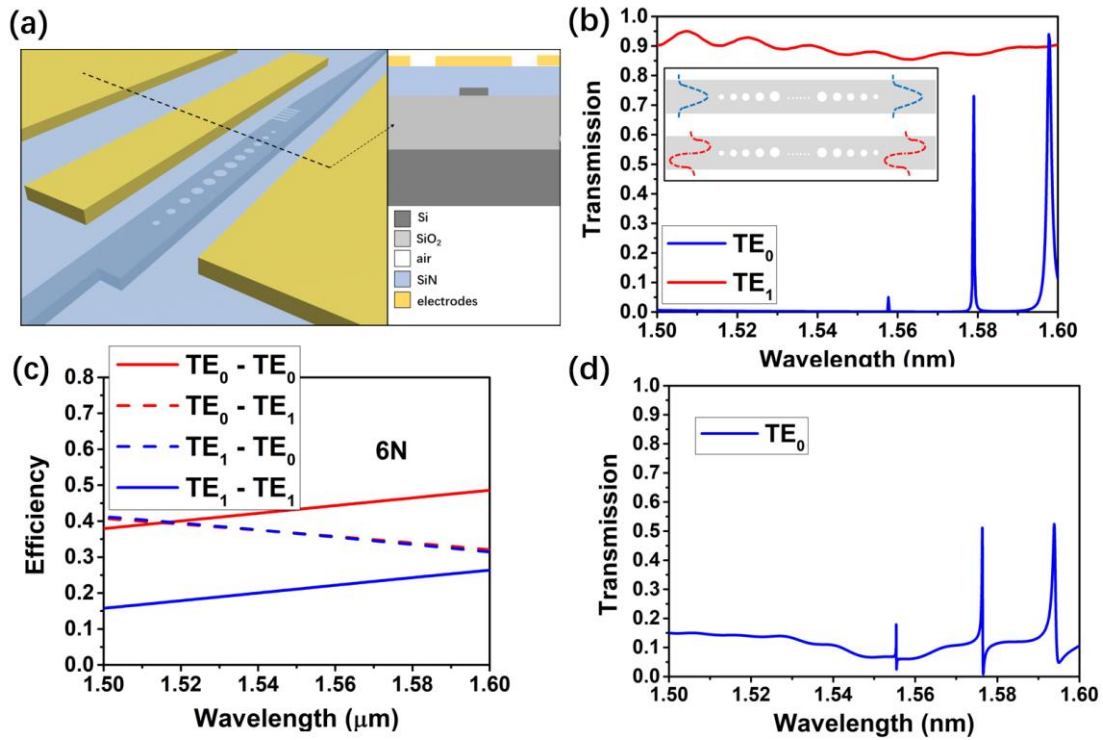
Figure 42. (a) Schematic of proposed Fano modulator based on strained silicon platform. (b) Transmission of the optical modes TE$_0$ and TE$_1$ in a silicon nanobeam cavity covered by silicon nitride. The total hole number is 60, with hole radius taper from 100nm at the center to 70 nm at the edge. (c) Performance of a 6-N silicon subwavelength mixer covered by silicon nitride. (d) Corresponding overall device performance with an input waveguide width of 500nm.
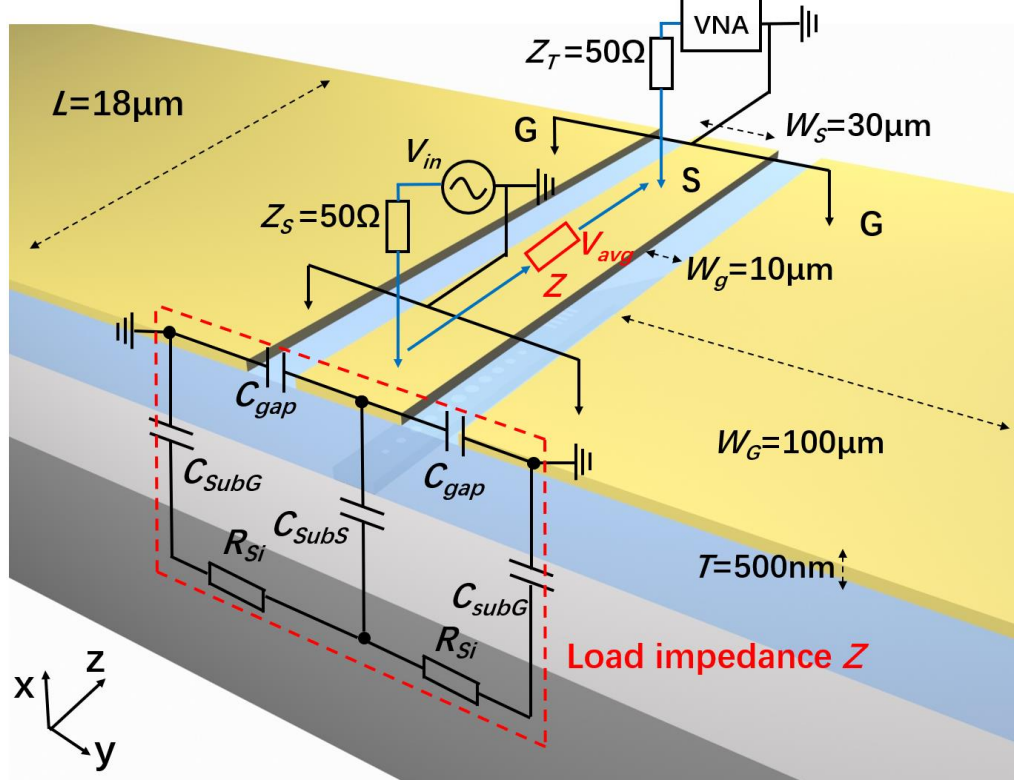
Figure 43. Schematic of equivalent electrical model of proposed strained silicon Fano modulator based

on a silicon-strained cladding structure. The loaded impedance that working with traveling-wave electrode is outlined by the red dot line. VNT: vector network analyzer.

$$V_{avg} = V_{in} \frac{2Z}{Z+Z_S} \frac{\exp(i\beta_o L)[V_+ + (\frac{Z_T-Z}{Z_T-Z})V_-]}{2[\exp(\gamma L)+(\frac{Z-Z_S}{Z+Z_S})(\frac{Z_T-Z}{Z_T-Z})\exp(-\gamma L)]} \tag{2.15}$$

Where the two voltage coefficients are represented by:

$$V_+ = \exp[+i\frac{(-i\gamma-\beta_o)L}{2}]\frac{\sin[(-i\gamma-\beta_o)L/2]}{[(-i\gamma-\beta_o)L/2]} \tag{2.16}$$

$$V_- = \exp[-i\frac{(-i\gamma+\beta_o)L}{2}]\frac{\sin[(-i\gamma+\beta_o)L/2]}{[(-i\gamma+\beta_o)L/2]} \tag{2.17}$$

where V_0 is amplitude of the driven signal, $Z = \sqrt{(R+i\omega L)\Big/(G+i\omega C)}$ and

$\gamma = \sqrt{(R+i\omega L)(G+i\omega C)} = \alpha + i\beta$ is the complex characteristic impedance and complex propagation constant of driven signal, respectively. It's considered by definition from shunt admittance $(G+i\omega C)$ and series impedance $(R+i\omega L)$. $\beta_o = \frac{\omega_m}{c}n_{go}$ is the microwave propagation constant (microwave frequency ω_m) and group velocity of the optical mode n_{go}. The frequency response can then be calculated as [158, 159]:

$$m(\omega_m) = |\frac{V_{avg}(\omega_m)}{V_{avg}(0)}| \tag{2.18}$$

Though the effective length of device is merely $18\mu m$, the length L of TWE is set at $50\mu m$ to ease the difficulty of probes contacting. With the electrode cross-sections mentioned above, the propagation losses α_{dB} ($\alpha_{dB} \approx 4.34\alpha$) and group index n_{gm} of the microwave driven signal are shown in Figures 44 (a) and (b).

Considering an optical group index of $n_{g0} \approx 4$, the S_{21} ($m(\omega_m)$) response is showed in Figure 45 (a). Due to the long-mismatched paths in 2mm and 4mm TWE, the 3dB bandwidth is limited at no more than 30GHz and 12GHz, respectively. Strong decay occurs even at low frequency, e.g. 1GHz. This strong voltage dissipation comes from the non-negligible microwave losses α and the considerable length of MZI.

This bandwidth limitation and voltage dissipation are well known for MZI modulators [54, 65], and especially critical in the design of a strained silicon modulator [160] in which high driven signal is in demand. In contrast, the 1dB bandwidth for our proposed Fano modulator can exceed more than 200GHz thanks to its ultra-short device length ($50\mu m$). Simultaneously, there is almost no voltage dissipation in the full frequency range. In this situation, we can almost consider an effective voltage of $V_{avg} \approx V_0$ applied all along the electrode of the designed Fano electro-optical modulator.
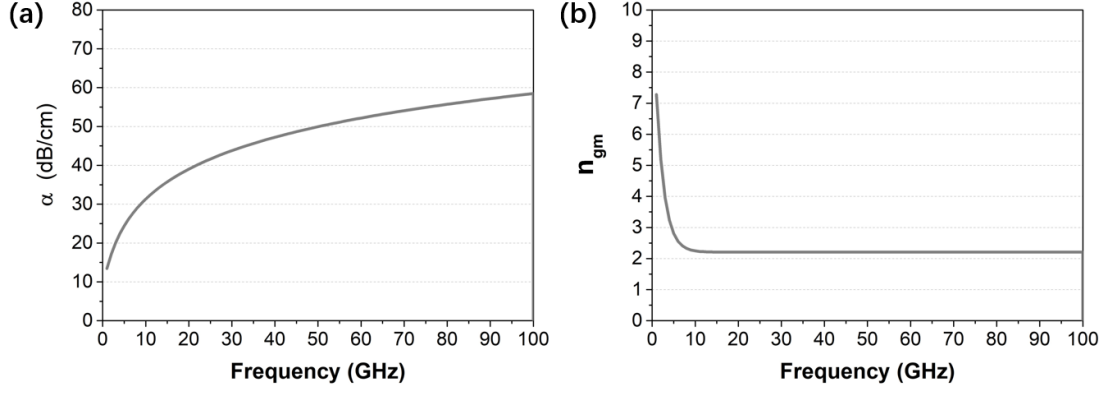
Figure 44. Propagation loss α_{dB} (a) and group index n_{gm} (b) of the traveling-wave electrodes. The gap, S pad width and the thickness of the gold electrode are chosen as $10\mu m$, $30\mu m$ and 500nm.
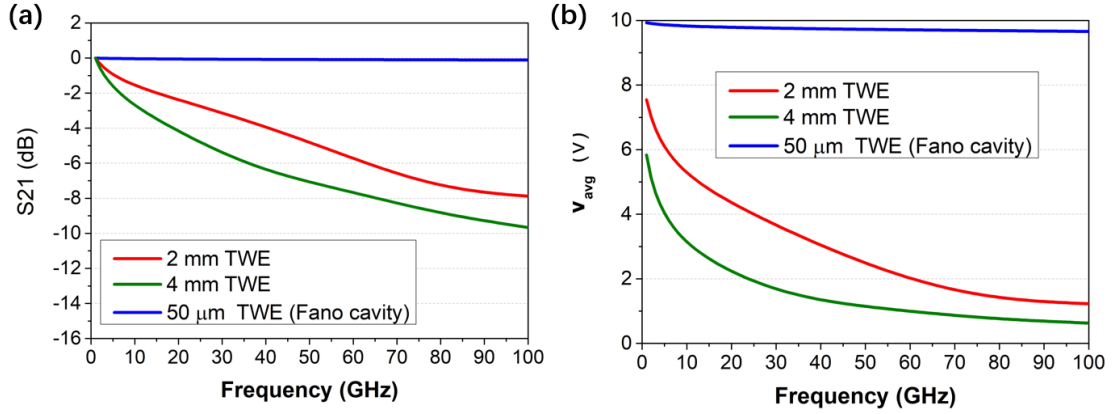
Figure 45. The A21 frequency response (a) and average effective voltage V_{avg} of the traveling-wave electrodes. The gap, S pad width and the thickness of the gold electrode are chosen as $10\mu m$, $30\mu m$ and 500nm. Propagation loss and group velocity is inherited from Figure 44.

Next, a voltage of $V_{in} = 10V$ is considered for microwave driving. The electrical potential and electric field distribution could be calculated using the finite element method (FEM) and are shown in Figure 46. In the region of the silicon core, the electric field is nearly homogeneous with an amplitude of $|E| \approx 1.4 \times 10^6 V/m$. Combining this value with the experimental second-order nonlinear susceptibility of $\Delta\chi_{yyx}^{(2)} = -1.8 \text{ pm/V}$ [63], a resulting index change in silicon [51, 160] of $\Delta n_{eff} = 2\Delta\chi_{yyx}^{(2)}E_x \approx 5.04 \times 10^{-6}$ can be obtained. According to the nearly linear wavelength change with respect to index variation, as shown in Figure 47, a wavelength detuning of 2 pm can be expected. Based on this index variation, a transmission extinction 1.3 dB and 0.5 dB can be obtained from the cavity optical model with Q factor of 34000 and 5600 (Figure 38 (c) and (d)). This is much more efficient than that previous demonstrations made using MZI where high microwave losses were present and a frequency detuning larger than 1 nm was needed to obtain a 3dB extinction [160, 63], which is in principal impossible to achieve with this low $\Delta\chi_{yyx}^{(2)} = -1.8 \text{ pm/V}$.

60

3dB extinction can be further expected with 5pm and 14 pm in the cavity with Q of 34000 and 5600, respectively, which indicates approximately a 200-fold and 60-fold improvements on extinction ratio. Based on these analyses, a Fano strained silicon modulator is expected possibly to run an eye-diagram which has not been done in [63] yet.
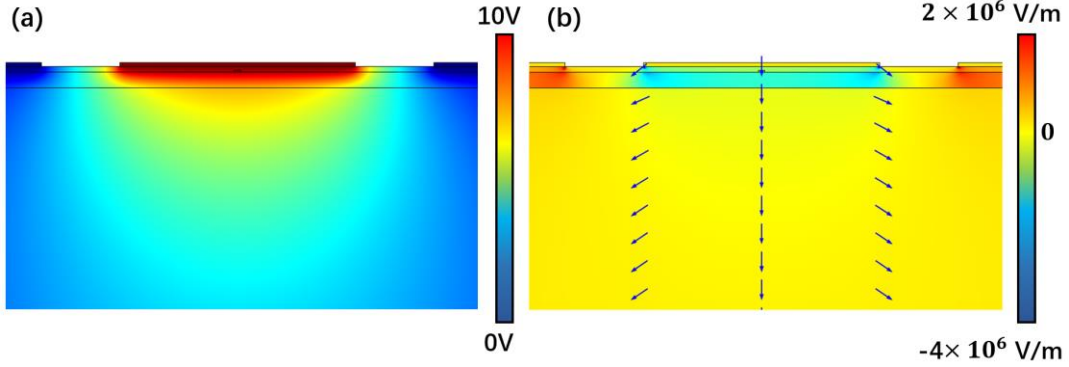
Figure 46. Electric potential (a) and electric field (b) distribution with 10V driving signal.
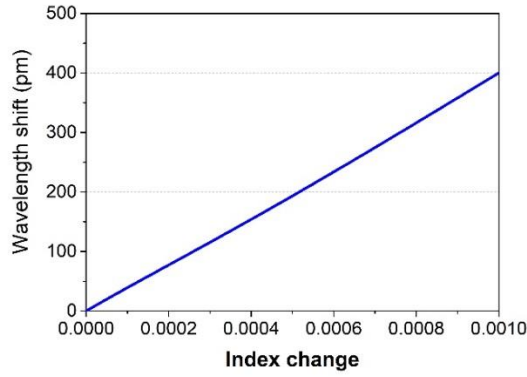
Figure 47. Wavelength shift results from the index variation of the Fano cavity.

Currently, an eye-opened diagram (e.g. 3dB extinction) is still not easily accessible since it requests higher availability of driven amplitude (e.g. 25V). However, instead of using such a 25V driven amplitude, we are also targeting a higher nonlinear susceptibility by reorganizing the cladding for higher strain. For instance, a triple of the nonlinear susceptibility $\Delta\chi_{yyx}^{(2)}$ (i.e. 4.5 pm/V, yet is still much lower than LiNbO$_3$) would be enough to propose a 3dB-ER eye-diagram. These studies on the materials and structures are current under progress to demonstrate this research outcome. Overall, the strong improvement of the optical extinction ration with low Q and the ultra-compact TWE give us a nontrivial possibility to run a high-rate and low-power silicon modulator with low nonlinear effect.

2.2   Conclusions and outlook

This chapter has developed an approach for improving the modulation efficiency of silicon resonant modulators. Taking the silicon modulator based on plasma

dispersion effect as the first example, a Fano cavity resonator enabled by sub-wavelength engineering (mixer) has led to simultaneously anticipated an ultra-low power consumption of less than 5 fj/bit with a small Q factor of only 5600 but yet with a high extinction ratio of 23 dB. Based on this result, high-speed (up to 40 Gb/s) modulation with clear eye diagram can be foreseen.

Additionally, more importantly, starting from the unusual performance of the optical cavity on-off transition, we have extended the method to design a strained silicon Fano modulator. Modulation based on the strain-induced Pockels effect in silicon usually suffers strongly from the weak amplitude of the exploited nonlinear effect and of the considerable microwave losses due to the needed large footprints. For example, previously a 3dB extinction required a wavelength shift of 1nm in MZI strained silicon [63], which is unreachable with the low second-order susceptibility level $\Delta\chi_{yyx}^{(2)} = -1.8\text{pm/V}$ presently available. By means of the proposed subwavelength structured Fano resonator, around 200-fold/60-fold (Q factor of 32000/5600) improvement on the extinction with the same driven voltage is theoretically predicted.

To sum, the reported results bring promise of huge progress regarding electro-optical modulation in silicon photonics. At the time being of the manuscript writing period, the fabrication of samples is currently under progress.

3 Subwavelength structured Self-Adaptive Boundary for Kerr nonlinearity

After the introduction and motivations in Chapter 1, Chapter 2 was devoted to the theme of electrooptical modulation by plasma and Pockels effects. Chapter 3 is now devoted to the use of third order non-linearities, in particular for the use of four-wave mixing (FWM) processes and the realization of light sources (frequency combs).

To first address some classical issues on the dispersion manipulation in FWM process, we introduce originally the Self-Adaptive Boundary (SAB) in a waveguide which is built to by extracting the similarities from a quantum well, for inter-mode four-wave mixing. With the proposed SAB, modes with different effective index values can automatically adapt to different spatial spans, giving room to satisfy the required phase matching condition for nonlinear processes in a new strategy. The model is investigated with detailed calculation and numerical confirmation. The feasibility of proposed concept for nonlinear wave generation is demonstrated using subwavelength grating waveguides relying on an equivalent index model.

Next, the proposed SAB subwavelength waveguides are adopted to extend the bandwidth of silicon soliton frequency combs where the generation of full spectra is built on a cascaded FWM process. The generation of soliton frequency combs is performed with different waveguide strategies for comparison which leads to the conclusion that the proposed SAB waveguide condition can powerfully enhance the operation of frequency micro-combs.

3.1 Self-Adaptive Boundary (SAB) in phase-matched optical waveguides

3.1.1 Reconsidering the momentum and energy conservation in FWM processes

In the implementation of wideband sources for silicon photonics [51, 161-162], especially the FWM-based parametric amplification [163-165] and mid-infrared light sources [166-168], the compensation of both the intrinsic material and nonlinearity-induced dispersion is a key point to maximize the conversion efficiencies. In a conventional single-mode FWM approach, depicted in Figure 48 a, energy is transferred from the pump into signal and idler propagating in the fundamental waveguide mode with different propagation constants. Thus, precise control of dispersion is required to fulfill the phase matching condition ($2k_{zP}=k_{zS}+k_{zI}$). Another approach to ease the request on the dispersion is to use inter-mode FWM [169-171] in which scheme more than one mode is involved in the nonlinear process. As shown in Figure 56 b, the working point (k, ω) is then distributed over 3 or 4 modes. By

fulfilling $\omega_{zP1} + \omega_{zP2} = \omega_{zS} + \omega_{zI}$ and $k_{zP1} + k_{zP2} = k_{zS} + k_{zI}$, four wave mixing processes can be potentially conducted in a with frequency span. This requires, however, appropriate and simultaneous control of the dispersion relationship of the different modes involved operating at different points (ω,k), as illustrated in Fig. 48 (b).
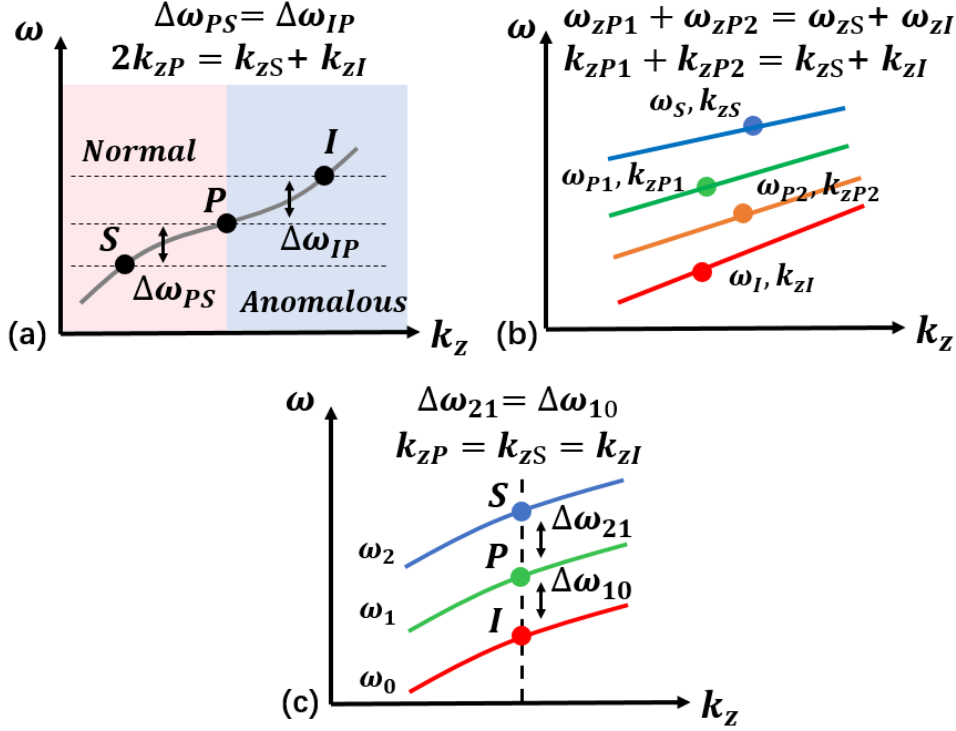
Figure 48. (a) Schematic of degenerate four wave mixing operating in a single-mode waveguide with anomalous dispersion. (b) Schematic of a classical inter-mode four-wave mixing. (c) Schematic of degenerate four wave mixing operating within an inter-modal scheme regardless the absolute dispersion provided that all dispersion curves are obtained by translating the same curve with a constant frequency step (e.g. $\Delta\omega_{21} = \Delta\omega_{10}$ here).

Instead of managing to yield anomalous dispersion in single-operation or searching the possible working points (ω,k) for inter-mode four mixing, **we propose to shape the index profile of the waveguide to support different spatial modes with the same propagation constant and equal frequency spacing, as shown in Figure 48 c**. In this proposal, energy is transferred from the pump into signal and idler propagating in different waveguide modes with the same propagation constant ($k_{zP} = k_{zS} = k_{zI}$). Therefore, the **phase matching condition is automatically satisfied**. Concurrently, energy conservation requires equal frequency spacing. Then, the bandwidth of the proposed scheme does not depend on the exact dispersion of the waveguide, but on the relative spacing of the dispersion curves of the modes, determining the wavelength range where energy conservation is fulfilled. **The key point is then to ensure that the dispersion curve of each mode is obtained by a simple frequency translation, as a whole, of a previous mode; in other words, that the dispersion curves of the modes involved in the non-linear interaction are**

parallel to each other. As the search for this condition is not natural, we devote most of the following pages to it, starting with the simplified case of planar optical waveguides in order to be able to carry out, in the first instance, a completely analytical resolution.

Let us thus consider a two-dimensional step-index slab waveguide presented in the inset of Figure 49 (a) (infinite depth along the x axis). As it is well known from textbooks, the eigen equation for modes propagating along the z axis with an electric field polarized along y axis then reads as [7]:

$$ha = \frac{m\pi}{2} + arctan(\frac{\gamma n_w^2}{hn_c^2}) \tag{3.1}$$

where n_w and n_c are the material index of waveguide core and cladding, while $h = \sqrt{(k_0^2 n_w^2 - k_z^2)}$ and $\gamma = \sqrt{(k_z^2 - k_0^2 n_c^2)}$ are the wavevector along the y axis, inside and outside the waveguide core, respectively. Silicon and silicon dioxide are chosen here as the core and cladding materials, considering material dispersion. The waveguide width $2a$ is set here at 700nm, which is enough to support 4 modes with effective index values higher than 2. From equation (3.1) we obtain the dispersion curves for the first four order modes (with corresponding mode order m=0, 1, 2, 3), as shown in Figure 49 (a). Obviously, the frequency spacings change in a nonlinear manner with the mode order m, resulting in an uneven spacing that precludes the satisfaction of energy conservation required for the proposed multi-mode FWM approach. Figure 49 (b) depicts the evolution of the frequency spacing $\Delta\omega_m = \omega_{m+1}$-$\omega_m$ and effective index as a function of the mode order. With the increasing mode order m (thus decreasing n_{eff}), the frequency spacing $\Delta\omega_m$ monotonously and rapidly increases.
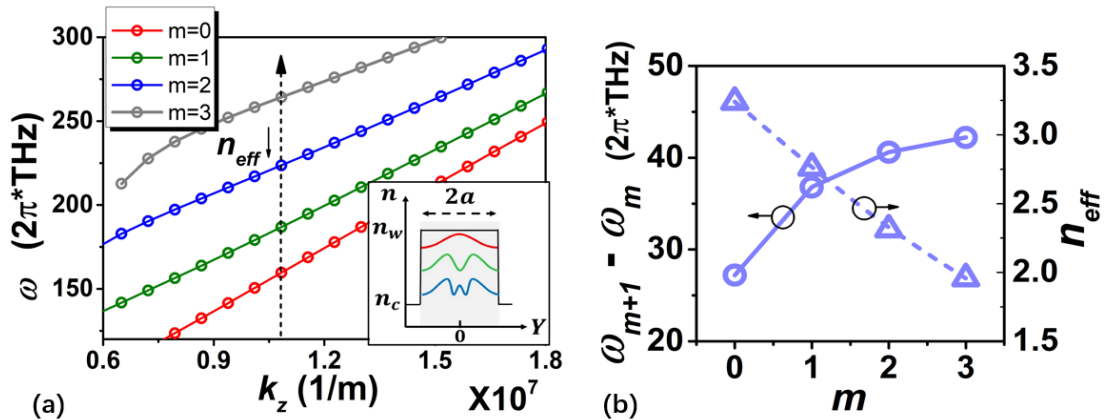
Figure 49. (a) Dispersion curves of first 4 modes of a two-dimension silicon waveguide with silica cladding, propagating along z axis. The width is $2a = 700$nm. The index profile of the waveguide and mode distribution are plotted in the inset. (b) Frequency spacings ω_{m+1}-ω_m and n_{eff} as a function of the mode order m, collected at $k_z = 1.08 \times 10^7$ in (a).

To better understand the evolution of frequency spacing $\Delta\omega_m$, we consider the derivative of the mode frequency with respect to the mode order m by considering it artificially (i.e. mathematically), for the analysis, as a continuous variable. Assuming that the k_z is a constant and ω is a function of n_{eff} and m, the frequency spacing between modes can therefore be expressed as:

$$\frac{d\omega}{dm} = \frac{d}{dm}\left(\frac{k_z c}{n_{eff}}\right) = \frac{k_z c}{-n_{eff}^2} \cdot \frac{dn_{eff}}{dm} = \frac{k_z c}{-n_{eff}^2} \bigg/ \frac{dm}{dn_{eff}} \tag{3.2}$$

From equation (3.2) we can infer that if dm/dn_{eff} is proportional to $-1/n_{eff}^2$, then the frequency spacing is fixed. Though the mode order number m is a discrete integer indicating the phase solution, mathematically it still can be represented as a function of ω and n_{eff}, from equation (3.1) that:

$$m = \frac{2}{\pi}\left[\frac{k_z \cdot a \sqrt{n_w^2 - n_{eff}^2}}{n_{eff}} - arctan(\frac{\gamma n_w^2}{hn_c^2})\right] = f_{m1} + f_{m2} \tag{3.3}$$

In which $f_{m1} = \frac{2k_z}{\pi} a \sqrt{\frac{n_b^2}{n_{eff}^2} - 1}$ describes the phase from standing waves, while

$f_{m2} = -\frac{2}{\pi} arctan(\dfrac{n_b^2 \sqrt{(n_{eff}^2 - n_c^2)}}{n_c^2 \sqrt{(n_b^2 - n_{eff}^2)}})$ accounts for the abrupt index change on the

boundary. The related first derivatives can therefore be written as:

$$\frac{df_{m1}}{dn_{eff}} = \frac{2k_z}{\pi}\frac{d}{dn_{eff}}\left(a\sqrt{\frac{n_w^2}{n_{eff}^2} - 1}\right) = \frac{-2ak_z n_w^2}{\pi n_{eff}^2 \sqrt{n_w^2 - n_{eff}^2}} \tag{3.4}$$

$$\frac{df_{m2}}{dn_{eff}} = -\frac{2}{\pi} \cdot \frac{d}{dn_{eff}} arctan(\frac{\gamma n_w^2}{hn_c^2}) = -\frac{2}{\pi} \cdot \frac{1}{1 + \frac{n_b^4(n_{eff}^2 - n_c^2)}{n_c^4(n_b^2 - n_{eff}^2)}} \cdot \frac{d}{dn_{eff}}(\frac{n_b^2\sqrt{(n_{eff}^2 - n_c^2)}}{n_c^2\sqrt{(n_b^2 - n_{eff}^2)}})$$

$$= -\frac{2}{\pi} \cdot \frac{n_{eff}}{-1 + n_{eff}^2(1/n_c^2 + 1/n_w^2)} \cdot \frac{1}{\sqrt{(n_{eff}^2 - n_c^2)}} \cdot \frac{1}{\sqrt{(n_w^2 - n_{eff}^2)}} \tag{3.5}$$

Confirmed by numerical intermediate calculation, for a =350nm, n_w =3.48, n_c=1.445 and n_{eff} from 1.6 to 3, we have $\frac{df_{m2}}{dn_{eff}} \in (-1.7, -0.19)$ while $\frac{df_{m1}}{dn_{eff}} \in$

$(-5, -3)$, from which we may assume that the $\frac{dm}{dn_{eff}}$ is almost governed by $\frac{df_{m1}}{dn_{eff}}$ for simplifying the analysis. Therefore, $\frac{dm}{dn_{eff}}$ can be approximately expressed as:

$$\frac{d\omega}{dm} = \frac{k_z c}{-n_{eff}^2}/(\frac{df_{m1}}{dn_{eff}} + \frac{df_{m2}}{dn_{eff}}) \approx \frac{k_z c}{-n_{eff}^2}/(\frac{df_{m1}}{dn_{eff}}) = \frac{c\pi\sqrt{n_w^2 - n_{eff}^2}}{2an_w^2} \tag{3.6}$$

The analytical $d\omega/dm$, calculated from equation (3.6) by considering a=350nm, n_w=3.48, n_c=1.445, is plotted in Figure 50 (a). The effective index n_{eff} of the first 4 modes are marked by the circles in the Figure. The corresponding values of $d\omega/dm$ range from $2\pi * 24$THz to $2\pi * 45$THz. Marked points are well coincident with the discrete calculation results coming from the dispersion curves shown in Figure 49 (b). From equation (3.6), it follows that $\frac{d\omega}{dm}$ is almost proportional to $\sqrt{n_w^2 - n_{eff}^2}$, which gives a good explanation on the monotonous and nonlinear evolution of $\Delta\omega_m$ observed in Figure 49 (b). This confirms that the analytical frequency spacing $\frac{d\omega}{dm}$ is a useful and simple tool to investigate how the frequency spacing evolves with the waveguide dimension and the index profile.
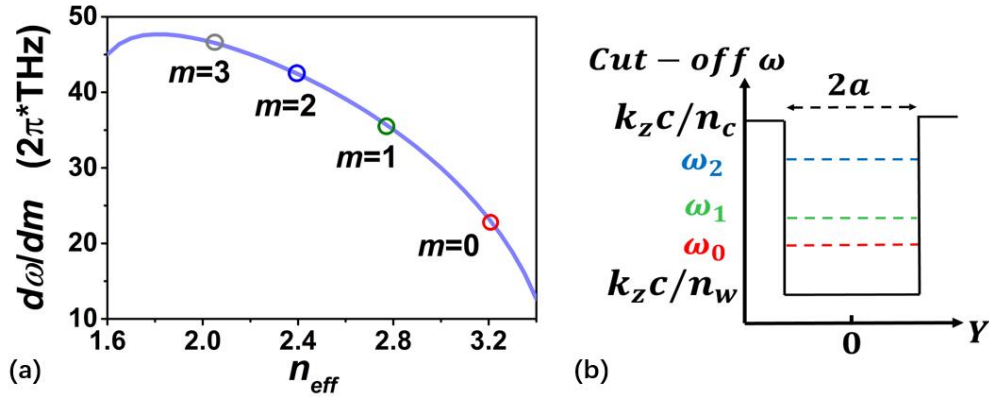
Figure 50. (a) Frequency spacings as a function of effective index n_{eff}, obtained from analytical calculation. (b) Schematic of the transverse photonic well described by the cut-off frequency for photon propagating along z axis with wavevector k_z.

The step-index slab waveguide can be understood from the point of view of quantum wells, just by considering the cut-off frequencies (the minimum frequency/energy for a photon to propagate along z axis with a wave vector of k_z) for the core ($k_z c/n_w$) and cladding ($k_z c/n_c$), for a given wavevector k_z [172-174]. Then, the behavior of frequency spacings is similar to the solutions of a harmonic oscillator in a finite-depth potential well. The square potential well formed by the step-index waveguide, depicted in Figure 50 (b), results in unevenly spaced

frequencies. Conversely, it is well known that parabolic potential wells yield equi-spaced frequencies [175].

3.1.2 Self-Adaptive Boundary (SAB)

Standing on the issue (non-equal frequency spacing) introduced above, we try to explore the possibility of equalizing the frequency spacing by reshaping the potential well with an index profile such as the one shown in Figure 51 (a). Concepts and therefore approaches are adopted from quantum mechanics. We consider a 2D graded-index slab waveguide (then with graded cut-off potential) with a waveguide width of $2a$. The indices for the waveguide core, waveguide edge and cladding are $n(0) = n_{cent}$, $n(a) = n_b$ and $n(|y| > a) = n_c$, respectively, as displayed in Figure 51 (b). When the condition that all effective indices of the modes are larger than the physical boundary index (i.e. $n_{eff} > n(a) = n_b$ for all the guided modes) into the index profile, the waveguide can be considered as splitting into five zones (zones 0, ∓ 1, ∓ 2). The central part (part 0) is within the $[-L_m, L_m]$ range in which $n(y)$ is larger than n_{eff} and can be expressed by a cos function as usually, instead of the physical boundaries (i. e. $y = \mp a$). The other four zones (zones ∓ 1, ∓ 2) are described by a decaying form because $n(y)$ is there smaller than n_{eff}.
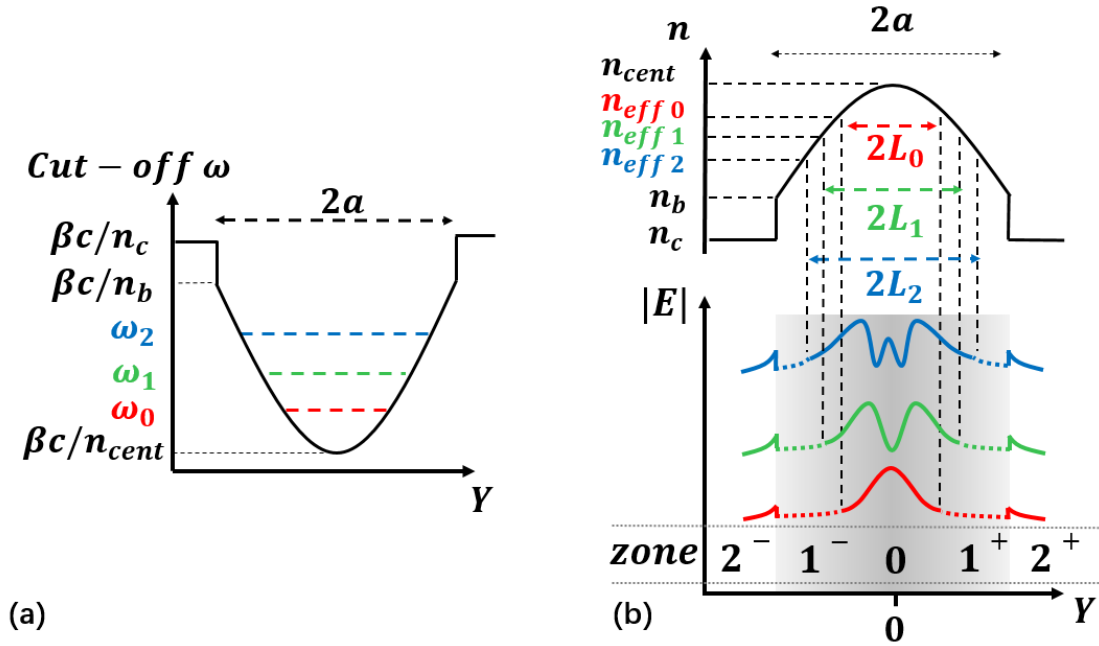
Figure 51. (a) Schematic of a graded-index potential well. (b) Sketch of a non-uniform index profile and the mode distribution of the first three modes propagating z axis. n_{cent}, n_b, n_c are the material index of the waveguide center, waveguide boundary and the surrounding for a waveguide with self-adaptive boundary ($n_{effm} > n_b$). The zero point of y axis is located at the center of the waveguide.

To satisfy the Maxwell's equations and the corresponding boundary condition for an electric field polarizing along y, the field can be expanded as follows we rewrite the wave equation inside the waveguide:

$$H_x = A_2^+ exp\left[k_0\sqrt{n_{eff}^2 - n_c^2} \cdot (y - a)\right], \quad a \le y \tag{3.7}$$

$$H_x = A_1^+ cosh[D(y)] + B_1^+ sinh[D(y)], \quad L \le y < a \tag{3.8}$$

$$H_x = A_0 cos[N(y) - \varphi], \quad -L < y < L \tag{3.9}$$

$$H_x = A_1^- cosh[D(y)] + B_1^- sinh[D(y)], \quad -a < y \le L \tag{3.10}$$

$$H_x = A_2^- exp\left[k_0\sqrt{n_{eff}^2 - n_c^2} \cdot (y + a)\right], \quad -a \ge y \tag{3.11}$$

in which the $A_{1,2}^+$ and $B_{1,2}^+$ are the amplitudes of the decaying components for the positive direction, while $A_{1,2}^-$ and $B_{1,2}^-$ stand for the negative one. φ is the biased phase that is related to the mode order ($\varphi = 0$ or $\varphi = {}^\pi/_2$, with respect to modes of symmetric and anti-symmetric parities). The pattern of zone 0 and zones ∓ 2, jointly determine the hyperbolic form of part 1. Due to the varying index profile, currently the total phases of the wave propagation along the y axis inside the waveguide can be transformed to the integral of position-related wavevector $\sqrt{(k_0^2 n^2(y) - k_z^2)}$ to y coordinate (N_m and D_m stand with respect to zone 0 and zones ∓ 1, respectively):

$$N_m(y) = \int_0^{L_m} \sqrt{(k_0^2 n^2(y) - k_z^2)} \, dy \tag{3.12}$$

$$D_m(y) = \int_{L_m}^y \sqrt{(k_z^2 - k_0^2 n^2(y))} \, dy \tag{3.13}$$

As it is shown in Figure 51, modes with different mode orders m are confined in different spatial spans, which sizes increase with m. Each spatial span L_m (for m =1,2,3, …) which can be called "effective length" for mode 'm' is defined through $n(L_m) = n_{effm}$. The condition $\boldsymbol{n_{eff} > n_b}$ is defined as "**Self-Adaptive Boundary (SAB)**" in the manuscript. By solving the equation 3.7-3.13, the eigen equation can be written as:

$$tan[N(L_m) \pm \varphi] = \frac{D'_m(L_m)}{N'_m(L_m)} = \lim_{y \to L_m} \frac{D'_m(y)}{N'_m(y)} = 1 \tag{3.14}$$

The Eigen equation for modes propagating along z axis with an electric field polarized along the y axis can be rewritten as:

$$N(L_m) = \int_0^{L_m} \sqrt{(k_0^2 n^2(y) - k_z^2)}\, dy = \frac{m\pi}{2} + \frac{\pi}{4} \qquad (3.15)$$

Previously, in the step-index waveguide, to respond to the approximately linear phase increas on the right part of equation (3.3), the changes of ω and n_{eff} were correlated through the relationship $a\left(\frac{\omega_{m+1}}{c}\right)\sqrt{n_w^2 - n_{eff,m+1}^2}$ − $a\left(\frac{\omega_m}{c}\right)\sqrt{n_w^2 - n_{eff,m}^2} = \frac{\pi}{2}$. When the proposed self-adaptive boundary $n_{eff,m} > n_b\ \forall m$ is introduced, the spatial integral range is automatically selected which exactly gives the room to trim the frequency spacing through the following condition :

$\frac{\omega_{m+1}}{c} \int_0^{L_{m+1}} \sqrt{n^2(y) - n_{eff,m+1}^2} - \frac{\omega_m}{c} \int_0^{L_m} \sqrt{n^2(y) - n_{eff,m}^2} = \frac{\pi}{2}$ .To consider the improvement from this new condition, a similar analysis for frequency spacings is carried out as previously with a general index profile described by $n(y) = (A + By)^p$. With this variable confinement strength effect, i.e. the Self-Adaptive Boundary (SAB), we first consider a linear index profile, i.e. $p = 1$ and $n(y) = Ay + B$. The phase $N(L_m)$ can be recalculated as:

$N(L_m) = \frac{m\pi}{2} + \frac{\pi}{4}$, ie:

$$N(L_m) = \frac{k_z n(y)}{2An_{eff,m}} \sqrt{n^2(y) - n_{eff,m}^2} - \frac{k_z n_{eff,m}}{2A} \log\left[\frac{k_z}{n_{eff,m}} \sqrt{n^2(y) - n_{eff,m}^2} + \right.$$
$$\left. \frac{k_z}{n_{eff,m}} n(y)\right]\Big|_0^L \qquad (3.16)$$

Because of the self-adaptive behavior related to the endpoint $n(L_m) = n_{effm}$ condition, the previous relationship can be greatly simplified in a common form for the different modes, with $n(0) = B = n_{cent}$, to:

$$N(L_m) = \frac{-k_z n_{eff,m}}{2A} \log[k_z] - \left(\frac{n_{cent}}{2A} \cdot \frac{k_z}{n_{eff,m}} \sqrt{n_{cent}^2 - n_{eff,m}^2} - \right.$$
$$\left. \frac{k_z n_{eff,m}}{2A} \log\left[\frac{k_z}{n_{eff,m}} \sqrt{n_{cent}^2 - n_{eff,m}^2} + \frac{k_z}{n_{eff}} n_{cent}\right]\right)$$
$$= \frac{k_z n_{eff,m}}{2A} \log\left(\sqrt{\frac{n_{cent}^2}{n_{eff,m}^2} - 1} + \frac{n_{cent}}{n_{eff,m}}\right) - \frac{k_z n_{cent}}{2A} \sqrt{\frac{n_{cent}^2}{n_{eff,m}^2} - 1} \qquad (3.17)$$

By doing the 1st derivative of $N(L)$, we have

$$\frac{dN(L_m)}{dn_{eff}} = \frac{k_z}{2A} \left(log\left[\sqrt{\frac{n_{cent}^2}{n_{eff,m}^2} - 1} + \frac{n_{cent}}{n_{eff,m}} \right] - \frac{\frac{n_{eff,m}^2}{\sqrt{n_{cent}^2 - n_{eff,m}^2}}}{\sqrt{n_{cent}^2 - n_{eff,m}^2} + n_{cent}} - 1 + \right.$$

$$\left. \frac{n_{cent}^3}{n_{eff,m}^2 \sqrt{n_{cent}^2 - n_{eff,m}^2}} \right)$$

$$= \frac{k_z}{2A} log\left(\sqrt{\frac{n_{cent}^2}{n_{eff,m}^2} - 1} + \frac{n_{cent}}{n_{eff,m}} \right) + \frac{k_z n_{cent} \sqrt{n_{cent}^2 - n_{eff,m}^2}}{2A n_{eff,m}^2} \qquad (3.18)$$

For a fixed k_z, we have $m = \frac{2}{\pi} \left(N(L_m) - \frac{\pi}{4} \right)$, therefore

$$\frac{d\omega}{dm} = \frac{k_z c}{-n_{eff,m}^2} / \frac{dm}{dn_{eff,m}} = \frac{\pi k_z c}{-2n_{eff,m}^2} / \frac{dN(L)}{dn_{eff,m}}$$

$$= -A\pi c / [n_{eff,m}^2 log\left(\sqrt{\frac{n_{cent}^2}{n_{eff,m}^2} - 1} + \frac{n_{cent}}{n_{eff,m}} \right) + n_{cent} \sqrt{n_{cent}^2 - n_{eff,m}^2}] \qquad (3.19)$$

Figure 52 (a) shows $d\omega/dm$ as a function of n_{eff}, calculated from equation 3.19, considering a=800nm, n_{cent}=3.48, n_b=1.8, n_c=1.45 and n_{eff} from 1.8 – 3.4. Though the frequency spacings is still changing monotonously, the function exhibits a totally new tendency with an increasing $d\omega/dm$ with n_{eff}. This trend is opposite to that of a step-index waveguide shown in Figure 58 (a). The dispersion curves of the first four modes, obtained from 2D FDTD are presented in Figure 60 (b), in which the narrowing effect of $d\omega/dm$ is consistent with the prediction shown in Figure 60 (a). Particularly, $d\omega/dm$ is flattened for $n_{eff} \sim 2$ (Figure 60 (b)), which indicates that identical frequency spacings can be found at more than one point.

Then, we study $d\omega/dm$ for an index profile characterized by $p \neq 1$ and $n(y) = (A + By)^p$. To do so, we expand $n(y)$ around y=0 to a summation of a 8-order polynomial using the Taylor series expansion: $N(L) = \int_0^L \sum_1^k [C_0 + C_1(n - n_{cent}) + \cdots + C_{10}(n - n_{cent})^k] dy$ and redo the analytical integral and derivative. The evolutions of $d\omega/dm$ as a function of n_{eff} for $p = 0.6$ and $p = 0.3$, are presented in Figure 52 (a). The flattened $d\omega/dm$ region shifts to higher n_{eff} values with decreasing p numbers. For $p = 0.3$ the flattened region appears near $n_{eff} = 2.85$, which is close to that of a fundamental mode in a silicon on insulator (SOI) waveguide. Figure 3 (d) shows the dispersion curves of the first 4 order modes calculated using the FDTD method for $p = 0.3$. Clearly, all the curves are almost

parallel and separated by a very close frequency spacing of ~ 20.5 THz. The evolution of frequency spacings, $\Delta\omega_m$, and the effective index, n_{eff}, for a wavevector of $k_z = 1.03 \times 10^7$ m^{-1} are presented in Figure 52 (b)
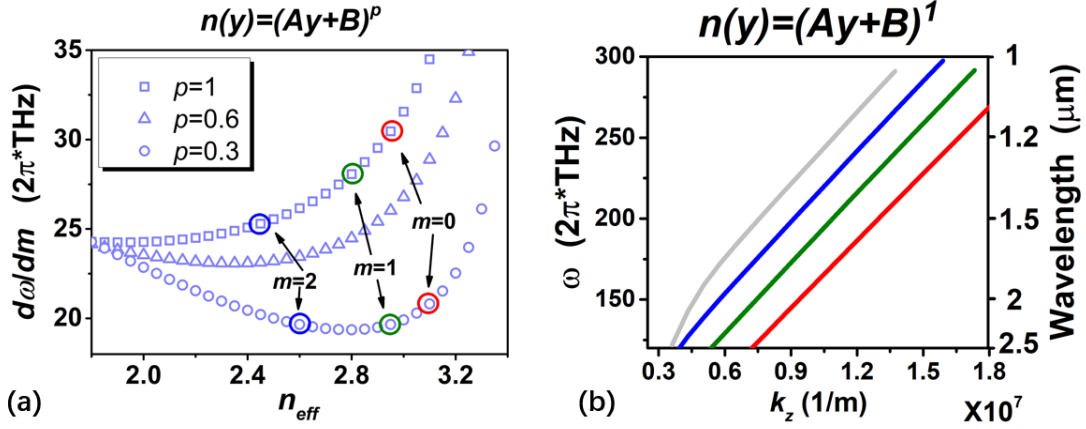
Figure 52. (a) Analytical Frequency spacings as a function of effective index n_{eff}, with different *order* numbers (different modes feeling different profiles). The other parameters are: $2a = 1600$nm. $n_{cent} = 3.48$, $n_b = 1.8$, $n_c = 1.45$. The n_{eff} points, corresponding to the first 3 modes, are labelled by the colored circles. (b) Dispersion curves of first 4 modes with *order* = 1, i.e. linear shape, using FDTD calculation.

Opposite to the step-index waveguide case studied in Figure 2 (b), the frequency spacing now remains almost constant when changing the mode order m, regardless of the sharply descending n_{eff}, which is perfectly coincident with the prediction indicated by the analytical calculation. **These results illustrate the potential of the proposed approach to achieve energy conservation and phase matching simultaneously, overcoming the major limitations of step-index waveguides.** All possibility of equal frequency spacing **rely on $n_{eff} > n_b$, i.e. the SAB** since it is what opens the rooms for reshuffling the mode bands. In **Appendix A1** we have discussed the configuration with traditional condition $n_{eff} < n_b$ and indicates the necessity of SAB to such a equi-frequency spacing result.
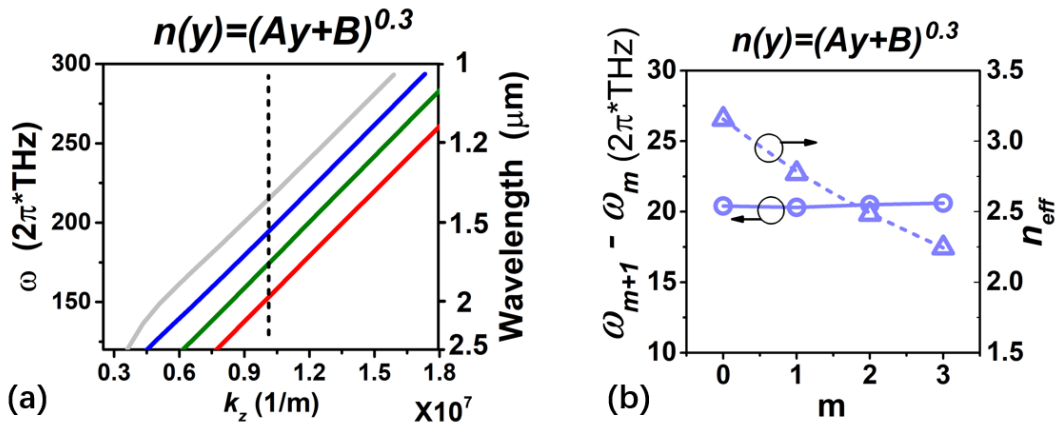
Figure 53. (a) Dispersion curves of first 4 modes with $order = 0.3$, using FDTD calculation. (b) Frequency spacings ω_{m+1}-ω_m and the n_{eff} as a function of the mode order m, collected at $k_z = 1.03 \times 10^7$ m^{-1} in (a).

3.2   Translating the SAB with subwavelength structures to 3D realistic waveguide geometries

3.2.1   Subwavelength structured waveguide with Self-Adaptive Boundary

It is easy to fulfill the condition of $n_{eff} > n_b$ and obtain relevant mode profiles by setting a continuous/multi-segment grade-index profile. Typical examples are shown in Figure 54. As expected, the effective width of each mode is different for each mode. However, this kind of configuration is almost impossible to access in practice using standard planar fabrication technologies.
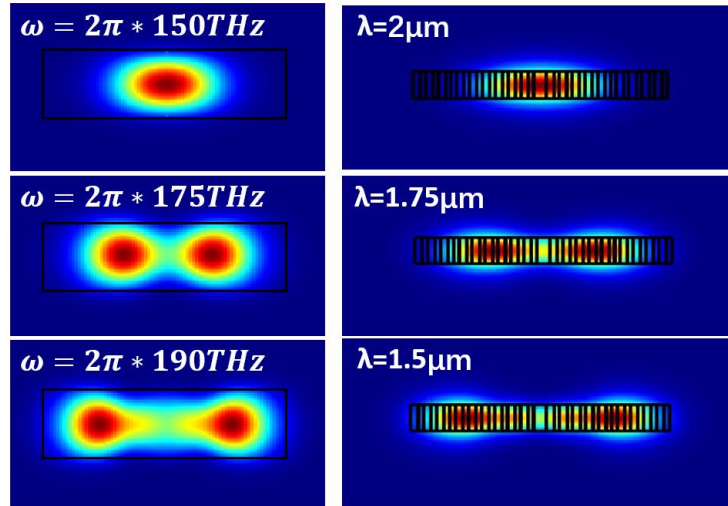
Figure 54. Mode profiles of first 3 modes in continuous/multi-segment grade-index waveguide, with Self-Adaptive Boundary $n_{effm} > n_b$. The material index is changed from center (3.48) to the boundary (1.8), with cladding index of 1. The waveguide widths are 800nm and 1400mm, respectively while thickness is 340nm.

Consistently with the main thread of this thesis, this kind of graded index profile can be more easily mimicked by the use of subwavelength structured waveguides [176, 177]. In Figure 55, the schematic of two possible implementations is presented for illustration, where the gradual index variation is implemented by apodization of the waveguide length. However, we would like to highlight the very general nature of the proposed approach, which can be seamlessly adapted to all types of geometries, photonic platforms (Si, III/V, polymer guides, etc.), and spectral ranges (near infrared, medium infrared).
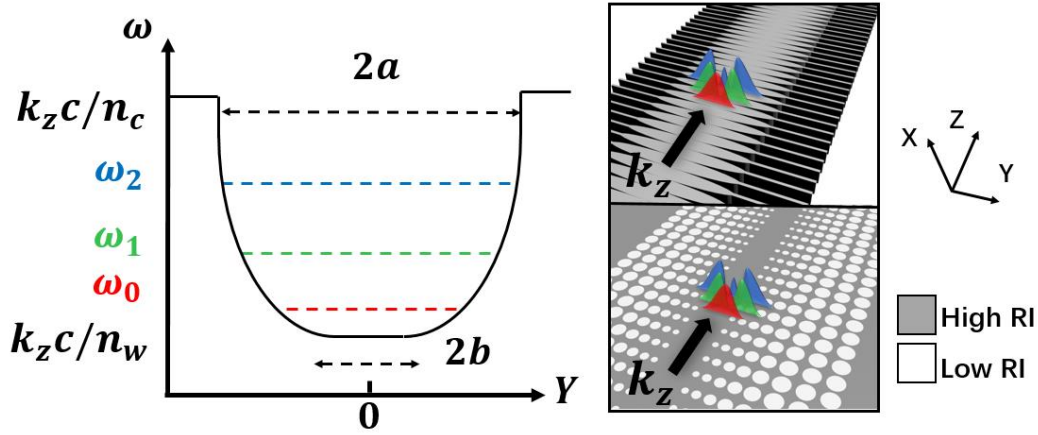
Figure 55. Schematic of the potential well of a graded-profile subwavelength waveguide. The equivalent cut-off frequency distribution indicated by the index.

As an example of the possible design of three-dimensional graded-profile waveguides with a self-adaptive boundary, a subwavelength structured waveguide with high-index strip tapered from center to the edge is chosen (Figure 55 top case). The period of 150nm is chosen for a balance of fabrication control and good index equivalence of the subwavelength region. The materials considered here are silicon and air, for the high-index and low-index regions, respectively. Graded-index is obtained by tapering the component width of silicon, from the center to the edge while keeping the period fixed. In this case, the width of the silicon components is changed from 150nm to 40nm, i. e. adjusting the filling factor from 1 to 0.267. According to the well-known equivalent properties of SWG waveguide, the index of SWG waveguide can be described as:

$$n_{SWG}(y) = \sqrt{\eta n_{cent}^2 + (1 - \eta)n_c^2} = \sqrt{\eta(n_{cent}^2 - n_c^2) + n_c^2} \tag{3.20}$$

which leads to an index ranging from around 3.48 to 1.8 for the C-band wavelengths. The $\eta(y) = (Ay + B)^p$ is the filling factor of silicon of the SWG waveguide at a transverse position y. The schematic of potential well that describes the cut-off frequency, as introduced before, is also presented in the inset of Figure 55. In order to approximately investigate the frequency spacings of this three-dimensional (3D) SWG waveguide, the effective index method [7] is adopted to find an equivalent simpler 2D waveguide with eight cladding regions. Then the phase item of the dispersion modes equation (3.15) can be rewritten again as:

$$N(L_m) = \int_0^{L_m} \sqrt{(k_0^2 n_{SWG}^2(y) - k_x^2 - k_z^2)}\, dy = \frac{m\pi}{2} + \frac{\pi}{4} \tag{3.21}$$

$$k_x t = \arctan\left(\frac{\gamma_x}{k_x}\right) \tag{3.22}$$

$$\gamma_x = \sqrt{k_0^2 n_{SWG}^2(y) - k_x^2 - k_0^2 n_c^2} \tag{3.23}$$

in which k_x and γ_x are the wavevectors along the x direction, inside and outside the waveguide, respectively. The corresponding index component can be depicted by $n_x = \frac{k_x}{k_0}$. Limited by the complicated expression of index of waveguide and the non-analytical solution of the dispersion equation along y, finding an accurate solution of equation (3.26) is difficult. Instead, using numerical fitting we simplify the n_x to a function $n_x^2 = C + D n_{SWG}^2(y)$ by numerically solving equation (3.22) and (3.23). Particularly, in order to ease the effect coming from n_x and simultaneously promote the effective index values of all the modes, we introduce additionally a shared section in which the index is fixed with a width of $[-b, b]$ as the central section shown in Figure 56 (a). The approximately analytical calculation of this 3D waveguide is addressed in **Appendix A2** and no shown here.
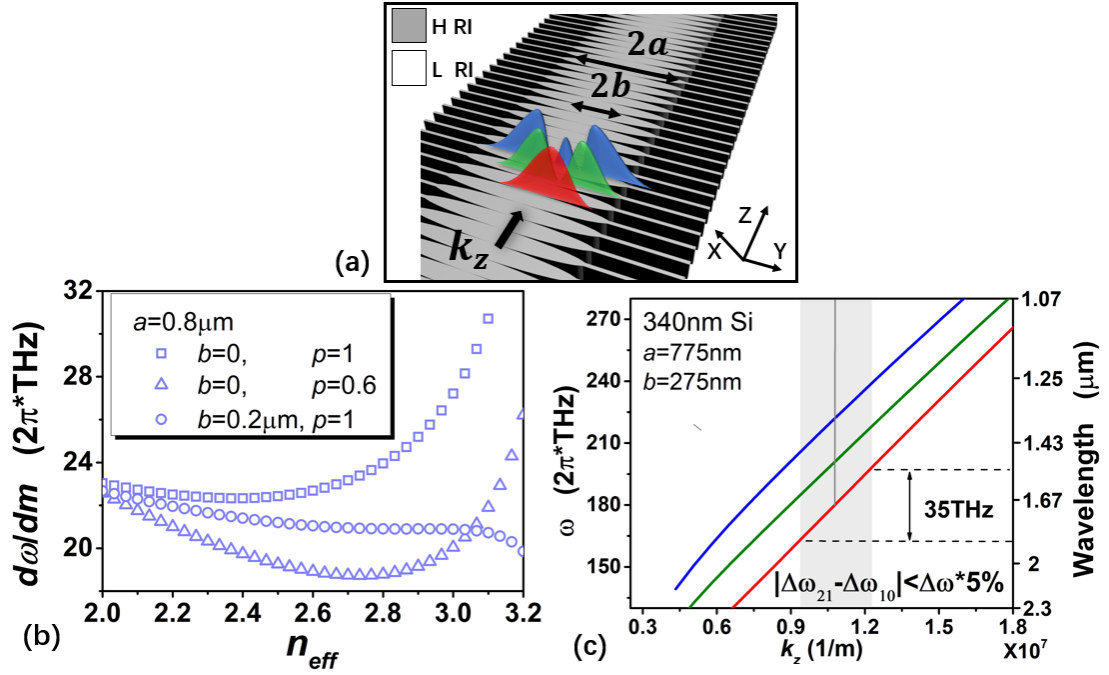
Figure 56. (a) Schematic of a graded-profile subwavelength waveguide. (b) Analytical Frequency spacings as a function of effective index n_{eff}, with different *order*s and b values. The other parameters were adopted as: $n_{cent} = 3.48$, $n_b = n_c$=1.8. (c) Frequency spacings as a function of the effective index n_{eff}, using 3D FDTD calculation. The perfect matching point and the 5% tolerant range are labeled by grey line and grey region, respectively.

Following then the same method as previously detailed, a set of waveguide parameters was found, with general structure as Figure 56 (a). Figure 56 (b) shows the calculated $d\omega/dm$ for waveguides with different parameters. First, we consider a fully graded index profile, with no fixed index region in the center ($b = 0$). For a

linear index profile, i.e. $p = 1$, the graded waveguide yields a flattened response near $n_{eff} = 2.4$. With a slower nonlinear index variation, i.e. $p = 0.6$, the flattened region can be shifted up to $n_{eff} = 2.75$. Further reduction of the p value compresses the flattened region to a narrow region which restricts the available design space. By introducing the fixed index region, we release a new degree of freedom that helps to widen the flattened region. By appropriately adjusting the value of b (e. g. to 200 nm), the slope between the local maximum and minimum can be substantially reduced, as shown in Figure 56 (b).

With optimized parameters of $a = 775\text{nm}$, $b = 275\text{nm}$ and $p = 1$, we can locally equalize the frequency spacing and make the dispersion curves parallel. In Figure 56 (c) we show the dispersion curves for the three first modes of the optimized waveguide, calculated using 3D FDTD simulations. With the point $\omega_2 - \omega_1 = \omega_1 - \omega_0$ located at $k_z = 1.07 \times 10^7$, the frequency range with condition $|\Delta\omega_{21} - \Delta\omega_{10}| < \Delta\omega * 5\%$ is as large as 35 THz (~300nm), which also evidences a good tolerance to the possible structure fabrication imperfections. Using this configuration, phase matching is achieved between signal frequency of 220THz (1.36µm) and idle frequency of 172THz (1.72µm). We have to mention that this result comes from the operation of the first 3 modes. However, this design strategy could be scaled up to higher order modes, e.g. to 5 modes. As mentioned earlier, these capabilities arise from the self-adaptive boundary (SAB) condition $n_{eff,m} > n_b, \forall m$ which is more than a simple graded-profile condition. **The results in Figure 56 strongly confirms us the feasibility to use subwavelength graded-structured waveguide to achieve the corresponding index-grated functions for dispersion engineering.**

3.2.2 Evaluation of the properties of the enabled FWM processes

Based on this result and structure (Figure 57 (b) inset), we explore now the capability and flexibility of the proposed approach with respect to degenerate four-wave mixing processes. Phase matching considering nonlinearities was described earlier as $\Delta k = 2\gamma P_P - (2k_{zP} - k_{zS} - k_{zI})$, which is governed by the nonlinear part $2\gamma P_P$ and linear part $\Delta k_L = 2k_{zP} - k_{zS} - k_{zI}$. Since $2\gamma P_P$ is normally positive in silicon, the linear dispersion Δk_L needs to be a bit larger than zero to fulfill the global phase matching condition, which is classically addressed by tuning the dispersion to its anomalous regime in a classical waveguide. In contrast, in our case, the condition is translated to the fact that the frequency spacing $\Delta\omega_{SP}$ (the matched frequency spacing between the pump and signal waves, i.e. between the 1st and 2nd modes, at the matched position) should be slightly different from $\Delta\omega_{PI}$ (frequency spacing between pump and idler wave, i.e. between 1st and 0th mode, at the matched position), which can be easily achieved just by slightly moving the operating point of

pump wave, as illustrated in Figure 57 (a). If the condition that $\Delta\omega_{SP} = \Delta\omega_{21} - \frac{\delta\omega}{2} =$

$\Delta\omega_{10} + \frac{\delta\omega}{2} = \Delta\omega_{SI}$ can be satisfied at the shifted position characterized by $2k_{zP} >$

$(k_{zS} + k_{zI})$, then the nonlinearity-induced phase mismatch can be compensated. This condition requires $\frac{d(\Delta\omega_{21} - \Delta\omega_{10})}{dk_z} > 0$, which can be easily satisfied by adjusting the structure profile. For example, we plot in Figure 57 (b), $\delta\omega$ for the optimized waveguide shown in Figure 56. Rightward the working point, we see that $\Delta\omega_{21} > \Delta\omega_{10}$ with increasing k_z (grey line). The negative-to-positive trend well validates the possibility of compensating the nonlinear mismatch. For silicon waveguides working at telecom wavelengths, the effective nonlinear Kerr nonlinearity γ can be described as $\gamma = \frac{\omega n_2 a \Gamma_V}{cV} \cdot \left(\frac{n_g}{n_{Si}}\right)^2$, in which n_2, a and $\frac{a\Gamma_V}{V}$ are the nonlinear refractive index, period of subwavelength structured waveguide and effective area of nonlinearity, respectively. By doing the 3D power integral in a single unit cell of [178, 179], we can obtain an energy confinement factor (energy confined in silicon) Γ_V of 0.87, 0.816 and 0.68 for the idler, pump and signal waves, respectively. With the parameters provided above and $n_2 = 2.8 \times 10^{-18}(m^2/W)$ [43], an effective nonlinear Kerr nonlinearity γ of 65 $(m \cdot W)^{-1}$ and therefore a nonlinear phase item $2\gamma P_P$ of 130 m^{-1} can be deduced. Inter-modal electric-field overlaps are verified as well by calculating the 3D integral $\frac{\iiint E_{yS} \cdot E_{yP} \cdot E_{yP}^* \cdot E_{yI}^* dr^3}{\iiint |E_{yP}|^2 dr^3 \sqrt{\iiint |E_{yS}|^2 dr^3} \cdot \sqrt{\iiint |E_{yI}|^2 dr^3}}$ in a single

unit cell [180], which gives a value of 0.12, E_{yS}, E_{yP} and E_{yI} corresponding to the field of signal, pump, and idler waves, respectively.

An important consideration is to discuss the tunability operation of the designed multimode waveguide, for which $1/V_g$, i. e. $\frac{dk_z}{d\omega}$, of the first 3 modes is shown in Figure 57 (c) and Figure 57 (b), V_g being the mode group velocity. As it is well known, the 3dB bandwidth of the FWM process can be described as $|\Delta k|L_{wg} = \Delta\omega_t(\frac{1}{V_{g2}} - \frac{1}{V_{g0}})L_{wg} < \pi$, in which L is the waveguide length. With a value of 0.07×10^{-8} (s/m) for $(\frac{1}{V_{g2}} - \frac{1}{V_{g0}})$ obtained from Figure 57 (b), we can predict an 3dB tunable bandwidth of around 1THz (~10nm) for a 1mm long waveguide, V_{g2} and V_{g0} corresponding to the second and fundamental modes, respectively.
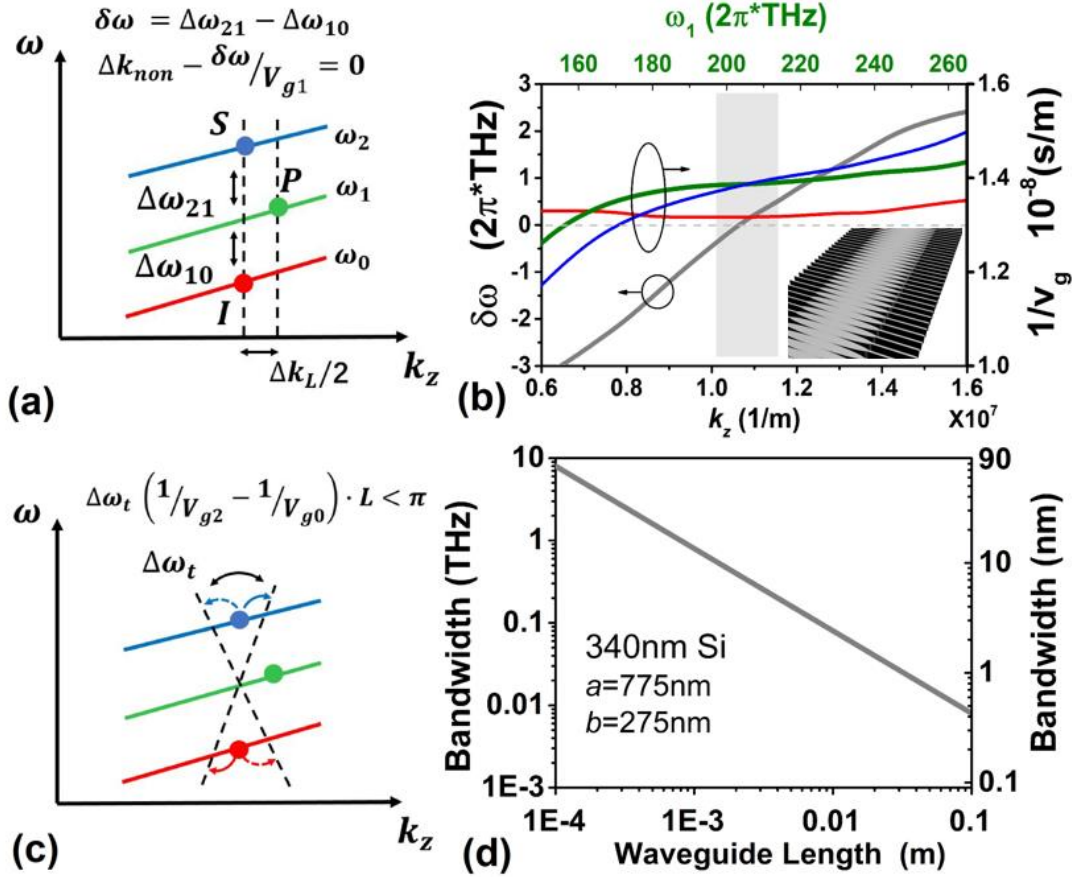
Figure 57. (a) Schematic of the proposed subwavelength structured waveguide for the simultaneous energy conservation and wavevector phase matching under the effect of a nonlinear effect. (b) The difference between frequency spacings $\delta\omega = \Delta\omega_{21} - \Delta\omega_{10}$ as a function of wavevector corresponds to the left axis. On the right side are the reciprocals of the group velocity of the first 3 modes. The working range is labelled by the gray region. (c) Schematic of using the proposed subwavelength structured waveguide for tunable four-wave mixing. (d) The tunable band width as a function of the waveguide length.

By generalizing this approach, the 3dB tunable bandwidth as a function of waveguide length was calculated and is plotted in Figure 57 (d). It can be seen that even in a non-fully-optimized waveguide, **the spectral operating band of the FWM process is as wide as few tens of nanometers for SOI sub-millimeter long waveguides**.

Additionally, we can easily adopt this approach to any other platforms, no matter what kinds of dispersion the waveguide modes exhibit. As an illustrative example of the highly adaptable nature of the method to different platforms with different thicknesses, targeting different frequency ranges, we have investigated its application to different situations. We have calculated the dispersion curves for Si sub-wavelength waveguides with Si thicknesses ranging between 220nm and 600nm. For the 220nm-thick Si waveguide with parameters a=700nm, b=300nm, the

optimized position for $\Delta\omega_{21}=\Delta\omega_{10}$ is located at wavevector around $k_z = 0.95 \times 10^7$ m-1, leading to a conversion span from 220 THz to 180 THz, as shown in Figure 58 (a). By raising a and reducing b to 750nm and 250 nm, we have been able to shift the optimized position continuously to $k_z = 1.53 \times 10^7$ m^{-1}, with starting and stop frequencies of 280 THz to 245 THz, respectively as shown in Figure 58 (b). In order to push the operating point to a lower frequency, with the purpose of generating light wavelengths up to $2\mu m$, larger waveguide cross-sections can be considered. Very interestingly, by simply enlarging the thickness to 600nm, the working frequency for the fundamental mode can be shifted to around 155THz, with conversion span over 40THz (from 1.53µm to 1.93µm, i.e. 400 nm), as shown in Figure 58 (c), with almost no displacement on k_z. Similar result can also be observed in another configuration (a=750nm, b=250nm), with a slightly shifted working point k_z (Figure 58 (d)). These gathered results unambiguously show the **simplicity and flexibility of our approach for degenerate four-wave mixing**, i. e., **1) for each waveguide thickness the waveguide is capable to offer adjustable working conditions in a wide frequency range, within a varying index-profile; 2) for a certain optimal lineshape, the strategy for shifting the working wavelength is simply to adjust the thin film slab thickness.** The flexibility pointed out here can be seamlessly adapted to different technology platforms. This strategy opens a new design space for versatile on-chip nonlinear applications can be adapted to different wavelength ranges and material platforms.
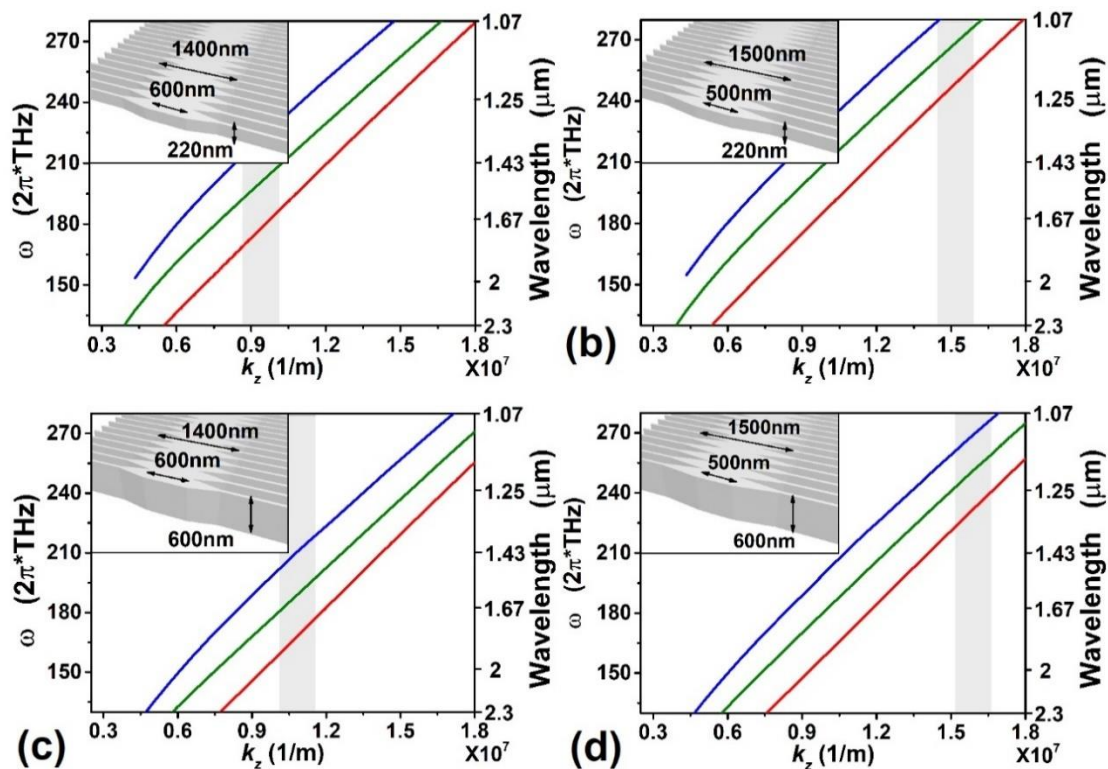
Figure **58.** (a), (b) Dispersion curves of first 3 modes in SWG waveguide with different lengths a, b and linear strategy ($order = 1$) and 220nm Si thickness. (c) and (d) Dispersion curves with same

strategy but with 600nm Si thickness. The working points at which energy conservation and phase matching is satisfied, is labelled by grey regions.

Overall, we foresee that the self-adaptive boundary concept will favor the development of a new generation of on-chip nonlinear circuits with an immense potential for light generation at mid-infrared wavelength, but also for nonlinear processes beyond FWM and applications in which dispersion manipulation is of major relevance. In the following section, this spirit will be embodied in the compensation of the dispersion on the request of frequency comb based cascaded FWM.

3.3 Frequency comb with SAB waveguides: towards controllable light sources

Controlling the dispersion relationship of optical waveguides is a very important preliminary step for the exploitation of third-order non-linear optical processes. This very important preliminary step leads to the exploitation of integrated non-linear functions. The generation of frequency micro combs is one of the main ones.

Consisting in discrete and equally spaced frequency lines spectra, frequency combs can be generated by different mechanisms, including periodic modulation (in amplitude and/or phase) of a continuous-wave laser, four-wave mixing in nonlinear media, or stabilization of the pulse train generated by a mode-locked laser. Since early research devoted to frequency comb generation [181] huge attention has been paid on this topic within the photonic community. In the last 10 years, much work has been devoted to the frequency combs, especially those based on the nonlinear Kerr gain (i.e. cascaded FWM) in dielectric media. As an elegant research field, frequency comb is expected as a strong candidate for novel on-chip silicon light sources [47], and provides a strong basis for many applications in on-chip spectroscopy [182], as well as novel research axes such as time-space-frequency mapping.

3.3.1 Issues in dispersion control for silicon frequency comb

Corresponding to dissipative Kerr soliton generation [183], soliton frequency combs strongly rely on the precise control on the dispersion and nonlinearity, gain and loss on optical waveguides. To balance the nonlinearities-induced phase mismatch, overall anomalous dispersion is generally expected, which can be supported directly from the materials (e.g. silica at telecom wavelengths) or induced by the waveguide dispersion with well-designed waveguide cross-sections. As a result, toroidal-shape cavities using silica [184] or MgF_2 [185, 186] are frequently used for frequency comb generation due to the high Q factor of up to few millions and low dispersion of these structures. Another classical material used for frequency comb demonstrations is

silicon nitride (SiN). Due to the high quality factor of ~ million and a much higher nonlinear index (SiN: $n_2 \approx 2.4 \times 10^{-19} m^2/W$, MgF$_2$: $n_2 \approx 1.5 \times 10^{-20} m^2/W$), high-performance frequency combs can be achieved on chip [187] and even integrated with commercial III-V integrated lasers [188]. Though silicon nitride presents normal material dispersion at around ~$1.5\mu m$ wavelength, its high enough index contrast with SiO$_2$ allows it to generate small anomalous dispersion to compensate nonlinear-induced phase mismatch. A typical spectrum of an on-chip SiN-based frequency comb is shown in Figure 59 (a). As displayed in Figure 59 (b), anomalous dispersion for broadband comb spectrum can be controlled by properly choosing the waveguide cross-section. Once the pump wavelength is chosen, the anomalous dispersion ($D > 0$) can be created by increasing the waveguide height and later be flattened with larger and larger widths. In the meanwhile, the peak position of the parabolic shape dispersion curve is then red shifted.

The dispersion parameter (D) that is related to the group velocity dispersion (GVD) is defined as:

$$D_\lambda = \frac{\partial}{\partial\lambda}\frac{1}{V_g} = -\frac{2\pi c}{\lambda^2} \cdot GVD = -\frac{2\pi c}{\lambda^2} \cdot \frac{\partial^2 k_z}{\partial\omega^2} \tag{3.24}$$

which can be written in an equivalent way as:

$$D_\omega = -\frac{\omega^2}{2\pi c} \cdot \frac{\partial^2 k_z}{\partial\omega^2} \tag{3.25}$$

where $\frac{d^2k}{d\omega^2} < 0$ or $D > 0$ corresponds to anomalous dispersion while $\frac{d^2k}{d\omega^2} > 0$ and $D < 0$ stands for normal one.
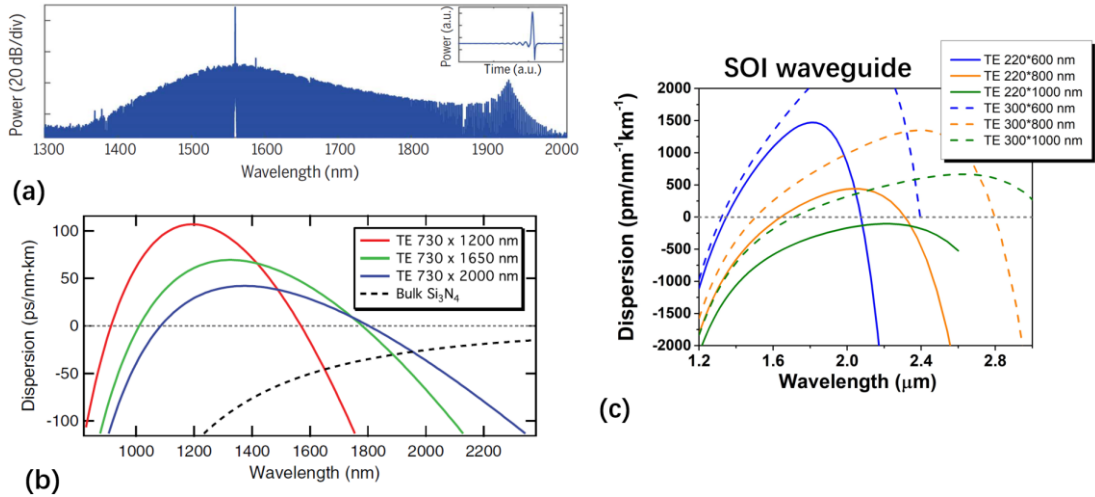
Figure 59. (a) Spectrum of a frequency comb running in silicon nitride ring resonator. (b) Dispersion curves of silicon nitride waveguide with different cross-section. Figures are reproduced from [183] and [76], respectively. (c) Dispersion curves of silicon-on-insulator waveguide with different cross-section.

Using equation 3.24, we can calculate the *D* parameter of SOI waveguides with different dimensions, as shown in Figure 59 (c). Absolute values and peak positions are controlled by the height and width of the waveguides, and it turns that dispersion curves rapidly change from negative to positive regions due to the high index contrast of SOI waveguides. To obtain a small anomalous dispersion region needed to phase matching purpose, waveguide dimensions need to be very carefully controlled or external materials should be used for dispersion compensation but these two approaches are neither easy to perform nor fully satisfying [180].

A flexible method to flatten silicon waveguide dispersion for frequency comb generation is thus highly expected. A strong interest is to explore how the dispersion shape influence the bandwidth and other properties of the comb spectrum, especially in situations when a target wavelength operation is provided in advance. The next sections of this chapter seek to address these questions and provide at least partial answers.

3.3.2 Dynamics of the soliton frequency comb

Before the introducing the SAB to trim the comb spectrum, dynamics and generation of soliton frequency comb need to be clarified. The propagation of short light pulses in waveguides has been extensively described in the literature, starting with fibers [182] and then, for more than 10 years, in the higher contrast index waveguides of integrated photonics, particularly in silicon photonics [183]. We refer the reader to **our Appendix A3 - Nonlinear Schrödinger equation in micro-ring resonator** and **Appendix A4 - Modeling the soliton frequency comb** for more details. In summary, the propagation of pulses in a waveguide with effective third order non-linearity results in a non-linear equation, often referred to as a ***non-linear Schrödinger equation*** (**NLSE, Appendix A3**):

$$\frac{\partial}{\partial z} A(z, \tau) = \left[i \sum_{k=2}^{n} \frac{\beta_k}{k!} \left(i \frac{\partial^k}{\partial \tau^k} \right) + i\gamma |A(z, \tau)|^2 - \frac{\alpha}{2} \right] A(z, \tau) \qquad (3.26)$$

Where $A(z, \tau)$ is the pulse amplitude described by the circumferential position z and the time variable τ that corresponding to a relative time frame. β_k, γ and α is the group velocity dispersion, Kerr nonlinear parameter and waveguide loss, respectively. The generation of frequency combs using ring microresonators is traditionally done from the configuration shown in Figure 60.
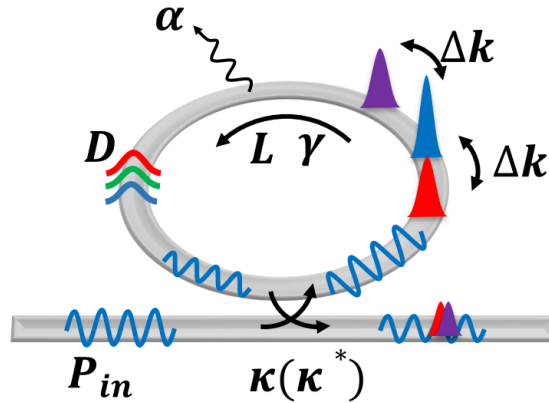
Figure 60. Schematic of the nonlinear ring-based frequency comb system.

A narrow spectrum continuous optical source (laser) is centered on an optical resonance of the ring resonator. If the chromatic dispersion of the ring is well chosen, it can result in a cascade of FWM processes in the frequency domain, which leads to the generation of a frequency comb. From a temporal point of view, the generation of such a broad-spectrum comb corresponds to a regime of short solitonic pulses, or even, in the best of cases, to a regime of mono-soliton propagation in the ring. The interpretation of comb generation gives us nontrivial instruction on designing the comb spectrum. In relation to what has been said above concerning the Schrödinger equation, the periodic injection of energy into the ring must be described, as well as the fact that the guide no longer has an indefinite length but is looped back on itself. This mainly results in a change in the boundary conditions of the Schrödinger equation. Another particularity also concerns the time scales of phenomena. In most of situations, the temporal dynamics of temporal soliton excitation is much slower than the characteristic time required for a pulse to complete a full rotation of the ring. As a result, the temporal problem can be decoupled according to these two-time scales, which leads to a considerable simplification of the problem to be solved. We refer the interested reader to **Appendix A3 - Nonlinear Schrödinger equation in micro-ring resonator** for further details and provide here only a brief summary of the main conclusions.

The overall process of comb generation [185, 189, A1-A12] is systematically discussed in **Appendix A4 - Modeling the soliton frequency comb** and briefly schematized in Figure 61.

At the beginning, the cavity detuning from the resonance is set at zero and it shifts away from the pump due to the Kerr effect as energy builds up within the ring. The anomalous dispersion allows modulation instability (MI) to generate the first comb lines in a degenerate FWM process from the driven mode to the primary offset symmetrically placed as soon as the parametric gain overcomes the loss of the cavity (Figure 61 (a)). The distance (in terms of relative mode number *m*) of the new lines to the pump depends on the pump power and the dispersion of the resonator, the

nonlinear phase (thus wavelength) shift (via self- and cross-phase modulation), and the pump laser detuning compensates one another. This stage consists of the formation of multiple stable cavity solitons. Further build-up of power then causes cascaded four-wave mixing (FWM) of these MI peaks within the anomalous dispersion region, which transfers the initial parametric amplification process to all emerging higher-order sidebands with the initial spacing frequency spacing due to the conservation of energy and momentum in parametric processes.
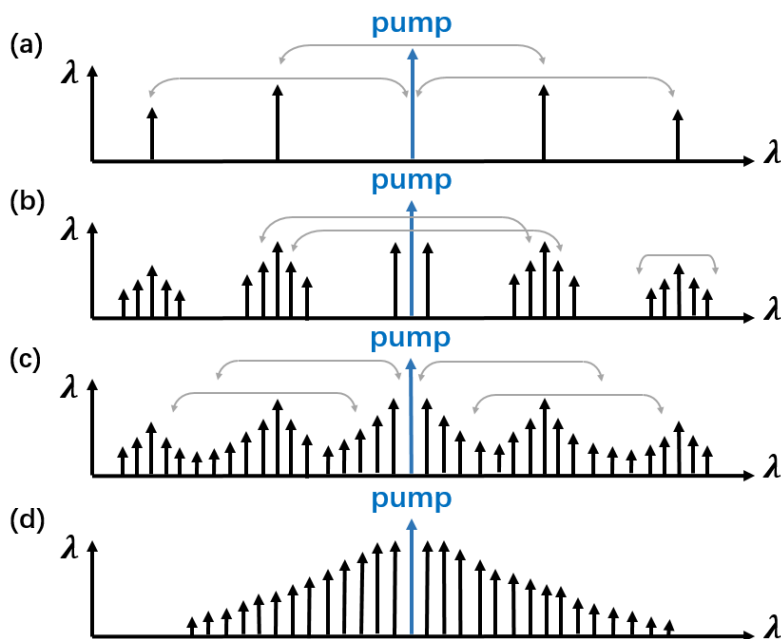
Figure 61. Sketch of a frequency comb formation based on a Kerr-enhanced resonator.

With the increased circulating power, the overall relative detuning is reduced, where secondary lines are generated adjacent to the primary lines via both degenerate or non-degenerate FWM processes (Figure 61 b). Modes adjacent to these primary modes created previously also experience MI from the pumped mode. Bundles of other combinations of FMW processes based on these secondary frequency lines give birth to the generation of sub-combs as soon as phase matching is satisfied with increased intracavity power (Figure 61 (c)). Continuously, as soon as the sub-combs overlaps one another, the spectrum gap may eventually be filled with the later contribution of multiple parametric gain process. In the meanwhile, the temporal characteristics change dramatically, forming stable cavity solitons with initial mode locking.

Later, the pump is tuned further closer to the Kerr-shifted resonance, the intracavity power increases, and the multi-pulse mode locking is lost due to instability of the cavity solitons. The pulses exhibit periodic amplitude fluctuations, interacting with each other causing destabilization resulting in the scene of random pulses circulating in the cavity. Further detuning of the pump leads to the surpassing over the Kerr-shifted resonance. This "*slightly red off-resonant*" step causes the drop of the

intracavity power, and mode locking is again established with non-periodic multiple cavity solitons formed inside. In the meanwhile, the bandwidth is also chopped a little and determined jointly with the lower intracavity power and phase locking. The frequency comb has decreased slightly in both total power and bandwidth.

Depending on the precise pump power and wavelength detuning conditions, a single-soliton solution can satisfy in some cases the **mean-field Lugiato-Lefever equation (LLE, Appendix A4)**, then featuring a pulse shape approximately described by equation (A4.16). Very Fine pump detuning is required for the dynamics to evolve to a single pulse by killing the others. The vanishing of the beat note of a multiple stable soliton is followed by the slight drop of the intracavity power. The remaining intracavity power with single soliton can be increased to higher power again.

Based on this process, we use a silicon nitride ring as an example to show the full dynamics, as shown in Figure 62. In this example, Q factor of 10^5, nonlinear parameter and $\gamma = 1 m^{-1} W^{-1}$, roundtrip loss of $\alpha_L = 0.012$, roundtrip length $L = 314 \mu m$, $\beta_k = -50 ps^2/km$ corresponding to a silicon nitride resonator is considered. The input power is set at 1.5W. In Figure 62, stage I corresponds to an initial blue-detuning stage where only the pump signal can survive in the cavity. With increasing the detuning increase from blue (negative) to red (positive), the intracavity power starts to increase, the overall phase matching is fulfilled for Kerr gain. Primary frequency lines and therefore sub-combs can be observed (stage II), then followed by the **first mode-locking** process with equally-spaced multiple solitons (stage III). Modulation instability caused by the high Kerr gain of the overlapped sub combs (stage IV) is observed with chaotic temporal solitonic effects, which tend to extend the existing sub-combs with increased coupled power.
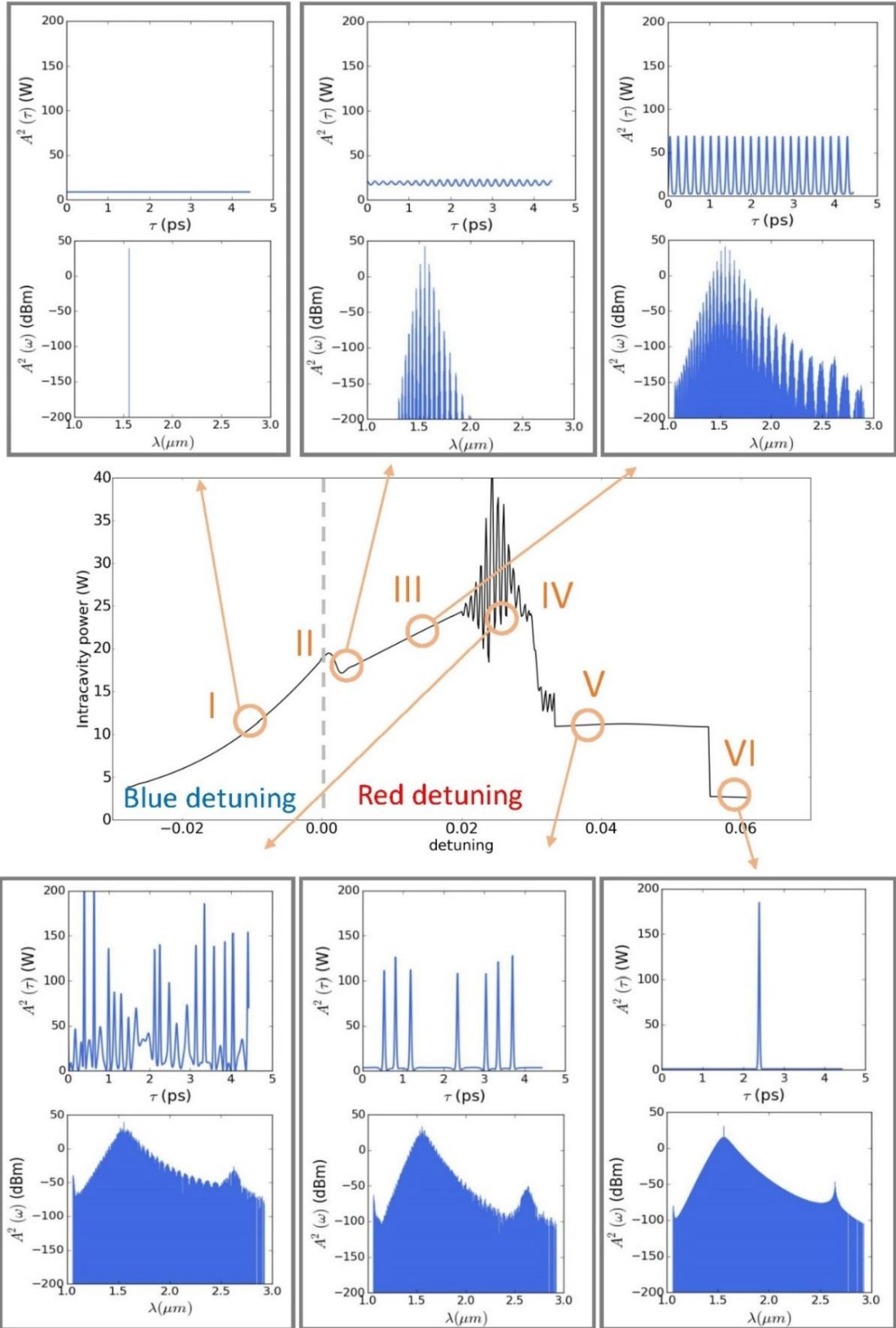
Figure 62. Dynamics of comb generation based on our modeling. In this example, a Q factor of 10^5, nonlinear parameter and $\gamma = 1m^{-1}W^{-1}$, roundtrip loss of $\alpha_L = 0.012$, roundtrip length $L = 314\mu m$, $\beta_k = -50ps^2/km$ corresponding to a silicon nitride resonator is considered. The input power is set at

1.5W. Typically, in the stage Typically, we see in stage IV strong fluctuations of the intracavity power due to the bi-stability behavior of the nonlinear ring cavity, as investigated earlier [190].

The intracavity power can be then described by:

$$P_{\text{in}} \cdot \frac{\gamma_t^2}{(\omega_0 - \Delta\omega_0 - \omega)^2 + \gamma_t^2} \cdot \left(n_2 \frac{V}{L_{\text{cav}}} \cdot \frac{L_{\text{cav}}}{m \cdot N_g} + n_T \frac{K}{V} \right) = \frac{C2\pi}{\omega_0 - \Delta\omega_0 - \omega} \tag{3.27}$$

, where $P_{\text{in}} \cdot \frac{\gamma_t^2}{(\omega_0 - \omega)^2 + \gamma_t^2}$ is the intracavity power and $n_2 \frac{V}{L_{\text{cav}}} \cdot \frac{L_{\text{cav}}}{m \cdot N_g}$ is Kerr wavelength shift per power. V is the cavity volume and KV gives the thermal wavelength shift per unit power. $\frac{C2\pi}{\omega_0 - \Delta\omega_0 - \omega}$ is the overall wavelength detuning of the pump. Two solutions $(\Delta\omega_0)$ can satisfy equation 3.27 with $\omega_0 > \omega$, corresponding to a small $\Delta\omega_0$ with a small intracavity power and a large $\Delta\omega_0$ with large intracavity power, respectively (blue-detuned input is unable here to make enough power for a full comb).

Next, stage V corresponds to a stable multiple-soliton state where **second mode-locking** and over detuning (**slightly red off-resonant)** occur. Sharp intra-cavity power drop is observed from stage IV to V. In stage VI, single soliton is observed with further detuning, at a cost of another power drop and the vanishing of other solitons.
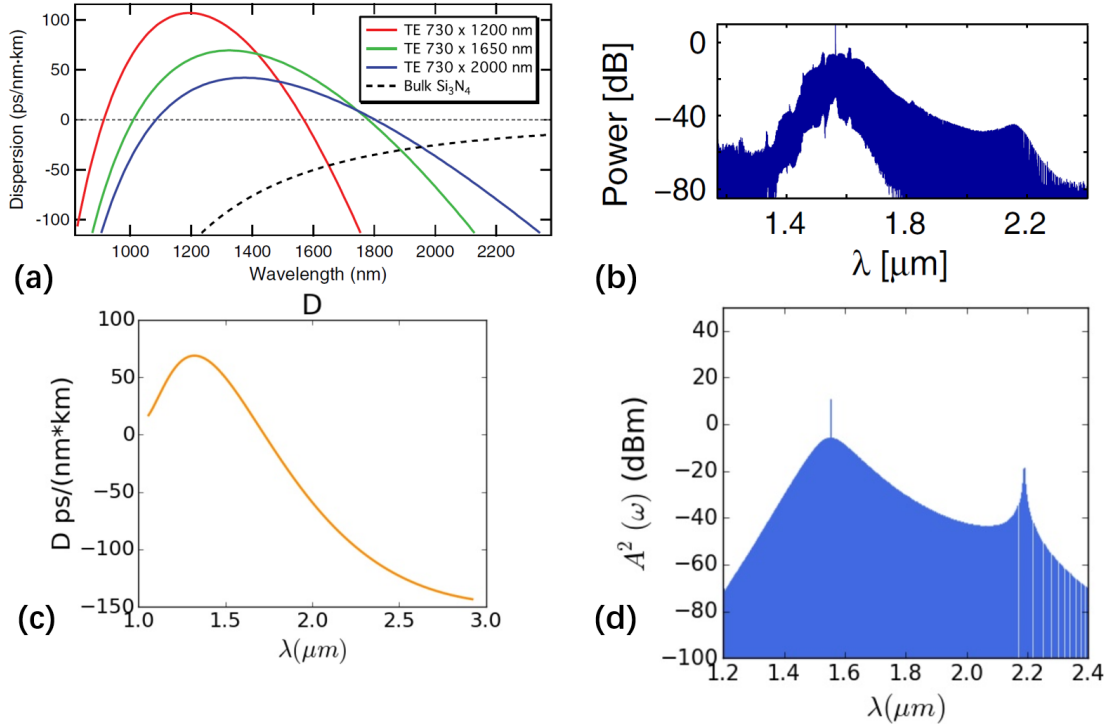
Figure 63. (a) dispersion (green line is experimentally used) and (b) experimental comb spectrum generated in a silicon nitride ring resonator, from [191]. (c) A recovered dispersion and (d) spectrum of a single soliton state of frequency comb based on the same parameters.

To further validate the applicability of our model, we benchmarked with respect to experimental works [191]. The dispersion of the silicon nitride waveguide thy used in this work (green line) is shown in Figure 63 (a), corresponding to an experimental comb spectrum in Figure 63 (b).

With a recovered dispersion that in shown in Figure 63 (c) and parameters (including Q factor, FSR, pump power) from [191], we achieve a single-soliton spectrum of frequency comb (Figure 63 (d)) using the comb generation model described above. Clearly, good coincidence is found in both the power level and the bandwidth. Based on this evidence, we are able to say that we have validated our model is capable to describe and be used to explore new theoretical work. In the following section, using this model, we will explore the silicon frequency comb and introduce our improvements for addressing several drawbacks of silicon frequency combs.

In summary, the ***dynamics of frequency comb generation is very complex*** and relies on very precise control of the chromatic dispersion of the waveguides and on precise experimental conditions (tunability of the pump signal in power and wavelength detuning). ***We have developed a programming code to generate and predict this type of phenomenon***. This code has been accurately calibrated by reproducing results from the literature [191, 184-187]. ***In the rest of this chapter, we describe our efforts to design frequency micro-comb engineering by freeing ourselves from two-photon absorption in silicon (by working beyond 2µm wavelengths) and using the SAB waveguides described at the beginning of this chapter***, i. e. specially designed to meet the phase matching conditions of FWM processes.

3.3.3   Reshaping silicon frequency combs with SAB engineered waveguides

In the rest of this chapter, we describe our efforts to design frequency micro-comb engineering by freeing ourselves from two-photon absorption in silicon (by working beyond 2µm wavelengths) and using the SAB waveguides described at the beginning of this chapter, i. e. specially designed to meet the phase matching conditions of FWM processes. To initially launch a silicon frequency comb, pump wavelength is chosen at around $\lambda = 2\mu m$ and an overall moderate waveguide loss of 4dB is considered. The dimensions of the silicon on insulator (SOI) wafer used here are 220nm and 800nm for height and width, as shown in Figure 64.

The waveguide dispersion curve was previously shown in Figure 59 (b) (yellow line) and redisplayed again in Figure 65 (a), where a peak value of chromatic dispersion around $D = 350\,pm/(nm*km)$ is found. The corresponding group velocity dispersion is shown in Figure 65 (b). An underestimated nonlinear gain coefficient of $\gamma = 30(m \cdot W)^{-1}$ is considered for interrogating the other parameters, especially the pump power. A coupling coefficient of 0.01 (working in under coupling) and 150mW pump power (in bus waveguide) are chosen, respectively to overwhelm

the losses. A free spectrum range of 0.23 THz corresponding to a ring radius of $50\mu m$ is chosen to build a moving frame with roundtrip time of $4.35\ ps$.

$$\gamma = 30\ (m \cdot W)^{-1}$$
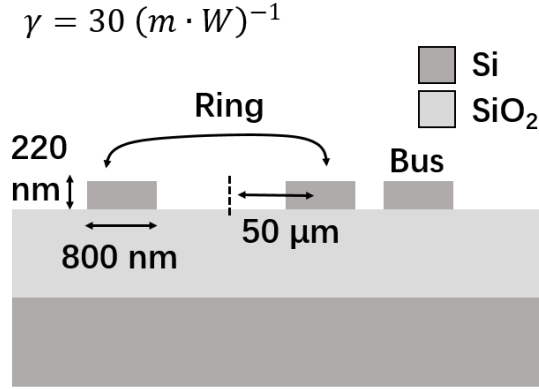
Figure 64. Cross-section of the silicon ring used for comb modeling.
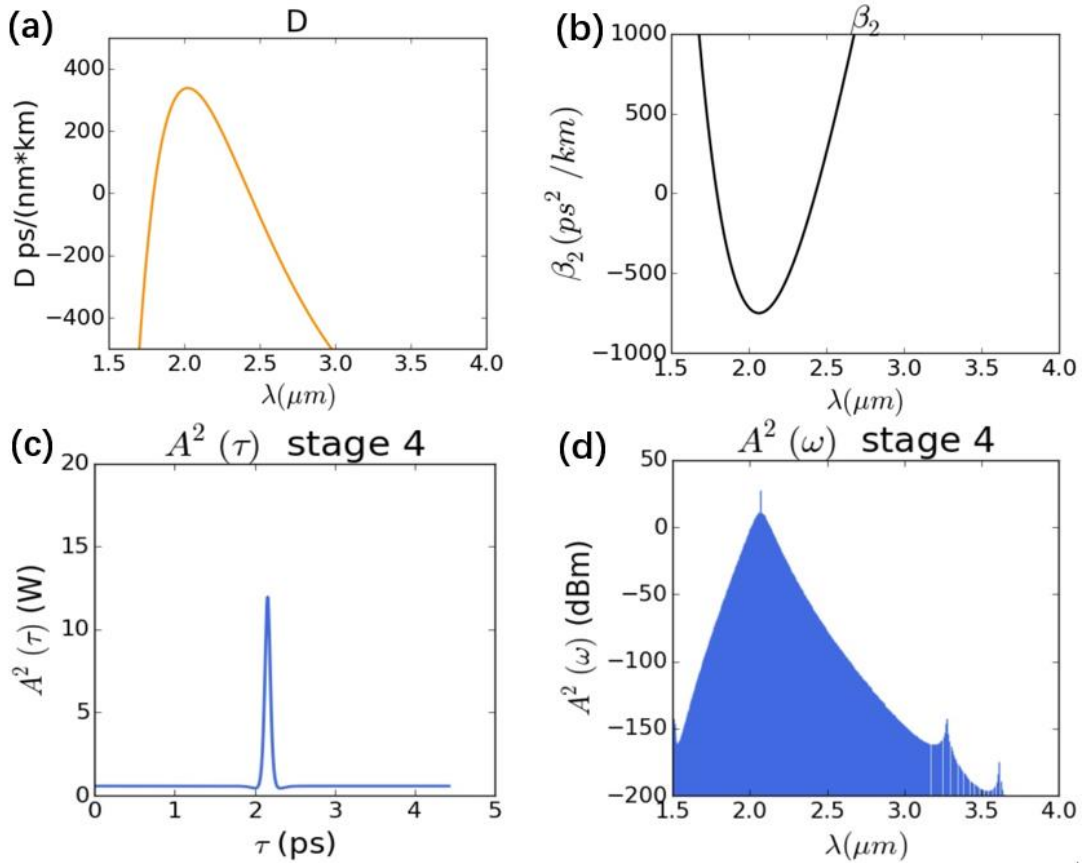
Figure 65. (a) Dispersion and (b) Group velocity dispersion of the SOI waveguide that shown in Figure 64. (c) Final soliton stage and (d) Corresponding soliton frequency comb.

Using the model described above, we achieved a single-soliton silicon frequency comb with intracavity pulse shape shown in Figure 65 (c). Compared to the intracavity pulse in the silicon nitride configuration shown in Figure 62, the intracavity energy inside silicon is almost 10-folds lower due to the much higher gain factor (from 1 to $30(m \cdot W)^{-1}$), which means that much less power is now required

to overwhelm propagation losses. This is also a strong point and original interest of using the silicon platform to achieve frequency combs. However, **it can be seen in Figure 65 (d) that, due to the much higher waveguide dispersion, the bandwidth of the silicon frequency comb is much worse than the one of silicon nitride**.

To summarize the current point of our discussion, it appears that by moving from Si_3N_4 to SOI waveguides, an advantage (lower pump power) and a drawback (reduced frequency comb spectral width) result simultaneously. Consequently, addressing the problem of the spectral width of µ-combs is an important point, naturally aiming to increase it by using waveguides with a particular chromatic dispersion profile.

To understand the bandwidth issue, we come back here to simulation results. In Figure 66 (a), the slightly red tuning gives birth to a situation where FWM parametric gain overwhelms the overall loss level. The first primary frequencies generated by DFWM, as in Figure 66 (a), are located very closely to the pump line. These primary lines are actually the pre-representation of the comb bandwidth since the following cascaded FWM and mode locking processes all originate from there. A snapshot of the separated sub combs that result from sufficient cascaded FWM mixing processes is shown in Figure 66 (b).
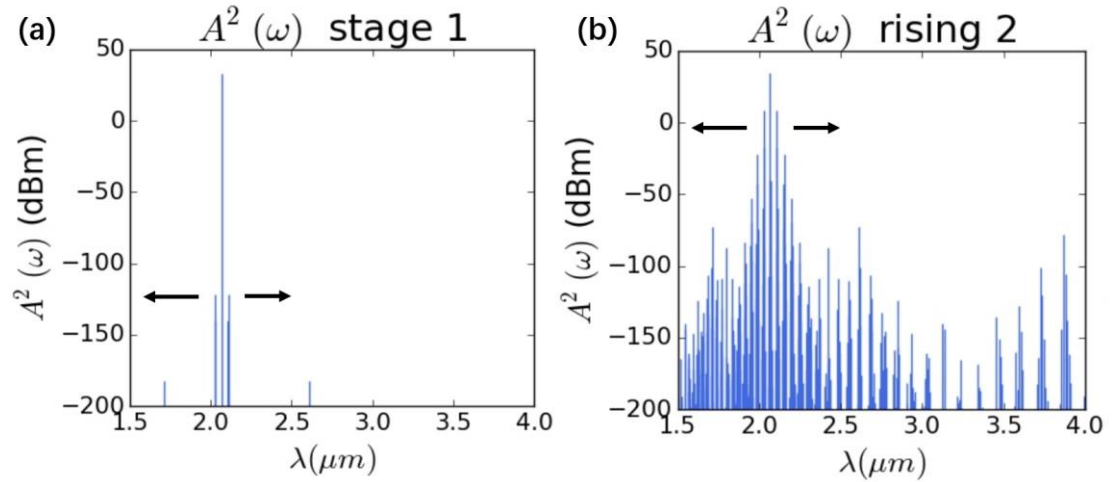
Figure 66. (a) Snapshot of the generation of primary frequency lines due to the degenerate four-wave mixing. (b) A later snapshot where multi frequency lines by are generated by cascaded four wave mixing.

Due to the strong dispersion D, FWMs are limited to small range according to phase matching. According to equation Appendix (A4.10), phase mismatching can be considered as:

$$\Delta k = 2\gamma P_{in} - D \frac{\lambda^2}{2\pi c} \cdot (nFSR_\omega)^2 = 2\gamma P_{in} - D2\pi c \cdot (\frac{n\lambda}{n_g L})^2 \tag{3.28}$$

for degenerate FWM with three waves spaced by one FSR ($n = 1$), the pump power for phase matching (following the same configuration, $\lambda = 2.1\mu m$, ring $L = 314\mu m$ and $\gamma = 30 m^{-1}W^{-1}$) is 27.8mW. In another words, for a pump power that we use (150mW), the phase matching occurs at the frequency lines of 2.8 FSR from pump,

which is coincident to what we observe in Figure 66 (a). So very straightforwardly, if we want to move the primary frequency lines to a further place for extending the bandwidth (black arrows in Figure 66), a much stronger power, which responds to the square-order growth of FSR number n, is needed to compensate the dispersion. This high power is way wasting since it i's far overwheled by optical losses and not accesible. On the contrary, it is very significant and interesting to reduce and flatten the dispersion D globally while keeping the other parameters fixed (γ, P_{in} etc.).

Flattened dispersion (SAB) waveguides:

With this objective in mind, we have endeavored to explore the use of SAB waveguides, whose dispersion properties have proven to be adapted to the problem of μ-combs. Figure 67 shows two types of waveguides with Self-Adaption Boundary condition $n_{eff} > n_b$, i.e. continuously graded-index waveguide (Figure 67 (a)) and discretely graded-index waveguides (Figure 67 (c)), in single-mode operation.

The structure of the continuously graded-index waveguide is shown in the inset of Figure 67 (b). The period thickness and width are chosen at 150nm, 340nm and 800nm, with a filling factor linearly tapered from center to edge. Dispersion of a strip waveguide and SAB waveguide with $n_b \approx 1.5$ and $n_b \approx 2.8$ is plotted in Figure 67 (b) for comparison. The SAB allow us to trim the dispersion of the "long" wavelength where $n_{eff} < n_b$. This is because the wave is confined by the index contrast of n_b/n_c and phase integral strongly depends on the index n_b. In contrast, due to the short wavelength ($n_{eff} > n_b$) is confined by the effective width of the waveguide where electric field pass smoothly, the dispersion doesn't vary a lot. In brief, the whole frequency range is separated into two part with diverse response and this allow us to globally reconFigure the dispersion for working point by flattening or steepening the dispersion accordingly. Using the discretely graded-index waveguides shown in Figure 67(c), we can further extend the anomalous dispersion range by locally squeezing a small anomalous dispersion. The bi-level SAB is used for confine separately the "blue" and "red" wavelength. This idea will practically be translated into a waveguide as in Figure 67 (d).

A commercial 340nm SOI platform was chosen to provide sufficient anomalous dispersion in up to $2\mu m$ range. The continuously graded-index waveguide with filling factor values varying from 1 to 0.83 is shown in Figure 68(a). The width of the fixed-index and the taper regions were chosen at 900nm and 240 nm. The whole structure is shown in the inset of Figure 68 (a). Compared to those classical strip/rib waveguides where the dispersion displays normally a parabolic shape, there is more than one peak existing in the center which totally give us a new freedom for the dispersion engineering. Since SAB can reduce the index contrast and dramatically reduce the anomalous dispersion for wavelengths not confined by the outer boundary, the region between two anomalous peaks are seperated by a normal region using bi-level SAB waveguide, as shown in Figure 68(b). In this case, a more appropriate index contrast with filling factor varying from 1 to 0.66 is achieved (dimension of the

waveguide is clarified in the inset). The whole wavelength range from $2.25\mu m$ to $3.25\mu m$ now has been totally flattened. In addition to the bi-level case, tri-level case can be further use to locally engineer the dispersion as in Figure 68 (c). The small ripple, can be eliminated by adjusting the length of each section once filling factor is determined, for instance, from Figure 68 (c) to (d). In a wide wavelength range, the anomalous dispersion can be controlled in very low value, as in Figure 68 (d).
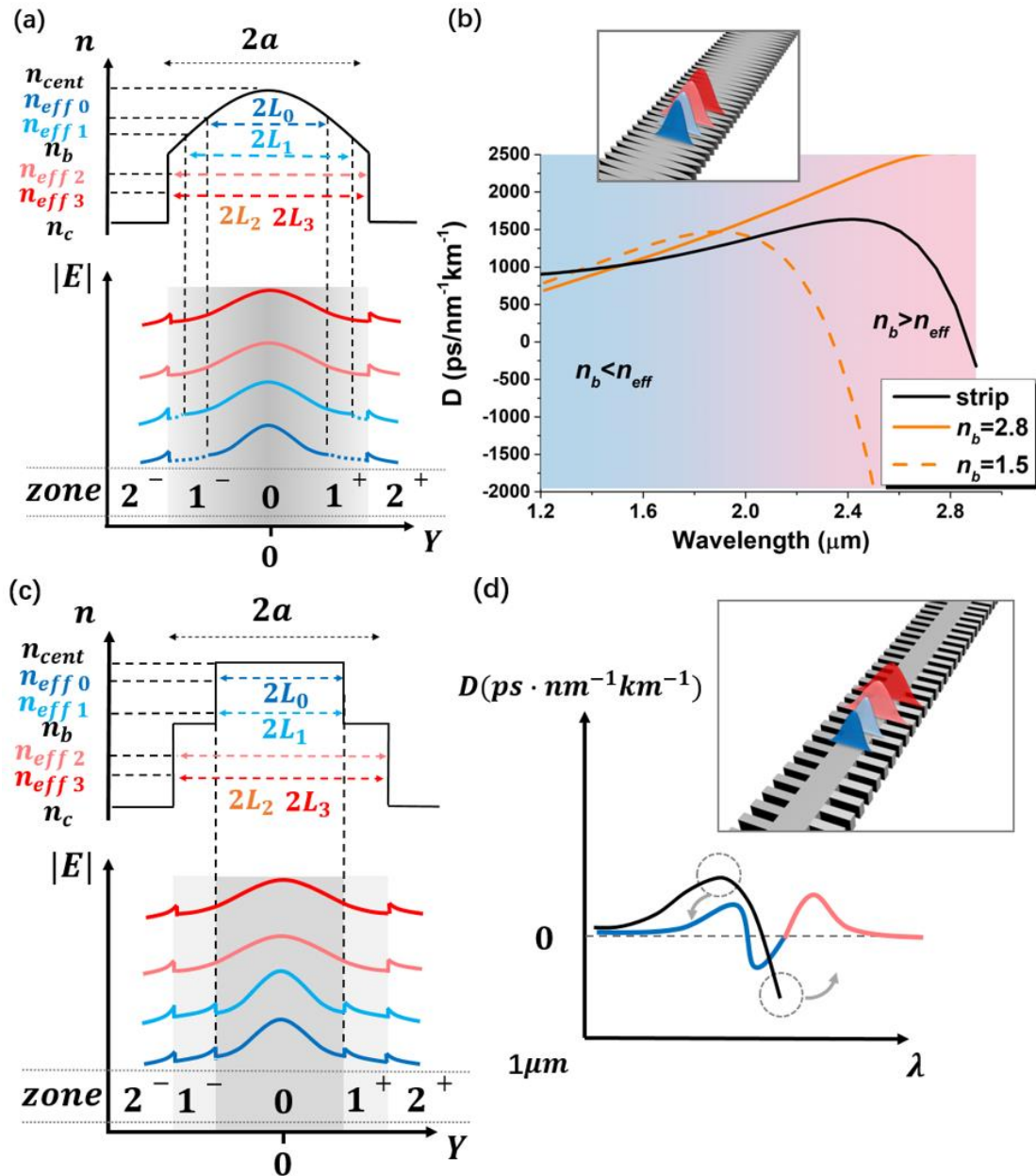
Figure 67. (a) Schematic of a graded-index waveguide with SAB operating in single-mode. (b) Cchromatic dispersion parameter D. Width and height of the waveguide are 750nm and 340nm. (c) Schematic of a bi-level graded-index waveguide with SAB operating in single-mode. (d) Sketch of the chromatic dispersion parameter D. Material dispersion is not considered here ($n = 3.48$).
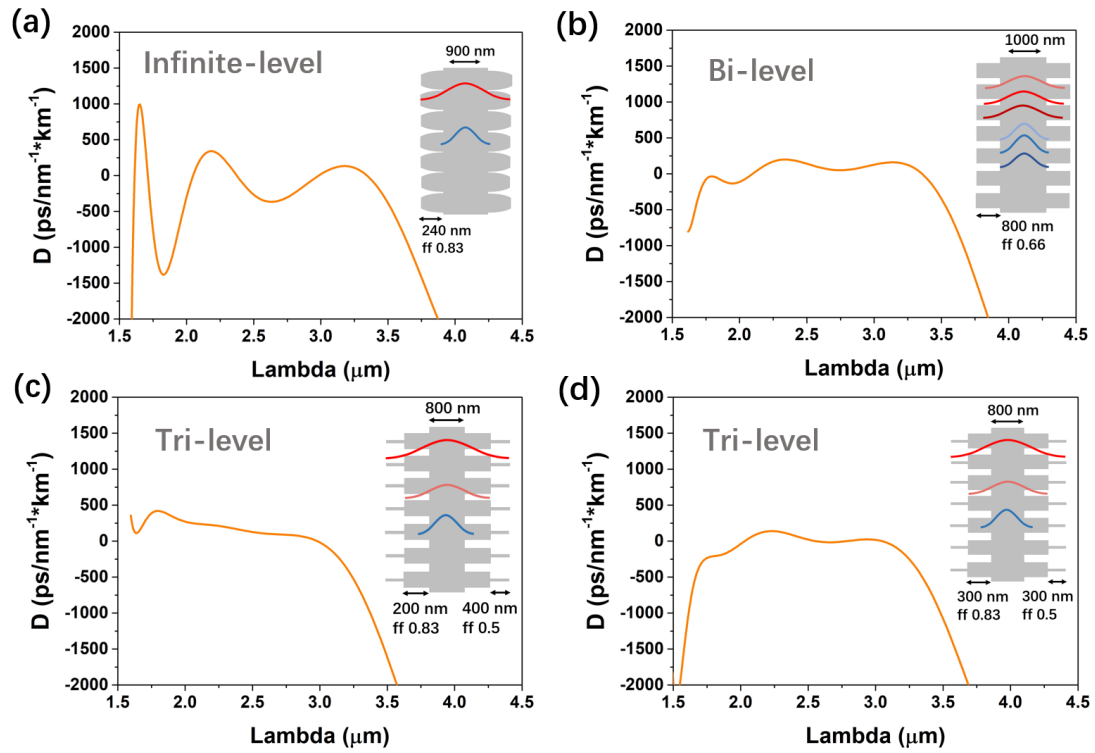
Figure 68. Dispersion of infinite-level (a), bi-level (b) and three tri-level (c) (d) subwavelength structured waveguides. The thickness of silicon and the period are both set at 340nm and 240nm. Other parameters are respectively shown in the insets.

Frequency comb generation with flattened dispersion waveguides:

Frequency comb generation was then considered with the flattened dispersion waveguides shown in Figure 68. Since periodic structures are introduced in this case, extra losses are needed to be taken into account. Though experimental demonstration [192-194] already indicated very promising loss level (smaller than 3dB/cm), we consider here a conservative higher waveguide loss level of 8dB/cm.
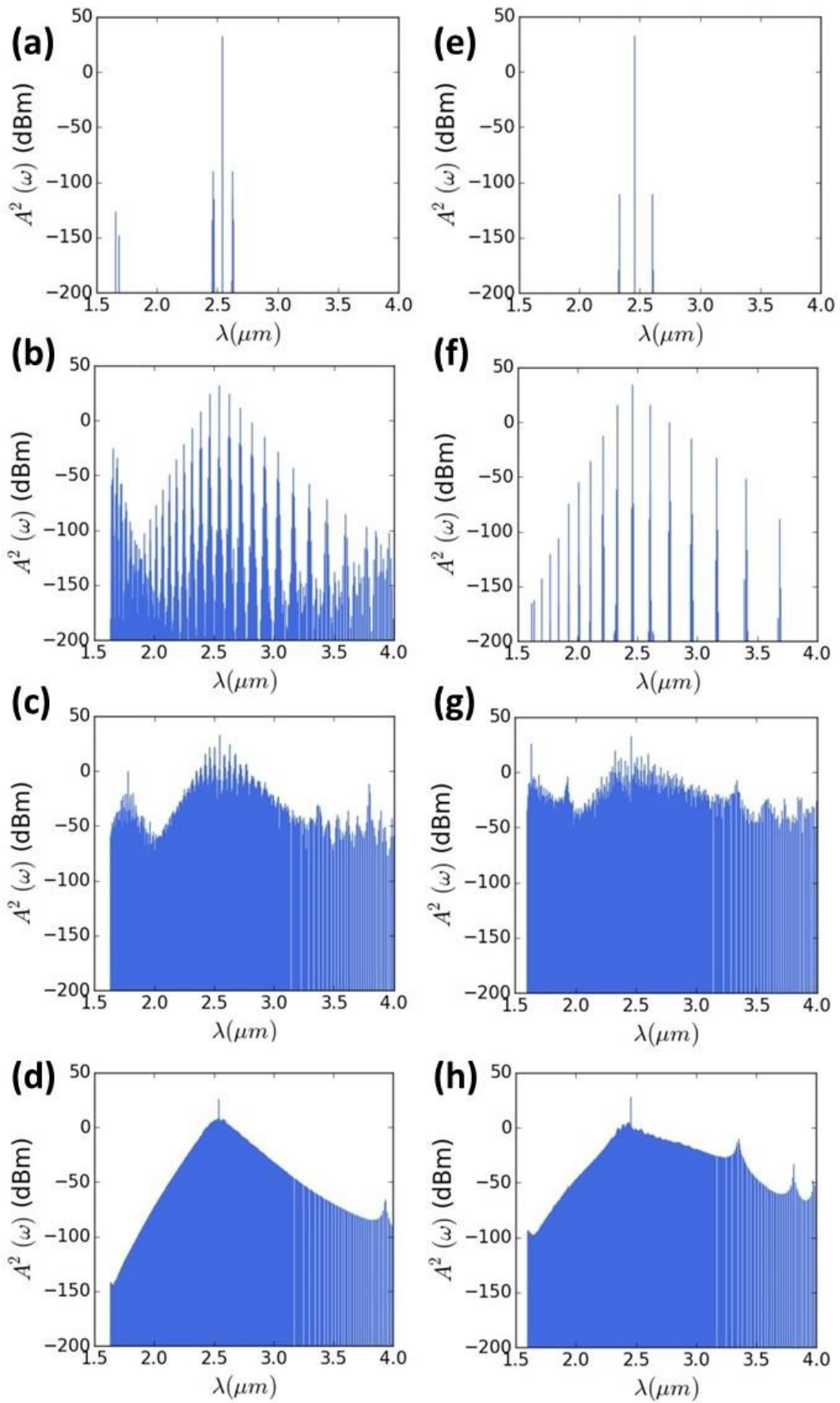
Figure 69. (a) and (e) Snapshot of the generation of primary frequency lines due to the degenerate four-wave mixing, corresponding to dispersion in Figure 68 (b) and 68 (d). (b) and (f) A later snapshot where multi frequency lines by are generated by cascaded four wave mixing, together with mode-locking multi soliton processes. (c) and (g) Multi-nonperiodic-soliton comb stage caused by modulation instability. (d) and (h) corresponding single-soliton frequency comb.

With all the other parameters being fixed (i.e. $p = 150mW$, ring $L = 314\mu m$ and $\gamma = 30m^{-1}W^{-1}$), we use again our model to evaluate the silicon soliton frequency comb with dispersion in Figure 68 (b) and 68 (d), of which the corresponding results are shown in 69 (a)-(d) and 69 (e)-(h), respectively. In Figure 69 (a) and (e), we obtain a new initial comb generation stage, where the primary frequency lines are way farther away from the pump line as compared to Figure 66 (a). The following mode-locking multi-soliton stage with cascaded sub combs is shown in Figure 69 (b) and (f), which is much better than that of 66 (b). There is no doubt that the comb bandwidth in stage of modulation instability and multi-soliton state in Figure 69 (c) and (g) and the final single-soliton frequency comb in Figure 69 (d) and (h) can be similarly broader. Bandwidth improvement is clearly witnessed with the introduction of Self-Adaptive Boundary, based on which the Cherenkov Radiation [195-196] can be further integrated for performance extension.

3.4   Conclusions of this chapter

We have begun this chapter by introducing idea proposal for using Self-Adaptive Boundary (SAB) waveguides to enable inter-mode four-wave mixing processes in a nearly universal phase-matched configuration. The analytical and numerical implementation of this SAB have been investigated. Beyond the concept, we have insisted on the fact that the practical implementation of this idea was based largely on the use of sub-wavelength photonic structures, and showed a number of examples design, based in particular on the SOI waveguides of silicon photonics.

Intuitively, we have noticed the strong potential of this Self-Adaptive Boundary waveguides for third-order nonlinear photonics with a unique capability of dispersion engineering. Driven by this, we have modeled the frequency micro-comb generation process through the resolution of the Nonlinear Schrödinger Equation in µ-rings fed by a continuous wave optical wave (Lugiato-Lefever equation). On top of this model, we indicate the limits especially the bandwidth in the spectrum of silicon-based frequency combs and indicates strong room for improvement that can be accessed with Self-Adaptive Boundary flattened dispersion waveguides. The study of several configurations proved to be very successful, demonstrating the significant widening of the µ-comb frequency spectral band through the use of this family of specific optical waveguides. This work has thus contributed to the development of an original path for the realization of optical frequency combs in the silicon platform beyond 2µm wavelengths, giving access to the whole range of applications of µ-frequency combs, particularly in metrology and on-chip spectroscopy.

4 Conclusions and perspectives

To meet the rapidly increasing demand for optical interconnects, efforts are continuously made to develop low power consumption, tens-to-hundreds-gigabits devices and on-chip light source with CMOS-compatible platform, especially silicon due to its versatility and low production cost. Second-order Pockels effect and the third-order Kerr effect can be exploited for light modulation and generation. To substantially take advantages of these nonlinearities, we have tried to introduce the advantages provided by subwavelength optical structures to explore new on-chip possibilities.

For improving the performance of optical modulators, instead of simply increasing the light-matter interaction by accumulating light power in an optical resonator, we have introduced a background mode into the nanobeam cavity to accelerate the on-off transition of the modulator. This background mode, excited in the high-order mode type and working in the subwavelength region, has been successfully demonstrated to trim the classical Lorentzian line shape in very compact footprint Fano lineshape structures. More than 23 dB extinction ratio is achieved with merely 366pm in nanobeam cavity with Q of merely 5600, which is about 6-fold efficient than the Lorentzian-lineshape resonance with the same Q factor where 1.96nm is needed from the same performance. This superior performance shows strong potential in reducing the power consumption of optical modulators while still leaving big room for high-rate modulation which suffers a lot in Lorentzian cavity from large photon lifetimes. With this robust method, we designed a Fano strained silicon modulator. Compared to the existing work using ultra-long MZI structures where strong radio frequency losses exist in the traveling-wave electrodes, the proposed compact design allows to be integrated with strained process. In the meanwhile, it potentially provides an electrical bandwidth larger than 200 GHz and shows a predicted 60-200 folds improvement on the E-O response (Q ranging from 5600 to 32000). This improvement gives new possibility for strain silicon modulator to run a few-dB extinction with voltages lower than 20V and a moderate Q factor (32000). Higher efficiencies can be further improved by rebalancing the mode ratio according to our Fano model. Though strained silicon platform where the second-order nonlinear effect stays tiny is taken as an example to clarify the merits of this Fano cavity, the generality of reducing the power consumption without sacrificing the modulation rate of modulators is highly expected and could be analogously adopted to other kinds of modulators. For instance, silicon modulators based on carrier depletion effect can present a sub fj/bit power consumption with more 20dB extinction and 30 Gb/s modulation rate based on the proposed subwavelength structured Fano cavity.

For the purpose of providing more flexible satisfaction of momentum conservation and improving the use of silicon Kerr nonlinearities, we have proposed

the use of Self-Adaptive Boundary (SAB) waveguides. The SAB condition has been first designed for automatically fulfilling the energy and momentum conservation laws in the inter-mode four-wave mixing (FWM) process by relying on a close analogy with quantum wells and transposed into silicon waveguide cross-sections with the assistance of subwavelength structures. This waveguide design proved to extend the FWM bandwidth of nonlinear active waveguides for which dispersion can be flexibly adjusted in a wide range.

Standing on the strong potential the capability of this Self-Adaptive Boundary waveguides in engineering the dispersion of optical waveguides, we have considered their use for the generation of Kerr frequency micro-combs. Frequency comb generation in close-loop micro-ring resonators fed by a continuous wave laser has been modeled by solving the relevant nonlinear Schrödinger equation (Lugiato-Lefever) to dynamically analyze the soliton comb spectrum generation in time and frequency. On top of this model, the limits, especially in term of spectrum bandwidth in Si ring resonator micro-combs, have been indicated, and room for improvement that can be accessed with Self-Adaptive Boundary has been highlighted. As a whole, it was shown that SAB-engineered optical waveguides are able to trim and extend the bandwidth of silicon soliton frequency combs

Overall, the main axis we have developed has been to try to show that combining subwavelength optics and nonlinearities can bring a great benefit in terms of lifting design locks of integrated non-linear function designs. This work has thus opened up prospects in terms of electro-optical modulation via constrained silicon, for which it will nevertheless be necessary to carry out guide engineering in order to strengthen the usable effective $\chi^{(2)}$ and the whole range of third order non-linear optical effects. In the short term, the fabrication and testing of SAB waveguides in multimode configuration will be a first key point, for example by measuring the parametric amplification efficiency or the signal-to-idler conversion rate in various configurations. For frequency micro-combs, a characterization of resonator quality factors and a demonstration of frequency comb generation will be the first steps. Depending on the difficulties encountered or not, the following steps will be open to multiple applications, including spectroscopy and metrology on a chip.

Appendix

A1.   The necessity of Self-Adaptive Boundary

With the classical condition that ($n_{eff} < n_b$), the eigen dispersion equation can be similarly written by replacing the $\frac{\pi}{4}$ with the boundary-induced phase item $arctan(\frac{n_b^2\sqrt{(k_z^2 - k_0^2 n_c^2)}}{n_c^2\sqrt{(k_0^2 n_b^2 - k_z^2)}})$, as:

$$N(a) = \int_0^a \sqrt{(k_0^2 n^2(y) - \beta^2)}\, dy = \frac{m\pi}{2} + arctan(\frac{n_b^2\sqrt{(k_z^2 - k_0^2 n_c^2)}}{n_c^2\sqrt{(k_0^2 n_b^2 - k_z^2)}}) \tag{A1.1}$$

$$m = \frac{2}{\pi} N(a) - \frac{2}{\pi} arctan(\frac{\gamma n_w^2}{h n_c^2}) = \frac{2}{\pi} N(a) + f_{m2} \tag{A1.2}$$

For a linear-index profile waveguide $n(y) = Ay + B$, then

$$N(a) = \left(\frac{(Ay+B)}{2A} \cdot \frac{\omega}{c} \sqrt{(Ay+B)^2 - n_{eff,m}^2} - \frac{k_z n_{eff,m}}{2A} log\left[\frac{\omega}{c}\sqrt{(Ay+B)^2 - n_{eff,m}^2} + \frac{\omega}{c}(Ay+B)\right] \right) \Big|_0^a$$

$$= \frac{k_z}{2A} \left(n_b \sqrt{\frac{n_b^2}{n_{eff,m}^2} - 1} - n_{cent}\sqrt{\frac{n_{cent}^2}{n_{eff,m}^2} - 1} + n_{eff,m}\, log\left[\frac{\sqrt{n_{cent}^2 - n_{eff,m}^2} + n_{cent}}{\sqrt{n_b^2 - n_{eff,m}^2} + n_b} \right] \right) \tag{A1.3}$$

Similarly,

$$\frac{d\omega}{dm} = \frac{k_z c}{-n_{eff,m}^2} \bigg/ \frac{d}{dn_{eff,m}}\left[\frac{2}{\pi} N(a) + f_{m2}\right] \tag{A1.4}$$

$$= \frac{\pi k_z c}{-2 n_{eff,m}^2} \bigg/ \Bigg\{ \frac{\beta k_z}{2A}\left[\frac{n_{cent}\sqrt{n_{cent}^2 - n_{eff,m}^2}}{n_{eff,m}^2} - \frac{n_b\sqrt{n_b^2 - n_{eff,m}^2}}{n_{eff,m}^2} + log\left(\frac{\sqrt{n_{cent}^2 - n_{eff,m}^2} + n_{cent}}{\sqrt{n_b^2 - n_{eff,m}^2} + n_b} \right) \right] +$$

$$\frac{-n_{eff,m}}{-1 + n_{eff,m}^2(1/n_c^2 + 1/n_b^2)} \cdot \frac{1}{\sqrt{(n_{eff,m}^2 - n_c^2)}} \cdot \frac{1}{\sqrt{(n_b^2 - n_{eff,m}^2)}} \Bigg\} \tag{A1.5}$$

Comparing equation (A1.5) to equation (3.6), the only change we can clearly see is the replacing from $\frac{d}{dn_{eff}} f_{m1}$ to $\frac{d}{dn_{eff}}\left[\frac{2}{\pi} N(a)\right]$, which we found, is not much different in the index ($n_{eff,m}$) range we adresse (i.e. $n_b > 3$). Based on equation (A1.5), frequency spacings in different configurations are investigated and presented in Figure A1. Compared to a step-index waveguide with $n_b = 3$ and $a = 350$nm, the frequency spacing of linear-shape graded-index waveguide presents a faster change

but in a basically similar line-shape. Even using a wider graded-index waveguide with a=500nm or smaller boundary index n_b=2.6, the lineshapes in the concerned range of effective index ($n_{eff} < n_b$, i.e. [1.6, 3] and [1.6, 2.6], respectively) still behave monotonously. The only thing that matters is the absolute value frequency spacing. This result unambiguously confirms us that, without the assistance of a variable "effective width" supported by the Self-Adaptive Boundary, there is no way to reshuffle the frequency spacings in the multi-mode scheme, since the integral range has a significant effect on the left part of eigen dispersion equation.
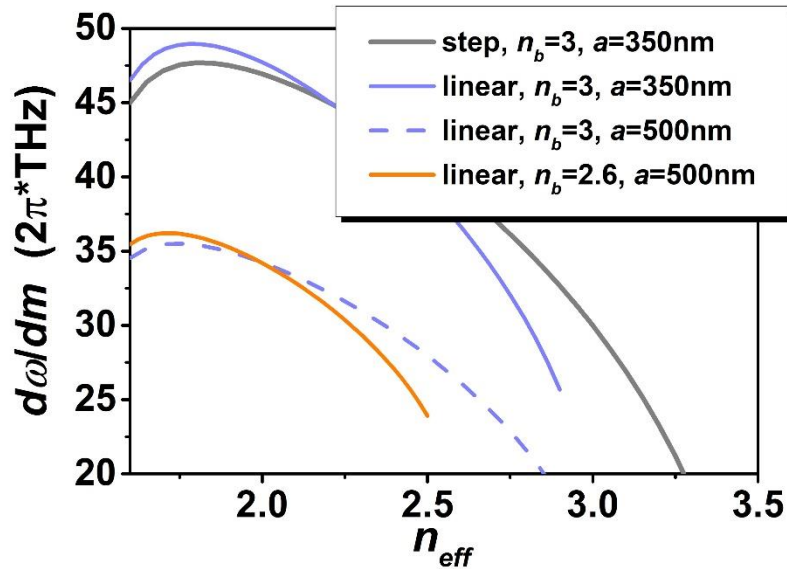
Figure A 1. Analytical Frequency spacings as a function of effective index n_{eff}, with different *order* and a values, using the classical condition $n_{eff} < n_b$.

A2.　　Approximate calculation of the 3D subwavelength waveguide grating

The effective core index n_x is approximated by function $n_x^2 = C + Dn_{SWG}^2(y)$ by numerically solving equation 3.22 and 3.23. The comparison between the analytical/numerical solving and the approximation, within the range of $n_{SWG} \in [1.8, 3.48]$, is shown in Figure A2.
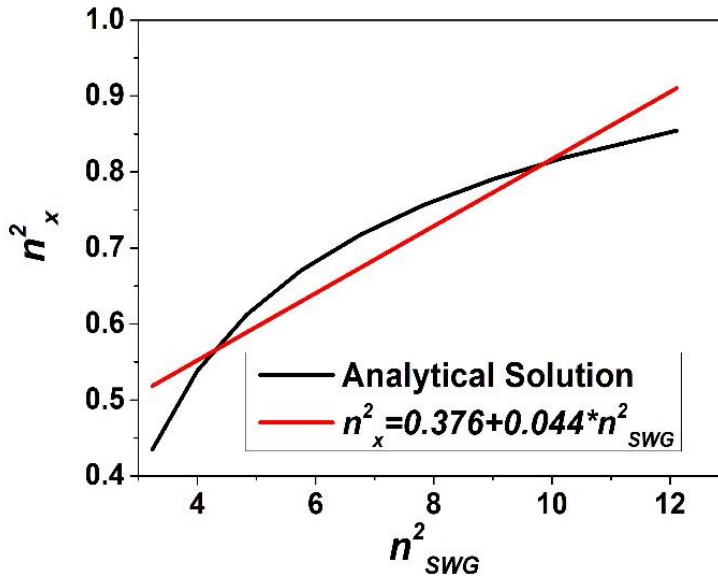
Figure A 2. Comparison between the analytical solution and the linear approximation of n_x^2, using $n_x^2 = C + Dn_{SWG}^2(y)$. The values C and D are directly shown in the Figure.

Based on this approximation, this case can be simplified as a two-dimension waveguide with an equivalent "material index" of:

$$n(y) = \sqrt{n_{SWG}^2(y) - n_x^2} = \sqrt{(1-D)n_{SWG}^2(y) - C}$$

$$= \sqrt{(1-D)[\eta(n_{cent}^2 - n_c^2) + n_c^2] - C} \tag{A2.1}$$

With this equivalent index, equation 3.21 can be simplified to the general form:

$$N(L_m) = \int_0^L \sqrt{(k_0^2 n^2(y) - k_z^2)}\, dy = \frac{m\pi}{2} + \frac{\pi}{4} \tag{A2.2}$$

Now the phase item shares the same expression as equation 3.15. Thus, we can adopt the method discussed before to optimize the waveguide. Very importantly, the

effective index n_{eff} is shifted to a lower level due to the limited thickness, which gives a maximum equivalent index of $n(0)=\sqrt{(1-D)[(n_{cent}^2-n_c^2)+n_c^2]-C}$.

Calculation is performed on a silicon platform with the period, thickness and the half waveguide width a set to 150 nm, 340 nm and 800 nm, respectively. The width of nano-arms is set to 40 nm which gives a boundary index of $n_b = n_c$=1.8. With a width of fixed-index region $2b$ while index between b and a follows the same law $(A + By)^p$ as in the previous section. By setting this, a minimum phase can be ensured and the total phase can be rewritten as:

$$N(L_m) = b\frac{\omega}{c}\sqrt{n^2(0) - n_{eff,m}^2} + \int_b^L \frac{\omega}{c}\sqrt{n^2(y) - n_{eff,m}^2}\, dy \qquad (A2.3)$$

Since $n(L_m) = n_{eff,m}$, if order = 1, that is to say $\eta(y) = (Ay + B)$, then

$$N(L_m) = bk_z\sqrt{\frac{n^2(0)}{n_{eff,m}^2} - 1} + \frac{-2k_z}{3An_{eff,m}(1-D)(n_{cent}^2-n_c^2)}\left[n^2(0) - n_{eff,m}^2\right]^{3/2} \qquad (A2.4)$$

We then obtain similarly the frequency spacings as:

$$\frac{d\omega}{dm} = \frac{-A\pi C(1-D)(n_{cent}^2-n_c^2)}{4} \Bigg/ \left(\frac{\left[n^2(0)-n_{eff,m}^2\right]^{3/2}}{3} + n_{eff,m}^2\sqrt{n^2(0) - n_{eff,m}^2} - \right.$$

$$\left. \frac{bAn^2(0)(1-D)(n_{cent}^2-n_c^2)}{2\sqrt{n^2(0)-n_{eff,m}^2}}\right) \qquad (A2.5)$$

Currently, the frequency spacing $\frac{d\omega}{dm}$ is no longer simply dominated by the effective index $n_{eff,m}$. Instead, also being affected by the new introduced item $\frac{bAn^2(0)(1-D)(n_{cent}^2-n_c^2)}{2\sqrt{n^2(0)-n_{eff,m}^2}}$, which gives us a new room to control the frequency spacing by providing additionally a local maximum-peak at the high n_{eff} range.

A3. Nonlinear Schrödinger equation in micro-ring resonator

Optical wave propagating in nonlinear media is described by nonlinear wave equations [51], as well known for optical parametric gain. To describe a frequency comb, wave equation needs to be considered jointly with the driven field and the waveguide-resonator interaction. Before deducing the nonlinear wave equations, Fourier Transform is first recalled with definition that will be intensively used later. For electromagnetic mode polarized along y and propagating along z, with mode distribution $F(x, y)$ considered constant and integrated into amplitude envelope function $A(z, t)$, the electric field can be written as:

$$E(z, t) = \frac{1}{2} A(z, t) e^{i(\beta z - \omega_0 t)} + conj.\{\frac{1}{2} A(z, t) e^{i(\beta z - \omega_0 t)}\} \tag{A3.1}$$

With conjugated component in the frequency domain:

$$E(z, \omega) = \frac{1}{2} A(z, \omega - \omega_0) e^{i\beta z} + conj.\{\frac{1}{2} A(z, \omega - \omega_0) e^{i\beta z}\} \tag{A3.2}$$

To simplify the calculation, we consider in the following context that:

$$E(z, t) = A(z, t) e^{i(\beta z - \omega_0 t)} \quad \text{and} \quad E(z, \omega) = A(z, \omega - \omega_0) e^{i\beta z}$$

Equation (A3.1) and (A3.2) are linked by the Fourier and inverse Fourier Transform as below:

$$E(z, \omega) = \int_{-\infty}^{\infty} E(z, t) e^{i\omega t} dt \tag{A3.3}$$

$$E(z, t) = \frac{1}{2\pi} \int_{-\infty}^{\infty} E(z, w) e^{-i\omega t} d\omega \tag{A3.4}$$

By cross-substitute (A3.3) and (A3.4) to each other, then we have

$$E(z, \omega) = \int_{-\infty}^{\infty} A(z, t) e^{[ik_z z + i(\omega - \omega_0)t]} dt = A(z, \omega - \omega_0) e^{ik_z z} \tag{A3.5}$$

$$E(z, t) = \frac{1}{2\pi} \int_{-\infty}^{\infty} A(z, \omega - \omega_0) e^{i(k_z z - \omega t)} d\omega = A(z, t) e^{i(k_z z - \omega_0 t)} \tag{A3.6}$$

Which can be simplified as

$$\int_{-\infty}^{\infty} A(z, t) e^{i(\omega - \omega_0)t} dt = A(z, \omega - \omega_0) \tag{A3.7}$$

$$\frac{1}{2\pi} \int_{-\infty}^{\infty} A(z, \omega - \omega_0) e^{-i(\omega - \omega_0)t} d\omega = A(z, t) \tag{A3.8}$$

Where $A(z, \omega - \omega_0)$ is exactly the Fourier spectrum centralized by carrier frequency ω_0. If assumes $\omega_0 = 0$, i.e. with the directional current (DC) input, then

$$\int_{-\infty}^{\infty} A(z,t)e^{i\omega t}dt = A(z,\omega)$$ (A3.9)

$$\frac{1}{2\pi}\int_{-\infty}^{\infty} A(z,\omega)e^{-i\omega t}d\omega = A(z,t)$$ (A3.10)

Which means Fourier spectrum is mirrored by the axis. Based on these, go considering the mode propagating with single frequency ω_0 and mode distribution $F(x,y)$ in a waveguide with non-negligible nonlinearities. The electric field of the confined mode can be written as:

$$E(z,t) = \frac{1}{2}F(x,y,\omega_0)A(z,t)_{\omega_0}e^{i(\beta_0 z - \omega_0 t)} + cc.$$ (A3.11)

In which $\beta_0 = \omega_0 n_{eff0}/c$ is the linear mode propagation wavevector determined by the waveguide cross-section and material properties. By submitting definition (A3.11) to wave equations (1.14) and expanding:

$$\left(\frac{\partial^2}{\partial x^2} + \frac{\partial^2}{\partial y^2}\right)F(x,y,\omega_0) \cdot A(z,t)_{\omega_0} + F(x,y,\omega_0) \cdot \left[-\beta_0^2 + 2i\beta_0\frac{\partial}{\partial z} + \frac{\partial^2}{\partial z^2}\right]A(z,t)_{\omega_0} +$$

$$k_0^2(\varepsilon_L + \varepsilon_{NL})F(x,y,\omega_0)A(z,t)_{\omega_0} = 0$$ (A3.12)

If we assume that the propagating mode in this nonlinear waveguide is well confined and both the losses and nonlinearities are only involved with the linear approximation, then simplify equation (A3.12) with $F(x,y)\frac{\partial^2}{\partial z^2}A(z,t)_{\omega_0} \approx 0$, then we have:

$$F(x,y,\omega_0)2i\beta_0\frac{\partial}{\partial z}A(z,t)_{\omega_0} + \left(\frac{\partial^2}{\partial x^2} + \frac{\partial^2}{\partial y^2}\right)F(x,y,\omega_0) \cdot A(z,t)_{\omega_0} + [k_0^2(\varepsilon_L + \varepsilon_{NL}) -$$

$$\beta_0^2]F(x,y,\omega_0)A(z,t)_{\omega_0} = 0$$ (A3.13)

Where $\left(\frac{\partial^2}{\partial x^2} + \frac{\partial^2}{\partial y^2}\right)F(x,y) \cdot A(z,t)_{\omega_0} + (k_0^2\varepsilon_L - \beta_0^2)F(x,y)A(z,t)_{\omega_0} = 0$ is exactly the typically Helmhotz Equation that determining the linear effective index, for the homogeneous material without variation along the propagation direction. Therefore equation (A3.13) can be translated as:

$$2i\beta_0\frac{\partial}{\partial z}A(z,t)_{\omega_0} + k_0^2\varepsilon_{NL}A(z,t)_{\omega_0} = 0 \text{ or } \frac{\partial}{\partial z}A(z,t)_{\omega_0} = \frac{ik_0\varepsilon_{NL}}{2n_{eff0}}A(z,t)_{\omega_0}$$

(A3.14)

Considering the weak 2nd and high order nonlinearity (>3rd), the nonlinear electric polarization can be written as $P_{NL} \approx 3\varepsilon_0\chi^3|E|^2E$ and $\varepsilon_{NL} = 3\chi^3|E|^2$ as claimed in chapter 1. Therefore, equation can be written as:

$$\frac{\partial}{\partial z}A(z,t)_{\omega_0} = ik_0 \frac{3\chi^3}{4n_1 n_{eff0}\varepsilon_0 c}(2n_1\varepsilon_0 c|A|^2)A(z,t)_{\omega_0} = ik_0 n_2 IA(z,t)_{\omega_0} \qquad (A3.15)$$

$n_1 = \sqrt{\varepsilon_L} = \sqrt{1+\chi^1}$ is the linear material refractive index while n_2 is the nonlinear refractive index which contributes to the mode propagation with the light intensity I.

Once a wave package propagating with carrier frequency ω_0 is introduced to this nonlinear waveguide, then the electric field of each frequency component (e.g. ω_1) of the mode can be written as:

$$E(z,t) = \frac{1}{2}F(x,y,\omega_1)A(z,t)_{\omega_1}e^{i(\beta_{L1}z-\omega_1 t)} + cc.$$

$$= \frac{1}{2}F(x,y,\omega_1)A(z,t)e^{i(\beta_0 z-\omega_0 t)} + cc. \qquad (A3.16)$$

Where $\beta_{L1} = \omega_1 n_{eff1}/c$ is the linear propagation wavevector determined by the waveguide cross-section and material properties for frequency ω_1. The mode amplitude $A(z,t) = A(z,t)_{\omega_1}e^{i(\omega_0-\omega_1)t}e^{i(\beta_{L1}-\beta_0)z}$ has already considered the phase deviation from the frequency detuning. This exposing ton he carrier frequency is made for the later consideration on the whole packet. Based on this, we can rewrite the wave equation as:

$$F(x,y,\omega_1)2i\beta_0 \frac{\partial}{\partial z}A(z,t) + \left(\frac{\partial^2}{\partial x^2}+\frac{\partial^2}{\partial y^2}\right)F(x,y,\omega_1)\cdot A(z,t) + [k_0^2(\varepsilon_L+\varepsilon_{NL}) -$$

$$\beta_0^2]F(x,y,\omega_1)A(z,t) = 0 \qquad (A3.17)$$

To simplify equation (A3.17), we introduce the frequency-related propagation wavevector $\beta(\omega_1)$, then equation (3.51) can be separated into two part.

$$\left(\frac{\partial^2}{\partial x^2}+\frac{\partial^2}{\partial y^2}\right)F(x,y,\omega_1)\cdot A(z,t) + [k_0^2(\varepsilon_L+\varepsilon_{NL})-\beta^2]F(x,y,\omega_1)A(z,t) = 0$$

$$(A3.18)$$

$$2i\beta_0 \frac{\partial}{\partial z}A(z,t) + (\beta^2-\beta_0^2)A(z,t) = 0 \qquad (A3.19)$$

where β is the wave vector first determine by (A3.18), which is used to described a dispersive wave envelop (frequency information is included in $A(z,t)$ and input to equation (A3.19).

In equation A3.19, we considering the weak 2nd and high order nonlinearity (>3rd) and ignoring similarly we have:

$$\beta(\omega_1) = \sqrt{k_0^2 n_1^2 + k_0^2 3\chi^3 |E|^2 + \frac{\left(\frac{\partial^2}{\partial x^2} + \frac{\partial^2}{\partial y^2}\right) F(x,y)}{F(x,y)}} \approx \sqrt{k_0^2 n_1^2 + \frac{\left(\frac{\partial^2}{\partial x^2} + \frac{\partial^2}{\partial y^2}\right) F(x,y)}{F(x,y)}} +$$

$$\frac{k_0 3\chi^3 |E|^2}{2n_1} \tag{A3.20}$$

$n_1 = \sqrt{\varepsilon_L} = \sqrt{1 + \chi^1}$ is the linear refractive index for frequency ω_1 while

$$\beta_L(\omega_1) = \sqrt{k_0^2 n_1^2 + \frac{\left(\frac{\partial^2}{\partial x^2} + \frac{\partial^2}{\partial y^2}\right) F(x,y)}{F(x,y)}} = \beta_{L1} = \omega_1 n_{eff1}/c \quad \text{is the solution of}$$

electromagnetic mode with frequency ω_1 propagating in a waveguide without nonlinearity ($k_0^2 3\chi^3 |E|^2 = 0$). With this the wavevector can be written as:

$$\beta(\omega_1) = \beta_L(\omega_1) + \frac{k_0 3\chi^3 |E|^2}{2n_1} \tag{A3.21}$$

In equation A3.19, since the nonlinear wavevector is normally order-of-magnitude smaller than the linear counterpart, we can take the approximation that:

$$2i\beta_0 \frac{\partial}{\partial z} A(z,t) + (\beta + \beta_0)(\beta - \beta_0) A(z,t) \approx 2i\beta_0 \frac{\partial}{\partial z} A(z,t) + 2\beta_0 (\beta - \beta_0) A(z,t) = 0$$

Therefore, a simplified version of (A3.19) is obtained:

$$\frac{\partial}{\partial z} A(z,t) = i(\beta - \beta_0) A(z,t) \tag{A3.22}$$

Putting the overall wavevector, i.e. equation (3.21) to (3.22), then we have:

$$\frac{\partial}{\partial z} A(z,t) = i(\beta_L - \beta_0) A(z,t) + i\frac{k_0 3\chi^3 |E|^2}{2n_1} A(z,t)$$

$$= i(\beta_L - \beta_0) A(z,t) + ik_0 \frac{3\chi^3}{4n_1^2 \varepsilon_0 c} (2n_1 \varepsilon_0 c |A|^2) A(z,t) \tag{A3.23}$$

Ignoring the nonlinearities-induced losses (i.e. $\alpha_2 = 0$), then

$$\frac{\partial}{\partial z} A(z,t) = i(\beta_L - \beta_0) A(z,t) + ik_0 n_2 I A(z,t) \tag{A3.24}$$

By considering the frequency-detuning (from carrier frequency ω_0) induced dispersion and Fourier transform, we can obtain

$$\frac{\partial}{\partial z} A(z,t) = i\sum_{k=1}^{n} \frac{\beta_k}{k!} \left(i\frac{\partial^k}{\partial t^k}\right) A(z,t) + ik_0 n_2 I A(z,t) \tag{A3.25}$$

In this equation, t is the absolute time of propagation. Considering a case in Figure A3 (a) that a pulse is propagating in a ring resonator, if the pulse is analyzed in

absolute time windows, the evolution of amplitude at different position would be difficult to visualized in multi-roundtrip observation.
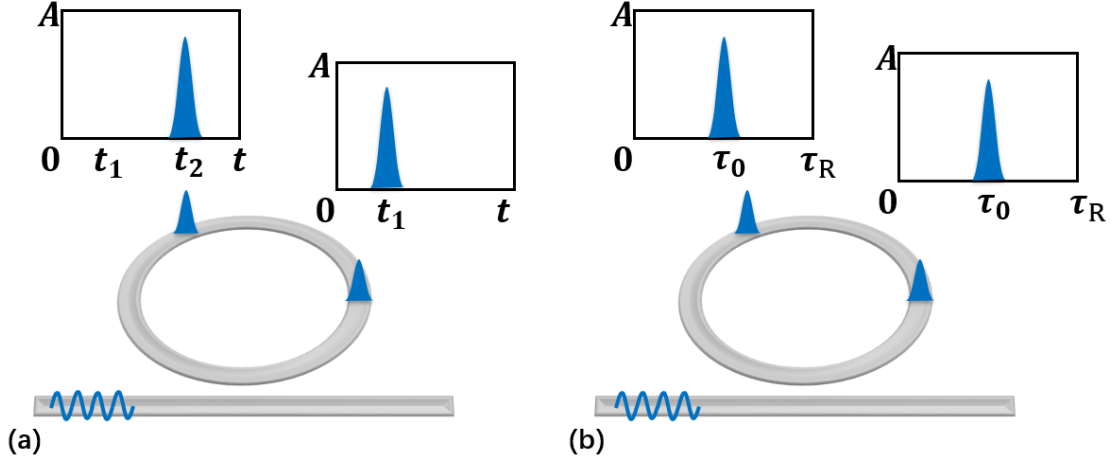
Figure A 3. Sketch of pulse propagating in resonator with absolute time variable t (a) and relative time variable τ that restrict within roundtrip time range (b).

To simplify the analysis, a moving time frame with a time variable limited in [0, roundtrip time (τ_R)] is adopted, by which the relative phase variation from the coupling point can be integrated into $A(z,t)$. With this approach, redundant time-relevant information is removed and the comparison between position in the same roundtrip and different roundtrips at the same position can be very straightforward. To consider the relative time frame at each position, we need to replace it with a variable $\tau = t - \frac{z}{v_g}$ to build a moving time frame, as in Figure A3 (b). By reconsider new component in position (i.e. $z + (\omega_0 - \omega_1)\frac{z}{v_g}$), equation (A3.25) can be furthered as:

$$\frac{\partial}{\partial z} A(z,\tau) = i \sum_{k=1}^{n} \frac{\beta_k}{k!} (i \frac{\partial^k}{\partial \tau^k}) A(z,\tau) + i(\omega_0 - \omega_1)\frac{1}{v_g} A(z,\tau) + ik_0 n_2 I A(z,\tau)$$

$$= i \sum_{k=2}^{n} \frac{\beta_k}{k!} (i \frac{\partial^k}{\partial \tau^k}) A(z,\tau) + ik_0 n_2 I A(z,\tau) \tag{A3.26}$$

Equation (A3.26) is then well developed for describing the amplitude envelope in a time frame of $\tau \in [\tau_1, \tau_2]$ moving along the propagation. With consideration on the absorption induced by the scattering and waveguide imperfection that $A(z) = A(0)e^{-\frac{\alpha}{2}z}$, the lossless nonlinear wave equation (A3.26) can be extended to:

$$\frac{\partial}{\partial z} A(z,\tau) = \left[i \sum_{k=2}^{n} \frac{\beta_k}{k!} (i \frac{\partial^2}{\partial \tau^2}) + ik_0 n_2 I - \frac{\alpha}{2}\right] A(z,\tau) \tag{A3.27}$$

Till now, we obtain a nonlinear wave equation for light frequency ω_1 propagating

$(A(z,t) = A(z,t)_{\omega_1} e^{i(\omega_0-\omega_1)t} e^{i(\beta-\beta_0)z})$ with carrier coefficient $e^{i(\beta_0 z-\omega_0 t)}$. Based on this, we can easily integrate all the wave equation, i.e.

$$\frac{\partial}{\partial z}\left[A(z,\tau)_{\omega_1} e^{i(\omega_0-\omega_1)t}\right] = \left[i\sum_{k=2}^{n}\frac{\beta_k}{k!}(i\frac{\partial^k}{\partial\tau^k}) + ik_0 n_2 I - \frac{\alpha}{2}\right] \cdot \left[A(z,\tau)_{\omega_1} e^{i(\omega_0-\omega_1)t}\right]$$

$$\frac{\partial}{\partial z}\left[A(z,\tau)_{\omega_2} e^{i(\omega_0-\omega_2)t}\right] = \left[i\sum_{k=2}^{n}\frac{\beta_k}{k!}(i\frac{\partial^k}{\partial\tau^k}) + ik_0 n_2 I - \frac{\alpha}{2}\right] \cdot \left[A(z,\tau)_{\omega_2} e^{i(\omega_0-\omega_2)t}\right]$$

...

$$\frac{\partial}{\partial z}\left[A(z,\tau)_{\omega_n} e^{i(\omega_0-\omega_m)t}\right] = \left[i\sum_{k=2}^{n}\frac{\beta_k}{k!}(i\frac{\partial^k}{\partial\tau^k}) + ik_0 n_2 I - \frac{\alpha}{2}\right] \cdot \left[A(z,\tau)_{\omega_m} e^{i(\omega_0-\omega_m)t}\right]$$

by doing the simple multiplication with Fourier Transform laid out before, we can conveniently conclude a general nonlinear wave equation describing a wave packet propagating with coefficient $e^{i(\beta_0 z-\omega_0 t)}$:

$$\frac{\partial}{\partial z} A(z,\tau) = \left[i\sum_{k=2}^{n}\frac{\beta_k}{k!}(i\frac{\partial^k}{\partial\tau^k}) + ik_0 n_2 I - \frac{\alpha}{2}\right] A(z,\tau) \tag{A3.28}$$

Unambiguously, the temporal signal can be obtained by the inverse Fourier Transform from $A(z,\omega-\omega_0)$. In equation (A3.28), the light intensity (with dimension W/m^2) is supposed to be jointly considered with the mode confinement and the effective mode area A_{eff}. By separating mode area from light intensity, we can obtain the nonlinear coefficient $\gamma = \frac{k_0 n_2}{A_{eff}} = \frac{\omega n_2}{c A_{eff}}$ and a modified nonlinear wave equation:

$$\frac{\partial}{\partial z} A(z,\tau) = \left[i\sum_{k=2}^{n}\frac{\beta_k}{k!}(i\frac{\partial^k}{\partial\tau^k}) + i\gamma P - \frac{\alpha}{2}\right] A(z,\tau) \tag{A3.29}$$

Where P is the optical power transmit through waveguide cross-section. By normalizing the electric field $A(z,\tau)$ to the dimension of power (with the optical resistance), then it can be further rewritten as:

$$\frac{\partial}{\partial z} A(z,\tau) = \left[i\sum_{k=2}^{n}\frac{\beta_k}{k!}(i\frac{\partial^k}{\partial\tau^k}) + i\gamma|A(z,\tau)|^2 - \frac{\alpha}{2}\right] A(z,\tau) \tag{A3.30}$$

To understand how the $[i\gamma|A|^2]$ influences the spectrum and produces energy on spectrum, just simply calculate the complex amplitude envelope.

$$A(z,t) = \frac{0.5\,A(z,t)\exp(-i\omega_0 t)+conj(0.5\,A(z,t)\exp(-i\omega_0 t))}{\cos(-\omega_0 t)}$$

Once a phase is added to $A(z,t)$, then

$$A(z,t)_{\Delta\varphi} = \frac{0.5\,A(z,t)\exp(i\Delta\varphi-i\omega_0 t)+conj(0.5A(z,t)\exp(i\Delta\varphi-i\omega_0 t))}{\cos(-\omega_0 t)} = \frac{\cos(\Delta\varphi-\omega_0 t)}{\cos(-\omega_0 t)}$$

Clearly, the variation of amplitude in at different time period (or different position in a roundtrip) is relative to propagating frequency.

Equation (A3.31) is the basic tool to consider an optical pulse propagation of supercontinuum generation or mode-lock laser [A1] with moving time frame. As it shares the generalized form of Nonlinear Schrödinger Equations [51, A1]:

$$i\frac{\partial}{\partial t}\psi = -\frac{1}{2}\frac{\partial^2}{\partial x^2}\psi + \kappa|\psi|^2\psi \qquad (A3.31)$$

Equation (A3.31) is often related and stated as the ***Nonlinear Schrödinger Equations (NLSE)*** [A2, A3] for nonlinear optics. Based on equation (A3.30), we can detail the generation of soliton frequency comb and related dynamics.

A4. Modeling the soliton frequency comb

Model using mean-field Lugiato-Lefever equation

Optical frequency combs display a complex and very rich dynamical behavior, which has led to the development of several theoretical models for their description. These include the Ikeda map, the modal expansion approach, and the Lugiato-Lefever equation. In a cold linear ring resonator, the resonant pattern of the pump wavelength will be stabilized with circulating time much longer than the ring roundtrip time τ_R, as illustrated in Figure A4 (a). However, in a Kerr ring resonator (Figure A4 (b)), the pump wave inside the cavity continuously generates new frequency with the Kerr gain. These circulating, new frequencies will constructively interference at certain positions where phase is well matched. Since then, this strong in-phase point will continuously move even though their respective resonant pattern is shaped, with almost all the energy concentrating locally (in space). These hot energy spots evolve with time and can considered as initial-solitons where light of different frequencies propagating with same velocity remain with a relatively constant phase.
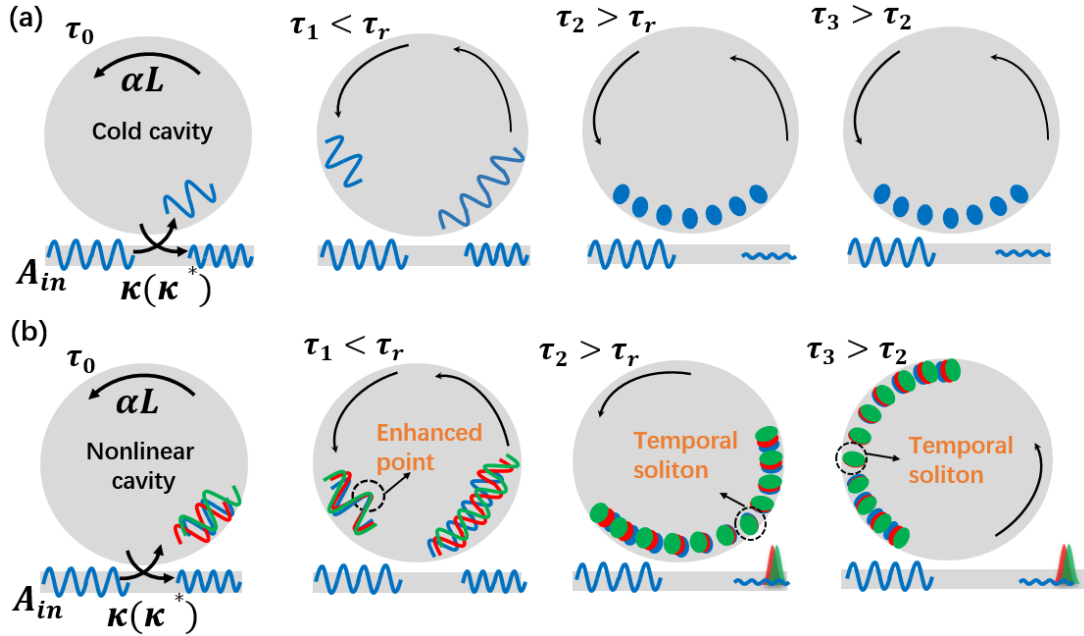
Figure A 4. Sketch of a continuous-wave driven linear (a) and nonlinear (b) ring system. κ, α and L is the ring-bus coupling efficiency, intra-cavity loss coefficient and roundtrip length, respectively.

To adapt equation (A3.30) to a ring/disk resonator system, ring-bus coupling is taken into account. As shown in Figure 71, the coupling coefficient and the roundtrip length of the resonator are represented by k and L, respectively. The system can be described as:

$$\frac{\partial}{\partial z}A(z,\tau) = \left[i\sum_{k=2}^{n}\frac{\beta_k}{k!}\left(i\frac{\partial^k}{\partial\tau^k}\right) + i\gamma|A(z,\tau)|^2 - \frac{\alpha}{2}\right]A(z,\tau) \tag{A4.1}$$

$$A(0,\tau)_{m+1} = \sqrt{1-\kappa}A(L,\tau)_m e^{i\Delta\varphi_0} + \sqrt{\kappa}A_{in}(\tau) \qquad \text{(A4.2)}$$

A_{in} is the driven amplitude while $\Delta\varphi_0$ is the phase detuning satifying $\Delta\varphi_0 = L\omega_0 n_g/c = 2\pi n - \varphi_0$ where ω_0 and ω_n are the pump frequency and ω_n the closest n-order resonant frequency of ring, respectively. φ_0 is the phase of the driven signal accumulated in the cavity。 For convenience, n is usually set with zero order by which $\Delta\varphi_0 = -\delta_0$. Driven wavelength red shifted or blue shifted are describedby$\delta_0 > 0$ and $\delta_0 < 0$, respectively. This approach was originally used to describe stationary states, instability and chaotic issues of the transmitted light in a ring cavity system [A4]. This method is now widely used to described the so-called Ikeda map of frequency combs.

Instead of counting every small step of the resonator, the **Lugiato-Lefever equation (LLE, based on the original form of Nonlinear Schrödinger Equations)**, as a temporal model, is more commonly used for describing the formation of microresonator frequency combs in the mean-field approximation. The model usually designated as Lugiato–Lefever equation was formulated in 1987 [A5, A6] as a paradigm for spontaneous pattern formation in nonlinear optical systems. The patterns originate from the interaction of a coherent field, that is injected into a resonant optical cavity, with a Kerr medium that fills the cavity. The LLE is a type of driven and damped NLSE that has previously been used to model transverse effects in diffractive optical ring cavities [A5], and temporal effects in dispersive fiber-ring resonators [A7]. In the context of microresonators, the LLE was first introduced by Matsko et al. [A8]. It describes the evolution of the slowly varying electric field envelope $A(z,\tau)$ over multiple passes of the resonator cavity. In this method, it is assumed that the field vary slowly enough over the duration of the round-trip so that the z-variation of $A(z,\tau)$ on the right-hand side of equation (A4.1) can be ignored. This can be formulated as a requirement that the detuning and the dispersion should be a small enough that phase variation in single round trip is much smaller than π. The mean-field approximation may still be applicable even if the intracavity field oscillating round-by-round. The solution of equation (A4.1) is then approximated as:

$$A(L,\tau)_m - A(0,\tau)_m = \left[i\sum_{k=2}^{n}L\frac{\beta_k}{k!}\left(i\frac{\partial^k}{\partial\tau^k}\right) + i\gamma L|A(0,\tau)_m|^2 - \frac{\alpha L}{2}\right]A(0,\tau)_m \quad \text{(A4.3)}$$

In the meanwhile, we also notice that in small perturbation, the transfer factor at the coupling region can be simplified as

$$\sqrt{1-\kappa}A(L,\tau)_m e^{-i\delta_0} \approx \left(1 - \frac{\kappa}{2} - i\delta_0\right)A(L,\tau)_m \qquad \text{(A4.4)}$$

By inserting equation (A4.3) and (A4.4) back to boundary equation (A4.2), we have:

$$A(0,\tau)_{m+1} = \sqrt{\kappa}A_{in}(\tau) + \left(1 - \frac{\kappa}{2} - i\delta_0\right)A(L,\tau)_m$$

$$= \sqrt{\kappa} A_{in}(\tau) + A(0,\tau)_m + \left[i \sum_{k=2}^{n} L \frac{\beta_k}{k!} (i \frac{\partial^k}{\partial \tau^k}) + i \gamma L |A(0,\tau)_m|^2 - \frac{\alpha L}{2} \right] A(0,\tau)_m -$$

$$\left(\frac{\kappa}{2} + i \delta_0 \right) A(0,\tau)_m - \left(\frac{\kappa}{2} + i \delta_0 \right) \left[i \sum_{k=2}^{n} L \frac{\beta_k}{k!} (i \frac{\partial^k}{\partial \tau^k}) + i \gamma L |A(0,\tau)_m|^2 - \frac{\alpha L}{2} \right] A(0,\tau)_m$$

Since the last term is very small with the scale of square of slow variation, the equation can be simplified as:

$$A(0,\tau)_{m+1} - A(0,\tau)_m \approx \sqrt{\kappa} A_{in}(\tau) - \left(\frac{\alpha L}{2} + \frac{\kappa}{2} + i \delta_0 \right) A(0,\tau)_m +$$

$$i \sum_{k=2}^{n} L \frac{\beta_k}{k!} \left(i \frac{\partial^k}{\partial \tau^k} \right) A(0,\tau)_m + i \gamma L |A(0,\tau)_m|^2 A(0,\tau)_m \tag{A4.5}$$

In the meanwhile, since basic step size is considered with the roundtrip time that $t = m\tau_R$, equation (A4.5) can be written in the differential form in which the roundtrip number can be jointly considered with time, therefore:

$$\tau_R \frac{\partial}{\partial t} A\left(\frac{t}{\tau_R} L, \tau \right) = \sqrt{\kappa} A_{in}(\tau) - \left(\frac{\alpha L + \kappa}{2} + i \delta_0 \right) A\left(\frac{t}{\tau_R} L, \tau \right) + i \sum_{k=2}^{n} L \frac{\beta_k}{k!} \left(i \frac{\partial^k}{\partial \tau^k} \right) A\left(\frac{t}{\tau_R} L, \tau \right) +$$

$$i \gamma L \left| A\left(\frac{t}{\tau_R} L, \tau \right) \right|^2 A\left(\frac{t}{\tau_R} L, \tau \right)$$

Or a more clear form that

$$\tau_R \frac{\partial}{\partial t} A(t,\tau) = \sqrt{\kappa} A_{in}(\tau) - \left(\frac{\alpha L + \kappa}{2} + i \delta_0 \right) A(t,\tau) + i \sum_{k=2}^{n} L \frac{\beta_k}{k!} \left(i \frac{\partial^k}{\partial \tau^k} \right) A(t,\tau) +$$

$$i \gamma L |A(t,\tau)|^2 A(t,\tau) \tag{A4.6}$$

Equation (A4.6) is widely referred as the **mean-field Lugiato–Lefever equation**. It is written by using a two-time scale approach, with τ being a fast time variable that describes the pulse field profile in a reference frame moving at the group velocity and spanning in the roundtrip time range. Meanwhile, t is a slow time variable that measures the evolution averaged field of the round-trip.

This two-time scale approach allows to treat the evolution of ring standing wave profile (propagation of light with respect to position, "transverse patterns") and the soliton temporal profile (light temporal evolution at a certain position, "longitudinal patterns") as independent variables. The frequency spectrum is obtained by taking the Fourier transform of the field $A(t,\tau)$ with respect to the fast time τ, and the amplitude of this spectrum is evolving on the slow time scale t. The LLE has two substantial advantages compared to the Ikeda map. For one thing it allows us numerically observe the dynamics by integrating the field with steps in roundtrip unit as usual but tremendously. In the meanwhile, it reduces the computational burden. For another thing, by taking the steady-state solutions of equation (A4.6) that states that $\frac{\partial}{\partial t} A(t,\tau) = 0$, it allows us to search its possible roots using the Newton-Rhapson

method and analytically investigate [A9-A10] faster with more general validity such as those based on the Ikeda map. For example, with $\frac{\partial}{\partial t}A(t,\tau) = 0$, a lowest approximation of soliton solution of equation (A4.16) can be considered as [A10]:

$$A(t,\tau) = -i\frac{\sqrt{\kappa}A_{in}}{\delta_0} + \sqrt{\frac{2\delta_0}{\gamma L}}sech\left(\sqrt{\frac{2\delta_0}{|\beta|L}}\tau\right)e^{i(\frac{\alpha L+\kappa}{\pi|A_{in}|}\sqrt{\frac{2\delta_0}{\gamma\kappa L}})} \tag{A4.7}$$

which gives straightforwardly the temporal profile for understanding the evolution of soliton combs although it does not yield insights into its dynamics. The combination of these two evolutions gives rise to a sequence of pulses (described with τ) in the output of the cavity that, which is intrinsically linked to the phenomenon of "Kerr frequency combs" in microresonators reported in 2007 [184]. According to equation A4.7, the typical shape of such a soliton solution could be portrayed like that in Figure A5 (a). The field hot spot in Gaussian shape in the center describes the collective interference of the multi-frequency optical field using the second term of equation (A4.7). The constant field around is a bias corresponding to the continuous pump field. By doing the inverse Fourier Transform of the soliton profile in Figure A5 (a), we can obtain a frequency comb spectrum in shape like that in Figure A5 (b).
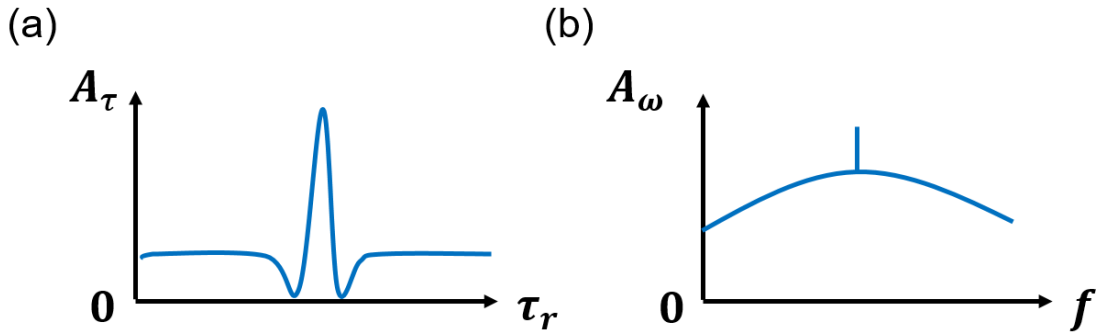
Figure A 5. Schematic of a single-soliton profile in (a) time domain and (b) frequency domain.

In addition to the solving the steady-state solution of the mean-field equation, we could also dynamically solve it using integration. Based on LLE introduced previously, we can establish a detuning-evolving comb model for investigating the generation and the dynamics of soliton frequency combs [A11, A12]. Open-access Python programming environment is chosen due to the high functionality and portability. A dynamics of comb generation is explained and shown in Figure 61 and 62. The dynamics of the frequency comb could also have been described in the frequency domain modal expansion approach [A13, A14], where a much higher level of computational complexity is then required, where the computational analysis is then also slown down by several orders of magnitude by the intensive use of Fourier transform calculations.

Dispersion and parameters control

The nonlinear ring system can be considered as that shown in Figure A6 (a).

$$\Delta k = 2\gamma P_{in} - D2\pi c \cdot \left(\frac{n\lambda}{n_g L}\right)^2$$
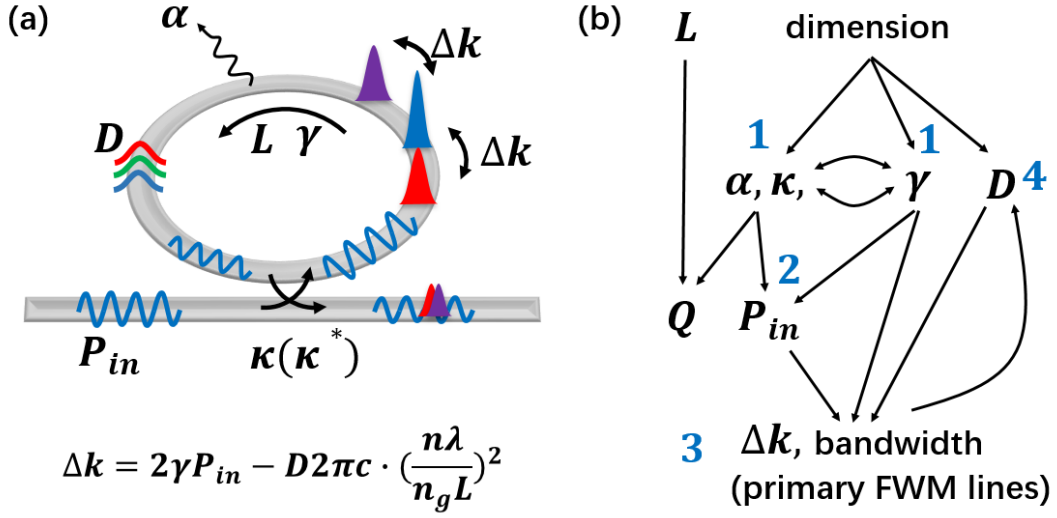
Figure A 6. (a) Schematic of the nonlinear ring-based frequency comb system. (b) A design map for managing the input parameters.

The free spectrum range (FSR) in frequency unit can be written as:

$$FSR_\omega = \frac{d\omega}{dm} = \frac{2\pi c}{n_g L} \tag{A4.8}$$

, where m is the azimuthal order of the mode interference. Therefore, the phase mismatch results from the nonlinear phase and chromatic dispersion can be considered as:

$$\Delta k = 2\gamma P_{in} - \Delta k_L = 2\gamma P_{in} - (2k_{zP} - k_{zS} - k_{zI})$$

$$\approx 2\gamma P_{in} - \left(\frac{dk}{d\omega}\bigg|_{\omega_1} \cdot nFSR_\omega - \frac{dk}{d\omega}\bigg|_{\omega_2} \cdot nFSR_\omega\right) = 2\gamma P_{in} + \frac{d^2 k}{d\omega^2}(nFSR_\omega)^2 \tag{A4.9}$$

Where n is the number of FSR that the three waves space to each other. Since

dispersion $D = \frac{-2\pi c}{\lambda^2} \cdot \frac{d^2 k}{d\omega^2}$, then

$$\Delta k = 2\gamma P_{in} - D\frac{\lambda^2}{2\pi c} \cdot (nFSR_\omega)^2 = 2\gamma P_{in} - D2\pi c \cdot \left(\frac{n\lambda}{n_g L}\right)^2 \tag{A4.10}$$

Based on dispersion matching described by equation A4.10, the design map for managing these parameters can be considered as shown in Figure A6 (b).

List of Figures

List of Tables

References

[I1] S. Miller, "Optical Fiber Telecommunications," Academic Press, New York, 1979.

[I2] L. A. Eldada, "Advances in telecom and datacom optical components," Optical Engineering 40:1165, 2001.

[I3] D. K. Borah, A. C Boucouvalas, C. C Davis, S. Hranilovic and K. Yiannopoulos, "A review of communication-oriented optical wireless systems," EURASIP Journal on Wireless Communications and Networking 91, 2012.

[I4] Stewart E. Miller, "Integrated Optics: An Introduction," Bell System Technical Journal banner 1969.

[I5] Cary Gunn, "CMOS Photonics for High-Speed Interconnects," IEEE Micro. 26:58, 2006.

[I6] K. Zhong, X. Zhou, J. Huo, C. Yu , C. Lu, and A. P. T. Lau, "Digital Signal Processing for Short-Reach Optical communications: A Review of Current Technologies and Future Trends," J. Light. Tech. 36:377, 2018.

[I7] Q. Cheng, M. Bahadori, M. glick, S. Rumley and K. Bergman, "Recent advances in optical technologies for data centers: a review," Optica 5:1354, 2018.

[I8] C. Xie, "Datacenter optical interconnects: Requirements and challenges," IEEE Optical Interconnects Conference (OI), 2017.

[I9] M. Glick, L. C. Kimerling and R. C. Pfahl, "A Roadmap for Integrated Photonics," OPTICS & PHOTONICS NEWS 38, 2018.

[I10] R. Llorente, M. Morant, A. Brimont, P. Sanchis, "The 5G fronthaul and enabling silicon photonics technology," Broadband Access Communication Technologies XIII 10945:08, 2019.

[I11] T. H. Szymanski, "Securing the Industrial-Tactile Internet of Things With Deterministic Silicon Photonics Switches," IEEE Acess 4:8236, 2016.

[I12] N. Hosseinzadeh, A. Jain, R. Helkey, J. F. Buckwalter, "RF silicon photonics for wideband, high dynamic range microwave and millimeter-wave signal processing," IEEE 18th Topical Meeting on Silicon Monolithic Integrated Circuits in RF Systems (SiRF) 17613916, 2018.

[I13] I. Rodríguez-Ruiz, T. N. Ackermann, X. Muñoz-Berbel and A. Llobera, "Photonic Lab-on-a-Chip: Integration of Optical Spectroscopy in Microfluidic Systems," ACS Analy. Chem. 88:6630, 2016.

[1] M. Zuffada, "The industrialization of the silicon photonics: Technology road map and applications," Solid-State Device Research Conference (ESSDERC), Proceedings of the European, 2012.

[2] Frédéric Boeuf, "Si-Photonics: Industrial Reality and Future Evolution," SILICON PHOTONICS WORKSHOP, STMicroelectronics, 2018.

[3] "Silicon photonics reaches tipping point, with transceivers shipping in volume," semiconductor TODAY Compounds & Advanced Silicon 13:3, 2018.

[4] C. R. Doerr, "Silicon photonic integration in telecommunications," frontiers in Physics 3:37, 2015.

[5] D. Thomson, A. Zilkie, J. E Bowers, T. Komljenovic, G. T Reed, L.Vivien, D. Marris-Morini, E. Cassan, L. Virot, J.-M. Fédéli, J.-M. Hartmann, J. H Schmid, D.-X. Xu, F. Boeuf, P. O'Brien, G. Z Mashanovich and M. Nedeljkovic, "Roadmap on silicon photonics," J. Opt. 18:073003, 2016.

[6] Jean Louis Malinge, "A view on the Silicon Photonics trends and Market prospective," 2nd Summer School on INtelligent signal processing for FrontIEr Research and Industry July 22nd

2014

[7] K. Okamoto, "Fundamentals of Optical Waveguides," Elsevier 2006.

[8] A. W. Synder and J. Love, "Optical Waveguide Theory," Chapman & Hall, Springer, 1983.

[9] H. Subbaraman, X. Xu, A. Hosseini, X. Zhang, Y. Zhang, D. Kwong and R. T. Chen, "Recent advances in silicon-based passive and active optical interconnects," Opt. Exp. 23:2487, 2015.

[10] D. Perez, I. Gasulla, F. J. Fraile , L. Crudgington, D. J. Thomson, A. Z. Khokhar, K. Li , W. Cao, G. Z. Mashanovich , "Silicon quantum photonics" IEEE Journal of Selected Topics in Quantum ElectronicsNat. Photon. 22:390, 2016.

[11] D. Marpaung, J. Yao and J. Capmany, "Integrated microwave photonics" Nat. Photon. 13:80, 2019.

[12] P. Chaisakul, V. Vakarin, J. Frigerio, D. Chrastina, G. Isella, L.Vivien and D. Marris-Morini, "Recent Progress on Ge/SiGe Quantum Well Optical Modulators, Detectors, and Emitters for Optical Interconnects" Photonics 6:24, 2019.

[13] Q. Xu, B. Schmidt, S. Pradhan and M. Lipson, "Micrometre-scale silicon electro-optic modulator," Nature 435:325, 2005.

[14] A. Shakoor, R. Lo Savio, P. Cardile, S. L. Portalupi, D. Gerace, K. Welna, S. Boninelli, G. Franz `o, F. Priolo, T. F. Krauss, M. Galli and L. O'Faolain, "Room temperature all-silicon photonic crystal nanocavity light emitting diode at sub-bandgap wavelengths" Las. Photon. Rev. 7:114, 2013.

[15] M. Fujita, Y. Tanaka and S. Noda, "Light Emission From Silicon in Photonic Crystal Nanocavity" J. Selected Topics Quantum Elec. 14:1090, 2008.

[16] P. Muñoz, G. Micó, L. A. Bru, D. Pastor, D. Pérez, J. D. Doménech, J. Fernández, R. Baños, B. Gargallo, R. Alemany, A. M. Sánchez, J. M. Cirera, R. Mas and C. Domínguez, "Silicon Nitride Photonic Integration Platforms for Visible, Near-Infrared and Mid-Infrared Applications," Sensors 17:2088, 2017.

[17] P. Muñoz, J. D. Doménech, C. Domínguez, A. Sánchez, G. Micó, L. A. Bru, D. Pérez, and D. Pastor, "State of the Art of Silicon Nitride Photonics Integration Platforms," ICTON TU.B5.3, 2017.

[18] H. Guo, C. Herkommer, A. Billat, D. Grassani, C. Zhang, M. H. P. Pfeiffer, W. Weng, C. Brès and T. J. Kippenberg, "Mid-infrared frequency comb via coherent dispersive wave generation in silicon nitride nanophotonic waveguides," Nat. Photon. 12:330, 2018.

[19] B. Stern, X. Ji, Y. Okawachi, A. L. Gaeta and M. Lipson, "Battery-operated integrated frequency comb generator," Nature. 562:401, 2018.

[20] G. Roelkens, L. Liu, D. Liang, R. Jones, A. Fang, B. Koch, and J. Bowers, "III-V/silicon photonics for on-chip and inter-chip optical interconnects," Laser Photonics Rev. 4:751, 2010.

[21] A. spott, J. peters, M. l. davenport, E. j. Stanton, C. d. Merritt, W. w. Bewley, I. Vurgaftman, C. S. Kim, J. R. Meyer, J. Kirch, L. j. Mawst, D. Botez, and John E. Bowers, "quantum cascade laser on silicon," Optica, 3:545, 2016.

[22] D. Liang, X. Huang, G. Kurczveil, M. Fiorentino and R. G. Beausoleil, "Integrated finely tunable microring laser on silicon," Nat. Photon., 10:719, 2016.

[23] M. Pu, L. Ottaviano, E. Semenova and K. yvind, "Efficient frequency comb generation in AlGaAs-on-insulator," Optica. 3:823, 2016.

[24] K. Hirose, Y. Liang, Y. Kurosaka, A. Watanabe, T. Sugiyama and S. Noda, "Watt-class

high-power, high-beam-quality photonic-crystal lasers" Phys. Rev. Lett. 8:406, 2014.

[25] I. Aharonovich, D. Englund and M. Toth, "Solid-state single-photon emitters," Nat. Photon. 10:631, 2016.

[26] M. Bazzana and C. Sada, "Optical waveguides in lithium niobate: Recent developments and applications," Appl. Phys. Rev. 2:040603, 2015.

[27] A. Rao ; S. Fathpour, "Compact Lithium Niobate Electrooptic Modulators," IEEE Journal of Selected Topics in Quantum Electronics 24,4 2018.

[28] C. Wang, M. Zhang, X. Chen, M. Bertrand, A. Shams-Ansari, S. Chandrasekhar,

P. Winzer and M. Lončar, "Integrated lithium niobate electro-optic modulators operating at CMOS-compatible voltages," Nature 562:101, 2018.

[29] M. He, M. Xu, Y. Ren, J. Jian, Z. Ruan, Y. Xu, S. Gao, S. Sun, X. Wen, L. Zhou, L. Liu, C. Guo, H. Chen, S. Yu, L. Liu and X. Cai, "High-performance hybrid silicon and lithium niobate Mach–Zehnder modulators for 100 Gbit s−1 and beyond," Nat. Photon. 13:359 2019.

[30] M. Yu, R. Zhu, H. Hu and M. Loncar, "Monolithic lithium niobate photonic circuits for Kerr frequency comb generation and modulation," Nat. Comm. 10:978, 2019.

[31] A. Boes, B. Corcoran, L. Chang, J. Bowers, and A. Mitchell, "Status and Potential of Lithium Niobate on Insulator (LNOI) for Photonic Integrated Circuits," Las. Photon. Rev. 1700256, 2018.

[32] L. Alloatti et al, "100 GHz silicon–organic hybrid modulator," Light Sci. App. 3:e173, 2014.

[33] C. Haffner et al, "All-plasmonic Mach–Zehnder modulator enabling optical high-speed communication at the microscale," Nat. Photon. 9:525, 2015.

[34] W. Heni, et al, "Silicon-Organic and Plasmonic-Organic Hybrid Photonics," ACS Photon. 4:1576, 2017.

[35] C. T. Phare, Y. D. Lee, J. Cardenas and M. Lipson, "Graphene electro-optic modulator with 30 GHz bandwidth," Nat. Photon. 9:511, 2015.

[36] Z. Sun, A. Martinez and F.Wang, "Optical modulators with 2D layered materials," Nat. Photon. 10:227, 2016.

[37] N. Youngblood and M. Li, "Integration of 2D materials on a silicon photonics platform for optoelectronics applications," Nanophotonics 0155, 2016.

[38] Y. D. Kim et al, "Bright visible light emission from graphene," Nat. Nano. 10:676, 2015.

[39] Y. Ye, Z. J. Wong, X. Lu, X. Ni, H. Zhu, X. Chen, Y.Wang and X. Zhang, "Monolayer excitonic laser," Nat. Photon. 9:733, 2016.

[40] H. Rong, A. Liu, R. Jones, O. Cohen, D. Hak, R. Nicolaescu, A. Fang and M. Paniccia, "An all-silicon Raman laser," Nature 433,292, 2005.

[41] H. Rong, S. Xu, O. Cohen, O. Raday, M. Lee V. Sih and M. Paniccia, "A cascaded silicon Raman laser," Nat. Photon. 2, 170, 2008.

[42] J. Chiles and S. Fathpour, "Silicon photonics beyond silicon-on insulator," J. Op. 19:053001, 2017.

[43] A. Z. Subramanian et al, A. Gaeta and M. lipson, "Silicon and silicon nitride photonic circuits for spectroscopic sensing on-a-chip," Photon. Res. 3:B47, 2015.

[44] S. A. Miller, M. Yu, X. Ji, A. G. Griffith, J. Cardenas, A. Gaeta and M. lipson, "Low-loss silicon platform for broadband mid-infrared photonics," Optica 4:707, 2017.

[45] J. Fedeli and S. Cicoletti, "Mid-Infrared (Mid-IR) Silicon-Based Photonics," PROCEEDINGS of the IEEE 2844565, 2018.

[46] P. Franken, A. E. Hill, C. Peters, and G Weinreich, "Generation of optical harmonics," Phys. Rev. Lett., 7:118, 1961.

[47] A. Pasquazi, M. Peccianti, L. Razzari, D. J. Moss, S. Coen, M. Erkintalo, Y. K. Chembo, T. Hansson, S. Wabnitzg, P. Del'Haye, X. Xue, A. M. Weiner, R. Morandotti, "Micro-combs: A novel generation of optical sources," Physics Reports 728:1, 2018.

[48] L. Caspani, C. Xiong, B. J Eggleton, D. Bajoni, M. Liscidini, M. Galli, R. Morandotti and D. J. Moss, "Integrated sources of photon quantum states based on nonlinear optics," Nanophotonics 6:e17100, 2017.

[49] C. Reimer, Y. Zhang, P. Roztocki, S. Sciara, L. R. Cortés, M. Islam, B. Fischer, B. Wetzel, A. Carmelo Cino, S. T. Chu, B. Little, D. Moss, L. Caspani, J. Azaña, M. Kues, R. Morandotti, "On-chip frequency combs and telecommunications signal processing meet quantum optics," Frontiers of Optoelectronics 11:134, 2018.

[50] H. Lin, Z. Luo, T. Gu, L. C. Kimerling, K. Wada, A. Agarwal and J. Hu, "Mid-infrared integrated photonics on silicon: a perspective," Nanophotonics 7:393 2018.

[51] G. P. Agrawal, "Nonlinear Fiber Optics," 5th edition, Elsevier, Oxford, 2013.

[52] J. Leuthold, C. Koos and W. Freude, "Nonlinear silicon photonics," Nat. Photon, 4:535, 2010.

[53] G. T. Reed, G. Mashanovich, F. Y. Gardes and D. J. Thomson, "Silicon optical modulators", Nat. Photon., 4:518, 2010.

[54] A. Liu, L. Liao, D. Rubin, Hat Nguyen, B. Ciftcioglu, Y. Chetrit, N. Izhaky and M. Paniccia, "High-speed optical modulation based on carrier depletion in a silicon waveguide," Opt. Exp. 15, 660, 2007.

[55] E. Timurdogan, C. M. Sorace-Agaskar, J. Sun, E. Shah Hosseini, A/ Biberman and M. R. Watts, "An ultralow power athermal silicon modulator," Nat. Comm., 5:4008 (2014).

[56] Govorkov, S. V., N. I. Koroteev, G. I.Petrov, I. L. Shumay and V. V. Yakovlev, "Laser nonlinear-optical probing of silicon/SiO2 interfaces: Surface stress formation and relaxation." Appl. Phys. A Solids Surf. 50:439, 1990.

[57] R. S. Jacobsen, et al., "Strained silicon as a new electro-optic material," Nature 441:199, 2006.

[58] M. Cazzanelli, et al, "Second-harmonic generation in silicon waveguides strained by silicon nitride," Nat. Mater. 11:148, 2012.

[59] C. L. Manganelli, P. Pintus, and C. Bonati, "Modeling of strain-induced Pockels effect in Silicon," Opt. Exp., 23:28649, 2015.

[60] B. Chmielak, et al., "Pockels effect based fully integrated, strained silicon electro-optic modulator," Opt. Exp. 19:17212, 2011.

[61] P. Damas, et al., "Wavelength dependence of Pockels effect in strained silicon Waveguides," Opt. Exp. 22:22095, 2014.

[62] Borghi, M. et al., "High-frequency electro-optic measurement of strained silicon racetrack resonators." Opt. Lett. 40:5287, 2015.

[63] M. Berciano, G. Marcaud, P. Damas, X. Le Roux, P. Crozat, C. A. Ramos, D. P. Galacho, D. Benedikovic, D. Marris-Morini1, E. Cassan and L. Vivien, "Fast linear electro-optic effect in a centrosymmetric semiconductor," Comm. Phys. 1:61, 2018.

[64] H. Xu, X. Li, X. Xiao, P. Zhou, Z. Li, J. Yu and Y. Yu, "High-speed silicon modulator with band equalization" Opt. Lett. 39:4839, 2014.

[65] D. Perez-Galacho, C. Baudot, T. Hirtzlin, S. Messaoudène, N. Vulliet, P. Crozat, F. Boeuf, L.

Vivien and D. Marris-Morini, "Low voltage 25Gbps silicon Mach-Zehnder modulator in the O-band" Opt. Exp. 25:011217, 2017.

[66] P. Dong, S. Liao, D. Feng, H. Liang, D. Zheng, R. Shafiiha, C.-C. Kung, W. Qian, G. Li, X. Zheng, A. V. Krishnamoorthy and M. A, "Low Vpp, ultralow-energy, compact, high-speed silicon electro-optic modulator," Opt. Exp. 17:22484, 2009.

[67] J. C. Rosenberg, W. M. J. Green, S. Assefa, D. M. Gill, T. Barwicz, M. Yang, S. M. Shank and Y. A. Vlasov, "A 25 Gbps silicon microring modulator based on an interleaved junction," Opt. Exp. 20:26411, 2012.

[68] H. C. Nguyen, S. Hashimoto, M. Shinkawa and T. Baba, "Compact and fast photonic crystal silicon optical modulators" Opt. Exp. 20:22465, 2012.

[69] Y. Yerada, K. Kondo, T. Abe and T. baba, "Full C-band Si photonic crystal waveguide modulator" Opt. Lett, 42:5110, 2017.

[70] M. Notomi, T.Tanabe, A. Shinya, E. Kuramochi and H. Taniyama, "On-Chip All-Optical Switching and Memory by Silicon Photonic Crystal Nanocavities" Advances in Optical Technologies, 568936, 2008.

[71] T. Tanabe, K. Nishiguchi, E. Kuramochi and M. Notomi, "Low power and fast electro-optic silicon modulator with lateral p-i-n embedded photonic crystal nanocavity" Opt. Exp. 17:22505, 2009.

[72] J. Hendrickson, R. Soref, J. Sweet and W.r Buchwald, "Ultrasensitive silicon photonic-crystal nanobeam electro-optical modulator: Design and simulation," Opt. Exp. 22:3271, 2014.

[73] R. Soref, J. R. Hendrickson and J. Sweet, "Simulation of germanium nanobeam electrooptical 2 × 2 switches and 1 × 1 modulators for the 2 to 5 μm infrared region" Opt. Exp. 24:9369, 2016.

[74] M. Sodagar, M. Miri, A. A. Eftekhar and A. Adibi, "Optical bistability in a one-dimensional photonic crystal resonator using a reverse-biased pn junction" Opt. Exp. 23:2676, 2015.

[75] Y. Gao, R. Shiue, X. Gan, L. Li, C. Peng, I. Meric, L. Wang, A. Szep, D. Walker Jr. J. Hone and D. Englund, "High-Speed Electro-Optic Modulator Integrated with Graphene- Boron Nitride Heterostructure and Photonic Crystal Nanocavity" ACS Photon. 15:2001, 2015.

[76] M. A. Foster, A. C. Turner, J. E. Sharping, B. S. Schmidt, M. Lipson and A. L. Gaeta, "Broad-band optical parametric gain on a silicon photonic chip," Nature 441:960, 2006.

[77] S. Azzini, D. Grassani, M. J. Strain, M. Sorel, L. G. Helt, J. E. Sipe, M. Liscidini, M. Galli and Daniele Bajoni, "Ultra-low power generation of twin photons in a compact silicon ring resonator," Opt. Exp. 20:23110, 2012.

[78] G. lin, A. Coillet and Y. K. Chembo, "Nonlinear photonics with high-Q whispering-gallery-mode resonators," Advances in Optics and Photonics 9:828, 2017.

[79] Z. Lin, T. Alcorn, M. Loncar, S. G. Johnson, and A. W. Rodriguez, "High-efficiency degenerate four-wave mixing in triply resonant nanobeam cavities," Opt. Exp. 89:053839, 2014.

[80] S. Combrie, G. Lehoucq, G. Moille, A. Martin and A. D. Rossi, "Comb of high-Q Resonances in a Compact Photonic Cavity," Las. Photon. Rev. 11, 1700099, 2017.

[81] X. Zeng, C. M. Gentry and M. A. Popović, "Four-wave mixing in silicon coupled-cavity resonators with port-selective, orthogonal supermode excitation," Opt. Lett. 40:2120, 2015.

[82] X. Zeng and M. A. Popović, "Design of triply-resonant microphotonic parametric oscillators based on Kerr nonlinearity," Opt. Exp. 22:15837, 2014.

[83] S. Azzini, D. Grassani, M. J. Strain, M. Galli, D. Gerace, M. Patrini, M. Liscidini, P. Velha and

Daniele Bajoni, "Stimulated and spontaneous four-wave mixing in silicon-on-insulator coupled photonic wire nano-cavities," Appl. Phys. Lett. 103:031117, 2013.

[84] X. Cui, W. zhang, J. Zhang, X. Le-Roux, C. Alonso-Ramos, L. Vivien, J.-J. He, E. Cassan, "Tailoring the mode splitting and degeneracy in silicon triply resonant nanobeam cavities," J. Opt. Soc. American B In publish, 2019.

[85] A. Di Falco, L. O'Faolain, and T. F. Krauss, "Dispersion control and slow light in slotted photonic crystal waveguides," Appl. Phys. Lett. 92:083501, 2008.

[86] J. F. McMillan, M. Yu, D.-L. Kwong and C. W. Wong, "Observation of spontaneous Raman scattering in silicon slow-light photonic crystal waveguides," Appl. Phys. Lett. 93:251105, 2008.

[87] B. Corcoran, C. Monat, C. Grillet, D. J.Moss, B. J. Eggleton, T. P. White, L. O'Faolain and T. F. Krauss, "Green light emission in silicon through slow-light enhanced third-harmonic generation in photonic crystal waveguides," Nat. Photon. 93:251105, 2008.

[88] C. Monat, B. Corcoran, M. Ebnali-Heidari, C. Grillet, B. J. Eggleton, T. P. White, L. O'Faolain and T. F. Krauss, "Slow light enhancement of nonlinear effects in silicon engineered photonic crystal waveguides," Opt. Exp. 3:206, 2009.

[89] S. Serna, P. Colman, W. Zhang, X. Le-Roux, C. Caer, L. Vivien and E. Cassan, "Experimental GVD engineering in slow light slot photonic crystal waveguides," Sci. Rep. 6:26956, 2016.

[90] M. A. Foster, A. C. Turner, R. Salem, M. Lipson, and A. L. Gaeta, "Broad-band continuous-wave parametric wavelength conversion in silicon nanowaveguides," Opt. Exp. 15:12949, 2007.

[91] X. Liu, R. M. O. Jr, Y. A. Vlasov and W. M. J. Green, "Mid-infrared optical parametric amplifier using silicon nanophotonic waveguides," Nat. Photon. 4:557, 2010.

[92] Rytov, S. M., "Electromagnetic properties of a finely stratified medium." Sov. Phys. JETP 2:466, 1956.

[93] M. C.Y. Huang, Y. Zhou and C. J. Chang-Hashain, "A surface-emitting laser incorporating a high-index-contrast subwavelength grating," Nat. Photon. 1:121, 2007.

[94] M. C.Y. Huang, Y. Zhou and C. J. Chang-Hashain, "A nanoelectromechanical tunable laser," Nat. photon. 2:180, 2008.

[95] K. Li, Y. Rao, C. Chase, W. Yang and C. J. Chang-Hashain, "Monolithic high-contrast metastructure for beam-shaping VCSELs," Optica 5:11 2018.

[96] W. Yang and Connie J. Chang-Hasnain, "High-contrast gratings for integrated Optoelectronics," Advances in Optics and Photonics 4:379, 2012.

[97] N. Yu, P. Genevet, M. A. Kats, F. Aieta, J. Tetienne, F. Capasso, Zeno Gaburro, "Light Propagation with Phase Discontinuities: Generalized Laws of Reflection and Refraction" Science 334:333, 2011.

[98] N. Yu and F. Capasso, "Flat optics with designer metasurfaces," Nat. Mat. 13:139, 2014/

[99] G. Li, S. Zhang& T. Zentgraf, "Nonlinear photonic metasurfaces," Nature Reviews Materials 2:17010, 2017.

[100] Z. Li, M. Kim, C.Wang, Z. Han, S. Shrestha, A. C. Overvig, M. Lu, A. Stein, A. M. Agarwal, M. Lončar and N. Yu, "Controlling propagation and coupling of waveguide modes using phase-gradient metasurfaces," Nat. Nano. 12, 675, 2017.

[101] D. Ortega, J. M. Aldariz, J. M. Arnold and J. Stewart Aitchison, "Analysis of "Quasi-Modes" in Periodic Segmented Waveguides," JOURNAL OF LIGHTWAVE TECHNOLOGY 17:369, 2009.

[102] P. Cheben, R. Halir, J. H. Schmid, H. A. Atwater and D. R. Smith, "Subwavelength integrated

photonics," Nature 560:565, 2018.

[103] R. Halir, A. Ortega-Moñux, D. Benedikovic, G. Z. Mashanovich, J. G. Wangüemert-Pérez, J. h. Schmid, Í. Molina-Fernández, and P. Cheben, "Subwavelength-Grating Metamaterial Structures for Silicon Photonic Devices," PROCEEDINGS OF THE IEEE 106:2144, 2018.

[104] R. Halir, P. Cheben, J. H. Schmid, R. Ma, D. Bedard, S. Janz, D.-X. Xu, A. Densmore, J. Lapointe, and Í. Molina-Fernández, "Continuously apodized fiber-to-chip surface grating coupler with refractive index engineered subwavelength structure," Opt. Lett. 35:3243, 2010.

[105] R. Halir, P. Cheben, J. M.Luque-Gonźalez, J. Darío Sarmiento-Merenguel, Jens H. Schmid, G. Wang̈uemert-Ṕerez, D. Xu, S. Wang, A. Ortega-Mõnux, and Í. Molina-Fernández, "Ultra-broadband nanophotonic beamsplitter using an anisotropic sub-wavelength metamaterial, Laser Photonics Rev. 10: 1039, 2016.

[106] P. Cheben, J/ H. Schmid, S. Wang, D. Xu, M. Vachon, S. Janz, J. Lapointe, Y. Painchaud and M.-J. Picard, "Broadband polarization independent nanophotonic coupler for silicon waveguides with ultra-high efficiency." Opt. Exp. 23:22553, 2015.

[107] J. G. Wangüemert-Pérez, A. Hadij-ElHouati, A. Sánchez-Postigo, J. Leuermann, D. Xu, P. Cheben, A. Ortega-Moñux, R. Halir, Í. Molina-Fernández, "Subwavelength structures for silicon photonics biosensing," Optics and Laser Technology 109:437, 2019.

[108] A. Y. Piggott, J. Lu, T. M. Babinec, K. G. Lagoudakis, J. Petykiewicz and J. Vučkovic, "Inverse design and implementation of a wavelength demultiplexing grating coupler," Sci. Rep. 4:7210, 2014.

[109] A. Y. Piggott, J. Lu, K. G. Lagoudakis, J. Petykiewicz. T. M. Babinec and J. Vučkovic, "Inverse design and demonstration of a compact and broadband on-chip wavelength demultiplexer," Nat. Photon, 9:374, 2015.

[110] S. Molesky, Z. Lin, A. Y. Piggott, W. Jin, J. Vučkovic and A. W. Rodriguez, "Inverse design in nanophotonics," Nat. Photon. 12:659, 2018.

[111] L. Su, R. Trivedi, N. V. Sapra, A. y. Piggott, D. Vercruysse and Jelena vučkovíc, "Fully-automated optimization of grating couplers," Opt. Exp. 4, 4024, 2018.

[112] P. Dong, S. Liao, H. Liang, W. Qian, X. Wang, R. Shafiiha, D. Feng, G. Li, X. Zheng, A. V.Krishnamoorthy, M. Asghari, "High-speed and compact silicon modulator based on a racetrack resonator with a 1 V drive voltage," Opt. Lett. 5:3246-3248, 2010.

[113] W. D. Sacher, W. M. J. Green, S. Assefa, T. Barwicz, S. M. Shank, Y.A. Vlasov, J. K. S. Poon, "Controlled Coupling in Silicon Microrings for High-Speed, High Extinction Ratio, and Low-Chirp Modulation," CLEO. PDPA8, 2011.

[114] S, Manipatruni, K. Preston, L. Chen, M. Lipson, "Ultra-low voltage, ultra-small mode volume silicon microring modulator," Opt. Exp. 18:18235-18242, 2012

[115] W.A. Zortman, A. L. Lentine, D. C. Trotter, M. R. Watts, "Low-voltage differentially-signaled modulators," Opt. Exp. 19:26017-26026, 2011.

[116] E. Timurdogan, C. M. Sorace-Agaskar, J. Sun, E. S. Hosseini, A. Biberman, M. R. Watts, "An ultralow power athermal silicon modulator," Nat. Comm. 5:4008, 2014.

[117] Miroshnichenko, A. E.; Flach, S.; Kivshar Y. S. Fano resonances in nanoscale structures. Review of Modern Physics 2010, 82, 2257-2298.

[118] W. Zhou; D. Zhao, Y. Shuai, H. Yang, S. Chuwongin, A. Chadha, J. H. Seo, K. X. Wang, V. Liu, Z. Ma, S. Fan, "Progress in 2D photonic crystal Fano resonance photonics," Progress in Quantum

Electronics 38:1-74, 2014.

[119] M. F. Limonov, M. V. Rybin, A. N. Poddubny, Y.S. Kivshar, "Fano resonance in photonics," Nat. Photon. 11:543-554, 2017.

[120] S. Fan, "Sharp asymmetric line shapes in side-coupled waveguide-cavity systems," Appl. Phys. Lett. 80:908-910, 2002

[121] P. Yu, T. Hu, H. Qiu, F. Ge, H. Yu, X. Jiang, J. Yang, "Fano resonances in ultracompact waveguide Fabry-Perot resonator side-coupled lossy nanobeam cavities," Appl. Phys. Lett. 103:091104, 2013.

[122] M. Heuck, P. T. Kristensen.; E. Yuriy, J. Mørk, "Improved switching using Fano resonances in photonic crystal structures," Opt. Lett. 38:2466-2468, 2013.

[123] K. Nozaki, A. Shinya, S. Matsuo, T. Sato, E. Kuramochi, M. Notomi, "Ultralow-energy and high-contrast all-optical switch involving Fano resonance based on coupled photonic crystal nanocavities," Opt. Exp. 21:11888, 2013.

[124] Y. Yu, Y. Chen, H. Hu, W. Xue, K. Yvind, J. Mørk, "Nonreciprocal transmission in a nonlinear photonic-crystal Fano structure with broken symmetry," Laser & Photon. Rev. 9:241-247, 2015.

[125] Y. Yu, W. Xue, E. Semenova, K. Yvind, J. Mørk, "Demonstration of a self-pulsing photonic crystal Fano laser," Nat. Photon. 11:81-84, 2017.

[126] Y. Yu, M. Heuck, H. Hu, W. Xue, C. Peucheret, Y. Chen, L. K. Oxenløwe, K. Yvind, J. Mørk, "Fano resonance control in a photonic crystal structure and its application to ultrafast switching," Appl. Phys. Lett. 105:061117, 2014

[127] Y. Yu, H. Hu, L. K. Oxenløwe, K. Yvind, J. Mørk, "Ultrafast all-optical modulation using a photonic-crystal Fano structure with broken symmetry," Opt. Lett. 40:2357-2360, 2015.

[128] E. Yablonovitch, "Inhibited Spontaneous Emission in Solid-State Physics and Electronics" Phys. Rev. Lett. 58:2059, 1987.

[129] J. D. Joannopoulos, R. D. Mead and J. N. Winn, "Photonic Crystals Molding the Flow of Light," Princeton, Princeton University Press, 1995.

[130] Y. Akahane, T. Asano, B.-S. Song and S. Noda, "High-Q photonic nanocavity in a two-dimensional photonic crystal," Nature 425:944, 2003.

[131] B. S. Song, S. Noda, T. Asano and Y. Akahane, "Ultra-high-Q photonic double heterostructure nanocavity," Nature 4:207, 2005

[132] T. Tanabe, M. Notomi, E. Kuramochi, A. Shinya and H. Taniyama, "Trapping and delaying photons for one nanosecond in an ultrasmall high-Q photonic-crystal nanocavity," Nat. Photon. 1:49, 2007.

[133] D.G. Rabus, "Integrated Ring Resonators," Berlin, Springer-Verlag Press, 2007.

[134] W. Bogaerts, P. D Heyn, T. V. Vaerenbergh, K. DeVos, S. K. Selvaraja, T. Claes, P. Dumon, P. Bienstman, D. V. Thourhout and R. Baets, "Silicon microring resonators," Las. Photon. Rev. 6:47, 2012.

[135] E. M. Purcell, H. C. Torrey and R. V. Pound, "Resonance Absorption by Nuclear Magnetic Moments in a Solid," Phys. Rev. 69:37, 1946.

[136] S. Noda, M. Fujita and T. Asano, "Spontaneous-emission control by photonic crystals and nanocavities," Nat. Photon. 1:449, 2007.

[137] F. Liang, N. Clarke, P. Patel, M. Loncar and Q. Quan, "Scalable photonic crystal chips for high sensitivity protein detection," Opt. Exp. 21:32306, 2013.

[138] E. Kuramochi, K. Nozaki, A. Shinya, K. Takeda, T. Sato, S. Matsuo, H. Taniyama, H. Sumikura and M. Notomi, "Large-scale integration of wavelength-addressable all-optical memories on a photonic crystal chip" Nat. Photon. 8:474, 2014.

[139] S. Chakravarty, C. Chen, N. Tang, W. Lai, Y. Zou, H. Yan, R. Y. chen, "Review of design principles of 2D photonic crystal microcavity biosensors in silicon and their applications," Front. Optoelectron. 9:206, 2016.

[140] M. Notomi, E. Kuramochi and H. Taniyama, "Ultrahigh-Q Nanocavity with 1D Photonic Gap," Opt. Exp. 16:11095, 2008.

[141] M. Eichenfield, R. Camacho, J. Chan, K. J. Vahala and O. Painter, "A picogram- and nanometre-scale photonic-crystal optomechanical cavity," Nature 459:550, 2009.

[142] M. Eichenfield, J. Chan, R. M. Camacho, K. J. Vahala and O. Painter, "Optomechanical crystals," Nature 462:78, 2009.

[143] S. Mandal, X. Serey and D. Erickson, "Nanomanipulation Using Silicon Photonic Crystal Resonators," Nano Lett. 10:99, 2010.

[144] S. Hu and S. M. Weiss, "Design of Photonic Crystal Cavities for Extreme Light Concentration," ACS Photonics 3:1647, 2016.

[145] W. S. Fegadolli, N. Pavarelli, P. O'Brien, S. Njoroge, V. R. Almeida, A. Scherer, "Thermally Controllable Silicon Photonic Crystal Nanobeam Cavity without Surface Cladding for Sensing Applications," ACS Photon. 2:470-474, 2015.

[146] A. Shakoor, K. Nozaki, E. Kuramochi, K. Nishiguchi, A. Shinya, A. Notomi, "Compact 1D-silicon photonic crystal electrooptic modulator operating with ultra-low switching voltage and energy," Opt. Exp. 22:28623-28634, 2014.

[147] M. Sodagar, M. Miri, A. A. Eftekhar, A. Adibi, "Optical bistability in a one-dimensional photonic crystal resonator using a reverse-biased pn junction," Opt. Exp. 23:2676-2685, 2015.

[148] Q. Quan, M. Loncar, "Deterministic design of wavelength scale, ultra-high Q photonic crystal nanobeam cavities," Opt. Exp. 19:18529-18542, 2011

[149] W. Suh, Z. Wang, S. Fan. "Temporal Coupled-Mode Theory and the Presence of Non-Orthogonal Modes in Lossless Multimode Cavities," IEEE JOURNAL OF QUANTUM ELECTRONICS 40:1511-1518, 2004.

[150] J. W. Yoon, R. Magnusson, "Fano resonance formula for lossy two-port systems," Opt. Exp. 21:17751-17759, 2013.

[151] M. L. Dakss, L. Kuhn, P. F. Heidrich, and B. A. Scott, "GRATING COUPLER FOR EFFICIENT EXCITATION OF OPTICAL GUIDED WAVES IN THIN FILMS," Appl. Phys Lett. 16:523, 1970.

[152] D. Taillaert, P. Bienstman, and R. Baets, "Compact efficient broadband grating coupler for silicon-on-insulator waveguides" Opt. Exp. 29:2749, 2004.

[153] A. R. Soref, B. R. Bennett, "Electrooptical Effects in Silicon," IEEE JOURNAL OF QUANTUM ELECTRONICS. 23:123-129, 1987.

[154] Y. Zhou, L. Zhou, H. Zhu, C. Wong, Y. Wen, L. Liu, X. Li, J. Chen, "Modeling and optimization of a single-drive push–pull silicon Mach–Zehnder modulator," Photon. Res. 4:153-160, 2016.

[155] D. Marris-Morini, L. Vivien, J. M. Fédéli, E. Cassan, P. Lyan, S. Laval, "Low loss and high-speed silicon optical modulator based on a lateral carrier depletion structure," Opt. Exp. 16:334-339, 2008.

[156] M. Imtsu, Y. Yamane, T. Sueta, "Broad-band traveling-wave modulator using a LiNb03 optical waveçuide," IEEE J. Quantum Electron., pp. 287-290, 1977.

[157] W. E. Stephens and T. R. Joseph, "System characteristics of direct-modulated and externally modulated W fiber-optic links," EEE J. Lightwave Technol., vol. LT-5, pp. 380-387, 1987.

[158] G. Ghione, Semiconductor Devices for High-Speed Optoelectronics. New York: Cambridge Univ. Press, 2009.

[159] H. Yu and W. Bogaerts, "An equivalent circuit model of the traveling wave electrode for carrier-depletion-based silicon optical modulators," J. Lightwave Technol. 30, 1602–1609 (2012).

[160] M. Berciano, "Low Nonlinéarités optiques du second ordre dans le silicium," PhD thesis, 2018.

[161] J. Hansryd, A. Andrekson, M. Westlund, J. Li, P. Hedekvist, "Fiber-based optical parametric amplifiers and their applications," IEEE J. Sel. Top. Quantum Electron. 8, 506 (2002).

[162] R. Salem, M. A. Foster, A. C. Turner, D. F. Geraghty, M. Lipson, A. L. Gaeta, "Signal regeneration using low-power four-wave mixing on silicon chip," Nature 2, 35 (2008).

[163] M. A. Foster, A. C. Turner, R. Salem, M. Lipson, and A. L. Gaeta, "Broad-band continuous-wave parametric wavelength conversion in silicon nanowaveguides," Opt. Exp. 15:12949, 2007.

[164] X. Liu, R. M. O. Jr, Y. A. Vlasov and W. M. J. Green, "Mid-infrared optical parametric amplifier using silicon nanophotonic waveguides," Nat. Photon. 4:557, 2010.

[165] A. C. Turner-Foster, M. A. Foster, R. Salem, A. L. Gaeta and M. Lipson, "Frequency conversion over two-thirds of an octave in silicon nanowaveguides," Opt. Exp. 18, 1904 (2010).

[166] X. Liu, R. M. O. Jr, Y. A. Vlasov and W. M. J. Green, "Mid-infrared optical parametric amplifier using silicon nanophotonic waveguides," Nat. Photon. 4, 557 (2010).

[167] S. Zlatanovic, J. S. Park, S. Moro, J. M. C. Boggio, I. B. Divliansky, N. Alic, S. Mookherjea and S. Radic, "Mid-infrared wavelength conversion in silicon waveguides using ultracompact telecom-band-derived pump source," Nat. Photon. 4, 561 (2010).

[168] X. Liu, B. Kuyken, G. Roelkens, R. Baets, R. M. O. Jr and W. M. J. Green, "Bridging the mid-infrared-to-telecom gap with silicon nanophotonic spectral translation," Nat. Photon. 6, 667 (2012).

[169] J. Cheng, Martin E. V. Pedersen, K. Charan, K. Wang, C. Xu, L. Gruner-Nielsen and D. Jakobseni, "Intermodal four-wave mixing in a higher-order-mode fiber," Appl. Phys. Lett. 101, 161106 (2012).

[170] S. M. M. Friis, I. Begleris, Y. Jung, K. Rottwitt, P. Petropoulos, D. J. RichardsonI P. Horak and F.Parmigiani, "Inter-modal four-wave mixing study in a two-mode fiber," Opt. Exp. 24, 30338 (2016).

[171] S. Signorini, M. Mancinelli, M. Borghi, M. Bernard, M. Ghulinyan, G. Pucker and L. Pavesi, "Intermodal four-wave mixing in silicon waveguides," Photon. Res. 6, 805 (2018).

[172] M. Eichenfield, J. Chan, R. M. Camacho, K. J. Vahala and O. Painter, "Optomechanical crystals," Nature. 462, 78 (2009).

[173] F. Alpeggiani, L. C. Andreani and D. Gerace, "Effective bichromatic potential for ultra-high Q-factor photonic crystal slab cavities," Appl. Phys. lett. 107, 261110 (2015).

[174] A. Simbula, M. Schatzl, L. Zagaglia, F. Alpeggiani, L. C. Andreani, F. Schäffler, T. Fromherz, M. Galli and D. Gerace, "Realization of high-Q/V photonic crystal cavities defined by an effective Aubry-André-Harper bichromatic potential," Appl. Phys. lett. 2, 056102 (2017).

[175] S. Combrie, G. Lehoucq, G. Moille, A. Martin and A. D. Rossi, "Comb of high-Q Resonances in a Compact Photonic Cavity," Las. Photon. Rev. 11, 1700099 (2017).

[176] N. Bloembergen, A. J. Sievers, Nonlinear optical properties of periodic laminar structures. Appl. Phys. Lett. 17, 483, 1970.

[177] J. P. Van Der Ziel, Phase-matched harmonic generation in a laminar structure with wave propagation in the plane of the layers. Appl. Phys. Lett. 26, 60, 1975.

[178] S. Serna, P. Colman, W. Zhang, X. L. Roux, C. Caer, L. Vivien and E. Cassan, "Suspended SOI waveguide with sub-wavelength grating cladding for mid-infrared Experimental GVD engineering in slow light slot photonic crystal waveguides," Sci. Rep. 6, 26956 (2016).

[179] M. Santagiustina, C. G. Someda, G. Vadal`a, Combri´e and A. De Rossi, "Theory of slow light enhanced four-wave mixing in photonic crystal waveguides," Opt. Exp. 18, 21024 (2010).

[180] S. Signorini, M. Mancinelli, M. Borghi, M. Bernard, M. Ghulinyan, G. Pucker and L. Pavesi, "Intermodal four-wave mixing in silicon waveguides," Photon. Res. 6, 805 (2018).

[181] J. L. Hall, "Nobel Lecture: Defining and measuring optical frequencies". Reviews of Modern Physics. 78: 1279, 2006.

[182] N. Picqué and T. W. Hänsch, "Frequency comb spectroscopy," Nat. Photon. 13:146, 2019.

[183] T. J. Kippenberg, A. L. Gaeta, M. Lipson, M. L. Gorodetsky, "Dissipative Kerr solitons in optical microresonators," Nat. Photon. 361:567, 2018.

[184] P. Del'Haye, A. Schliesser, O. Arcizet, T. Wilken, R. Holzwarth and T. J. Kippenberg, "Optical frequency comb generation from a monolithic microresonator". Nature 450:1214, 2007.

[185] T. Herr, K. Hartinger, J. Riemensberger, C. Y. Wang, E. Gavartin, R. Holzwarth, M. L. Gorodetsky and T. J. Kippenberg, "Universal formation dynamics and noise of Kerr-frequency combs in microresonators". Nat. Photon. 6: 480, 2012.

[186] T. Herr, V. Brasch, J. D. Jost, C. Y. Wang, N. M. Kondratiev, M. L. Gorodetsky and T. J. Kippenberg, "Temporal solitons in optical microresonators". Nat. Photon. 8: 145, 2014.

[187] V. Brasch, M. Geiselmann, T. Herr, G. Lihachev, M. H. P. Pfeiffer, M. L. Gorodetsky and T. J. Kippenberg, "Photonic chip–based optical frequency comb using soliton Cherenkov radiation". Science 351: 357, 2016.

[188] B. Stern, X. Ji, Y. Okawachi, A. L. Gaeta and M. Lipson, "Battery-operated integrated frequency comb generator". Nature 562:401, 2018.

[189] A. G. Griffith, R. K.W. Lau, J. Cardenas, Y. Okawachi, A. Mohanty, R. Fain, Y. Ho D. Lee, M. Yu, C. T. Phare, C.B. Poitras, A. L. Gaeta and M. Lipson, "Silicon-chip mid-infrared frequency comb generation". Nat. Comm. 6: 6299, 2014.

[190] D. W. M. Laughlin, J. V. Moloney, A. C. Newell, "Solitary waves as fixed points of infinite-dimensional maps in an optical bistable ring cavity". Phys. Rev. Lett. 51: 75, 1983.

[191] Y. Okawachi, K. Saha, J. S. Levy, Y. H. Wen, M. Lipson and A. L. Gaeta1, "Octave-spanning frequency comb generation in a silicon nitride chip". Opt. Lett 36: 3398, 2011.

[192] J. S. Penades, A. Ortega-moñux, M. Nedeljkovic, J. G. Wangüemert-pérez, R. Halir, A. Z. Khokhar, C. Alonso-ramos, Z. Qu, I. Molina-fernández, P. Cheben and G. Z. Mashanovich, "Suspended silicon mid-infrared waveguide devices with subwavelength grating metamaterial cladding". Opt. Exp. 24: 022908, 2016.

[193] H. Lin, Z. Luo, T. Gu, L. C. Kimerling, K. Wada, A. Agarwal and J. Hu, "Mid-infrared integrated photonics on silicon: a perspective". Nanophotonics 7: 393, 2018.

[194] S. A. Miller, M. Yu, X. ji, A. G. griffith, J. Cardenas, A. Gaeta and M. Lipson, "Low-loss silicon platform for broadband mid-infrared photonics". Optica 4: 707, 2017.

[195] N. Akhmediev and M. Karlsson, "Cherenkov radiation emitted by solitons in optical fibers," Phys. Rev. A 51: 2602, 1995.

[196] M. Erkintalo, Y. Q. Xu, S. G. Murdoch, J. M. Dudley and G. Genty, "Cascaded Phase Matching and Nonlinear Symmetry Breaking in Fiber Frequency Combs," Phys. Rev. Lett 109: 223904, 2012.

[A1] J. M. Dudley, G. Genty, S. Coen, "Supercontinuum generation in photonic crystal fiber". Reviews of Modern Physics. 78: 1135, 2006.

[A2] V. E. Zakharov and A. B. Shabat, "Exact theory of two-dimensional self-focusing and one-dimensional self-modulation of waves in nonlinear". SOVIET PHYSICS JETP 34: 62, 1972.

[A3] I. V. Barashenkov and Yu. S. Smirnov, "Existence and stability chart for the ac-driven, damped nonlinear Schrödinger solitons". Phys. Rev. E 54: 5707, 1996.

[A4] K. Ikeda, "Multiple-valued stationary state and its instability of the transmitted light by a ring cavity system". Opt. Comm. 30: 257, 1979.

[A5] L. Lugiato and R. Lefever, " Spatial Dissipative Structures in Passive Optical Systems". Phys. Rev Lett. 58: 2209, 1987.

[A6] L. A. Lugiato, F. Prati, M. L. Gorodetsky and T. J. Kippenberg, "From the Lugiato – Lefever equation to microresonator based soliton Kerr frequency combs". Trans. R. Soc. A 376: 20180113, 2018.

[A7] M. Haelterman, S. Trillo and S. Wabnitz, " Dissipative modulation instability in a nonlinear dispersive ring cavity ". Opt. Comm. 91: 401, 1992.

[A8] A. B. Matsko, A. A. Savchenkov, W. Liang, V. S. Ilchenko, D. Seidel, and L. Maleki, " Mode-locked Kerr frequency combs ". Opt. Comm. 36: 2845, 2011.

[A9] S. Coen and M. Erkintalo, " Universal scaling laws of Kerr frequency combs". Opt. Lett. 38: 1790, 2013.

[A10] T. Hansson and S. Wabnitz" Dynamics of microresonator frequency comb generation: models and stability". Nanophotonics 5: 231, 2016.

[A11] M. R. E. Lamont, Y. Okawachi, and A. L. Gaeta, "Route to stabilized ultrabroadband microresonator-based frequency combs ". Opt. Exp. 38: 3478, 2013.

[A12] H. Guo, M. Karpov, E. Lucas, A. Kordts, M. H. P. Pfeier, V. Brasch, G. Lihachev, V. E. Lobanov, M. L. Gorodetsky and T. J. Kippenberg, "Universal dynamics and deterministic switching of dissipative Kerr solitons in optical microresonators ". Nat. Phys. 13: 94, 2017.

[A13] Y. K. Chembo, D.V. Strekalov, and N. Yu, "Spectrum and Dynamics of Optical Frequency Combs Generated with Monolithic Whispering Gallery Mode Resonators". Phys. Rev. Lett. 104: 103902, 2010.

[A14] Y. K. Chembo and N. Yu, "Modal expansion approach to optical-frequency-comb generation with monolithic whispering-gallery-mode resonators". Phys. Rev. A 82: 033801, 2010.

Synthèse en français du manuscrit de thèse

<u>Titre</u>: Ingénierie de guides et de cavités silicium sub-longueur d'onde

pour la photonique non linéaire

La photonique silicium est basée sur l'idée de réutiliser les méthodes et procédés de fabrication CMOS et de les transférer à des structures guidantes pour la réalisation de circuits intégrés photoniques. La photonique silicium a acquis depuis quelques années une place croissante, notamment pour les télécommunications optiques, les centres de données et le calcul haute performance. En tirant parti des fortes densités de données et de la transmission sur de plus longues distances en photonique silicium, il est possible d'atteindre des niveaux élevés d'intégration avec de faibles coûts de fabrication en utilisant des infrastructures de circuits intégrés silicium classiques. Malgré toutes les qualités de la plate-forme silicium, la photonique silicium présente également des inconvénients importants. L'augmentation rapide de la demande d'interconnexions optiques entraîne une forte demande de fonctions actives efficaces et fonctionnelles, basse puissance, en particulier de sources lumineuses à base de silicium et de modulateurs optiques silicium.

Visant à explorer les fonctions actives de la photonique silicium, cette thèse est centrée sur l'exploitation des non-linéarités du silicium en utilisant tout particulièrement une ingénierie de structures sub-longueur d'onde. En particulier, l'effet Pockels de deuxième ordre et l'effet Kerr de troisième ordre sont exploités pour la modulation de la lumière à grande vitesse et faible puissance et la génération de lumière sur puce en photonique silicium.

Guidé par ces orientations, le travail effectué peut être classé en deux grandes parties :

1. Etude et optimisation de résonateurs Fano en silicium pour la réalisation de modulateurs électro-optiques à base de silicium contraint (donc à effet Pockels).

2. Guide d'onde à limite de confinement auto-adaptative à structure sub-longueurs d'onde pour l'ingénierie de dispersion et l'application au mélange à quatre ondes et à la génération de peignes de fréquence Kerr.

Chacune de ces étapes a conduit aux résultats que nous présentons ci-après.

1. Résonateurs Fano silicium pour modulateurs optiques à effet Pockels

Une longue durée de vie des photons dans un résonateur à facteur de qualité Q élevé nuit de manière générale à la rapidité des modulateurs électrooptiques (Figure 1) et limite leur largeur de bande de modulation pour un rapport d'extinction donné. Par exemple, pour un facteur de qualité de seulement 10^4, la largeur de bande f_{3dB} limitée par la durée de vie des photons (en supposant une constante de temps RC négligeable) peut être calculée comme suit : $\frac{1}{f_{3dB}^2} = (2\pi\tau)^2 + (2\pi RC)^2 \approx (2\pi\tau)^2$, où $\tau = \frac{Q}{\omega} = \frac{\lambda Q}{2\pi c}$, ce qui donne un maximum de 20GHz pour une longueur d'onde de travail autour de 1.5μm [66]. Cette inefficacité relative de modulation provient en fait en grande partie de la forme de la résonance spectrale utilisée, très symétrique, et qui implique donc un décalage significatif en fréquence afin d'induire un rapport d'extinction on/off>>1. En générant une asymétrie spectrale de la réponse du résonateur, sans aucune augmentation du facteur Q (Figure 1), on peut profiter d'une réponse plus rapide et améliorer simultanément le rapport de modulation (ER) obtenu.
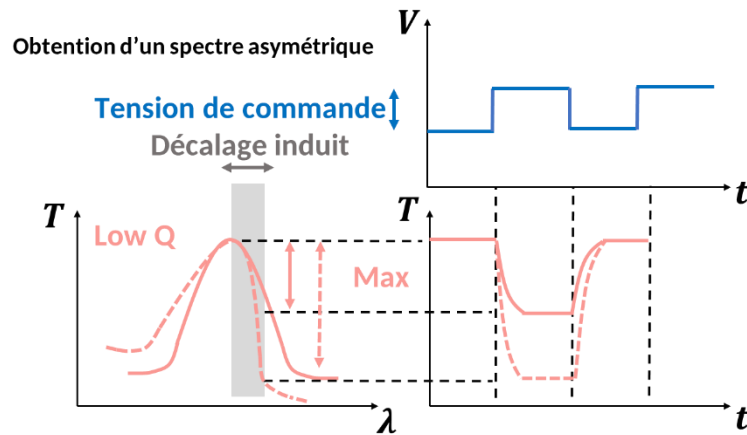
Figure 1. Représentation schématique de l'effet d'une forme de ligne de résonance asymétrique sur les propriétés de modulation d'un modulateur électro-optique.

Pour réaliser un spectre asymétrique dans un résonateur à guide d'onde unique, résultat très attendu pour la réalisation de modulateurs électro-optiques rapides et à basse puissance consommée, nous propose d'exploiter des cavités multimodes et d'en coupler les modes comme suit. La cavité montrée en Figure 2 (a) produit deux résonances de Fano, c'est-à-dire pour chacun des deux modes de polarisation quasi-TE considérés. La condition de Bragg traditionnelle de création d'un miroir distribué est en effet λ=2n_{eff}×a, où n_{eff} et a sont respectivement l'indice effectif du mode de propagation et de la période du réseau. Le principe de base de l'approche que nous proposons de mettre en œuvre est donc de concevoir une structure à guide unique mais à résonance double, dont l'un des modes connaît une transmission résonante tandis que le mode supérieur fonctionne en régime sub-longueur d'onde, et donc à transmission élevée. Leur combinaison, basée sur un mélangeur de modes (à

structuration sub-longueur d'onde), conduit à un jeu d'interférences à signature de résonance de Fano pour chacune des deux résonances.

Sur la base des dispositifs fabriqués (voir Figure 2 (b)), des signatures spectrales de type Fano ont été clairement observées pour les modes de cavité du 1er et du 2ème ordres, comme le montre la Figure 3 (a), avec des longueurs d'onde de résonance situées respectivement à environ 1515 nm et 1531 nm. Les distributions simulées pour ces deux modes sont présentées dans les encarts de la Figure 3 (b).

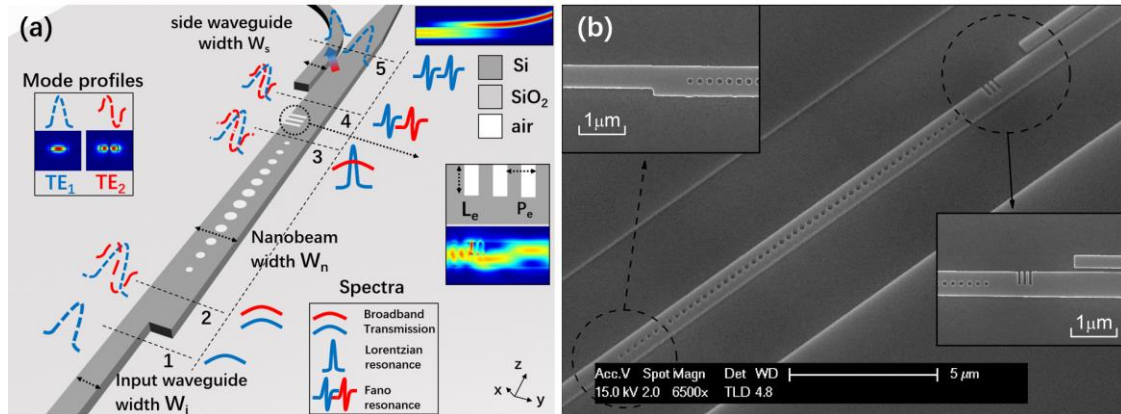**Figure 2.** a) Schéma de la cavité de Fano proposée, constituée d'une structure d'entrée de type MMI, d'une cavité nanométrique, d'un mélangeur sub-longueur d'onde et d'un coupleur directionnel. Les courbes en pointillés bleus et rouges représentent les profils de mode spatial (en bas à droite) des modes de propagation TE0 et TE1. Les courbes solides bleues et rouges représentent les formes de lignes spectrales des modes de propagation TE0 et TE1. Encart supérieur droit : la distribution du mode TE1 couplée au mode TE0 du guide d'onde latéral et convertie en celui-ci. b) Image MEB de la cavité Fano proposée avec un guide d'onde d'entrée de 400 nm de largeur. La période, le facteur de remplissage et la longueur du réseau de trous de longueur d'onde secondaire sont respectivement P_e=200 nm, ff=0,5 et L_e=400nm.

Le spectre du 1er mode de cavité est montré en Figure 3 (c). Nous voyons qu'avec un désaccord de longueur d'onde de seulement 56pm, le niveau de transmission optique de la cavité subit une chute de transition d'environ 17 dB. Une analyse similaire a également été effectuée pour le deuxième mode de cavité, qui a permis d'obtenir un rapport d'extinction de plus de 23,2 dB pour un désaccord de longueur d'onde de 366pm avec un facteur Q de 5600, comme illustré en Figure 3 (d). Un spectre de Lorentz expérimental avec presque le même facteur Q de 5600 est également reporté (courbe verte) en Figure 38 (d) pour comparaison, qui s'avère nettement moins efficace. Pour une résonance Lorentzienne sans perte $\frac{\gamma_t^2}{(\omega_0-\omega)^2+\gamma_t^2}$ avec le même facteur Q de 5600 (γ_t=2π * 17.75GHz), le rapport d'extinction (ER) pour un désaccord de longueur d'onde de 366pm ($\Delta\omega \approx 2\pi*46.83$GHz) est -10log($\frac{\gamma_t^2}{(\Delta\omega)^2+\gamma_t^2}$)=9dB. Cette valeur est inférieure de 14dB à celle de la résonance de Fano rapportée expérimentalement (23dB). D'un autre point de vue, avec le même

facteur Q (5600) et le même facteur ER (23 dB), le désaccord de longueur d'onde requis dans un cas Lorentzien est de 1,96 nm ($\Delta\omega \approx 2\pi*251\text{GHz}$), ce qui conduirait à une puissance de commande bien supérieure à celle du modulateur à résonance Fano. Cette performance supérieure montre un fort potentiel de réduction de la consommation d'énergie tout en laissant une grande place à la modulation à haut débit sans subir les effets d'une durée de vie excessive des photons. Dans l'ensemble, notre cavité comprime efficacement les dimensions physiques d'une cavité Fano et donne ainsi une grande commodité à la conception des modulateurs électrooptiques.
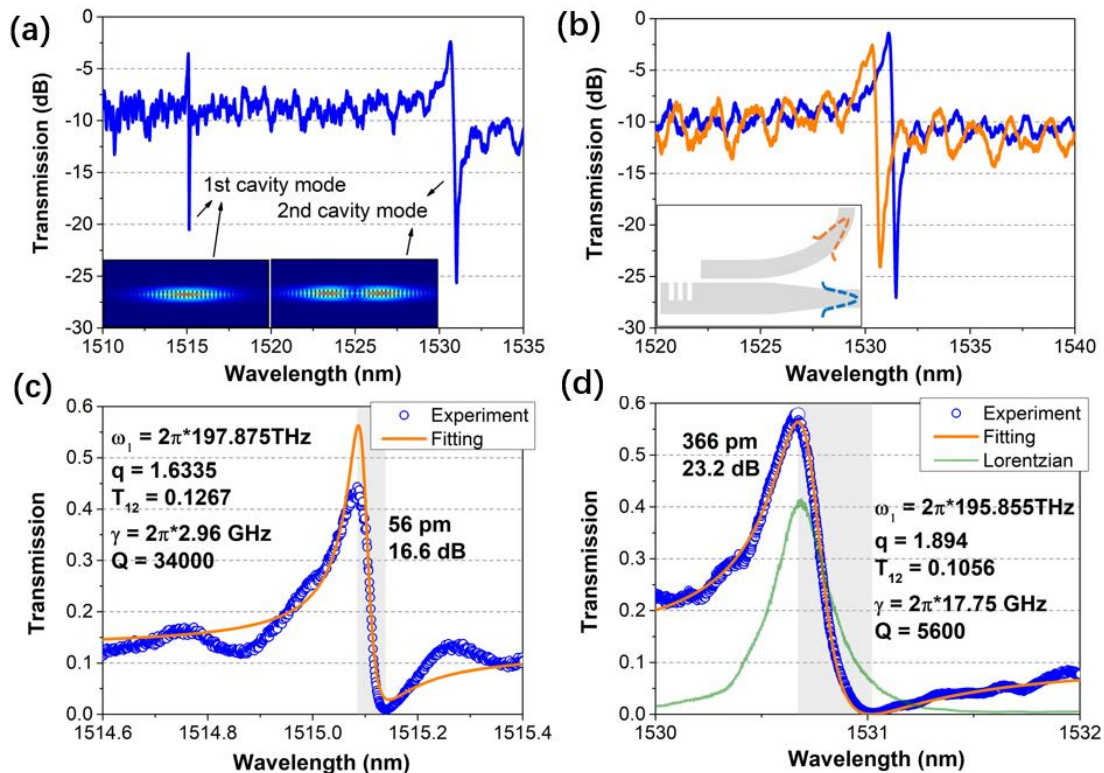
Figure 3. (a) Transmission expérimentale du guide d'onde à cavité. (b) Transmission expérimentale autour du deuxième mode de cavité détecté. c) Courbe expérimentale de transmission et courbe d'ajustement du premier mode, représentées par des cercles bleus et une courbe orange, respectivement. d) Courbe expérimentale de transmission et courbe d'ajustement du deuxième mode de cavité. La courbe de Lorentz est marquée par une courbe verte tandis que la transition entre le maximum et le minimum est représentée par des régions grises.

En nous appuyant sur cette méthode robuste, nous avons conçu un modulateur silicium exploitant l'effet d'une contrainte mécanique des couches (générant un effet Pockels dans le silicium) combiné à une telle cavité Fano mono-guide d'onde (voir Figure 4). Par rapport aux travaux existants utilisant des structures interférométriques longues (interféromètres Mach-Zehnder de plusieurs mm) où des pertes radio-fréquences élevées sont présentes dans les électrodes à ondes progressives, notre conception ultra-compacte permet d'intégrer le résonateur sur une surface de quelques centaines de µm^2 tout en fournissant une bande passante supérieure à

200GHz, associée à une forte amélioration de la réponse électro-optique. Par exemple, auparavant, une extinction de 3 dB nécessitait un décalage de longueur d'onde de 1nm dans le silicium sous contrainte, ce qui est inatteignable avec le faible niveau de sensibilité du second ordre $\Delta\chi_{yyx}^{(2)} = -1.8\text{pm/V}$ actuellement disponible. Au moyen du résonateur Fano à corrugation sub-longueur d'onde proposé, on prévoit théoriquement une amélioration d'environ 200 fois/60 fois (facteur Q de 32000/5600) de l'extinction avec la même tension appliquée. Cette amélioration donne une nouveau champ aux modulateurs silicium à contrainte, leur permettant de fonctionner à quelques dB d'extinction avec une tension accessible (<20V) et un facteur Q modéré (32000, ici).
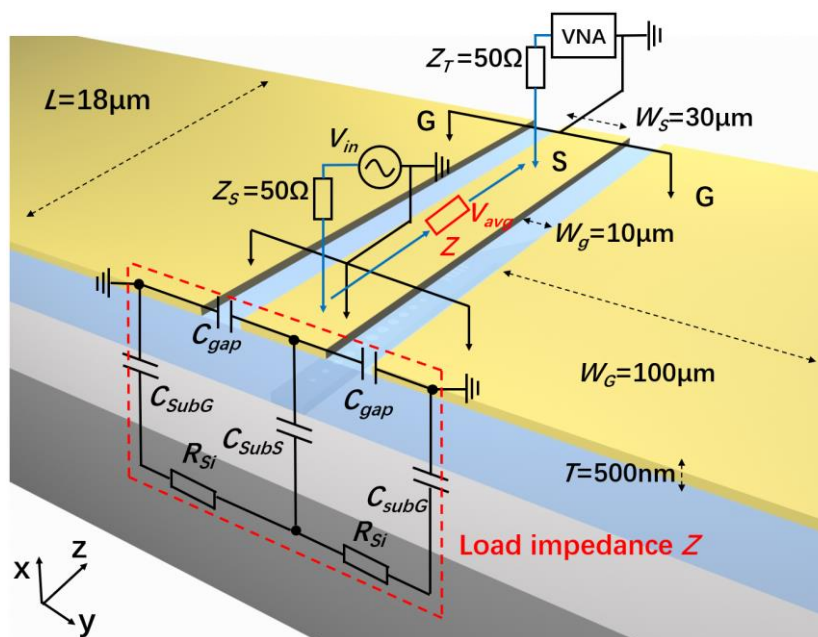
Figure 4. Schéma d'un modèle électrique équivalent du modulateur de Fano en silicium contraint proposé. L'impédance de charge de l'électrode à ondes progressives est définie par la ligne en pointillés rouges. VNA : analyseur de réseau vectoriel.

2. Guide d'onde à confinement auto-adaptatif conçu par ingénierie sub-longueur d'onde appliqué au mélange à quatre ondes et la génération de peignes de fréquence Kerr

Nous avons proposé l'utilisation de guides d'ondes SAB (Self-Adaptive Boundary) pour la réalisation d'un accord de phase quasi-universel des processus nonlinéaires d'ordre 3. La condition SAB a d'abord été conçue pour satisfaire automatiquement les lois de conservation de l'énergie et du vecteur d'onde dans le procédé de mélange intermode à quatre ondes (FWM) en s'appuyant sur une analogie étroite avec les puits quantiques (Figure 5a) et transposée en sections de guide d'ondes silicium (Figure 5b). La mise en œuvre de l'égalisation de l'espacement en fréquence entre modes, obtenu en remodelant le profil du puits de potentiel avec un profil d'indice graduel, est

illustrée en Figure 5 (b). Nous considérons un guide d'onde 2D à gradient d'indice (alors avec un « potentiel de coupure » à gradient) avec une largeur de guide d'onde de $2a$. Les indices du cœur, du bord interne du guide, et de la gaine du guide d'onde sont respectivement $n(0) = n_{cent}$, $n(a) = n_b$ and $n(|y| > a) = n_c$, comme le montre la Figure 5 (b). Lorsque la condition stipulant que tous les indices effectifs des modes guidés utilisés sont supérieurs à l'indice de limite physique (c'est-à-dire $n_{eff} > n(a) = n_b$ pour tous les modes guidés) est vérifiée, on peut considérer que le guide d'onde se divise en cinq zones (zones 0, ∓1, ∓2). La partie centrale (partie 0) se situe dans la plage $[-L_m, L_m]$ dans laquelle $n(y)$ est supérieur à n_{eff} et peut être exprimée par une fonction cosinus, comme habituellement, au lieu des limites physiques (c'est-à-dire y=$\mp a$). Les quatre autres zones (zones ∓1, ∓2) sont décrites par une forme décroissante car $n(y)$ y est plus faible que n_{eff}.
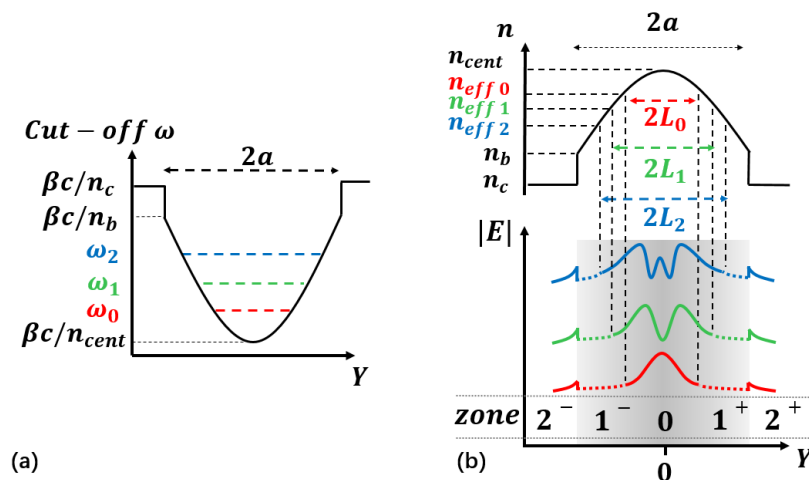

Figure 5. (a) Schéma d'un puits à indice de potentiel graduel. (b) Esquisse d'un profil d'indice non uniforme et de la distribution modale des trois premiers modes de propagation de l'axe z. n_{cent}, n_b, n_c sont les indices du centre du guide d'onde, de la limite intérieure du guide d'onde, et de son environnement (tout en vérifiant la condition SAB selon laquelle $n_{effm} > n_b$). Le point zéro de l'axe est situé au centre du guide d'onde.

En tirant parti de l'équivalence d'indice de l'ingénierie des structures sub-longueurs d'onde, nous sommes en mesure de créer un guide d'ondes vérifiant la condition SAB effectivement réalisable en photonique silicium (voir Figure 6 (a)). Avec des paramètres optimisés suivants : a=775nm, b=275nm, nous pouvons égaliser localement l'espacement en fréquence et rendre les courbes de dispersion bien parallèles, ce qui la condition sine qua non à un accord de phase généralisé pour le mélange à quatre ondes intermodes. En Figure 6 (c), nous montrons les courbes de dispersion pour les trois premiers modes du guide d'ondes optimisé. Avec le point $\omega_2 - \omega_1 = \omega_1 - \omega_0$ situé à $k_z = 1.07 \times 10^7$, la gamme de fréquence avec condition $|\Delta\omega_{21} - \Delta\omega_{10}| < \Delta\omega * 5\%$ est aussi large que 35 THz (~300nm), ce qui montre également une bonne tolérance aux éventuelles imperfections de fabrication des structures. En utilisant cette configuration, l'adaptation de phase est réalisée entre la fréquence du signal de 220THz (1.36µm) et la fréquence idler de 172THz (1.72µm).

Les résultats de la Figure 6 nous confirment ainsi la faisabilité d'une utilisation des guides d'ondes structurés à l'échelle sub-λ.

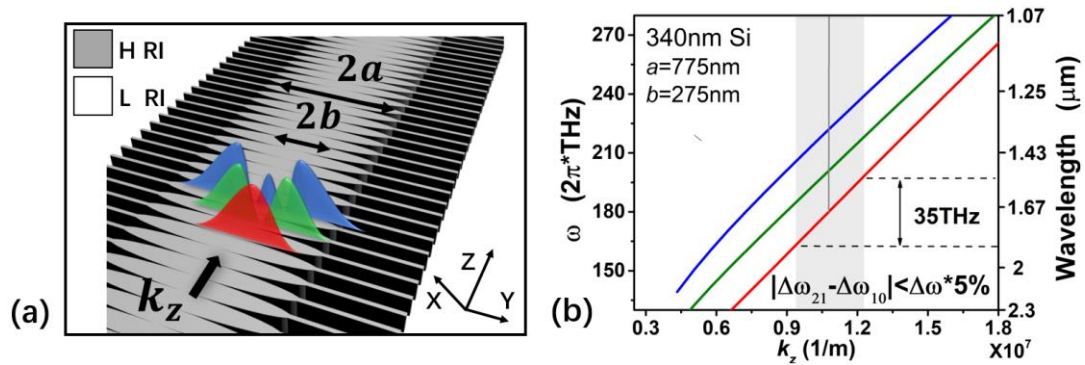**Figure 6.** (a) Schéma d'un guide d'ondes à profil gradué et à structuration sub-λ. b) Espacement des fréquences en fonction de l'indice effectif n_{eff}, à l'aide d'un calcul FDTD 3D. Le point d'appariement parfait et la plage de tolérance de 5 % sont marqués respectivement par une ligne grise et une zone grise. Les paramètres suivants ont été adoptés : n_{cent}=3.48, n_b=n_c=1.8.

Compte tenu du fort potentiel de ces guides d'ondes multimode à confinement latéral auto-adaptatif pour l'ingénierie de la dispersion, nous avons étendu leur étude à un fonctionnement monomode pour la génération de peignes de fréquence Kerr, comme illustré en Figures 7(a) et 7(b). Les courbes de dispersion d'un guide d'ondes ruban ('strip') et d'un guide d'ondes graduel SAB avec $n_b \approx 1.5$ et $n_b \approx 2.8$ sont représentées en Figure 7(b), pour comparaison. Les guides SAB permettent d'ajuster la dispersion de la longueur d'onde "longue" où $n_{eff} < n_b$. C'est parce que l'onde est confinée par le contraste d'indice n_b/n_c et que l'intégrale de phase dépend fortement de l'indice n_b. En revanche, en régime de courte longueur d'onde ($n_{eff} > n_b$), une limitation par la largeur effective du guide d'ondes apparait, la dispersion ne variant alors pas beaucoup. Au total, toute la gamme de fréquences est séparée en deux parties avec des réponses différentes, ce qui nous permet de reconFigurer globalement la dispersion du guide pour le point de travail visé en aplatissant ou en accentuant la dispersion en conséquence.
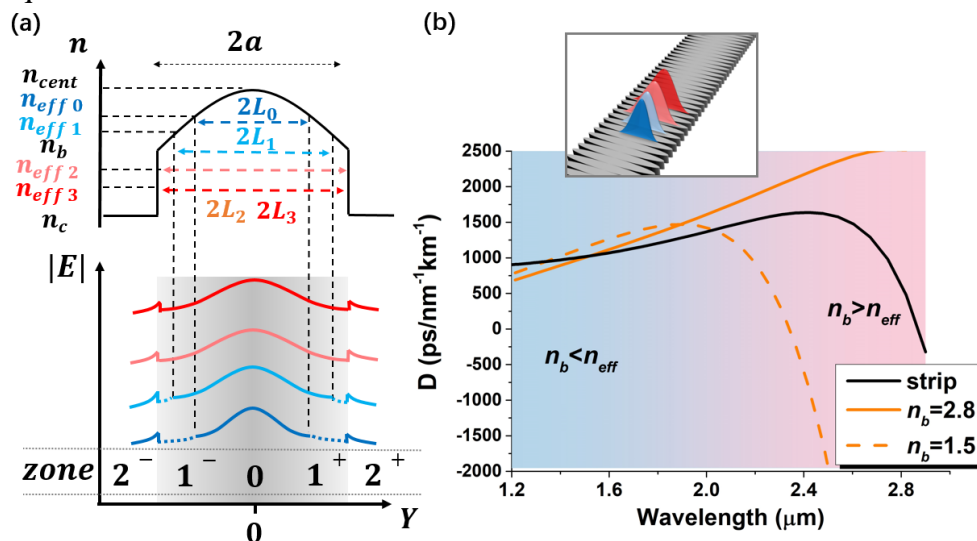
Figure 7. (a) Schéma d'un guide d'ondes monomode à gradient d'indice et condition SAB. b) Paramètre de dispersion chromatique D. Largeur et hauteur du guide d'ondes : 750 nm et 340 nm. (c) Schéma d'un guide d'ondes à deux niveaux à gradient d'indice avec condition SAB et fonctionnement monomode. d) Evolution du paramètre de dispersion chromatique D. La dispersion des matériaux n'a pas été considérée ici (n=3,48).

A partir de là (c'est-à-dire à partir de ces guides), nous avons considéré la dynamique de la génération d'un peigne de fréquences solitons basé sur un résonateur en anneau non linéaire Kerr, comme le montre la Figure 8 (a). Utilisation l'équation de Schrödinger non-linéaire (sous la forme de l'équation de Lugiato-Lefever) :

$$\frac{\partial}{\partial z}A(z,\tau) = \left[i\sum_{k=2}^{n}\frac{\beta_k}{k!}(i\frac{\partial^k}{\partial\tau^k}) + i\gamma|A(z,\tau)|^2 - \frac{\alpha}{2}\right]A(z,\tau)$$

, nous avons modélisé la formation de peignes de fréquence, de la déduction du spectre du peigne de solitons à l'analyse dynamique du spectre du peigne de solitons, comme l'illustrent les Figures 8 (c)-(e).
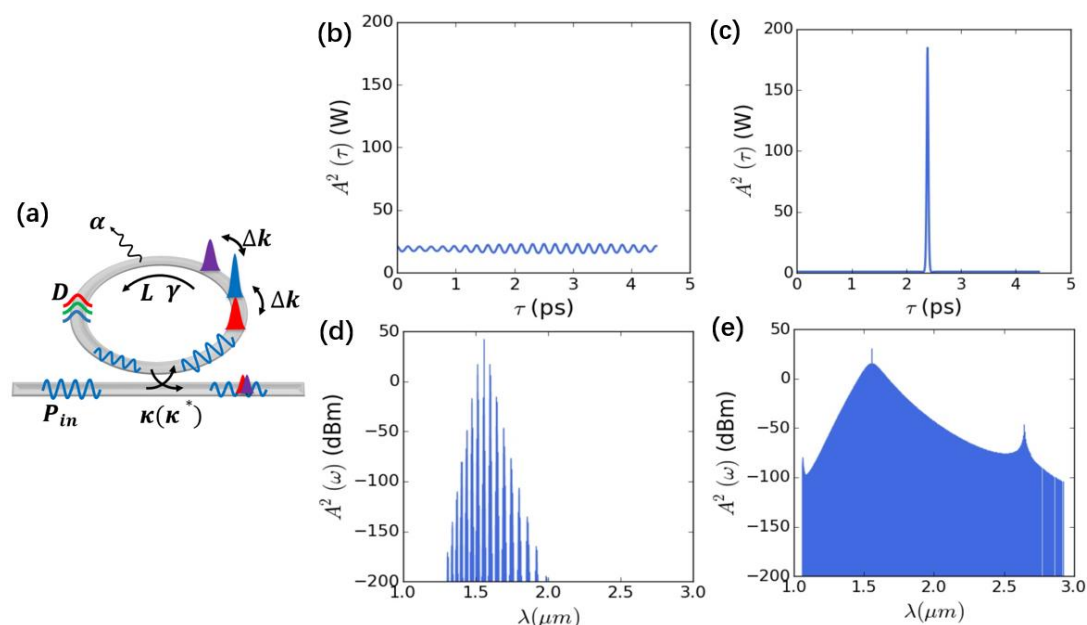
Figure 8. a) Schéma de principe d'un anneau non linéaire (Kerr) pour la génération d'un peigne de fréquence. (b) et (c) : Evolutions temporelles et spectrales au cours de la génération du peigne de fréquences au sein duquel des raies sont générées par un mélange à quatre ondes en cascade, (c) et (e) Forme temporelle et signature spectrale d'un peigne de fréquence mono-soliton (état final)

Nous nous sommes ensuite tout particulièrement intéressés à la largeur spectrale totale des peignes de fréquence réalisables par effet Kerr à partir de guides et de résonateurs silicium. En partant de guides silicium de dimensions 220 nm (épaisseur) et de 800 nm de largeur, avec une dispersion de guide d'ondes correspondante illustrée à la Figure 9 (a), nous avons trouvé une valeur maximale de dispersion chromatique autour de D=350 pm/(nm*km). En utilisant le modèle décrit ci-dessus, nous avons obtenu un peigne de fréquences silicium mono-soliton avec une largeur de bande de peigne beaucoup plus faible que pour les résonateurs nitrure de silicium (voir Figure

9(b)), un avantage (plus faible puissance de pompe) étant contre-balancé par un inconvénient (plus faible bande passante de conversion par mélange à quatre ondes).

Sans ambiguïté, en introduisant les guides silicium à condition SAB, nous avons obtenu une courbe de dispersion très aplatie, comme le montre la Figure 9 (c). En utilisant à nouveau notre modèle pour évaluer les propriétés des peignes de fréquences, nous avons pu alors démontrer une très nette amélioration de la largeur spectrale des peignes de fréquence à solitons unique, comme illustré sur un exemple en Figure 9 (d). Il ne fait aucun doute que la largeur de bande du peigne en phase d'instabilité de modulation est étendue et que l'amélioration de la largeur de bande est clairement observée avec l'introduction des guides d'ondes à limite auto-adaptative (SAB).
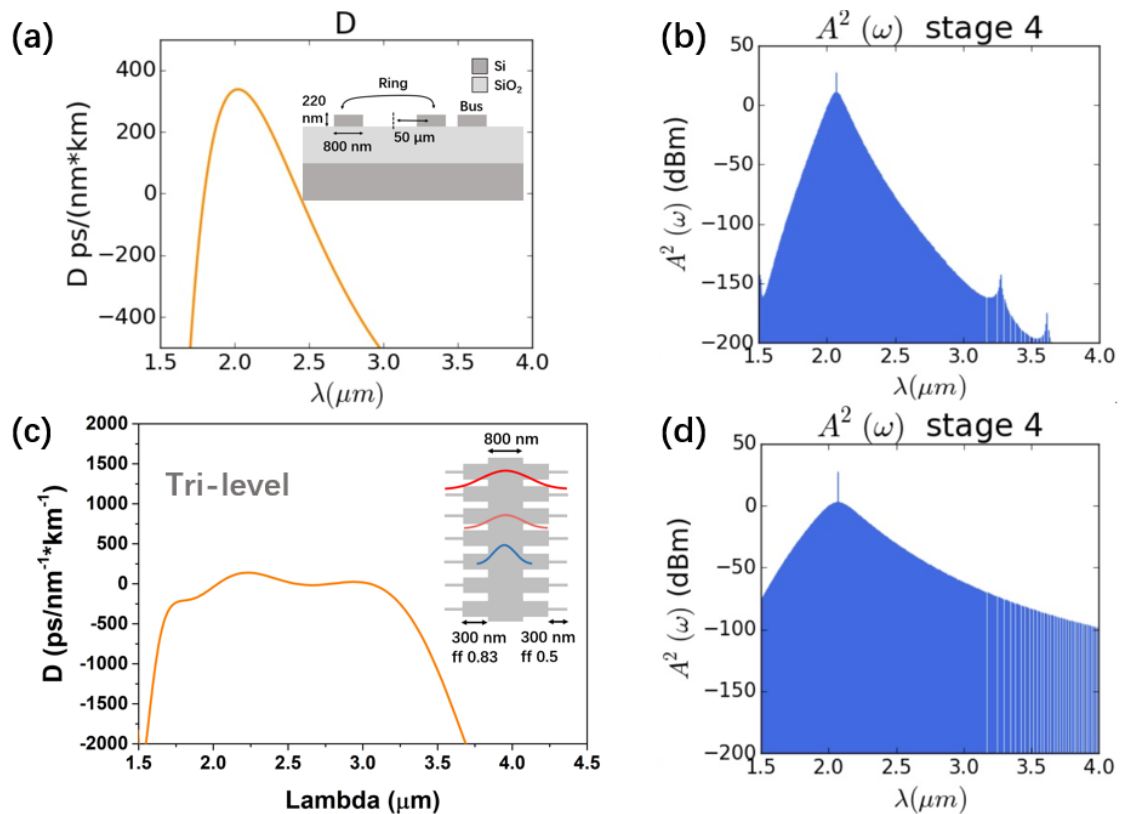
Figure 9. (a) Dispersion et (b) spectre de peigne à soliton unique correspondant au guide d'onde SOI qui Figure dans l'encadré. (c) Dispersion et (d) spectre du peigne à soliton unique correspondant au guide d'ondes à limite auto-adaptative (SAB). L'épaisseur du silicium et la période sont toutes deux fixées à 340 nm et 240 nm. D'autres paramètres sont affichés dans les encadrés.

Conclusion

L'axe principal que nous avons développé a été d'essayer de montrer que la combinaison de l'optique sub-longueur d'onde et des non-linéarités peut apporter des solutions à plusieurs verrous de la conception de fonctions non linéaires intégrées. Ces travaux ont ainsi ouvert des perspectives en termes de modulation électro-optique via le silicium contraint, pour laquelle il sera néanmoins nécessaire de réaliser une ingénierie de guidage afin de renforcer la susceptibilité nonlinéaire effective ($\chi_{eff}^{(2)}$) et toute la gamme des effets optiques non linéaires de troisième ordre ($\chi_{eff}^{(3)}$). Il est clair

que les degrés de liberté apportés par les structures sub-longueur d'onde sont non seulement profitables aux circuits photoniques passifs qui ont été intensivement développés au cours des dix dernières années, mais qu'elles présentent également un fort potentiel pour la réalisation de fonctions actives. Les technologies de fabrication en constante évolution donnent par ailleurs à beaucoup d'idées anciennes un nouveau souffle. Par exemple, sans les structures de guides d'ondes sub-longueur d'onde, la condition de guidage à confinement auto-adaptatif proposée serait difficile à réaliser. Dans un avenir proche, nous nous concentrerons sur la fabrication et le test de guides d'ondes SAB pour le mélange à quatre ondes, et sur la réalisation de résonateurs à guides SAB pour la génération de peignes de fréquence Kerr, avec comme point de mire ultérieur l'exploration d'applications en spectroscopie et métrologie sur puce.

Publications

[1] J. Zhang, V. Pelgrin, C. Alonso-Ramos, L. Vivien, S. He and Eric Cassan, "Trimming and ultra-wide bandwidth expansion of silicon frequency comb spectra with self-adaptive boundary waveguides," *Arxiv*, 190.11774, 2019.

[2] J. Zhang, C. Alonso-Ramos, L. Vivien, S. He and Eric Cassan, "Self-adaptive waveguide boundary for inter-mode four-wave mixing," *Journal of Selected Topics in Quantum Electronics*, 26(2): 5100108, 2019.

[3] J. Zhang, X. Leroux, E. Duran-Valdeiglesias, C. Alonso-Ramos, D. Marris-Morini, L. Vivien, S. He, E. Cassan, "Generating Fano Resonances in a Single-Waveguide Silicon Nanobeam Cavity for Efficient Electro-Optical Modulation," *ACS Photonics*, 5:4229, 2018.

[4] J. Zhang, J. Rönn, W. Zhang, A. Matikainen, X. Leroux, C. Alonso-Ramos, Z. Tu, H. Lipsanen, N. Vulliet, F. Boeuf, L. Vivien, Z. Sun and E. Cassan, "Ultra-high on-chip optical gain in erbium-based hybrid strip waveguides," under review.

[5] C. Alonso-Ramos, X. Leroux, J. Zhang, D. Benedikovic, V. Vakarin, E. Durán-Valdeiglesias, D. Oser, D Pérez-Galacho, F. Mazeas, L. Labonté, S. Tanzilli, É. Cassan, D. Marris-Morini, P. Cheben and L. Vivien, "Diffraction-less propagation beyond the sub-wavelength regime: a new type of nanophotonic waveguide ," *Sci. Rep.*, 9:5347, 2019.

[6] J. Zhang, W. Zhang, E. Duran-Valdeiglesias, C. Alonso-Ramos, X. Leroux, L. Vivien and E. Cassan, "Nanobeam cavity engineering for the realization of active functions in integrated Si photonics," *OEDI*, OT3A.4, 2018.

ÉCOLE DOCTORALE

**Physique et ingénierie :
électrons, photons,
sciences du vivant (EOBE)**

universite
PARIS-SACLAY

Titre : Ingénierie des sous-longueurs d'onde de guides d'ondes et de cavités en silicium pour la photonique non linéaire

Mots clés : Photonique non linéaire; sous-longueur d'onde; guides d'ondes et cavités

Résumé :

Les effets Pockels de deuxième ordre et les effets Kerr de troisième ordre font partie des effets importants exploités pour la modulation de la lumière et la génération de sources dans les plateformes technologiques de la photonique intégrée. Pour tirer parti de ces non-linéarités en photonique au silicium, l'utilisation de structures optiques sub-longueurs d'onde a été explorée. Dans ce contexte, ce travail de thèse s'est concentré sur deux aspects principaux, notamment : 1) L'exploration d'un nouveau schéma de cavité photonique pour tirer profit de l'effet Pockels électro-optique dans les structures de silicium contraint pour la réalisation de modulateurs ultra-rapides à faible consommation ; 2) L'exploration d'une nouvelle famille de guides d'ondes conduisant à une satisfaction automatique des lois de conservation énergie/vecteur d'onde pour la génération de peignes de fréquence Kerr au sein des plateformes photoniques intégrées (notamment silicium).

Pour améliorer les performances des modulateurs optiques Si résonants intégrés, nous avons mis au point un nouveau résonateur à cavité de Fano qui, grâce à une ingénierie sub-longueur d'onde (λ=1.55µm), a permis d'obtenir simultanément un taux d'extinction élevé (23 dB) avec un faible facteur Q de seulement 5600, et caractérisé par une très faible consommation électrique inférieure à 5 fj/bit quand on utilise l'effet de modulation par dispersion plasma des porteurs libres. Nous avons étendu la méthode à la conception d'une structure de modulation Fano en silicium contraint dont les performances souffrent traditionnellement de la faible amplitude de l'effet Pockels induit par la déformation exploitée et des pertes micro-ondes considérables dues à des composants de grande surface.

Au moyen du résonateur Fano ultra-compact à structuration sub-longueur d'onde, une amélioration d'environ 200 fois/60 fois (facteurs Q de 32000/5600) du rapport d'extinction de modulation avec la même tension de commande a été théoriquement prévue.

Pour améliorer l'exploitation des non-linéarités Kerr des structures silicium, nous avons proposé une nouvelle famille de guides d'ondes optiques pour satisfaire automatiquement les lois de conservation de l'énergie et du vecteur d'onde des procédés de mélange à quatre ondes (FWM). La conception de la section des guide d'ondes est basée sur un principe hérité des puits quantiques et des concepts hérités des structures sub-longueur d'onde pour la réalisation des profils d'indice particuliers. En nous basant sur ces guides d'ondes spécifiques en terme de dispersion chromatique, nous les avons appliqués à la modélisation des micro peignes de fréquence (en utilisant des résonateurs à micro anneaux) en résolvant l'équation non linéaire pertinente (Lugiato-Lefever) pour analyser de façon dynamique le processus de génération du spectre des peignes à solitons dans diverses configurations. En complément de ce modèle, les guides d'ondes sub-longueur d'onde à accord de phase automatique ont été considérés pour étendre la largeur de bande des peignes de fréquence à solitons, démontrant une largeur de bande élargie et une meilleure flexibilité dans la réalisation des peignes de fréquence relativement aux démonstration des travaux précédents.

Dans l'ensemble, l'une des caractéristiques dominantes de notre étude a été de contribuer à montrer que les structures photoniques sub-longueur d'onde pouvaient apporter des solutions concrètes aux problèmes utiles à la réalisation de fonctions non linéaires sur puce.

ÉCOLE DOCTORALE

**Physique et ingénierie :
électrons, photons,
sciences du vivant (EOBE)**

Les nano-structures sub-longueur d'onde permettent non seulement une amélioration des circuits photoniques passifs, sujet intensivement développé depuis dix ans, mais ont également un fort potentiel pour la réalisation des fonctions actives. Cette boîte à outils de structures sub-longueur d'onde est décisive dans la pratique pour la réalisation concrète de fonctions optiques nonlinéaires intégrées, en particulier en photonique silicium.

Title : Subwavelength engineering of silicon waveguides and cavities for nonlinear photonics

Keywords : Nonlinear photonics; subwavelength; waveguides and cavities;

Abstract :

Second-order Pockels and the third-order Kerr effects are among the important effects exploited for light modulation and light generation in integrated photonic platforms. To take advantage of these nonlinearities in silicon photonics, especially due to the lack of second order effect in bulk Si, the use of subwavelength optical structures is explored. In this context, this thesis work has focused on two main aspects, including: 1) Exploration of a novel photonic cavity scheme to take benefit of the electro-optical Pockels effect in strained Si structures for the realization of ultra-fast lower-consumption compact silicon modulators; 2) Exploration of a new family of waveguides leading to an automatic satisfaction of energy/momentum conservation for the purpose of Kerr frequency comb generation in integrated photonic platforms.

For improving the performances of integrated silicon resonant optical modulators, we have developed a novel Fano cavity resonator enabled by sub-wavelength engineering, leading simultaneously to high extinction ratio (23 dB) with a small Q factor of only 5600, and characterized by an ultra-low power consumption of less than 5 fj/bit when relying on the free carrier plasma dispersion effect. We have further extended the method to design a strained silicon Fano modulation structure which performances traditionally suffer from the weak amplitude of the exploited strain-induced Pockels effect and from considerable microwave losses due to large footprint components. By means of the proposed ultra-compact subwavelength structured Fano resonator, around 200-fold/60-fold (Q factor of 32000/5600) improvement on the modulation extinction ratio with the same driven voltage was theoretically predicted.

For improving the exploitation of silicon Kerr nonlinearities, we have proposed a novel family of graded index optical waveguides intending to automatically fulfill the energy and momentum conservation laws of four-wave mixing processes. The design of the waveguide section is based on a principle inherited from quantum wells of wave mechanics and concepts inherited from subwavelength structures for the practical realization of the rather particular index profiles. Standing on these specific waveguides in term of light dispersion, we have applied them to the modeling of frequency micro-combs (e.g. frequency combs generated using micro-ring resonators and a CW light source) by solving the nonlinear relevant equations (Lugiato-Lefever) to dynamically analyze the soliton comb spectrum generation process in various configurations. On top of this model, the specifically automatically phase-matched sub-wavelength-enabled graded-index waveguides were considered to trim and extend the bandwidth of silicon soliton frequency combs, demonstrating enlarged bandwidth and improved spectrum design flexibility with respect to previous works.

Overall, one of the dominant features of our study was to contribute to showing that sub-long wavelength photonic structures could provide concrete solutions to problems useful for the realization of on-chip non-linear functions. Subwavelength/nano structures not only benefit to passive photonic circuits which have been intensively developed in the past ten years, but also show strong potentials in the realization of active functions. This subwavelength toolbox is decisive in practice for the concrete achievement of the objectives pursued.